Analysis and Synthesis of Multi-Qubit, Multi-Mode Quantum Devices

Von der Fakultät für Mathematik, Informatik und Naturwissenschaften der RWTH Aachen University zur Erlangung des akademischen Grades eines Doktors der Naturwissenschaften genehmigte Dissertation

vorgelegt von

M. Sc.

Firat Solgun

aus Istanbul (Türkei)

Berichter: Universitätsprofessor Dr. David DiVincenzo
Universitätsprofessor Dr. Guido Burkard

Tag der mündlichen Prüfung: 27.03.2015

To my parents,

Summary

In this thesis we propose new methods in multi-qubit multi-mode circuit quantum electrodynamics (circuit-QED) architectures. In Chapter 2 we describe a direct parity measurement method for three qubits, which can be realized in 2D circuit-QED with a possible extension to four qubits in a 3D circuit-QED setup for the implementation of the surface code. In Chapter 3 we show how to derive Hamiltonians and compute relaxation rates of the multi-mode superconducting microwave circuits consisting of single Josephson junctions using an exact impedance synthesis technique (the Brune synthesis) and applying previous formalisms for lumped element circuit quantization. In the rest of the thesis we extend our method in Chapter 3 to multi-junction (multi-qubit) multi-mode circuits through the use of state-space descriptions which allows us to quantize any multiport microwave superconducting circuit with a reciprocal lossy impedance response.

Zusammenfassung

Wir entwerfen in dieser Arbeit neue Methoden für Architekturen der Quantenelektrodynamik elektrischer Leiter (circuit-QED) mit mehreren Eigenmoden, die aus mehreren Qubits bestehen.

Wir beschreiben im zweiten Kapitel eine direkte Messmethode für die Parität eines Systems dreier Qubits, die durch eine Architektur zweidimensionaler circuit-QED realisiert werden kann. Dieses Verfahren kann auf vier Qubits in einer dreidimensionalen circuit-QED Architektur erweitert werden. Mit dieser Methode kann der Oberflächen-Code (surface code) verwirklicht werden.

Im dritten Kapitel zeigen wir, wie für den supraleitende Stromkreis mit mehreren Eigenmoden, der aus einem einzelnen Josephson-Kontakt besteht und im Mikrowellenbereich operiert, Hamilton-Operatoren abgeleitet und Relaxationsraten berechnet werden können. Wir verwenden eine exakte Methode zur Impedanzsynthese (die Brune-Synthese) und verwenden bekannte Methoden für die Quantisierung von konzentrierten Elementen.

Im weiteren Teil der Arbeit erweitern wir unsere Methode aus dem dritten Kapitel für die Zustandsraumdarstellung mehrerer Josephson-Kontakte (das heißt mehrere Qubits), die jeweils mehrere Eigenmoden haben. Diese Methode erlaubt es uns jedes supraleitende Bauteil aus dem Mikrowellenbereich, das mehreren Tore hat, mit einer umkehrbaren, verlustbehafteten Impedanz zu quantisieren.

Contents

CHAPTER 1

Introduction

Quantum computing is a new computing paradigm which allows the solution of certain types of computationally hard problems which would otherwise be impossible even with the fastest supercomputer in the world. This includes the factoring problem [1] on which the most popular secure communication scheme in use today is based. This security scheme is used for example to encrypt online credit card transactions which constitutes a big portion of the total volume of money transfers today. Fortunately quantum computing has applications in many other disciplines which might be more useful for mankind than breaking cryptosystems. This includes quantum chemistry in which a quantum computer might help to discover new drugs by simulating molecules which might be otherwise impractical to experiment with in a lab or to simulate with a classical computer [2, 3].

1.1 Bits and Qubits

The bit is the currency of all classical information processing machines such as our laptops, mobile phones or the fastest supercomputer in the world. It can be in one of two definite states which is usually denoted by "0" and "1". The bit is physically encoded in transistor electronics as in the registers of computer processors, in computer memories or in a magnetic medium as in harddisks. A quantum computer however operates on quantum bits or "qubits". A qubit is the encoding of information in a two level quantum system. It can be in one of the states $|0\rangle$ and $|1\rangle$ or in a superposition of them $|\psi\rangle = \alpha\,|0\rangle + \beta\,|1\rangle$ which is allowed by quantum mechanics where α and β are complex numbers satisfying $|\alpha|^2 + |\beta|^2 = 1$. Any state in the Hilbert space of a single qubit can be described by a point on the Bloch sphere shown in Fig. (1.1). The state of a multi-qubit quantum processor lies in the tensor product of single qubit Hilbert spaces and information can be stored in an entangled state which has no classical counterpart. An entangled state of a multi-qubit system is a state which can not be decomposed into a tensor product of individual qubit states. It is believed that it this ability of the quantum computer to explore those large multi-qubit Hilbert spaces that brings its computational power over the classical computers.

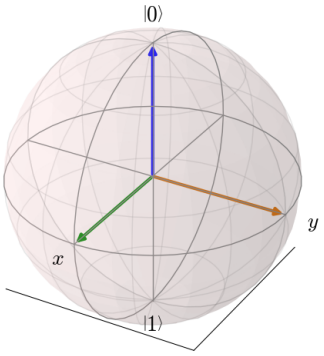

Figure 1.1: The Bloch sphere (image generated by the software package QuTiP [4]). Any single qubit state $|\psi\rangle = \alpha|0\rangle + \beta|1\rangle$ can be uniquely mapped to a point on the Bloch sphere. Three different states are shown on the Bloch sphere. $|0\rangle$ state (blue vector) corresponds to the north pole of the Bloch sphere. The state on the x-axis represented with a green vector is the quantum state $\psi_x = \frac{1}{\sqrt{2}}(|0\rangle + |1\rangle)$. The state shown on the y-axis with an orange arrow is the state $\psi_y = \frac{1}{\sqrt{2}}(|0\rangle + i|1\rangle)$. The state $|1\rangle$ is at the south pole of the Bloch sphere (not shown with an arrow vector).

Unfortunately quantum states are fragile. They correspond to the quantized states of systems consisting of a few degrees of freedom. Those degrees of freedom are coupled to the outside world which is a macroscopic system usually modeled as consisting of an infinite number of degrees of freedom. The quantum system can not be decoupled completely from its environment since it needs to be addressed to do quantum gates and to be read-out. Hence it loses energy in an irreversible way by interacting with its environment. This process is called relaxation. The same process causes also fluctuations in the system parameters such as the qubit frequency. This leads to dephasing which is the loss of phase information of the qubit or the coherence of the quantum state. Relaxation and dephasing processes are together referred to as decoherence. It is the decoherence that prevented the quantum computer to become a reality up to present.

1.2 Quantum Error Correction

Error correction is needed to correct errors happening due to the noise generated in decoherence channels that couple to qubits. In [5] Shor proposed the first quantum error correcting code by showing that the state of a single qubit can be protected

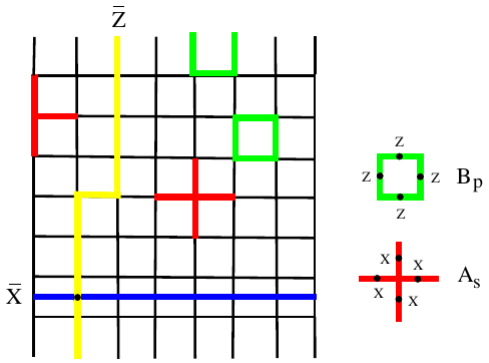

Figure 1.2: (Image taken from [8]) The square lattice (in general of size $L \times L$) of the surface code with logical operators $\bar{X}$ and $\bar{Z}$ and parity operators A_s and B_p. Parity check operators are star A_s of X-checks and plaquette B_p of Z- checks acting locally on four qubits. At the boundaries they act on only three qubits. The logical $\bar{X}$ is an X-string connecting left to right boundary and the logical $\bar{Z}$ is a Z-string connecting top to bottom boundary.

against bit-flip and phase-flip errors by encoding it in a nine-qubit state. Shor has also showed [6] that the quantum computer can be made fault-tolerant at the cost of an overhead. That is he showed that by introducing redundancy through the use of quantum error correcting codes a quantum computation can be completed free of errors if the error rate of individual components are below a certain threshold. Since then many other quantum error correcting codes have been proposed.

Among them is the "Surface Code" which is widely accepted today as being the code with the most realistic requirements that the first faul-tolerant quantum processors might be built on. Surface code requires only local interactions and has a relatively high error threshold (estimated to be around 1%). It is derived from Kitaev's original proposal [7] to implement the quantum computer in topologically protected 2D quantum systems. It is a stabilizer code on a square lattice as shown in Fig. (1.2) with qubits sitting on the edges. Parity check operators are plaquette operators B_p consisting of local Z-checks on four qubits and star operators A_s of X-checks on neighboring four qubits as shown on Fig. (1.2). The logical $\bar{X}$ operator is any string of X's connecting left and right boundaries and logical $\bar{Z}$ is any string of Z's connecting the top boundary to the bottom. In Chapter (1.8) down below we will discuss a proposal on how to implement the surface code as a skew-lattice in the circuit-QED architecture (see Chapter (1.6)).

1.3 Superconducting Electronics

There are many proposals to realize the quantum processor in a physical system. One such system is trapped ions where the qubits are encoded in the electronic states of ions trapped by lasers. Another proposal is to use electron spins in semiconductor structures. Single electrons are captured in confined regions by applying potentials at metalic gates. Here our focus will be on the realization of quantum processors in superconducting electronics.

Below a critical temperature T_c electrons in a superconductor form Cooper pairs and condense into a quantum state that can be described by a wavefunction with a single degree of freedom φ, the phase of the superconductor. Such a state is robust enough to exhibit quantum behavior at the macroscopic scale.

Two superconductors separated by an insulating barrier form a "Josephson junction". If the insulating barrier is thin enough Cooper pairs can tunnel coherently through the barrier to form a supercurrent I which is related to the phase difference δ across the junction, i.e. the difference of the phases of superconductors at each side of the junction, by the following formula

$$I = I_c sin\delta \tag{1.1}$$

where I_c is the critical current of the junction. This relation corresponds to a nonlinear inductor. The voltage V across the junction is related to the phase difference δ by the Josephson relation

$$V = \frac{\Phi_0}{2\pi}\dot{\delta} \tag{1.2}$$

where $\Phi_0 = h/2e \simeq 2.07 \times 10^{-15}\, T \cdot m^2$ is the flux quantum.

The Josephson junction is a nonlinear non-dissipative circuit element which provides the anharmonicity needed to get qubit levels in superconducting circuits.

Superconducting qubit coherence times have increased dramatically over the 16 years since the first experimental demonstration of the coherent superposition of charge states in a Cooper Pair box circuit [9]. Research has been done on designing lumped element circuits with Josephson junctions to make qubits less susceptible to noise. This research has resulted in a variety of superconducting qubit circuit designs such as the Cooper Pair Box (CPB) [10], the flux qubit [11], the phase qubit [12], the Transmon [13] and more recently the Fluxonium [14] which are arranged in the table in Fig. (1.3) in a Mendeleev's Periodic Table like configuration. In the section below we will review the research that has led to the invention of the Transmon qubit which has been the most popular qubit for the experiments running in the labs around the world nowadays due its simplicity of design and its long coherence times.

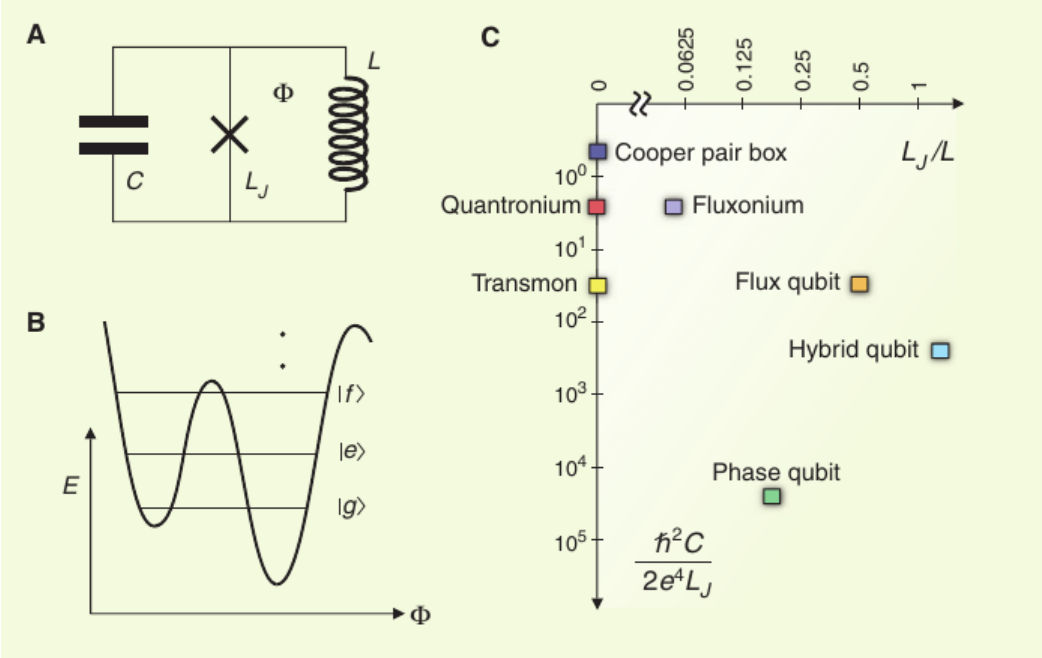

Figure 1.3: A Mendeleev-like Table for Superconducting Qubits (image taken from [15]). (A) Various superconducting qubit circuits can effectively be represented by a parallel connection of a capacitor C, a Josephson junction L_J and an inductor L. (B) Potential shapes can be engineered by tuning the circuit parameters in (A). (C) Superconducting qubits arranged in 2D in analogy with the Periodic Table of Elements as a function of the ratios of circuit parameters in (A). The vertical axis is the axis of the ratio E_J/E_C.

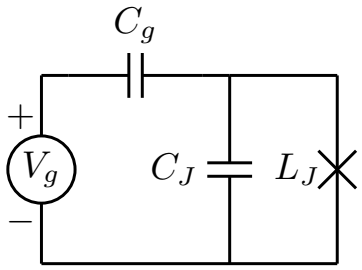

Figure 1.4: Circuit representation of the Cooper Pair Box. The Josephson junction with capacitance C_J and linear inductance L_J is biased by a voltage source through a gate capacitance C_g. A superconducting island is formed by the right plate of the gate capacitor C_g and the upper electrode of the Josephson junction. Cooper pairs tunnels to this island through the Josephson junction. In the limit $E_C \gg E_J$ the number of Cooper pairs on the island is a good quantum number.

1.4 Superconducting Qubits

The Cooper Pair Box (CPB) is one of the first superconducting qubits. Its circuit representation is shown in Fig. (1.4). It has a Hamiltonian of the following form

$$\hat{H} = \frac{\left(\hat{Q} - C_g V_g\right)^2}{2C_\Sigma} - E_J \cos\left(2\pi\hat{\Phi}/\Phi_0\right) \tag{1.3}$$

where $\hat{\Phi}$ is the operator corresponding to the flux across the Josephson junction and $\hat{Q}$ is the operator corresponding to the charge on the superconducting island formed by the right plate of the gate capacitor C_g and the upper electrode of the Josephson junction in Fig. (1.4). $\hat{\Phi}$ and $\hat{Q}$ are conjugate variables satisfying $\left[\hat{\Phi}, \hat{Q}\right] = i\hbar$. $C_\Sigma = C_g + C_J$ is the total capacitance and $E_J = I_c\Phi_0/2\pi$ is the Josephson energy. Deriving the Hamiltonian of a lumped element superconducting circuit - even for a circuit as simple as the CPB - is not a trivial task and one usually needs to resort to formalisms based graph theoretical network analysis to get the Hamiltonians [16, 17, 18]. One can rewrite the CPB Hamiltonian in Eq. (1.3) as

$$\hat{H} = 4E_C\left(\hat{n} - n_g\right)^2 - E_J\cos\left(\hat{\varphi}\right) \tag{1.4}$$

where $\hat{n} = \hat{Q}/2e$ is the operator counting the number of Cooper pairs that have been tunneled into the superconducting island and $\hat{\varphi} = 2\pi\hat{\Phi}/\Phi_0$ is the phase operator conjugate to $\hat{n}$. The effective gate charge n_g is defined by $n_g = C_g V_g/2e$

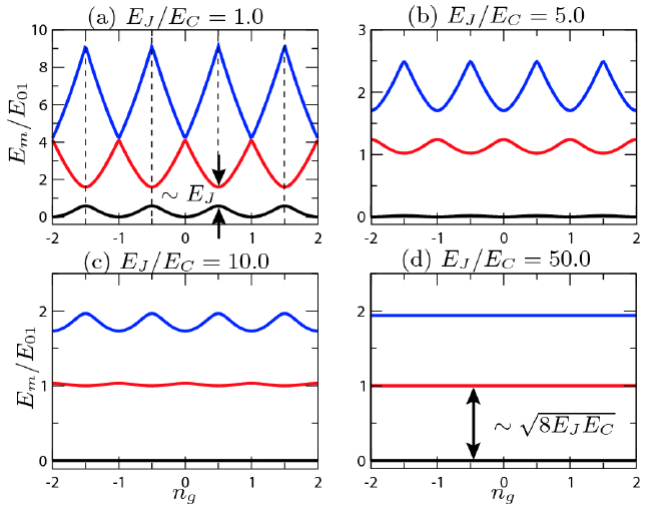

Figure 1.5: (Taken from [13]) Evolution of the charge dispersion for the CPB Hamiltonian in Eq. (1.4) from $E_J/E_C = 1$ to the Transmon regime $E_J/E_C = 50$. The first three energy levels are plotted (in units of the transition energy E_{01} between $|0\rangle$ and $|1\rangle$ states) as a function of the offset gate charge n_g for four different values of the ratio E_J/E_C. Vertical arrows indicate charge sweet spots.

and the charging energy by $E_C = e^2/2C_\Sigma$.

The CPB operates in the $E_C \gg E_J$ regime which makes it highly sensitive to the charge noise, i.e. to the fluctuations in the gate charge n_g. This leads to dephasing since the qubit frequency corresponding to the energy difference between ground state and first excited state of the Hamiltonian in Eq. (1.4) is a function of the gate charge n_g as shown in Fig. (1.5). This problem has been cured first by the introduction of Quantronium [19] which is a CPB voltage biased at a sweet spot where the qubit is insensitive to first order to the charge noise.

1.5 The Transmon Qubit

Later it has been realized that by operating the CPB in the $E_J \gg E_C$ regime it is possible to make the energy levels of the CPB Hamiltonian in Eq. (1.4) insensitive to the charge noise for all values of charge bias n_g as shown in Fig. (1.5). The CPB circuit operating at the $E_J \gg E_C$ limit has been named the "Transmon" qubit [13]. The $E_J \gg E_C$ limit has been achieved by shunting the Transmon by a large capacitor C_J. The charge sensitivity is shown [13] to be reduced exponentially as a function of the energy ratio E_J/E_C. The price paid for this exponential reduction

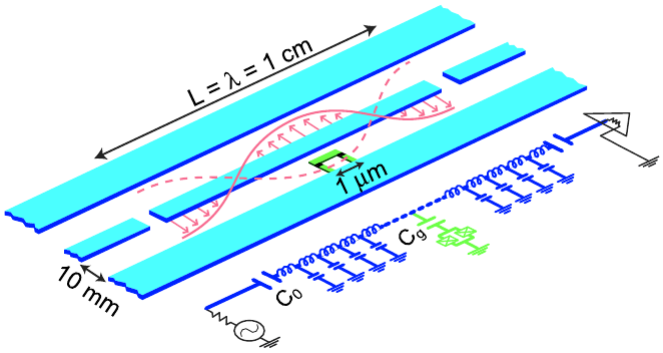

Figure 1.6: The circuit QED Architecture (image taken from [20]). A coplanar waveguide cavity resonator formed by interrupting the center line by capacitive gaps at each end. On each side of the center line are the ground planes. The qubit is placed between the center line and ground planes and is coupled to the electric field of electromagnetic mode in the cavity resonator. The qubit is placed at an antinode of the electric field to give a strong dipole coupling to the photon in the resonator. The coupling strength g is higher than the rate κ of photon loss in the cavity so that the microwave photon has enough time to interact with the qubit before getting lost.

is a decrease in the anharmonicity of qubit which is only polynomial in the ratio E_J/E_C. Hence for $E_J/E_C \simeq 50$ one already gets flat energy levels insensitive to the charge noise while still keeping around 5% of anharmonicity which corresponds to 250 MHz for a qubit frequency of 5 GHz .

1.6 The Circuit QED Architecture

By placing the Transmon qubit at a voltage maximum in the area between two metallic conductors of a CPW (Co-Planar Waveguide) resonator as shown in Fig. (1.6) one can achieve strong coupling of the qubit to the microwave photon trapped in the resonator. Transmon's capacitance is coupled to the electric field of the electromagnetic mode in the cavity by an electric dipole interaction. Such a system is analogous to the cavity quantum electrodynamics setups of quantum optics where atoms are coupled to the modes of an optical cavity; hence the name "circuit quantum electrodynamics (circuit QED)" [20]. In circuit QED architecture the qubit plays the role of the atom and the microwave field in the resonator plays the role of the light. Although atoms in cavity QED experiments are flying through

the cavity the qubits are stationary in the circuit QED architecture.

Assuming a two-level system for the superconducting qubit circuit one can write a Jaynes-Cummings Hamiltonian for the circuit QED structure in Fig. (1.6)

$$\hat{H} = \hbar\omega_r \left(\hat{a}^\dagger \hat{a} + \frac{1}{2}\right) + \frac{\hbar\omega_q}{2}\hat{\sigma}_Z + \hbar g \left(\hat{a}^\dagger \hat{\sigma}_- + \hat{a}\hat{\sigma}_+\right) \tag{1.5}$$

where $\hat{a}$ is the operator that destroys a photon in the cavity, ω_r the cavity resonance frequency, $\hat{\sigma}_Z$ is the Pauli Z operator corresponding to the qubit, ω_q the qubit frequency, g the qubit-cavity coupling rate and $\hat{\sigma}_-$ and $\hat{\sigma}_+$ are lowering and raising operators for the qubit, respectively.

In circuit-QED qubits are usually operated in the dispersive regime, that is when the qubit frequency ω_q is detuned from resonator frequency ω_r such that $|\omega_q - \omega_r| \gg g$. When operated in the dispersive regime the qubit embedded inside the resonator is protected from decoherence since the microwave resonator suppress spontaneous emission rate of the qubit by acting as a Purcell filter.

In the dispersive regime of circuit QED one can re-write the Hamiltonian in Eq. (1.5) for the qubit-cavity system to the second order in the coupling rate g

$$\hat{H} = \hbar \left(\omega_r + \frac{g^2}{\triangle}\hat{\sigma}_Z\right)\hat{a}^\dagger \hat{a} + \frac{\hbar}{2}\left(\omega_q + \frac{g^2}{\triangle}\right)\hat{\sigma}_Z \tag{1.6}$$

where $\triangle = (\omega_q - \omega_r)$ is cavity-qubit detuning. From the Hamiltonian in Eq. (1.6) we see that the cavity resonant frequency ω_r is shifted by an amount $\pm\frac{g^2}{\triangle}$ depending on the state of the qubit. This feature of the circuit QED Hamiltonian is used to do a quantum non-demolition (QND) measurement of the qubit state. The QND measurement of the qubit state is done by driving the cavity by a probe signal of appropriate power at the cavity resonance frequency ω_r and measuring the phase of the transmitted signal by homodyne detection. The transmitted signal then acquires different phases depending on the state of the qubit. To see why such a measurement is of QND character we note that the qubit operator $\hat{\sigma}_Z$ that's been probed is a constant of motion and commutes with the interaction term $\hat{H}_{int} = \frac{g^2}{\triangle}\hat{\sigma}_Z\hat{a}^\dagger\hat{a}$ in the Hamiltonian in Eq. (1.6), i.e. $\left[\hat{\sigma}_Z, \hat{H}_{int}\right] = 0$.

Single qubits rotations are simply done by driving the microwave resonator at the qubit frequency. To do two-qubit gates the cavity resonator is used as a quantum bus to entangle qubits separated by distances at the scale of centimeters. Two qubits placed along the center line of a CPW resonator can interact through the virtual excitations in the resonator mode. In this case one can write an effective Hamiltonian of the following form for two qubits detuned from the resonator but in resonance with each other [20]

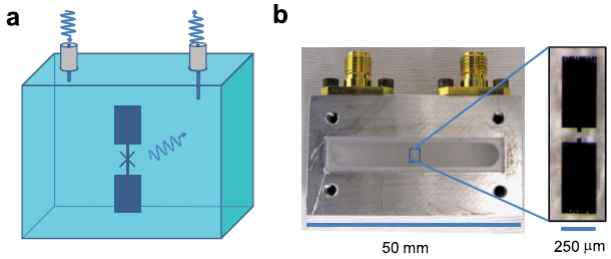

Figure 1.7: The 3D Transmon (Image taken from [22]).

$$\hat{H}_{2Q} = \hbar\left(\omega_r + \frac{g^2}{\triangle}\hat{\sigma}_Z^a + \frac{g^2}{\triangle}\hat{\sigma}_Z^b\right)\hat{a}^\dagger\hat{a} + \tag{1.7}$$

$$+ \frac{1}{2}\hbar\left(\omega_a + \frac{g^2}{\triangle}\right)\hat{\sigma}_Z^a + \frac{1}{2}\hbar\left(\omega_b + \frac{g^2}{\triangle}\right)\hat{\sigma}_Z^b + \hbar\frac{g^2}{\triangle}\left(\hat{\sigma}_+^a\sigma_-^b + \hat{\sigma}_-^a\sigma_+^b\right) \tag{1.8}$$

where a and b are qubit labels. See [20] for more details on the circuit-QED architecture and [21] for different protocols to do single and two-qubit gates in the circuit-QED architecture.

1.7 The 3D Transmon

For the Transmon qubits coupled to 2D circuit-QED structures as shown in Fig. (1.6) it was suspected that one of major loss channels was the dielectric losses happening at the metal/dielectric interfaces. In Fig. (1.7) the Transmon is put in the middle of a 3D Aliminium cavity with a large dipole antenna coupling the Transmon to the fundamental mode of the cavity. By taking the feature sizes of the circuit-QED system to such an extreme the ratio of the electromagnetic energy stored in the dielectric medium to total energy decreases. In such a case one would expect a reduction in the dielectric loss hence an increase in the coherence time of the Transmon. This is exactly what is measured in [22] where the 3D architecture for the Transmon qubit was first proposed. 3D Transmon is the superconducting qubit exhibiting the longest coherence times as of today.

1.8 A Two Dimensional Fabric for Fault-Tolerant Quantum Computation

The quantum computer will need at least thousands and ideally millions to billions of qubits to solve a practical problem which is impossible with the classical

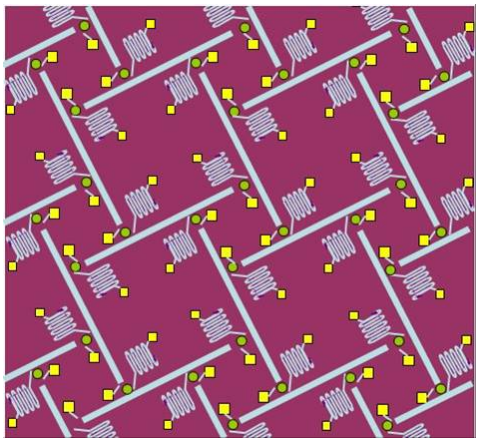

Figure 1.8: The skew-lattice implementation for the surface code in the circuit-QED architecture originally proposed in [23]. Green dots are qubits. Each qubit is coupled to only two bus resonators (grey rectangles). Yellow squares are I/O ports.

computers. At the lowest hardware level the quantum processor should satisfy five DiVincenzo criteria proposed in [24]. Since physical qubits won't be ideal the quantum processor will need to run a quantum error-correction protocol at a higher level. As we noted in Chapter (1.2) above the most practical quantum error-correction scheme known today is the surface code. The ultimate goal of various research groups around the world is to implement the surface code in their physical architecture of choice for the quantum computer. With coherence times for the qubits approaching the threshold the question now is how to scale things up without sacrificing the performance of individual components.

For superconducting qubit systems one answer to this question is given in [23]. It is based on a tiling of the 2D plane in a skew-lattice with cells consisting of superconducting qubits and resonators coupled according to the circuit-QED architecture as shown in Fig. (1.8). Each qubit (green dots) is only coupled to two bus resonators (grey bars) and has its own individual bias, drive/readout lines (yellow squares are I/O ports).

In Fig. (1.9) we see a 3-qubit quantum processor recently designed by IBM which is the result of the efforts of implementing the building blocks of the surface code skew-lattice in Fig. (1.8). Three superconducting transmon qubits are coupled to two CPW resonators. Airbridges are used to short ground planes on each side of the transmission lines' central conductors to suppress couplings of spurious modes to the qubits. The spurious modes cause decoherence through the radiative loss.

As is apparent from the Fig. (1.9) scaling the quantum processor up will be a big scientific and engineering challenge. As the complexity of the circuit increases

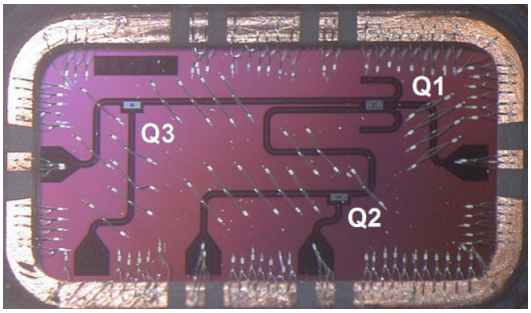

Figure 1.9: IBM's three qubit quantum processor chip. Qubits Q1, Q2 and Q3 are coupled to two transmission line resonators in the 2D circuit-QED architecture implemented in a CPW structure. Each qubit has its own bias line and each resonator has a separate drive line. Airbridges shorting different ground planes are used to suppress spurious modes which are a potential source of radiation loss.

spurious modes appear in microwave waveguide circuits as in Fig. (1.9). Qubits coupled to those spurious modes lose energy which results in decoherence [25]. Solutions like airbridges are fine for small scale processors. However to scale those small quantum processor up to the level of the surface code in Fig. (1.8) one needs to understand better the multi-mode microwave interactions happening in those superconducting circuits.

Multiple modes however are not always a nuisance for the quantum engineer. Superconducting quantum circuits can also be engineered to benefit from the multi-mode physics to design new types of measurement and two-qubit gate protocols. In Chapter (2) we propose a new multi-qubit direct parity measurement protocol in circuit-QED which needs two or more almost degenerate microwave modes. The direct parity measurement protocol removes the need for CNOT gates which are required by the standard implementations of the surface code. For another example of the use of multiple microwave modes see [26] where they describe how to use multi-mode physics in the circuit-QED architecture for the benefit of getting higher contrast in two-qubit gates.

As we noted earlier in this chapter there has been a rapid progress in the performance of superconducting qubit circuits in the last two decades. With the Q-factors of superconducting qubit and cavity components getting closer to the error-correction threshold we need highly accurate models for their design, optimization and predictability. This is the main focus of this thesis starting from Chapter (3) where we propose new methods to get highly accurate Hamiltonian descriptions of multi-qubit multi-mode low-loss superconducting circuits and show how to do dissipation treatment to estimate relaxation rates in those circuits.

CHAPTER 2

Multi-qubit parity measurement in circuit quantum electrodynamics

In this chapter we present a concept for performing direct parity measurements on three or more qubits in microwave structures with superconducting resonators coupled to Josephson-junction qubits. We write the quantum-eraser conditions that must be fulfilled for the parity measurements as requirements for the scattering phase shift of our microwave structure. We show that these conditions can be fulfilled with present-day devices. We present one particular scheme, implemented with two-dimensional cavity techniques, in which each qubit should be coupled equally to two different microwave cavities. The magnitudes of the couplings that are needed are in the range that has been achieved in current experiments. A quantum calculation indicates that the measurement is optimal if the scattering signal can be measured with near single photon sensitivity. A comparison with an extension of a related proposal from cavity optics is presented. We present a second scheme, for which a scalable implementation of the four-qubit parities of the surface quantum error correction code can be envisioned. It uses three-dimensional cavity structures, using cavity symmetries to achieve the necessary multiple resonant modes within a single resonant structure. The material in this chapter is directly taken from our published work in [27] with minor modifications.

2.1 Introduction

The essence of error correcting either quantum or classical information is parity checking. In all practical quantum error correction codes [28], the error-free state is signalled by parities of a selection of subsets of qubits all being "even"; conversely, the occurrence of "odd" parities indicates a non-trivial *error syndrome*, with which the particular form of errors can be diagnosed. Calculations show that remarkably simple codes are very effective as the substrate of fault tolerant quantum computation; the subsets subjected to parity checks are geometrically local on a two-dimensional lattice. In addition, the weight of the parity checks is low; for the canonical code of this class, the Kitaev toric code [29], the weights of all

checks are four.

It has been standard to assume that a qubit parity should be obtained by computation, in particular by a series of two-qubit quantum logic gates. Thus for the weight-4 case, the circuit involves four controlled-NOT gates from each of the four qubits in succession to a fifth, ancilla qubit. The ancilla then holds the value of the parity (or is, perhaps, in an entangled superposition of the two different parity states), so that a measurement of the ancilla reveals (or fixes) this parity. In this paper, we show that, by use of standard microwave scattering techniques, the parity of a small subset of qubits may be measured *directly*, without the need of an intermediate calculation requiring a logic circuit. We hope that this will simplify the process of error correction, and improve thereby its error robustness.

We first discuss some features of the parity determination that are of a particularly quantum-mechanical character. First, it cannot be trivially assumed that after a quantum measurement records some value, the state of quantum object necessarily still has that value. For example, if a polarization-sensitive photodetector "clicks" to indicate the polarization of the photon, the photon possessing that polarization will have vanished. In quantum mechanics there is a name for measurements for which the quantum object remains in the state that is recorded: these are called *quantum nondemolition* (QND) measurements. Fortunately, there are many implementations of QND-type measurements, and the types of scattering measurements proposed here will have the QND character.

Second, there is a choice of basis involved in defining parity. Thus, while in the classical basis(called the "Z basis" [28]) we would call 0000, 0011, 0110, etc., the even parity states, it is possible to take the basis of the qubit to be, for example $|+\rangle = (|0\rangle + |1\rangle)/\sqrt{2}$ and $|-\rangle = (|0\rangle - |1\rangle)/\sqrt{2}$. In this "X basis", the even parity states are $++++$, $++--$, $+--+$, etc. In fact, both the X- and Z-type parity checks are needed in quantum error correction. We will introduce a parity measurement for just one basis, understanding that it is possible apply one-qubit gates to rotate the qubits so that the parity detection is either of X- or of Z-type. In the superconducting qubit systems that we discuss, these one-qubit rotations can be performed very accurately and quickly.

Third, it is crucial that the parity measurement reveal *only* the parity, and nothing more. For example, the states 0000 and 0011 should both give parity "even", and should be seen as identical in the measurement process. This concept has no meaning in the classical setting, where 0000 and 0011 represent objectively different states. Quantum mechanics permits a state like $(|0000\rangle + |0011\rangle)/\sqrt{2}$, which does not have a specific, definite bit state, but which nevertheless has a definite parity. In fact, we employ here a strengthening of the idea of QND, which traditionally requires only that a quantum state remain in a certain subspace after measurement. For the measurements that we need, the state is to remain

exactly unchanged, and two states with the same parity should reveal nothing of the differences between them.

In quantum physics, this final concept has been given a name, the *quantum eraser* [30]. This name refers to the fact that typically in the course of the measurement process, information is temporarily imprinted on the measurement probe, which is however erased by the end of the measurement process. In interferometry this information is the *welcher weg* ("which path") information which temporarily exists while a photon is moving through the interferometer. This information is erased by the passage of the photon through the final beam splitter of the interferometer. In the implementation we develop below, the measurement probe will temporarily have "which bitstring" information, which, by the time the scattering process is complete, will be all erased, except for a single bit of parity information. We will show explicitly two different microwave protocols which will permit this *quantum eraser condition* to be satisfied; we will in fact precisely quantify the degree to which this condition is fulfilled.

Discussions of parity measurements are not new to quantum computing theory; it was understood almost from the beginning that two-qubit parity measurement permitted the implementation of standard two-qubit logic gates [31]. A wide variety of two-qubit implementations have been proposed, in electron optics [32], for spin qubits in quantum dots [33], and for charge qubits [34]. The previous discussions of two-qubit parity measurement for atoms in optical cavities [35], and for superconducting qubits [36, 37], will be particularly relevant for the present work. Other theoretical work has simulated the details of the parity measurement process [38, 39], and more generally of "joint measurement", in which other two-qubit operators other than the parity are detected. Such joint measurements have been achieved in the area of circuit QED [40, 41, 42, 43], the implementation that we discuss here.

Especially for the application to fault-tolerant error correction [44, 45], it is very important to go beyond two-qubit parity. While quantum error correction codes are known for which two-qubit parity measurements do suffice [46], they are found to have much worse threshold-rate behavior than the Kitaev code [29], which requires 4-qubit checks [47]. The Bacon-Shor codes [48] also permit error correction with only two-bit parity checks, and have rather good error correction performance [49], but cannot achieve fault-tolerant operation by only local operations [50]. Many architectural details of a quantum computer employing the surface code have been worked out [51], and the outlook seems quite favorable [47, 52, 53]. Much less is known about the efficacy of 3-qubit parity measurements for error correction, although there is a very promising, recent preliminary result [54].

Extending existing two-qubit parity measurements to more than two is not trivial. Classically combining many two-bit parity results to obtain a multi-qubit

parity is not permitted, as the overall quantum eraser condition is not satisfied in this case. A real modification of the measurement protocol or of the coupling structure is necessary. For some other existing schemes [36, 37] we see no reasonable extension to more than two qubits; in the case of Kerchhoff *et al.* [35] such an extension is possible, as we note below. There is another related proposal for a multiqubit parity measurement in optical systems [55] based on the acquisition of successive small phase shifts by a probe beam; this scheme seems to require some fine tuning, and has no clear extension beyond three qubits. A very recent proposal shows another technique related to the one we present here for extracting multi-qubit parities [56].

We present here a new solution, requiring a specifically designed cavity (or multi-cavity) structure with multiple, closely spaced resonant modes. We first provide a detailed proposal for performing the 3-qubit parity measurement, with accurate satisfaction of the quantum eraser condition, in circuit quantum electrodynamics using superconducting qubits. In the current work the preferred type of superconducting qubit is the "transmon" type [13], although other types would also be possible [57]. We will always require that the couplings between qubits and microwave resonators be in the well-studied "dispersive regime" [21, 20], in which the qubit transition frequency and the microwave resonant frequency are well separated. In this regime, the qubit gives a state-dependent shift to the resonant frequency of a microwave cavity – one shift for qubit state $|0\rangle$, and a different shift for qubit state $|1\rangle$ (note that state 0 and state 1 are at different energies). In this regime, the requirements of the multi-qubit parity measurement reduce to those of a classical microwave design problem.

Our first proposal requires a particular hardware arrangement, involving a capability that has been developed only in the most recent experimental literature [58, 59]. In particular, we require the qubits involved in a 3-qubit parity measurement each to have equal dispersive coupling to two different resonant modes. In the first version of our proposal described below, these two different modes are realised as the fundamental modes of two different microwave resonators. Crucial for the proposal is that each resonance should occur at nearly (but not exactly) the same frequency. This near-coincidence allows a scattering phase shift to wind through $2 \times 2\pi$ over a narrow range of frequency. For the 4-qubit parity, a winding of 6π is needed, requiring three closely spaced resonant modes to be involved. Our second proposal will deal with this case. We will show that multiple *resonances* need not require multiple *resonators*. This proposal will use the currently popular "3D" cavity [22], but one having a nearly cubical shape so that the three lowest TE_{101}-type modes (see Chap. 10.07 of [60]) are nearly degenerate. We will show a hypothetical scalable implementation of the surface code within this scheme.

2.2 Results – 2D resonant structure

We will first show that the necessary quantum-erasure function can be realized by the choice of circuit hardware illustrated in Fig. (2.1). We will work through and discuss the case of the parity measurement for three qubits; generalizing our construction to more qubits is clear, and will be discussed below. In this construction we have two resonators (we envision 1/4-wave coplanar waveguide resonators [61, 62], as illustrated schematically); in each we will employ one resonant mode, with creation operators $a^\dagger$ and $b^\dagger$. It would be normal to use the lowest-frequency (fundamental) modes; all other modes are far separated in frequency (the next being at three times the fundamental, in a 1/4-wave structure) and will be ignored. In our scheme, these two fundamental frequencies ω_a and ω_b should be almost, but not exactly, degenerate. The qubit-cavity coupling will be the standard one given by the Jaynes-Cummings model in the dispersive regime [20]. It will be non-standard only in that each qubit will couple to both resonators, so that each qubit j will have a physical coupling strength $g_{j,a}$ to the a resonator and $g_{j,b}$ to the b resonator. The Hamiltonian of the system of resonators and qubits can be written [21]

$$H = \left(\omega_a + \sum_{j=1}^{3} \chi_a^j \sigma_z^j\right) a^\dagger a + \left(\omega_b + \sum_{j=1}^{3} \chi_b^j \sigma_z^j\right) b^\dagger b + \frac{1}{2}\sum_{j=1}^{3} \omega_j \sigma_z^j. \tag{2.1}$$

Here ω_j are the qubit frequencies, and the dispersive coupling parameters are $\chi_a^j = g_{j,a}^2/\Delta_{j,a}$ with $\Delta_{j,a} = \omega_j - \omega_a$, and similarly for χ_b^j and $\Delta_{j,b}$. Note that we assume that the system should be engineered so that there is no direct coupling between qubits.

As indicated in Fig. (2.1), this resonator/qubit structure is to be coupled capacitively to a scattering probe. Rather than extend our Hamiltonian to include all these other details, we proceed in the following way: Since H commutes with each σ_z^j, we can examine the Hamiltonian separately in each of its 2^3 qubit eigensectors; within each of these sectors H describes a harmonic bosonic system, with qubit-dependent resonant-frequency parameters. Thus, the full scattering experiment can be described quite economically using the classical language of impedance and scattering parameters; the conclusions we draw from this classical discussion will have an immediate, standard quantum interpretation in terms of coherent-state propagation.

From ordinary electrical transmission line theory, the impedance between point A in Fig. (2.1) and ground is given by

$$Z_A(\omega) = iZ_0 \tan\left(\frac{\pi}{2}\frac{\omega}{\omega_{r,a}}\right). \tag{2.2}$$

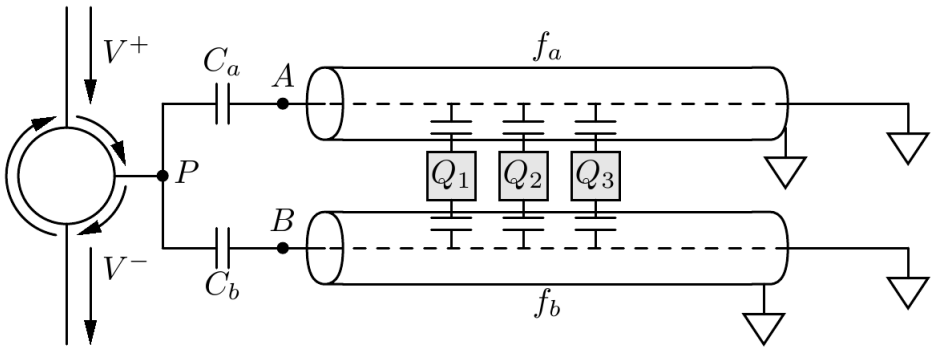

Figure 2.1: A schematic circuit QED setup for measuring the parity of three qubits. Two transmission-line resonators have slightly different resonant frequencies f_a and f_b. The three qubits $Q_{1,2,3}$ (which could be of the transmon type) each couple equally to the two resonators. The parity information is contained in the phase of the reflection coefficient at point P, which, throughout the action of the circulator [63, 64], appears as a phase change of the output signal V^- relative to the input tone V^+.

Here $Z_0 = 50\Omega$ is the impedance of the waveguide. The effective resonant frequency ω_r is dependent on the state of the three qubits $|s_1 s_2 s_3\rangle$ according to

$$\omega_{r,a} = \omega_a + \sum_{j=1}^{3} (-1)^{s_j} \chi_a^j. \tag{2.3}$$

This same discussion applies to the qubit-state-dependent impedance $Z_B(\omega)$ of the B resonator. The impedance $Z_P(\omega)$ of the entire structure at point P is then given by ordinary series- and parallel-combination rules. In fact in the frequency range of interest, the response is very well represented by the lumped circuit of Fig. (2.2).

The measurable quantity for this structure is the reflection coefficient r at P. This is given by [61]

$$r(\omega) = \frac{V^-(\omega)}{V^+(\omega)} = \frac{Z_P(\omega) - Z_0}{Z_P(\omega) + Z_0}. \tag{2.4}$$

Note that because Z_P is purely imaginary (lossless), $|r| = 1$, so that only the phase of r,

$$\theta(\omega) \equiv \arg r(\omega) \tag{2.5}$$

contains information (which can in fact be measured interferometrically).

Our object is to find a probe frequency ω_p such that the reflected signals for all the even-parity qubit states, and all the odd-parity states, are indistinguishable,

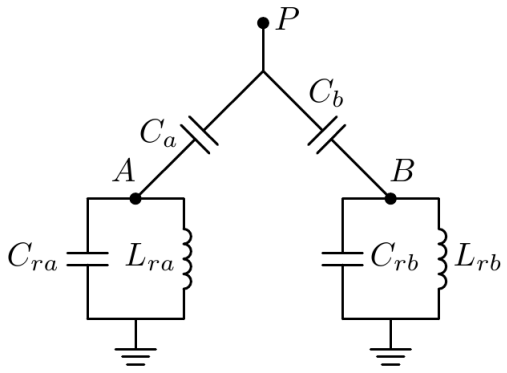

Figure 2.2: Equivalent circuit for the double-resonator structure [61]; $C_{ra} = \frac{\pi}{4\omega_{r,a}Z_0}$, $L_{ra} = \frac{1}{\omega_{r,a}^2 C_{ra}}$, $C_{rb} = \frac{\pi}{4\omega_{r,b}Z_0}$, $L_{rb} = \frac{1}{\omega_{r,b}^2 C_{rb}}$.

but that the reflection coefficient for the even and odd cases *are* distinct. This will give us conditions on the reflected phase $\theta_{s_1 s_2 s_3}(\omega_p)$ for the different qubit state settings. A general feature of the θ function will make this possible in our two-resonance setting. If ω passes through a resonance of the system (pole of Z_P), then, while the phase change of the impedance is π, the change of the reflected phase is 2π (cf. Eqs. (2.4), (2.5)). We will arrange that Z_P has two poles within a narrow range of frequency; this means that $\theta(\omega)$ will vary smoothly over 4π in that range. But, from the point of view of a scattered tone, θ and $\theta + 2\pi n$ are indistinguishable. Thus, the $\theta(\omega)$ function varies over a sufficient range that we can satisfy our quantum eraser condition for the parity measurement in the following way:

$$\theta_{\text{even}} \equiv \theta_{000}(\omega_p) = \theta_{011}(\omega_p) + 2\pi, \tag{2.6}$$

$$\theta_{\text{odd}} \equiv \theta_{111}(\omega_p) = \theta_{001}(\omega_p) - 2\pi. \tag{2.7}$$

Since the χ coefficient for all qubits is taken to be equal, the other necessary conditions, $\theta_{011}(\omega_p) = \theta_{101}(\omega_p) = \theta_{110}(\omega_p)$ and $\theta_{001}(\omega_p) = \theta_{010}(\omega_p) = \theta_{100}(\omega_p)$, are satisfied automatically. It is also necessary that $\theta_{\text{even}} \neq \theta_{\text{odd}} \pmod{2\pi}$, with the best case (most distinguishable) being $\Delta\theta \equiv \theta_{\text{even}} - \theta_{\text{odd}} = \pi$.

One can show that for any choice of parameters in the two-pole circuit, there exists a probe frequency ω_p and a dispersive shift constant χ such that the parity-measurement conditions Eqs. (2.6), (2.7) are satisfied. However, if the resonant frequencies ω_a and ω_b are far apart compared with the width of the resonances, $\theta_{\text{even}} - \theta_{\text{odd}}$ is very small. By placing the resonances close to one another and choosing the capacitance values carefully, a favorable solution can be found. We note that for further optimization of this structure, there would be no difficulty in replacing the simple pair of capacitors $C_{a,b}$ with a capacitance bridge in a wye- or

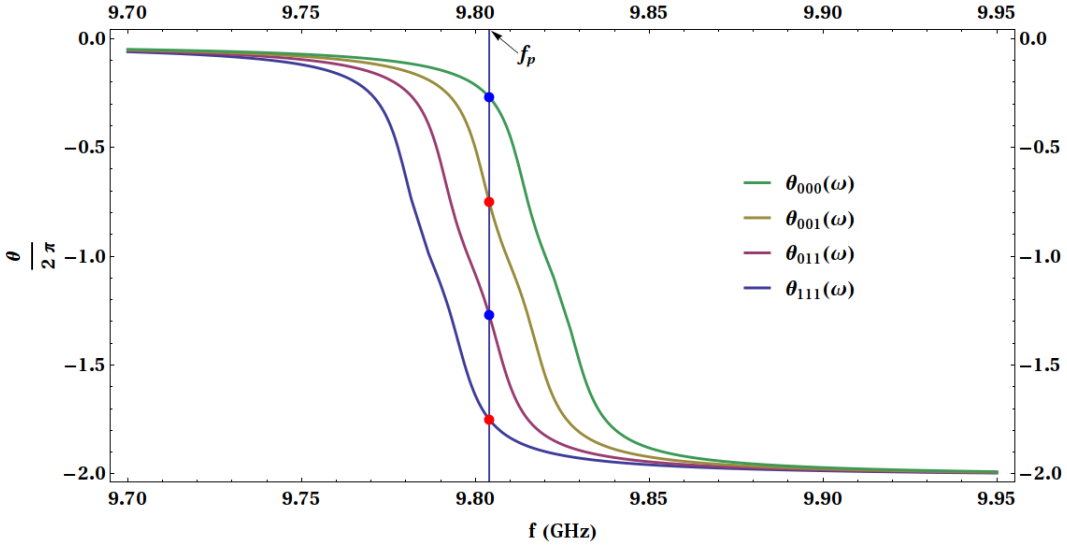

Figure 2.3: Solution for realistic values $\omega_a = 2\pi(9.99\text{ GHz})$, $\omega_b = 2\pi(10.01\text{ GHz})$, $C_a = C_b = 10\,fF$; with $\omega_p = 2\pi(9.804\,GHz)$, $\chi = 5.77\,MHz$, giving $\Delta\theta = 172.9°$. Blue points correspond to even states whereas red points correspond to odd states. Vertical blue line shows the probe frequency $f_p = 9.804\,GHz$.

delta-configuration [61].

Figure (2.3) shows a solution for the case of a realistic set of parameters. The choices are $\omega_a = 2\pi(9.99\text{ GHz})$, $\omega_b = 2\pi(10.01\text{ GHz})$, $C_a = C_b = 10\,fF$; note that realistic values for coupling capacitors are in $0.5-50fF$ range (see Ref. [65]). Our Eqs. (2.6), (2.7) are satisfied (after a simple, efficient numerical search) for $\omega_p = 2\pi(9.804\,GHz)$ and $\chi = 5.77\,MHz$, giving the nearly optimal value $\Delta\theta = 172.9°$. Note that the coupling capacitors will introduce T_1 qubit relaxation, but we can estimate that capacitances on this scale give a cavity loss rate of $\kappa \sim 5$MHz. The Purcell formula for the resulting qubit relaxation time is $T_{1(P)} = \frac{\Delta^2}{\kappa g^2} = \frac{\Delta}{\kappa\chi}$. If we assume $\Delta = 5$GHz, this gives $T_{1(P)} \sim 200\mu s$. Thus, the Purcell mechanism for relaxation will not be a severe limit on the lifetime of the qubits.

We can qualitatively assess the result of applying the measurement tone for a finite length of time. The signal-to-noise ratio for distinguishing even from odd is largely a technical matter involving the noise performance of amplifiers and the effective temperature of filters associated with the resonator-qubit structure. The quantum-erasure property sets a more fundamental limit. If the measurement time is T, the measurement signal will then have a bandwidth $W \sim 1/T$ around the probe frequency ω_p. Because the dispersion of the reflection response is different for the different even and odd states (that is, $\frac{d\theta}{d\omega}$ is different for the distinct states,

see Fig. (2.3)). Thus we expect that to maintain the quantum-eraser condition, the bandwidth W should be kept to a small fraction of the resonance width, so perhaps $T \sim 10/\chi$. This gives a measurement time $T \sim 2\mu s$. While this is shorter than the expected T_1 in current devices, it would be desirable to shorten T; we expect that further optimization of the scattering structure could make all the $(\frac{d\theta}{d\omega})_{\text{odd}}$ and $(\frac{d\theta}{d\omega})_{\text{even}}$ more nearly equal, so that perhaps T could approach $1/\chi$.

A detailed calculation, given in the Appendix (6.1), confirms these qualitative considerations. This calculation involves a quantum treatment of the input tone V^+, in which it is written as a coherent state [66] $|\alpha\rangle$, pulsed with a gaussian time profile with characteristic time $T = 1/W$. The pulse has mean photon number $|\alpha|^2$, and therefore energy $\hbar\omega_p|\alpha|^2$. The output tone V^- is also a coherent state $\beta_{\mathbf{s}}$, but dependent on the qubit state $|\mathbf{s}\rangle = |s_1 s_2 s_3\rangle$. The coherent state amplitude is always unchanged, $|\beta_{\mathbf{s}}| = |\alpha|$, but it is dispersed differently for each state because of the scattering phase shift.

The relevant result from the Appendix (6.1) is

$$\langle\beta_{\mathbf{s}}|\beta_{\mathbf{s}'}\rangle = 1 - \frac{|\alpha|^2 b^2 W^2}{2} + O(|\alpha|^4 b^4 W^4), \quad \text{qubit parities } \mathbf{s} \text{ and } \mathbf{s'} \text{ the same,} \tag{2.8}$$

$$\langle\beta_{\mathbf{s}}|\beta_{\mathbf{s}'}\rangle = e^{-|\alpha|^2(1-\cos\Delta\theta)}\left(1 + O\left(W\frac{d\theta}{d\omega}\right)\right), \quad \text{qubit parities } \mathbf{s} \text{ and } \mathbf{s'} \text{ different.} \tag{2.9}$$

The new parameter b is the first-order difference of phase dispersion,

$$b \equiv \theta'_{\mathbf{s}}(\omega_p) - \theta'_{\mathbf{s}'}(\omega_p). \tag{2.10}$$

The quantum-eraser condition requires that the "same parity" cases be indistinguishable ($\langle\beta_{\mathbf{s}}|\beta_{\mathbf{s}'}\rangle = 1$), and the "different parity" cases be perfectly distinguishable ($\langle\beta_{\mathbf{s}}|\beta_{\mathbf{s}'}\rangle = 0$). Noting that, on dimensional grounds, $b \sim 1/\chi$, these quantum-erasure conditions are well approximated so long as $T = 1/W > |\alpha|b \sim |\alpha|/\chi$. This confirms the qualitative discussion above, with the additional insight that it is best if the probe is not too strong, i.e., if α is not too large (or course, it should be greater than one to satisfy the "different parity" condition). If the photon number is taken to be $|\alpha|^2 = 5$, and the pulse duration is $T \approx 1\mu s$, the peak pulse power will be about $P = \frac{|\alpha|^2\hbar\omega_p}{T} = -135\,dBm$. This is indeed a weak signal, but in the detectable range with the current state of the art [67].

The effect of transient dynamics on the fidelity is computed using stochastic master equations in [68]. It is shown that a measurement fidelity of 95% is possible with our direct parity measurement scheme assuming realistic values for the decoherence parameters.

2.2.1 Comparison with Kerchhoff *et al.*

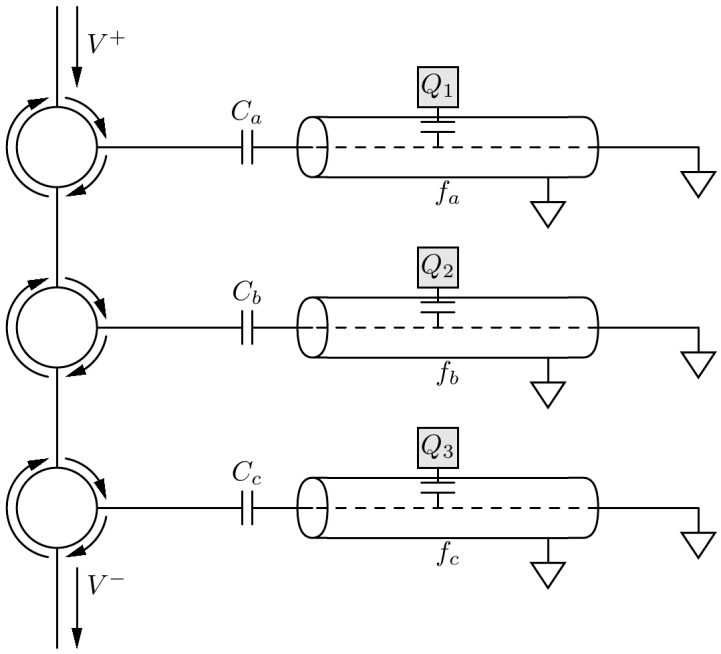

Figure 2.4: Circuit for three-qubit extension of the scheme proposed as a cavity-optics experiment in [35], as it would be implemented with microwave components in circuit QED.

Before presenting our second proposal, we can compare our concept for three-qubit parity with the three-qubit extension of the two-qubit parity measurement that was recently proposed by Kerchhoff, Bouten, Silberfarb, and Mabuchi [35]. They propose sequential scattering from a set of cavities, each coupled to one qubit; the extension of their idea to three qubits, as rendered in plausible microwave components, is shown in Fig. (2.4). Note that for n-qubit parity this scheme uses n resonators, while a generalisation of our scheme above would use $\lceil (n+1)/2 \rceil$ resonators (see the following section). The Kerchhoff *et al.* scheme is certainly elegant, and simpler in that each qubit only needs to couple to a single cavity. The idea is to choose the coupling and the probe tone such that there is a phase difference of π between qubit state 0 and 1; then this network constructs a sum of the phases for each qubit[1]. Each cavity should have exactly the same resonant frequency (perhaps by tuning). This scheme is more obviously scalable to more

[1]We have learned that the method stated here of synthesising a desired circuit response by cascaded circulators was known a long time ago; it is attributed to Desoer and Belevitch [69] in Chap. 3 of [70].

qubits than ours, and it would be possible in this scheme to get rid of the first-order dispersion effects which degrade the quantum-eraser condition, as calculated above. But, as we show in the Appendix (6.1), the second-order dispersion difference, which would still be present, leads to similar qualitative limits on the measurement time and fidelity. Also, we point out that the quantum-eraser condition would also be degraded by imperfections in the circulators, unlike in our scheme. Given that there presently are no on-chip circulators suitable for qubit experiments (but see progress in [71, 72]), we believe that our scheme is closer to being realized with currently-available components.

2.3 Results – 3D resonant structures

The theoretical generalization of our scheme to the measurement of the arguably more important case of 4-qubit parity is straightforward. We require three closely spaced resonances f_a, f_b and f_c , equal coupling χ of each qubit to each of the three resonances, and a network that couples resonators to a single reflected probe. In this case again all measurable quantities will emerge from a single reflected-phase function $\theta_{\mathbf{s}}(\omega)$. Since this function will vary smoothly over 6π, it will be possible to satisfy the three quantum-eraser equations for this case:

$$\theta_{\text{even}} = \theta_{0000}(\omega_p) = \theta_{0011}(\omega_p) + 2\pi = \theta_{1111}(\omega_p) + 4\pi \tag{2.11}$$

$$\theta_{\text{odd}} = \theta_{0111}(\omega_p) = \theta_{0001}(\omega_p) - 2\pi \tag{2.12}$$

Tuning the f_i values, χ and ω_p gives enough freedom so that these equations should always be solvable. The analogous conditions for n-qubit parity are straightforward to write down; if we use the notation $\theta_{\mathrm{W}t.i}$ to indicate the phase shift if i of the quibits are 1, then the condition is

$$\theta_{\mathrm{W}t.i}(\omega_p) = \theta_{\mathrm{W}t.i+2k}(\omega_p) + 2k\pi. \tag{2.13}$$

Combined with the desire that $\theta_{\mathrm{W}t.0}(\omega_p) \approx \theta_{\mathrm{W}t.1}(\omega_p) + \pi$, we see that the θ function should vary by at least πn. For even n this will be accomplished with $n/2 + 1$ resonances (so that θ winds through phase $\pi(n + 2)$), while for odd n, $(n + 1)/2$ resonances suffice (θ winds through phase $\pi(n+1)$ in this case). For both even and odd n, the number of resonances required can be written $\lceil (n + 1)/2 \rceil$, as stated above.

Returning to the consideration of 4-qubit parity, we see that some new hardware elements would be required to achieve this by an extension of the “2D" (coplanar waveguide) scheme above. The requirement that each qubit be equally coupled to each of three different CPW resonators has not previously been achieved. It seems likely that it is doable with the use of air bridges, which have only recently

entered the toolkit of quantum microwave engineering (see [73, 74]). Another possible way to obtain the multiple resonant modes needed for multi-qubit parity measurement would involve the use of multi-conductor CPWs [73], which naturally support modes that are closely spaced in frequency.

But given these difficulties, we explore a second protocol to achieve the implementation of 4-qubit parity measurement, involving "3D" superconducting cavities [22]. These high quality factor rectangular cavities have recently been proven to be excellent implementations of nearly decoherence-free Jaynes-Cummings physics [56]. In these the qubit-cavity coupling is provided by antenna structures extending out from the transmon qubits [22]. Multi-qubit structures [75] have been achieved in this technology, and bridging qubits, antenna-coupled to two different cavities, are now possible[2] [56]. This second protocol illustrates a further fact, which is that *multiple*, closely spaced resonances can be achieved within a *single* resonant structure.

Figure (2.5) illustrates the concept of this second protocol, also showing how it could be extended to be part of a scalable implementation of the surface code architecture [51, 76]. The key modification in this structure is that the 3D cavities, rather than having a large aspect ratio in which $w >> l >> h$ (w=width, l=length, h=height), should be nearly, but not exactly, cubical. Thus, the three lowest resonant modes would be nearly degenerate in frequency, since their wavelengths will be set by π/w, π/l, and π/h. (Be warned that the traditional labels for these modes are TE_{101}, TE_{011}, and TM_{110} (see Chap. 10.07 of [60]).) Each cavity is coupled, via antenna structures, to four qubits, two on the front surface in Fig. (2.5) and two on the back (not shown). Each antenna runs along the body diagonal (i.e., $\langle 111 \rangle$ axis) of the cubical cavity; with this geometry the coupling is equal to each of the three eigenmodes, whose modal electric field patterns point straight along one of the three coordinate axes.

Unlike for our first ("2D") proposal, we will not provide calculations of the performance of the structure of Fig. (2.5). While the structure of Fig. (2.1) can be analyzed using elementary transmission line theory and a few component parameter values whose ranges are well understood, the system of Fig. (2.5) is a complex, three-dimensional structure whose electromagnetic response can only be obtained reliably by detailed calculations that are beyond the scope of this paper. It is encouraging that progress is being made in the detailed modeling of couplings in such a 3D geometry [78]. We note that many details of Fig. (2.5), such as the thin-film metallisation around the qubit, contacts between chip conductors and antenna and cavity metal, the shape of the antennas, and the exact geometry of the cavities, should be optimised by detailed simulation. One comment on the cavity structure: while the cubical cavity satisfies the requirement of three closely spaced modes in

[2] J. M. Gambetta, private communication.

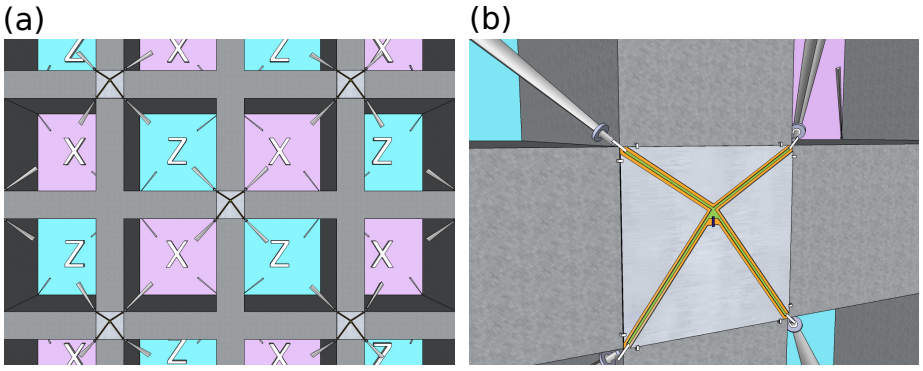

Figure 2.5: Potentially scalable implementation of the surface code using direct 4-qubit parity measurements (rendering by Google Sketchup). a) Overview of the proposed structure. A solid plate of metal (Al or Cu, as in recent experiments [22, 77]) is perforated with nearly square holes. The thickness of the plate is close to the dimension of the square. When closed with thin top and bottom plates (not shown), these holes become nearly cubical microwave cavities. Qubit structures are grown on chips (lighter squares) using existing thin-film techniques. The insulating side of the chip is mounted to a junction point in the perforated plate; half of the junctions contain chips at the front surface of the plate, and the other half are on the back side (not visible). Each qubit is in electrical contact, via leads going to the corners of the chip, with four antenna structures (tapered rods) projecting diagonally into the four cubical cavities surrounding the chip. Each cavity will enable a four qubit parity measurement, either ZZZZ or XXXX, as indicated. The external feed lines needed to interrogate each cavity by reflectometry will enter via one of the unoccupied corners of the cubes (not shown). b) Close-up around one qubit chip. It could be made in the conventional way, in which a thin film of metal is etched away in slot regions, exposing the underlying insulating substrate (orange). This forms four short segments of coplanar waveguide structures, with the center conductor (green) going to each of the corners of the chip. One small structure (blue) containing a Josephson junction connects the central region of center conductor to one of the ground planes (light grey). The four triangular ground-plane regions are tied to the metal plate, and therefore to each other, by bridges or wire bonds near the corners of the chips. Such bridge/bond connections are also made between the four center conductors and the antenna rods. Insulating support structures isolating the antennas from the conducting walls are only schematically shown. The consequence of this connection arrangement is that the Josephson junction is shunted by four capacitances in series, each formed by an antenna and the side walls of the cavity containing it. Presumed optimal dimensions for the chip (sub-millimeter) and cavity (few centimeter) are not accurately depicted.

an elegant way, it will be perhaps discouragingly large (centimeter-scale) from the point of view of potential scale-up of the surface code. Work is commencing on much different forms of resonator geometries, which by being "quasi-lumped" [79], can be much more physically compact. It will not be necessary to remain only with the Platonic cavities.

2.4 Discussion and Conclusions

We consider our basic schemes of Figs. (2.1) and (2.5) to be realistic for implementation by experiment. For Fig. (2.1), a precise thin-film layout of an on-chip structure (to the right of point P in Fig. (2.1)) could be devised based on the parameter values we have determined. It is clear that detailed electromagnetic modelling would be useful to guide the layout design [80]. The values obtained for C_a and C_b correspond to well-known few-finger interdigitated capacitors. We foresee three main difficulties: 1) Coupling each qubit to the two resonators. 2) Tuning the qubits to achieve the equal-χ condition. The topology of the chip layout would preclude bringing flux-bias lines to each qubit; it is possible that only two of the three qubits would need to be tuned, and one of these tunings could be from an external magnetic field. 3) Measuring few-photon signal levels. It appears that the standard HEMT amplifier arrangements would have too much noise for the conditions we have calculated; adoption of new, quantum-limited amplification will be needed for high-fidelity readout.

The 3D scheme of Fig. (2.5) will require more work to assess its optimal implementation. Achieving the parameter values envisioned by our theory will require detailed simulation of the complex structure that we have proposed, with many details subject to variation. Since the direct, ancillaless approach studies here is so different from the existing technique of collecting error syndromes with the action of a quantum circuit using ancillas, we believe that it is impossible to know which approach will be superior. Further studies and refinement of both approaches will be necessary to determine which will provide the best way forward.

So, it may be that our proposals can only attain satisfactory performance in structures in which the resonators are tuneable (as in [81, 82, 83]), or qubits are tuneable in frequency (as in [42] and in many other works) or in effective coupling strength (as in [84]). Application of these device construction techniques, as well as near-quantum limited amplification [67], will be likely be needed to achieve high-fidelity, single-shot parity measurement as envisioned in the proposals we give here. We hope that following this route will indeed be facilitated by the many interesting experimental [85, 86, 87] and theoretical [39, 88, 89] innovations in the application of circuit QED that we see presently.

The proposals of this chapter are not the blueprint for a scalable quantum

computer; they are concepts on which further detailed studies to determine optimal device functionality can be based. While the structures that we suggest here will by no means be trivially realised, we believe that the crucial role played by parity measurement in the implementation of reliable quantum computation makes these approaches worthwhile to pursue.

CHAPTER 3

One-port Brune Quantization

3.1 Introduction

Superconducting electronics is one of the most promising ways to realize the quantum computer's hardware. As we have seen in the previous chapters, a typical superconducting processor consists of microwave cavities connected by microwave waveguide structures and components. The anharmonicity necessary for getting qubits is supplied by Josephson junctions which are usually positioned inside the cavities and coupled to the cavity modes.

Superconducting qubit lifetimes have increased from a couple of nanoseconds in 1999 [9] to tens of microseconds in 2011 [22]. The increase in Q-factors of superconducting qubits and cavities requires highly accurate models for their design, optimization and predictability. The common approach to model such systems has been to use Jaynes-Cummings type Hamiltonians borrowed from quantum optics. However several problems arise like convergence issues when one wants to include higher levels of superconducting qubits or higher modes of cavities in such models [91].

To remedy those issues a method is proposed in [78] to derive Hamiltonians and compute relaxation rates for weakly anharmonic superconducting circuits. In this method the linear electromagnetic environment shunting the Josephson junction, as extracted, for example, using microwave simulation software, is lumped together with the junction's linear inductance, to give a "blackbox" impedance function $Z_{sim}(\omega)$. This response is then fitted, pole by pole, to an analytic function $Z(\omega)$. Then an approximate version of Foster's theorem [92] in the low loss limit [93], applied to $Z(\omega)$, gives an equivalent circuit as a series connection of resonant RLC stages, one stage for each term in the partial fraction expansion of $Z(\omega)$. In this method, which we refer to as the "lossy Foster" method, Q factors for each resonant mode are computed using $Q_p = \frac{\omega_p}{2}\frac{\mathrm{Im}[Y'(\omega_p)]}{\mathrm{Re}[Y(\omega_p)]}$ where $\omega_p = (L_p C_p)^{-1/2}$ is the resonant frequency of the mode and $Y = Z^{-1}$ is the admittance. The lifetime of the mode is given by $T_p = Q_p/\omega_p$.

Lossy Foster, while simple to apply, is not always accurate or even well-conditioned. Terms in the partial-fraction expansion of $Z(\omega)$ do not always correspond to stages

of a physical circuit [94, 95]. As Brune showed [96], the property that an impedance function must have in order to correspond to a passive physical network is termed "PR (Positive-Real)". We note that even if all terms in the expansion of $Z(\omega)$ are individually PR, one might still need to remove terms by inspection to get a better fit, making the method dependent on ad-hoc decisions. As applied in [78], lossy Foster parameters are dependent not only on the properties of the electromagnetic environment, but also on the precise value of the junction inductance.

In this chapter we propose a new method to derive highly accurate Hamiltonians for systems consisting of a single Josephson junction connected to lossy microwave environments. Most of the material in this chapter is taken from our published work at [97]. Our method is general enough to treat fully non-linear systems, as was done in [98] for one-dimensional (1D) resonator systems. In the following chapters we will show also how to extend the method to treat systems consisting of multiple Josephson junctions. We treat the linear and passive part of the circuit as a blackbox as in [78]. We however don't combine linear Josephson inductance with the response of the environment. A Josephson junction connected to the blackbox will define a port at its connection terminals.

The blackbox is characterized by its linear response which might be an impedance matrix, an admittance matrix or a scattering matrix. Response of the blackbox might be either measured or computed using for example a finite-element simulator such as HFSS [99]. The output of such a simulation is usually in the form of response values sampled at discrete frequency points.

The response of the blackbox is fitted to a finite pole-residue model which is equivalent to a rational function(rational matrix in the multiport case) model. For this purpose we use Vector Fitting MATLAB package [100]. Vector Fitting uses the following finite pole-residue model for the fit

$$\mathbf{Z}(s) = \sum_{k=1}^{M} \frac{\mathbf{R}_k}{s - s_k} + \mathbf{D} + \mathbf{E}s \tag{3.1}$$

to minimize the error between the data and the fit over a finite bandwidth by choosing a proper set of poles $\{s_1, \ldots, s_M\}$ and residues $\{\mathbf{R}_1, \ldots, \mathbf{R}_M\}$.

Vector Fitting is an algorithm to approximate a sampled impedance/admittance response by a rational function. It takes a dataset Z_{sim} simulated at sampled frequency points, and the number of poles M required for the fit, as its input and gives a set of poles $\{s_1, \ldots, s_M\}$ and residues $\{\mathbf{R}_1, \ldots, \mathbf{R}_M\}$ as its output (See [101] for models with infinite number of poles) minimizing the error between Z_{sim} and $\mathbf{Z}(s)$ in Eq. (3.1) over the simulation bandwidth. Ref. [102] discusses details of VF. Its passivity enforcement subroutine [103] makes sure that the real part of the resulting rational approximation is positive definite. This feature is crucial for our analysis since we require the impedance response to be PR (see Chapter

(3.2.1)) for the existence of a finite passive network having the same impedance across its terminals. Note that passivity enforcement may not always work if the accuracy of the microwave simulation is not high enough and we have taken care to run the simulation with suitably high resolution in the example discussed in Chapter (3.4).

Once an impedance fit $\mathbf{Z}(s)$ as in Eq. (3.1) is obtained we apply Brune's method of circuit synthesis to get a lumped element circuit which admits the same impedance $\mathbf{Z}(s)$ at its terminals. This circuit we call the "Brune's circuit". Resistors in the Brune's circuit are coupled to the reactive part of the circuit in a non-trivial way. We resort to the formalisms developed in [17, 18] for lumped element circuit quantization to quantize the Brune's circuit and compute relaxation rates. The accuracy of our Hamiltonian and dissipation analysis gives an exact description except for small errors, introduced in fitting.

In this chapter we introduce Brune's method of synthesis for one-port impedances. Brune's algorithm will be described in s-domain (frequency domain) where s is the Laplace variable. This is the classical network theory approach. We will then apply formalisms [17, 18] developed for lumped element circuit quantization to get a quantum model for the Brune circuit and compute relaxation rates $1/T_1$.

3.2 The Impedance Synthesis Problem

Impedance synthesis problem is an old problem of electrical network theory. Given an impedance function $Z(s)$ the problem is to find an electrical network which has the impedance $Z(s)$ at its terminals. Foster [92] gives a solution for the lossless one-port networks. He writes the form of the impedance of the most general finite network consisting of capacitors, inductors and mutual inductors but containing no resistors. He further shows that any such lossless impedance function can be realized in the form of networks in Figs. (3.1)-(3.2).

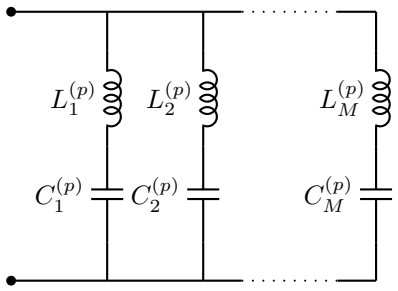

Figure 3.1: First Foster form

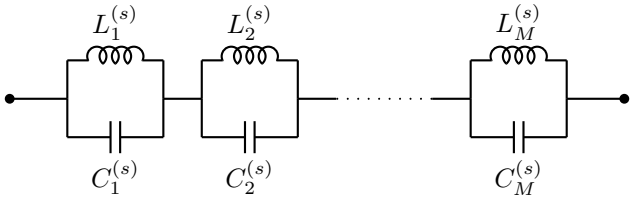

Figure 3.2: Second Foster form

The synthesis problem for lossy responses is a tricky one. Guillemin [94] proposes the construction shown in Fig. (3.3) and makes the false claim that one can synthesize any one-port impedance by such a circuit. Inductors in the circuit should be understood as belonging to a multiport mutual inductor with couplings between any two ports. We can see why Guillemin's claim is false by studying the simple circuit shown in Fig. (3.4) and showing that it is non-mapable to a circuit in the form in Fig. (3.3).

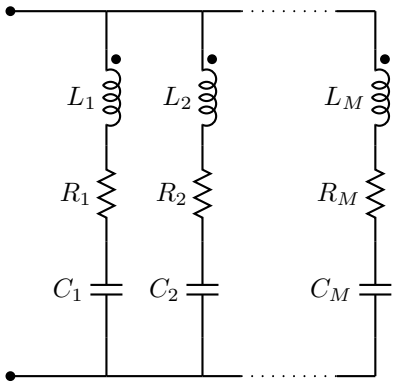

Figure 3.3: Canonical circuit proposed by Guillemin in [94] for the realization of any PR impedance function.

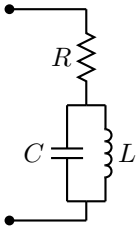

Figure 3.4: Simple circuit to show why Guillemin's proposition is in error.

The correct answer to the lossy impedance synthesis problem is given by Brune [96]. He shows that any one-port impedance corresponding to a finite passive

network can be realized by a circuit in the form shown in Fig. (3.9). In Section (3.2.2) we describe the algorithm proposed by Brune [96] to synthesize such a circuit given an impedance function. An important question is how to check if a given function is the response of a finite physical network. There will be a finite passive network which has a given impedance across its terminals only if the impedance function satisfy certain conditions. Brune discovered those conditions and called them "PR (Positive-Real)" conditions [96]. Below we define PR property and describe Brune's algorithm. For more details see [94].

An important feature of Brune's algorithm is that it gives a circuit with a minimum number of reactive elements. This allows a Hamiltonian description for the system with a minimum number of degrees of freedom. The number of resistors is however not minimum. In the following we adhere to the electrical engineering convention for the imaginary unit $j = -i$.

3.2.1 PR property

A scalar impedance function $Z(s)$ is PR if the following two conditions are met

1) $Z(s)$ is a rational function which is real for real values of s.

2) $Re[Z(s)] \geq 0$ for $Re[s] \geq 0$.

The second condition is equivalent to the following

1) No poles lie in the right half plane.

2) Poles on the j-axis have finite positive real residues and are simple.

3) $Re[Z(j\omega)] \geq 0$.

Physically the first condition requires the network to be stable whereas the third condition requires it to be passive, i.e. that it doesn't generate energy.

3.2.2 Brune's algorithm

As input, this algorithm for extracting all parameter values of the Brune circuit in Fig. (3.9) takes the impedance function $Z(s)$ in rational-function form, or (equivalently) partial fraction expansion form. $Y(s) = 1/Z(s)$ can be easily computed in these representations. The algorithm proceeds by looping over the following steps 1-5:

1. If $Z(s)$ or $Y(s)$ has j-axis poles, remove them by realizing terms corresponding to those poles in the partial fraction expansion. Those terms correspond to parallel LC resonators(connected in series) in case of $Z(s)$ poles and series LC resonators(connected in parallel) for $Y(s)$ poles. Repeat until no j-axis pole is left.

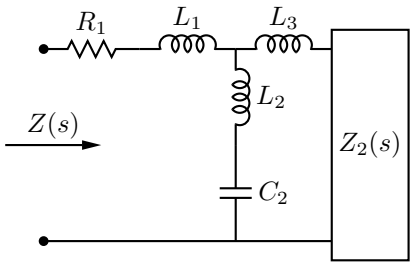

Figure 3.5: Brune circuit extraction step

2. Find ω_1 and R_1 such that $R_1 = \min_{\omega} \mathrm{Re}[Z(j\omega)]$ and $\mathrm{Re}[Z(j\omega_1)] = R_1$. Define $Z_1(s) = Z(s) - R_1$. This step fixes the value of the resistor R_1 in Fig. (3.5). See below for the degenerate case when $\omega_1 = \infty$.

3. Define $L_1 = Z_1(j\omega_1)/(j\omega_1)$. If we extract the inductance L_1 as shown in Fig. (3.5), $1/(Z_1(s) - L_1 s)$ is the admittance corresponding to the rest of the circuit and has a pole at $s = j\omega_1$, hence we can write

$$\frac{1}{Z_1(s) - L_1 s} = \frac{(1/L_2)\, s}{s^2 + \omega_1^2} + \frac{1}{W(s)} \tag{3.2}$$

4. The first term in Eq. (3.2) corresponding to the pole at $s = j\omega_1$ is realized with a shunt LC branch consisting of inductance L_2 connected in series with capacitance $C_2 = 1/(L_2\omega_1^2)$ as shown in Fig. (3.5).

5. $W(s)$ has a pole at infinity such that

$$\lim_{s\to\infty} W(s) = -\frac{L_1 L_2 s}{L_1 + L_2} = L_3 s \tag{3.3}$$

This pole is removed by constructing $Z_2(s) = W(s) - L_3 s$ which corresponds to connecting in series an inductance of value $L_3 = -L_1 L_2/(L_1 + L_2)$. $Z_2(s)$ is PR, and one loops though steps 1-5 whole applied to Z_2.

Steps 1 to 5 reduce degrees of both numerator and denominator of $Z(s)$ by 2 so that the algorithm terminates once a constant $Z_2(s) = R_{M+1}$ is reached. For more details on Brune's algorithm, see Chap. 9 of [94].

The circuit in Fig. (3.5) involves negative values for either inductance L_1 or L_3 [94]. However one can replace the T-shaped inductive part of the circuit in Fig. (3.5) with a "tightly coupled" inductor as shown in Fig. (3.6) where the inductances are all physically realisable and given by

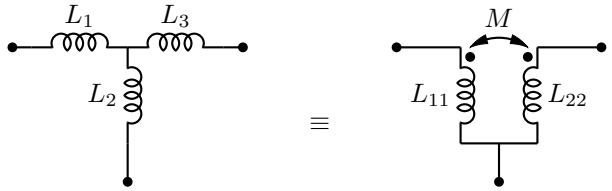

Figure 3.6: Equivalence of T-shaped inductive circuit in Fig. 3.5 to a coupled inductor

$$L_{11} = L_1 + L_2 \tag{3.4}$$
$$L_{22} = L_3 + L_2 \tag{3.5}$$
$$M = L_2 \tag{3.6}$$

Note that lower terminals of the coupled inductor are short-circuited. A generic two-port coupled inductor is shown in Fig. (3.7) with the following constitutive relations

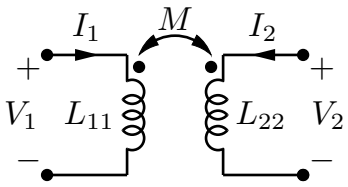

Figure 3.7: Generic 2-port coupled inductor with convention chosen for current directions and voltage polarities

$$\begin{pmatrix} \Phi_1 \\ \Phi_2 \end{pmatrix} = \begin{pmatrix} L_{11} & M \\ M & L_{22} \end{pmatrix} \begin{pmatrix} I_1 \\ I_2 \end{pmatrix} \tag{3.7}$$

assuming the conventions shown in Fig. (3.7) for current directions and voltage polarities. With the current directions chosen the stored energy in the coupled inductor is given by

$$E = \frac{1}{2}\left(L_{11}I_1^2 + 2MI_1I_2 + L_{22}I_2^2\right) \tag{3.8}$$

Note that at any stage in the application of step (2) above, one may find $\omega_1 = 0$ or $\omega_1 = \infty$. In case of $\omega_1 = \infty$ we have the degenerate circuit in Fig. (3.8) which corresponds to the circuit in Fig. (3.6) with $L_1 = L_2 = L_3 = 0$. C_j in Fig. (3.8) is given by

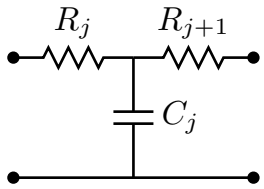

Figure 3.8: A degenerate stage in Brune circuit

$$C_j = \lim_{s \to \infty} \frac{1}{s\,(Z_j - R_j)} \tag{3.9}$$

3.3 Quantization of the one-port Brune circuit

3.3.1 Hamiltonian Derivation

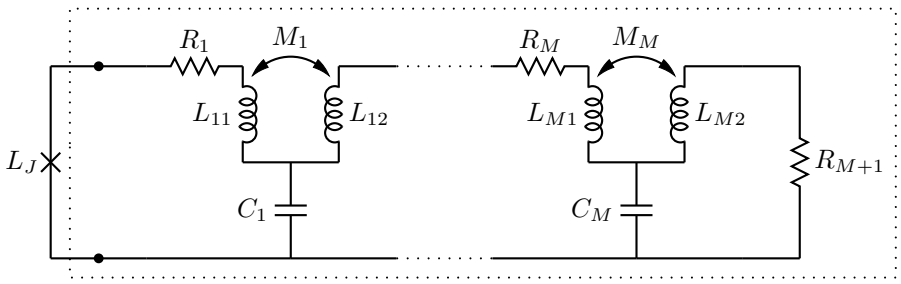

Figure 3.9: Brune circuit (in dotted box) shunted by a Josephson junction.

In this section we will quantize the circuit in Fig. (3.9) generated by Brune's algorithm. Note that in Fig. (4.3) we show another equivalent form of the Brune circuit which is quantized using the "effective Kirchhoff" technique described in Chapter (4.3).

Brune's circuit consists of M stages each containing a tightly-coupled inductor pair ($M_j = \sqrt{L_{j1}L_{j2}}$), a capacitor C_j, and a series resistor R_j. As we will show below, this interleaving of M lossless stages with $(M+1)$ resistors results in a non-trivial coupling between the modes of the circuit and the dissipative environment represented by these resistors. Since the Brune circuit has a non-trivial topology, we resort to [17, 18] to derive its Hamiltonian and compute the relaxation rates.

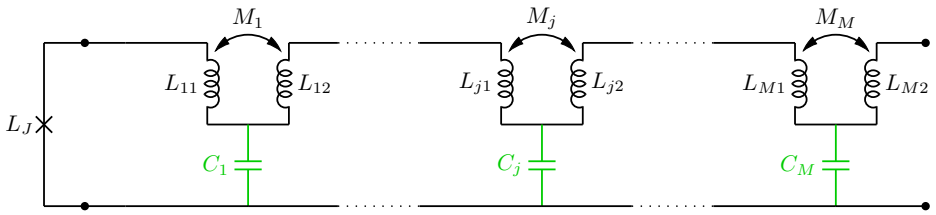

Figure 3.10: Lossless part of the Brune circuit. This is the circuit that corresponds to the Hamiltonian in Eq. (3.24) below. The lossless circuit is obtained from the circuit in Fig. (3.9) by taking $R_1, \ldots, R_M \to 0$ and $R_{M+1} \to \infty$ limits. Low-impedance treatment of $R_1 - R_M$ needs [18] whereas high-impedance treatment of R_{M+1} requires [17].

Lossless part of the Brune circuit is shown in Fig. (3.10). This is the circuit that corresponds to the Hamiltonian in Eq. (3.24) that is derived below. In the case

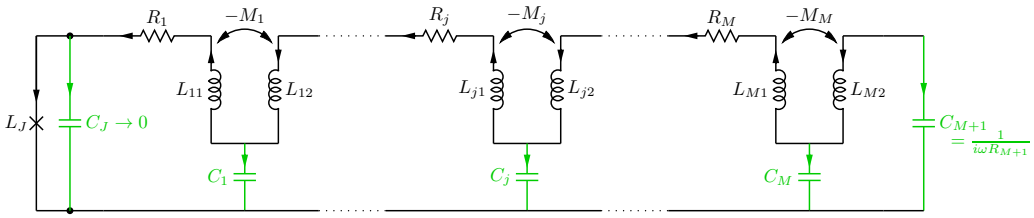

Figure 3.12: Modified Brune circuit. Tree branches are shown in black and chord branches are shown in green. Current directions are chosen to have the matrix $\mathcal{F}_C$ in Eq. (3.10) with all positive entries. Formal capacitance C_{M+1} is introduced for a technical reason: with the substitution $C_{M+1} = \frac{1}{i\omega R_{M+1}}$ we are able to compute dissipation rate due to R_{M+1} in the formalism of [17]. After the coordinate transformations we take $C_J \to 0$ limit so that this element is removed. To get $\mathcal{F}_C$ in Eq. (3.10) with all positive entries we reversed the direction of currents through and inverted the polarity of voltages across right coupled inductor branches which requires the update $M_j \to -M_j$ for mutual inductances. See Fig. (3.7) for the definition of the coupled inductor.

of unity turns ratios, this circuit is the (dual) lossless Foster form in Fig. (3.1) as shown by the equivalence in Fig. (3.11).

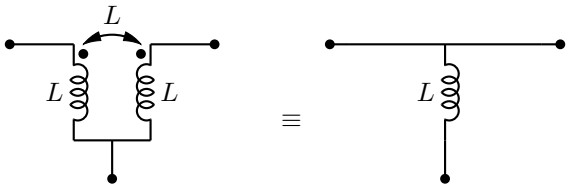

Figure 3.11: In the case of unit turns ratios, tightly-coupled inductor pairs simplify to ordinary inductors. In this case linear part of the circuit in Fig. (3.10) reduces to one of the classic Foster canonical forms [92, 94] shown in Fig. (3.1).

To apply analysis methods in [17, 18], we need to modify the original Brune circuit in Fig. (3.9) to get the augmented Brune circuit shown in Fig. (3.12). We replace the last resistor R_{M+1} with the capacitor C_{M+1} for a technical reason. It will be included in our analysis later through the substitution $C_{M+1} \leftarrow 1/(i\omega R_{M+1})$. Its contribution to the relaxation rate will be computed by referring to the equation of motion Eq. (61) in [17]. We also shunt the Josephson junction with the "formal" capacitance C_J. This is required for a non-singular capacitance matrix if there is no degenerate stage (see Chapter (3.3.3) for the treatment of a single

degenerate stage).

With the ordering $\{L_{12}, L_{22}, \ldots, L_{M2}, L_{11}, L_{21}, \ldots, L_{M1}\}$ for the tree inductors (note that the right coupled inductor branches come first and there is no chord inductor) and the ordering $\{C_1, \ldots, C_{M+1}\}$ for chord capacitors we construct the $\mathcal{F}_C$ matrix defined in Eq. (21) of [18] (To get $\mathcal{F}_C$ with all positive entries we reversed the direction of currents through and inverted the polarity of voltages across right branches of the coupled inductors which requires the update $M_j \leftarrow -M_j$ for mutual inductances. See Fig. (3.12) for the directions of the branch currents and Fig. (3.7) and Eq. (3.7) for the definition of the coupled inductor.)

$$\mathcal{F}_C = \begin{pmatrix} 1 & 1 & \cdots & 1 & 1 \\ & 1 & \cdots & 1 & 1 \\ & & \ddots & \vdots & \vdots \\ & 0 & & 1 & 1 \\ & & & & 1 \\ 1 & 1 & \cdots & 1 & 1 \\ & 1 & \cdots & 1 & 1 \\ & & \ddots & \vdots & \vdots \\ 0 & & & 1 & 1 \end{pmatrix} \tag{3.10}$$

where $\mathcal{F}_C$ is a $(2M+1) \times (M+1)$ matrix. We then compute the capacitance matrix in Eq. (22) of [18]

$$\mathcal{C}_0 = \begin{pmatrix} C_J & 0 \\ 0 & 0 \end{pmatrix} + \mathcal{F}_C \mathbf{C} \mathcal{F}_C^t \tag{3.11}$$

where $\mathbf{C}$ is a diagonal matrix with capacitances $\{C_1, \ldots, C_{M+1}\}$ on the diagonal.

Coupled inductors in the circuit in Fig. (3.12) satisfy the "tight coupling" condition $M_j = \sqrt{L_{j1} L_{j2}}$. The inductance matrix defined in Eq. (15) of [18] becomes singular in this tight coupling limit. To get around this issue we first introduce a small parameter L_0 controlling the deviation from the tight coupling limit ($L_0 \to 0$) by writing

$$M_j = \sqrt{L_{j1} L_{j2} - L_0^2} \tag{3.12}$$

Respecting the directions of the coupled inductor currents in Fig. (3.12) we can then write the inverse inductance matrix L_t^{-1} defined in Eq. (16) of [18]

$$L_t^{-1} = \frac{1}{L_0^2} \begin{pmatrix} L_{11} & & 0 & M_1 & & 0 \\ & \ddots & & & \ddots & \\ 0 & & L_{M1} & 0 & & M_M \\ M_1 & & 0 & L_{12} & & 0 \\ & \ddots & & & \ddots & \\ 0 & & M_M & 0 & & L_{M2} \end{pmatrix} \tag{3.13}$$

$\mathcal{G}$ matrix defined in Eq. (32) of [18] is given by

$$\mathcal{G} = \begin{pmatrix} 0 \\ \mathbf{I}_{(2M \times 2M)} \end{pmatrix} \tag{3.14}$$

and M_0 defined in Eq. (31) of [18] is

$$M_0 = \mathcal{G} L_t^{-1} \mathcal{G}^t \tag{3.15}$$

$$= \begin{pmatrix} 0 & 0 \\ 0 & L_t^{-1} \end{pmatrix} \tag{3.16}$$

To remove the singularities due to tight coupling condition we will rotate the coordinates to identify a subspace of the phase-space with finite eigenvalues and truncate the subspace with infinite eigenvalues. Note that this is a generalized eigenvalue problem for the matrices $\mathcal{C}_0$ and M_0 and we took care to ensure that finite eigenvectors have no support in the infinite subspace. We define the following rotation matrix U

$$U = \begin{pmatrix} 1 & 0 & & \cdots & & 0 \\ 0 & \frac{1}{\sqrt{1+t_1^2}} & & 0 & \frac{t_1}{\sqrt{1+t_1^2}} & 0 \\ & & \ddots & & & \ddots \\ \vdots & 0 & & \frac{1}{\sqrt{1+t_M^2}} & 0 & \frac{t_M}{\sqrt{1+t_M^2}} \\ & -\frac{t_1}{\sqrt{1+t_1^2}} & & 0 & \frac{1}{\sqrt{1+t_1^2}} & 0 \\ & & \ddots & & & \ddots \\ 0 & 0 & & -\frac{t_M}{\sqrt{1+t_M^2}} & 0 & \frac{1}{\sqrt{1+t_M^2}} \end{pmatrix} \tag{3.17}$$

where $t_j = \sqrt{\frac{L_{j1}}{L_{j2}}}$. We compute $U^t M_0 U$ and truncate it to its upper-left $(M+1) \times (M+1)$ sector (after taking the tight-coupling $L_0 \to 0$ limit) which corresponds to the subspace with finite eigenvalues to get

$$M_0' = \begin{pmatrix} 0 & \cdots & & 0 \\ \vdots & 1/L_1 & & 0 \\ & & \ddots & \\ 0 & 0 & & 1/L_M \end{pmatrix} \tag{3.18}$$

where $L_j = L_{j1} + L_{j2}$. We also transform $\mathcal{C}_0$ in Eq. (3.11) by computing $U^t \mathcal{C}_0 U$ and truncate it to get $\mathcal{C}_0'$.

$\mathcal{C}_0'$ and M_0' give a valid representation of the dynamics of the system. Although M_0' is diagonal, $\mathcal{C}_0'$ is in general non-zero in all its entries. There is however another transformation which is band-diagonal and brings the dynamics into a nearly diagonal form. The following transformation matrix T makes the Lagrangian of the system (i.e., both $\mathcal{C}_0'$ and M_0') band-diagonal:

$$T = \begin{pmatrix} 1 & & & \\ -\frac{\sqrt{1+t_1^2}}{1-t_1} & -\frac{\sqrt{1+t_1^2}}{1-t_1} & & 0 \\ & \frac{\sqrt{1+t_2^2}}{1-t_2} & \frac{\sqrt{1+t_2^2}}{1-t_2} & \\ & & \ddots & \ddots \\ & 0 & (-1)^M \frac{\sqrt{1+t_M^2}}{1-t_M} & (-1)^M \frac{\sqrt{1+t_M^2}}{1-t_M} \end{pmatrix} \tag{3.19}$$

Applying T to $\mathcal{C}_0'$ and M_0' we get

$$\mathcal{C} = T^t \mathcal{C}_0' T \tag{3.20}$$

$$= \begin{pmatrix} C_J + C_1' & t_1 C_1' & & 0 \\ t_1 C_1' & t_1^2 C_1' + C_2' & & \\ & \ddots & \ddots & \\ & & t_{M-1}^2 C_{M-1}' + C_M' & t_M C_M' \\ 0 & & t_M C_M' & t_M^2 C_M' + C_{M+1} \end{pmatrix} \tag{3.21}$$

and

$$\mathbf{M_0} = T^t M_0' T \tag{3.22}$$

$$= \begin{pmatrix} \frac{1}{L_1'} & \frac{1}{L_1'} & & & \\ \frac{1}{L_1'} & \frac{1}{L_1'}+\frac{1}{L_2'} & \frac{1}{L_2'} & & \\ & \frac{1}{L_2'} & \frac{1}{L_2'}+\frac{1}{L_3'} & \ddots & \\ & & \ddots & \ddots & \\ & & & \frac{1}{L_{M-1}'}+\frac{1}{L_M'} & \frac{1}{L_M'} \\ & & & \frac{1}{L_M'} & \frac{1}{L_M'} \end{pmatrix} \tag{3.23}$$

where $C_j' = C_j/\left(1-t_j\right)^2$, $L_j' = L_{j2}\left(1-t_j\right)^2$.

A Lagrangian $\mathcal{L}_0$ (and equivalently a Hamiltonian $\mathcal{H}_S$) can be written as

$$\mathcal{L}_S = \frac{1}{2}\dot{\mathbf{\Phi}}^T \mathcal{C}\dot{\mathbf{\Phi}} - U\left(\mathbf{\Phi}\right), \mathcal{H}_\mathcal{S} = \frac{1}{2}\boldsymbol{Q}^T\mathcal{C}^{-\mathbf{1}}\boldsymbol{Q} + U\left(\mathbf{\Phi}\right), \tag{3.24}$$

where

$$U\left(\mathbf{\Phi}\right) = -\left(\frac{\Phi_0}{2\pi}\right)^2 L_J^{-1}\cos\left(\varphi_J\right) + \frac{1}{2}\mathbf{\Phi}^T\mathbf{M_0}\mathbf{\Phi}. \tag{3.25}$$

$\mathbf{\Phi}$ is the vector of transformed(and truncated) coordinates of length $(M+1)$. φ_L is the phase across the Josephson junction. One can relate $\mathbf{\Phi}$ to the original branch fluxes in the Brune circuit by introducing an auxiliary vector $\mathbf{\Phi'}$ of length $(M+1)$ and keeping track of the two coordinate transformations U and T applied as follows

$$\mathbf{\Phi'} = T\mathbf{\Phi} \tag{3.26}$$

with

$$\mathbf{\Phi'} = \left(\Phi_J, \Phi_1', \cdots, \Phi_M'\right) \tag{3.27}$$

$$= U^t\left(\Phi_J, \mathbf{\Phi}_L\right)^t \tag{3.28}$$

where

$$\left(\Phi_J, \mathbf{\Phi}_L\right) = \left(\Phi_J, \Phi_{12}, \Phi_{22}, \cdots, \Phi_{M2}, \Phi_{11}, \Phi_{21}, \cdots, \Phi_{M1}\right) \tag{3.29}$$

is the vector of fluxes of tree branches in the Brune circuit in Fig. (3.12) , $\Phi_J = \left(\frac{\Phi_0}{2\pi}\right)\varphi_J$ and

$$\Phi_j' = \frac{1}{\sqrt{1+t_j^2}}\left(\Phi_{j2} - t_j\Phi_{j1}\right) \tag{3.30}$$

for $1 \leq j \leq M$. Note that $\mathbf{\Phi}_1 = \Phi_J$. We assume that the vector $U^t \left(\Phi_J, \mathbf{\Phi}_L\right)^t$ is truncated to its first $(M+1)$ rows before assignment to $\mathbf{\Phi}'$ in Eq. (3.28). From the truncated sector of the equation $\mathbf{\Phi}' = U^t \left(\Phi_J, \mathbf{\Phi}_L\right)^t$ we get the relations

$$\frac{1}{\sqrt{1+t_j^2}} \left(t_j \Phi_{j2} + \Phi_{j1}\right) = 0 \tag{3.31}$$

for $1 \leq j \leq M$, which gives using Eq. (3.30)

$$\Phi'_j = \sqrt{1+t_j^2}\Phi_{j2} \tag{3.32}$$

for $1 \leq j \leq M$.

By Eq. (3.26) we can write the j^{th} component of $\mathbf{\Phi}'$ for $1 \leq j \leq M$ as

$$\Phi'_j = (-1)^j \frac{\sqrt{1+t_j^2}}{1-t_j} (\Phi_j + \Phi_{j+1}) \tag{3.33}$$

Hence by Eq. (3.31) and Eq. (3.32) we have

$$\Phi_{j1} = (-1)^{j+1} \frac{t_j}{1-t_j} (\Phi_j + \Phi_{j+1}) \tag{3.34}$$

$$\Phi_{j2} = (-1)^j \frac{1}{1-t_j} (\Phi_j + \Phi_{j+1}) \tag{3.35}$$

for $1 \leq j \leq M$. We see that the flux variables Φ_{j1} and Φ_{j2} of coupled inductor branches are functions of only two consecutive flux variables in the new coordinates $\mathbf{\Phi}$.

3.3.2 Dissipation Analysis

In this section our aim is to compute relaxation rates. We treat resistors in Caldeira-Leggett formalism with each resistor representing a bath of harmonic oscillators with a smooth frequency spectrum. Couplings of the baths to the circuit degrees of freedom are given by $\bar{\mathbf{m}}$ vectors as defined in Eqs. (64) and (27) of [17] and [18], respectively.

We start by rearranging the equation of motion Eq. (29) of [18] (correcting the typo in the sign of $\mathcal{C}_Z$)

$$\mathcal{C} * \ddot{\mathbf{\Phi}} = -\frac{\partial U}{\partial \mathbf{\Phi}} + \mathcal{C}_Z * \ddot{\mathbf{\Phi}} \tag{3.36}$$

$\mathcal{C}_Z$ is given in frequency domain in Eq. (26) of [18] as

$$\mathcal{C}_Z(\omega) = \bar{\mathbf{m}}\bar{\mathbf{C}}_Z(\omega)\bar{\mathbf{m}}^T \tag{3.37}$$

Comparing Eq. (3.36) to the equation of motion Eq. (61) in [17] we identifiy in frequency domain

$$\mathbf{M}_d(\omega) = \omega^2 \mathcal{C}_Z(\omega) \tag{3.38}$$

Using Eq. (3.37) and (3.38)

$$\mathbf{M}_d(\omega) = \omega^2 \bar{\mathbf{m}}\bar{\mathbf{C}}_Z(\omega)\bar{\mathbf{m}}^T \tag{3.39}$$

Comparing Eq. (3.39) to the Eq. (64) in [17] we make the identification

$$\bar{\mathbf{L}}_Z^{-1}(\omega) = \omega^2 \bar{\mathbf{C}}_Z(\omega) \tag{3.40}$$

Note then that the $\bar{\mathbf{m}}$ vectors of both [17] and [18] are identical.

We will treat resistors one at a time. In such a case $\bar{\mathbf{C}}_Z(\omega)$ defined in Eq. (28) of [18] is a scalar function which allows us to write the kernel defined in Eq. (73) of [17] using Eq. (3.40) above

$$K(\omega) = \omega^2 \bar{\mathbf{C}}_Z(\omega) \tag{3.41}$$

Applying Eq. (124) of [17] we get the contribution to the relaxation rate from the resistor R_j $(1 \leq j \leq M+1)$:

$$\frac{1}{T_{1,j}} = \frac{4}{\hbar} \left|\langle 0 \left|\bar{\mathbf{m}}_j \cdot \mathbf{\Phi}\right| 1\rangle\right|^2 J_j(\omega_{01}) \coth\left(\frac{\hbar\omega_{01}}{2k_B T}\right) \tag{3.42}$$

$|0,1\rangle$ are the qubit eigenstates of the system Hamiltonian in Eq. (3.24) and ω_{01} is the transition frequency between them. Calculating these quantities requires solving the Schrodinger equation for the system Hamiltonian in Eq. (3.24) above; this can be a difficult task, but many effective accurate methods have been developed for doing this, in many works right up to the present [17, 18, 20, 104, 105]. The vector $\bar{\mathbf{m}}_j$ represents the coupling of the system to the bath of the resistor R_j. Note that our use of the non-normalized coupling vector $\bar{\mathbf{m}}_j$ and the flux vector $\mathbf{\Phi}$ implies removal of the factor $\mu\left(\frac{\Phi_0}{2\pi}\right)^2$ from the definition of the spectral function of the bath J in Eq. (93) of [17] (See Eqs. (3.47) and (3.50) below).

For $1 \leq j \leq M$, using Eqs. (26-28) in [18] we compute

$$\bar{\mathbf{m}}_j = \begin{pmatrix} 0 \\ \vdots \\ 0 \\ \frac{(-1)^{j-1}C_j}{(1-t_j)} \\ \frac{(-1)^{j}C_{j+1}}{(1-t_{j+1})} + \frac{(-1)^{j-1}t_jC_j}{(1-t_j)} \\ \vdots \\ \frac{(-1)^{M-1}C_M}{(1-t_M)} + \frac{(-1)^{M-2}t_{M-1}C_{M-1}}{(1-t_{M-1})} \\ \frac{(-1)^{M-1}t_MC_M}{(1-t_M)} \end{pmatrix} \tag{3.43}$$

where $\bar{\mathbf{m}}_j$ are vectors of length $(M+1)$ and

$$\bar{\mathbf{C}}_{Z,j}(\omega) = \frac{i\omega R_j}{1 + i\omega R_j \left(\sum_{k=j}^{M} C_k \right)} \tag{3.44}$$

We then have

$$K_j(\omega) = \omega^2 \bar{\mathbf{C}}_{Z,j}(\omega) \tag{3.45}$$

$$= \frac{i\omega^3 R_j}{1 + i\omega R_j \left(\sum_{k=j}^{M} C_k \right)} \tag{3.46}$$

Hence we obtain

$$J_j = Im\left[K_j(\omega)\right] \tag{3.47}$$

$$= \frac{\omega^3 R_j}{1 + \omega^2 R_j^2 \left(\sum_{k=j}^{M} C_k \right)^2} \tag{3.48}$$

To treat the last resistor R_{M+1} we first replace C_{M+1} in the last row of capacitance matrix by $1/(i\omega R_{M+1})$. This gives a term $-\frac{1}{R_{M+1}}\dot{\varphi}_M$ on the right hand side of the Euler-Lagrange equations of motion (Eq. (29) of [18]). Such a simple replacement in one term is valid because the flux variable of this capacitive branch never appears as an independent variable. The reason for this special treatment of the last resistor is that, because of its shunt position, its resistance should be sent to infinity rather than zero to get the lossless limit; thus, $1/R_{M+1}$ should be

the small parameter controlling dissipation. To perform a quantum treatment of all these dissipative contributions, we introduce a Caldeira-Leggett environment following the prescription of [17]. Following the notation of this treatment, we get a dissipation matrix for resistor R_{M+1}

$$\mathbf{M}_d = K_{M+1}(\omega)\,\bar{\mathbf{m}}_{M+1}\bar{\mathbf{m}}_{M+1}^T, \tag{3.49}$$

where $K_{M+1}(\omega) = \frac{i\omega}{R_{M+1}}$ and $\bar{\mathbf{m}}_{M+1} = \begin{pmatrix} 0 \\ \vdots \\ 0 \\ 1 \end{pmatrix}$ is a vector with $(M+1)$ rows. We then have

$$J_{M+1}(\omega) = Im\left[K_{M+1}(\omega)\right] = \frac{\omega}{R_{M+1}}, \tag{3.50}$$

We note that this formalism has been thoroughly studied in previous work [104], where it was seen that it gives a good accounting for relaxation of nearly harmonic systems, obtaining results in agreement with classical arguments.

Finally, we note that while the formulation given above appears to be highly singular for the case of any turns ratio $t_i \to 1$ in both the Hamiltonian (Eqs. (3.21) and (3.23) above), and in the decay rates (Eqs. (3.42) and (3.43) above), we have confirmed by examining other representations that all observable properties of the dynamics, such as ω_{01} and T_1, are smooth functions of t_i as it passes through unity.

3.3.3 Degenerate stages

The circuit extracted at each stage of the Brune's algorithm is shown in Fig. (3.5). It is possible that the extraction of the minimum resistance R_1 happens at $\omega_1 = 0$ or $\omega_1 = \infty$. Such cases we describe as being degenerate. In the case of an odd number of poles there will be necessarily a degenerate stage. In this section we will show how one can deal with the case $\omega_1 = \infty$ and how to update the Hamiltonian matrices in Eqs. (3.21), (3.23) and the coupling vectors $\mathbf{m}_j$ in Eq. (3.43).

We consider a degenerate case appearing at k^{th} stage. Such a stage corresponds to the limit of $L_k' \to 0$ and $t_k \to 0$. To remove the singularity we define a transformation

$$T_d = \begin{pmatrix} 1 & & & & \\ & \ddots & & & 0 \\ & & 1 & & \\ row & (k+1)\to & -1 & -1 & \\ & & & & \ddots \\ & 0 & & & -1 \end{pmatrix} \tag{3.51}$$

Applying this tranformation to the matrices $\mathbf{M_0}$ and $\mathcal{C}$ and removing the coordinate of the degenerate stage(this corresponds to the removal of $(k+1)^{th}$ row and $(k+1)^{th}$ column from both matrices) we get

$$T_d^t \mathbf{M_0} T_d = \begin{pmatrix} \frac{1}{L_1'} & \frac{1}{L_1'} & & & & & & \\ \frac{1}{L_1'} & \frac{1}{L_1'}+\frac{1}{L_2'} & \frac{1}{L_2'} & & & & & \\ & \frac{1}{L_2'} & \frac{1}{L_2'}+\frac{1}{L_3'} & \ddots & & 0 & & \\ & & \ddots & \ddots & & & & \\ & & & & \frac{1}{L_{k-1}'}+\frac{1}{L_{k+1}'} & \frac{1}{L_{k+1}'} & & \\ & & & & \frac{1}{L_{k+1}'} & \frac{1}{L_{k+1}'}+\frac{1}{L_{k+2}'} & \ddots & \\ & & 0 & & & \ddots & \ddots & \\ & & & & & & \frac{1}{L_{M-1}'}+\frac{1}{L_M'} & \frac{1}{L_M'} \\ & & & & & & \frac{1}{L_M'} & \frac{1}{L_M'} \end{pmatrix} \tag{3.52}$$

$$T_d^t \mathcal{C} T_d = \begin{pmatrix} C_J+C_1' & t_1C_1' & & & & & & \\ t_1C_1' & t_1^2C_1'+C_2' & \ddots & & & 0 & & \\ & \ddots & \ddots & & & & & \\ & & & t_{k-1}^2C_{k-1}'+(C_{k+1}'+C_k') & t_{k+1}C_{k+1}' & & & \\ & & & t_{k+1}C_{k+1}' & t_{k+1}^2C_{k+1}'+C_{k+2}' & \ddots & & \\ & & & & \ddots & \ddots & & \\ & 0 & & & & & t_{M-1}^2C_{M-1}'+C_M' & t_MC_M' \\ & & & & & & t_MC_M' & t_M^2C_M'+C_{M+1} \end{pmatrix} \tag{3.53}$$

Note that the matrices above are of size $M \times M$.

One needs to update also $\bar{\mathbf{m}}$ vectors. To do this we have to apply the transformation T_d to $\bar{\mathbf{m}}$ vectors and remove the entry corresponding to the degenerate coordinate (i.e. the $(k+1)^{th}$ row). Now we define some auxiliary vectors

$$\bar{\mathbf{m}}_a(j) = \begin{pmatrix} 0 \\ \vdots \\ 0 \\ j^{th}\ row \longrightarrow (-1)^{j-1}\frac{C_j}{(1-t_j)} \\ \vdots \\ (-1)^{k-2}\frac{C_{k-1}}{(1-t_{k-1})} \\ (-1)^{k+1}\frac{C_{k+1}}{(1-t_{k+1})} \\ \vdots \\ (-1)^{M}\frac{C_M}{(1-t_M)} \\ 0 \end{pmatrix} \tag{3.54}$$

$$\bar{\mathbf{m}}_b(j) = \begin{pmatrix} 0 \\ \vdots \\ 0 \\ (j+1)^{th}\ row \longrightarrow (-1)^{j-1}\frac{t_jC_j}{(1-t_j)} \\ \vdots \\ (-1)^{k-2}\frac{t_{k-1}C_{k-1}}{(1-t_{k-1})} \\ (-1)^{k+1}\frac{t_{k+1}C_{k+1}}{(1-t_{k+1})} \\ \vdots \\ (-1)^{M}\frac{t_MC_M}{(1-t_M)} \end{pmatrix} \tag{3.55}$$

$$\bar{\mathbf{m}}_{C_k} = \begin{pmatrix} 0 & \cdots & 0 & C_k & 0 & \cdots & 0 \end{pmatrix}^t \tag{3.56}$$

where C_k is in k^{th} row. Now we can write coupling vector $\bar{\mathbf{m}}_j$ to the bath of the resistor R_j as a function of the vectors defined in Eqs. (3.54), (3.55), (3.56) above as

$$\begin{aligned} \bar{\mathbf{m}}_j &= \bar{\mathbf{m}}_a(j) + \bar{\mathbf{m}}_b(j) + \bar{\mathbf{m}}_{C_k}, \qquad if\ j \le k \\ &= \bar{\mathbf{m}}_a(j) + \bar{\mathbf{m}}_b(j), \qquad if\ j > k \end{aligned} \tag{3.57}$$

Note that vectors above are all of length M. Spectral densities $J_i(\omega)$ are the same as in the non-degenerate case (Eqs. (3.47),(3.50)) for all resistors. Note also that dissipation treatment for the last resistor R_{M+1} is unaffected since C_{M+1} is untouched in Eq. (3.53).

3.4 Example

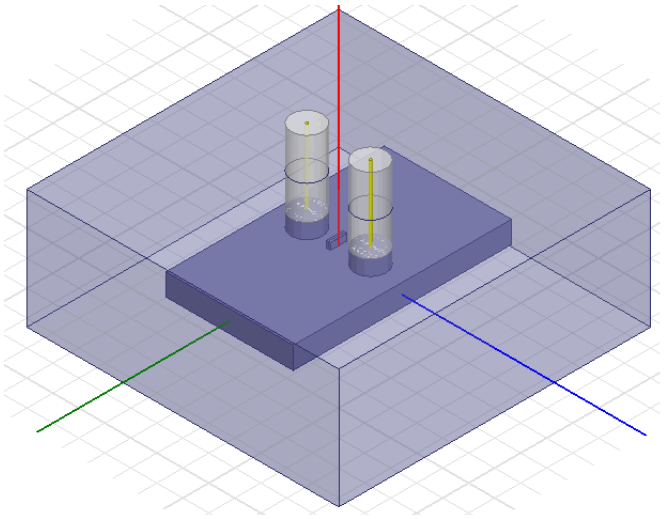

Figure 3.13: Geometry of the 3D transmon qubit simulated in HFSS. Light blue is perfect conductor and dark blue is the vacuum. The qubit port terminals are defined on a dielectric substrate located at the position of the red line. Two coaxial ports are positioned symmetrically on each side of the substrate. The cavity dimensions are $(height,\ length,\ width) = (4.2mm,\ 24.5mm,\ 42mm)$.

To show the application of the synthesis method we have just described, we analyse a dataset produced to analyse a 3D transmon similar to the one reported in a recent experiment at IBM [77]. Our modeling is performed using the finite-element electromagnetics simulator HFSS [99]. Since the systems we want to model admit very small loss [22, 106], they are very close to the border which separates passive systems from active ones. Therefore it is necessary to take care that the simulation resolution is high enough to ensure the passivity of the simulated impedance. Otherwise the fitted impedance $Z(s)$ does not satisfy the PR conditions in Chapter (3.2.1) meaning that there is no passive physical network corresponding to $Z(s)$.

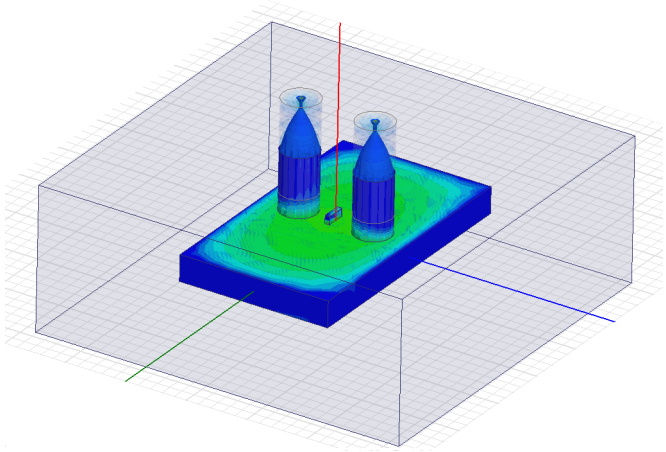

Figure 3.14: Fundamental mode (the $TE101$ mode) of the cavity with frequency $f_{TE101} = 6.875GHz$. Green color indicates electric field regions of higher magnitude compared to blue regions.

The simulated device is a 3D transmon, inserted with appropriate antenna structures into the middle of a rectangular superconducting (aluminium) box cavity, which is standard in several labs presently for high-coherence qubit experiments. Fig. (3.13) shows a perspective rendering of the device, and Fig. (3.14) shows an intensity map of the fundamental mode of the cavity. The simulation includes two coaxial ports entering the body of the cavity symmetrically on either side of the qubit. HFSS is used to calculate the device's three-port S matrix over a wide frequency range, from 3.0 to 15.0 GHz. The three ports are those defined by the two coaxial connectors and the qubit terminal pair. That is, the metal defining the Josephson junction itself is absent from the simulation, so that its very small capacitance and (nonlinear) inductance can be added back later as a discrete element as in Fig. (3.9). The conversion from the S matrix to Z_{sim} is calculated using standard formulas [70, 61], in which it is assumed that the two coaxial ports are terminated with a matched (Z_0=50Ω) resistor. We have confirmed that the lossy part of the resulting impedance is mostly determined by these port terminations, rather than by the (physically rather inaccurate) HFSS model of cavity-metal losses; this is consistent with the Q of the system being determined by its external couplings [77].

k	Pole s_k (GHz)	Residue R_k
1	-1.6152×10^{-6}	8363.13
2,3	$-0.00110372 \pm j6.87473$	$5.69612 \pm j0.00369273$
4, 5	$-0.00671733 \pm j7.05711$	$(6.26609 \pm j1.34164) \times 10^{-5}$
6, 7	$-1.34901 \pm j8.98453$	$(7.33283 \pm j5.61551) \times 10^{-3}$
8, 9	$-0.00272701 \pm j12.0048$	$7.15159 \pm j0.0227882$
10, 11	$-0.00918635 \pm j12.8561$	$(1.98602 \pm j0.0134996) \times 10^{-3}$
12, 13	$-1.40214 \pm j13.7644$	$(-8.60807 \pm j9.40397) \times 10^{-3}$
14, 15	$-0.131778 \pm j17.7404$	$23.8075 \pm j1.17404$
16, 17	$-3.14927 \pm j88.3524$	$(1.19527 \pm j0.120033) \times 10^{4}$

Table 3.1: Poles and residues for the fit to the HFSS dataset Z_{sim} as in Eq. (3.1).

To obtain the fitted rational impedance function $Z(s)$ as in Eq. (3.1), we use the MATLAB package Vector Fitting (VF) [100]. Applying VF to the simulated data Z_{sim} gives the partial fraction expansion form in Eq. (3.1) with the poles s_k and residues R_k listed in Table (3.1), with $e = 0$ and $d = 2.80407\Omega$. We fixed the number of poles M by increasing M until VF could not improve the fit further, stopping at $M = 17$. Note that some of the poles obtained in the fit have frequencies (imaginary part of s_k) outside the range of the simulation data; this is a normal feature of the fitting routine, used to guarantee a highly accurate fit throughout the entire simulated frequency band.

i	$R_i\,(\Omega)$	$C_i\,(nF)$	$L_{i1}\,(nH)$	$L_{i2}\,(nH)$
1	5.71974×10^{-5}	1.17020×10^{-4}	1.32810×10^{-1}	3.02058×10^{1}
2	5.53199×10^{-2}	2.49081×10^{-6}	8.75272×10^{1}	3.74225×10^{3}
3	1.84087×10^{2}	6.01727×10^{-8}	4.12954×10^{3}	1.98121×10^{4}
4	1.79021×10^{4}	1.44153×10^{-9}	4.56024×10^{4}	2.67489×10^{5}
5*	6.57108×10^{5}	2.01906×10^{-10}	0	0
6	4.90091×10^{5}	9.69933×10^{-12}	1.56173×10^{7}	1.55436×10^{7}
7	4.14678×10^{7}	1.64015×10^{-12}	3.09821×10^{8}	3.1134×10^{8}
8	2.33793×10^{7}	6.32007×10^{-11}	4.74168×10^{6}	1.95174×10^{6}
9	1.22342×10^{8}	1.70536×10^{-11}	7.42302×10^{6}	1.10608×10^{7}

$R_{10} = 6.35712 \times 10^{8}\Omega$

Table 3.2: Parameter values for synthesized Brune circuit. Note the strong (orders of magnitude) increase in impedance (in R and $\sqrt{L/C}$ values) as we go deep in the circuit. 5^{th} stage is degenerate treated in more detail in Chapter (3.3.3).

We have applied both Brune's algorithm and a lossy Foster analysis to our fitted

$Z(s)$. Circuit parameters obtained for the Brune circuit are listed in Table (3.2). We see that the series resistor connected directly to the qubit is quite tiny – the qubit is nearly lossless. The progressive increase of the resistance values in further stages of the circuit does not imply a large contribution of these resistors to loss, as they are seen by the qubit only through a kind of LC "filter". Indeed, the strong trend towards increasing impedance from stage to stage in the Brune network (both in the R and $\sqrt{L/C}$ values) means that the first few stages of the Brune network already give a good approximation of the cavity response $Z(s)$.

In fitting our data with the lossy Foster method (see Appendix (6.3)) one must be careful about residues with negative real parts or significant imaginary parts. Note that one cannot apply the lossy Foster approximation to terms corresponding to poles 12 and 13 in Table (3.1) since they have residues with negative real parts — there is no physical network to approximate those terms alone. We also drop DC and high-frequency terms corresponding to poles 1 and $14-17$ respectively: such a choice gives a better approximation for the real part of the impedance in the frequency band of interest. Thus, the best approximating Foster network consists of five RLC stages, representing the ten remaining pole pairs.

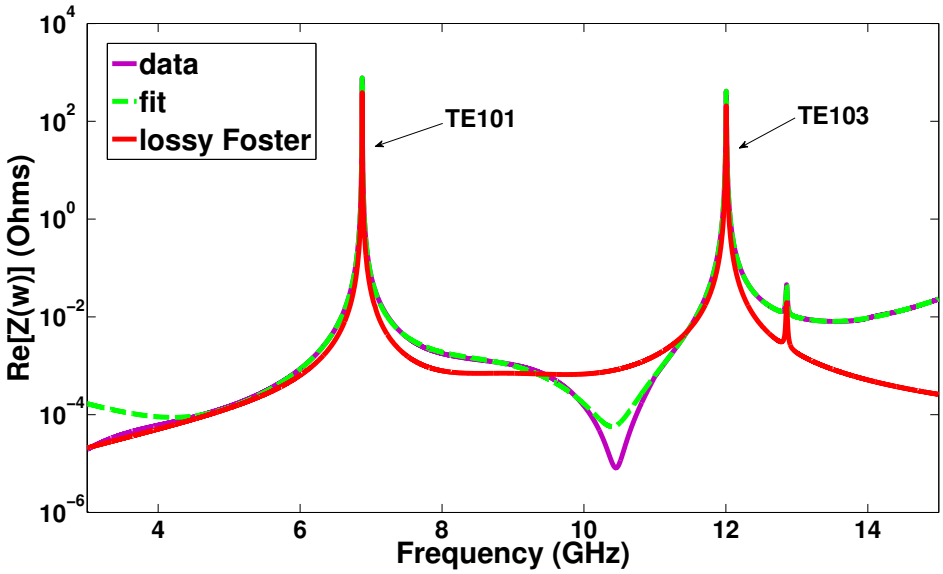

Figure 3.15: Real part of open-circuit response. Dotted green is open-circuit response for the Brune circuit which we identify with the open-circuit fit. Solid magenta is the simulated response. Red is the response of lossy Foster circuit. $TE101$ and $TE103$ are the resonances associated with classical rectangular cavity modes [60].

In Fig. (3.15) we compare these open-circuit impedances, as represented by the Brune and lossy-Foster methods, over the full range of our simulation data. The Foster representation clearly captures the main features of the response, notably the two classical box resonances of the cavity. But in finer details, especially far away from the resonances, the Brune representation, which is essentially indistinguishable from the fit obtained from VF, matches much better than the best lossy Foster circuit.

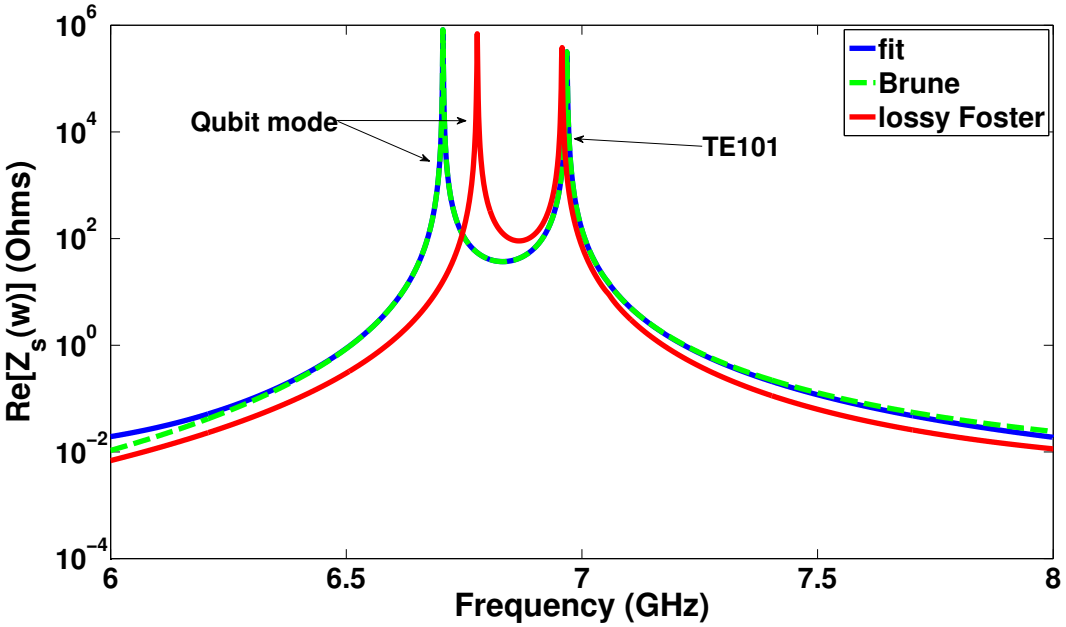

Figure 3.16: Real part of impedance in a small range of frequencies around the qubit pole ($f_{qb} = 6.7052$ GHz where f_{qb} is the qubit resonance for the exact fit) for the system shunted (with impedance Z_s) by a linear inductance $L_J = 4.5\,nH$ representing the Josephson junction for three different cases. The $TE101$ mode is not strongly affected by the presence of L_J.

We now show the improvements that can be expected by using the Brune circuit when representing the dynamics of the qubit-cavity system. Here we perform only simple calculations involving a harmonic qubit[1] (i.e., one represented by a linear inductance L_J), but our results give evidence that the Brune circuit will provide high-quality predictions even for more complex, strongly anharmonic qubits. In Fig. (3.16) we show the lossy part of the impedance when the cavity is shunted

[1]For the purely harmonic system, the quantization discussed here was already treatable with the methods of [107].

by a linear inductance $L_J = 4.5\,nH$. The fundamental cavity resonance (TE_{101}) is not significantly changed from the open circuit case, but the qubit appears as a new pole in the response. This "qubit pole" is again very accurately represented by the Brune circuit[2] ; however, using the lossy-Foster circuit derived from the open circuit case above, the qubit pole is significantly misplaced, by about 100MHz.

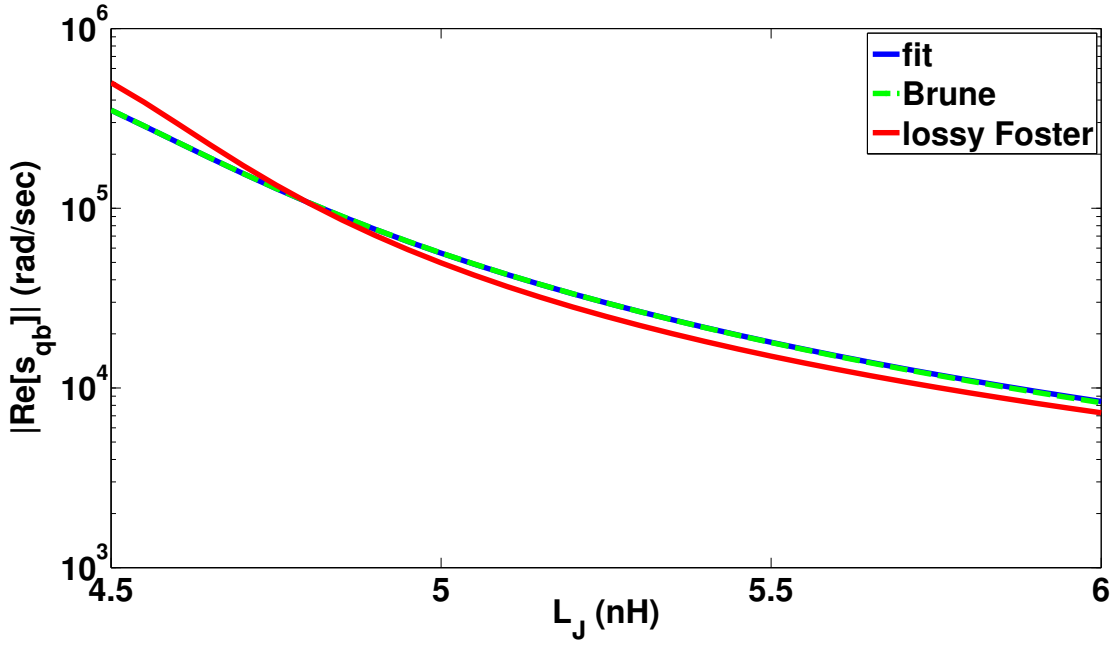

Figure 3.17: Magnitude of the real part of qubit pole s_{qb} as a function of linear inductance representing the Josephson junction shunting the system for three different cases: exact fit for the system shunted by the linear inductance, Brune circuit shunted by the linear inductance and lossy Foster circuit shunted by the linear inductance. The overall decreasing trend of this rate is simply due to the movement of the qubit pole to decreasing frequency as L_J is increased. T_1 relaxation rate of the qubit is given by $T_1^{-1} = \omega_{qb}/Q_{qb}$, where the quality factor $Q_{qb} = \omega_{qb}/|\xi_{qb}|$ with $\xi_{qb} = Re\,[s_{qb}]$, and $\omega_{qb} = Im\,[s_{qb}]$ is the frequency of the qubit mode.

Of course, in current applications of the Foster approach [78], one can do much better by refitting the Foster form with the linear inductance included in the response, and thus adding a new RLC stage to explicitly represent the qubit pole.

[2]The identification of this pole as the "qubit pole" is established by calculating the eigenmode of this pole, and observing that it has its highest weight on the Josephson junction branch of the circuit. Its mode frequency is also strongly dependent on L_J.

This is an effective strategy[3], but the results in Fig. (3.17) will indicate its limitations.

Here we compare the use of the Brune and (fixed) lossy-Foster circuit in giving the real part of the qubit pole, which is proportional to the relaxation rate $1/T_1$ Eq. (3.42), as the inductance L_J is varied. We see again that the Brune circuit matches the "fit" result, obtained directly from the HFSS data, very closely. The deviations of the lossy-Foster result are up to 20%, and the decrease of the loss rate with L_J is significantly underestimated. This suggest that no single lossy-Foster network, incorporating some fixed amount of linear inductance, will be able to match this trend.

Thus, while the Foster approach has been of considerable value in modelling nearly harmonic qubits like transmons [78], it appears that the exactness of the Brune approach will be of real value as we consider other, more anharmonic cavity-coupled qubits. A clear application in this direction will be the cases of fluxonium [108] or flux qubits [109] – our approach should provide a highly accurate multi-mode Hamiltonian for modelling dynamics in those cases.

[3]But note a drawback of the approach of including the linear part of the Josephson response in the model circuit: in the resulting circuit there is no one branch circuit variable that represents the physical response of the Josephson device, unlike in our approach where a single variable (φ_J of Eq. 3.25) plays this role directly.

CHAPTER 4

State-Space Brune Quantization

4.1 Introduction

In Chapter (3) we presented Brune's algorithm in s-domain (or frequency domain), s being the complex Laplace variable. In s-domain the impedance is given as a rational function of s (or as a rational matrix for multiports). As we saw in Section (3) Brune's algorithm needs partial fraction expansion operation in Eq. (3.2) to find L_2 which is related to the residue at the finite pole ω_1. Partial fraction expansion is an ill-conditioned operation since it requires finding roots of polynomials. Root finding is a numerically unstable problem since the roots become very sensitive to small perturbations in the coefficients as the degree of the polynomial increases. This is illustrated by Wilkinson's polynomial [110]. The problem becomes even more severe if one wants to apply multiport generalizations of synthesis algorithms(see [70]) since the degrees of polynomials increase with the number of ports.

Synthesis methods given in s-domain are usually referred to as classical network synthesis. See [70] for a comprehensive summary of classical synthesis algorithms. Classical synthesis methods appeared first in the historical development of the subject and played a key role in building the theory and expressing synthesis procedures. However classical frequency domain methods are not suitable for computer implementations due to the stability issues mentioned above.

The situation however is not so hopeless. Network synthesis algorithms can also be expressed in state-space formalism. State-space approach can be seen as a reformulation of the synthesis problem in the time-domain. See [111] for a comprehensive coverage of network theory in state-space. Most synthesis methods reexpressed in state-space requires the solution of a type of Riccati equation [111]. Solving the Riccati equation when the system's poles approach the imaginary axis is a "hard" problem. Since superconducting circuits have very little loss we usually encounter hard instances of Riccati equations in our models. Brune's algorithm expressed in state-space terms provides a method for solving such hard Riccati equations. Since Brune's algorithm reduces the complexity of the problem by a small amount at each step it avoids numerical instabilities appearing in more

direct methods which try to complete the synthesis in fewer steps. See [112] for a discussion of how Brune's method in state-space might help in solving hard Riccati equations. In the following section we briefly review state-space formalism and present Brune's impedance synthesis algorithm expressed in state-space terms.

In the last section of this chapter we introduce a new technique for the quantization of the one-port Brune circuit with ideal transformers. We call this new technique "effective Kirchhoff" method. We will see how much the effective Kirchhoff method simplify the analysis of the Brune circuit presented in the previous chapter. However the full power of the effective Kirchhoff method will be apparent in the next chapter when we will apply it to quantize the multiport Brune circuit. The earliest appearance (and the only one that we could find) of this technique in the literature is in [113] where ideal transformer variables are eliminated from mesh equations to compute some effective mesh impedance matrices.

4.2 State-Space Formalism

In state-space formalism (see Chapter 3 of [111] for more details on the state-space formalism in the context of network synthesis or [114] in the context of dimensionality reduction theory) the state of a linear time-invariant system with m inputs and n outputs is given by a real vector $\mathbf{x}$ of length N. The time evolution of the state is described by a first-order differential equation

$$\dot{\mathbf{x}} = \mathbf{A}\mathbf{x} + \mathbf{B}\mathbf{u} \tag{4.1}$$

where $\mathbf{u}$ is the input vector of length m, $\mathbf{A}$ a $(N \times N)$ matrix and $\mathbf{B}$ a $(N \times m)$ matrix. The output vector $\mathbf{y}$ is related to the input vector $\mathbf{u}$ by the following algebraic relation which involves also the state vector $\mathbf{x}$

$$\mathbf{y} = \mathbf{C}\mathbf{x} + \mathbf{D}\mathbf{u} \tag{4.2}$$

The output vector $\mathbf{y}$ is of length n, $\mathbf{C}$ is a $(n \times N)$ matrix and $\mathbf{D}$ a $(n \times m)$ matrix. If $\mathbf{u}$ holds the currents and $\mathbf{y}$ holds voltages at the ports of a network then $m = n$ and the multiport impedance is given by

$$\mathbf{Z}(s) = \mathbf{D} + \mathbf{C}(s\mathbf{I} - \mathbf{A})^{-1}\mathbf{B} \tag{4.3}$$

We will only consider real realizations here such that the matrices $\{\mathbf{A}, \mathbf{B}, \mathbf{C}, \mathbf{D}\}$ are all real.

Now let's assume that we transform the state $\mathbf{x}$ by a non-singular transformation $\mathbf{T}$ such that the new state $\mathbf{x}_1$ is given by

$$\mathbf{x}_1 = \mathbf{T}\mathbf{x} \tag{4.4}$$

Then using Eqs. (4.1) and (4.2) the state-space description for the state $\mathbf{x}_1$ is given by

$$\begin{aligned} \dot{\mathbf{x}}_1 &= \mathbf{A}_1\mathbf{x}_1 + \mathbf{B}_1\mathbf{u} && (4.5)\\ \mathbf{y} &= \mathbf{C}_1\mathbf{x}_1 + \mathbf{D}_1\mathbf{u} && (4.6) \end{aligned}$$

where

$$\begin{aligned} \mathbf{A}_1 &= \mathbf{T}\mathbf{A}\mathbf{T}^{-1} && (4.7)\\ \mathbf{B}_1 &= \mathbf{T}\mathbf{B} && (4.8)\\ \mathbf{C}_1 &= \mathbf{C}\mathbf{T}^{-1} && (4.9)\\ \mathbf{D}_1 &= \mathbf{D} && (4.10) \end{aligned}$$

The important point to note here is that the input-output relationship is unchanged that is $\{\mathbf{A}_1, \mathbf{B}_1, \mathbf{C}_1, \mathbf{D}_1\}$ is another state-space realization for the impedance $\mathbf{Z}(s)$, if $\mathbf{u}$ and $\mathbf{y}$ are the currents and voltages at the ports of the network corresponding to $\mathbf{Z}(s)$, respectively. To show this let $\mathbf{Z}_1(s)$ be the impedance corresponding to the realization $\{\mathbf{A}_1, \mathbf{B}_1, \mathbf{C}_1, \mathbf{D}_1\}$ then by Eq. (4.3)

$$\begin{aligned} \mathbf{Z}_1(s) &= \mathbf{D}_1 + \mathbf{C}_1(s\mathbf{I} - \mathbf{A}_1)^{-1}\mathbf{B}_1 && (4.11)\\ &= \mathbf{D} + \mathbf{C}\mathbf{T}^{-1}\left(s\mathbf{I} - \mathbf{T}\mathbf{A}\mathbf{T}^{-1}\right)^{-1}\mathbf{T}\mathbf{B} && (4.12)\\ &= \mathbf{D} + \mathbf{C}(s\mathbf{I} - \mathbf{A})^{-1}\mathbf{B} && (4.13)\\ &= \mathbf{Z}(s) && (4.14) \end{aligned}$$

where in the second line above we used Eqs. (4.7)-(4.10). For more details see Theorem (3.3.9) of [111].

4.2.1 Minimal Realizations

Given the impedance $\mathbf{Z}(s)$, a fundamental question in state-space theory is how to find a set of real matrices $\{\mathbf{A}, \mathbf{B}, \mathbf{C}, \mathbf{D}\}$ such that

$$\mathbf{Z}(s) = \mathbf{D} + \mathbf{C}(s\mathbf{I} - \mathbf{A})^{-1}\mathbf{B} \tag{4.15}$$

is satisfied with the dimension N of the state-space being minimum. In state-space theory minimal realizations are defined in a more abstract way. The set $\{\mathbf{A}, \mathbf{B}, \mathbf{C}, \mathbf{D}\}$ is called a *minimal realization* for the impedance $\mathbf{Z}(s)$ if $[\mathbf{A}, \mathbf{B}]$ is *completely controllable* and $[\mathbf{A}, \mathbf{C}]$ is *completely observable*.

Given the time evolution equation

$$\dot{\mathbf{x}} = \mathbf{A}\mathbf{x} + \mathbf{B}\mathbf{u} \tag{4.16}$$

$[\mathbf{A}, \mathbf{B}]$ is said to be *completely controllable*, if given the system is at state $\mathbf{x}(t_0)$ at time t_0, there exists a control $\mathbf{u}(t)$ defined over $[t_0, t_1]$ such that the system can be brought to the zero state $\mathbf{x}(t_1) = 0$ at time t_1 under the driven time evolution in Eq. (4.16).

Complete observability is defined for a triple $\{\mathbf{A}, \mathbf{B}, \mathbf{C}\}$ with $\mathbf{D} = 0$ such that we have the state-space equations

$$\dot{\mathbf{x}} = \mathbf{A}\mathbf{x} + \mathbf{B}\mathbf{u} \tag{4.17}$$

$$\mathbf{y} = \mathbf{C}\mathbf{x} \tag{4.18}$$

The pair $[\mathbf{A}, \mathbf{C}]$ is said to be *completely observable* if, given the input and ouput functions $\mathbf{u}(t)$ and $\mathbf{y}(t)$ over an interval $[t_0, t_1]$ it is possible to determine $\mathbf{x}(t_0)$ uniquely.

For more details on the properties of state-space realizations and the minimal realizations we refer the reader to Chapters 3.3 and 3.4 of [111].

For a scalar impedance function $z(s)$ the problem of finding a minimal state-space realization is relatively easy to answer. Without loss of generality we can assume that $z(\infty) = 0$. Let $z(s)$ be given as

$$z(s) = \frac{b_n s^{n-1} + \ldots + b_2 s + b_1}{s^n + a_n s^{n-1} + \ldots + a_2 s + a_1} \tag{4.19}$$

We assume that the numerator and the denominator polynomials in Eq. (4.19) have no common factors. If we define $\mathbf{A}$ in *companion matrix* form as

$$\mathbf{A} = \begin{pmatrix} 0 & 1 & 0 & \cdots & 0 \\ 0 & 0 & 1 & & 0 \\ \vdots & & & \ddots & \vdots \\ 0 & 0 & 0 & & 1 \\ -a_1 & -a_2 & -a_3 & \cdots & -a_n \end{pmatrix} \tag{4.20}$$

together with the following definitions for $\mathbf{B}$ and $\mathbf{C}$

$$\mathbf{B} = \begin{pmatrix} 0 \\ 0 \\ \vdots \\ 0 \\ 1 \end{pmatrix} \tag{4.21}$$

$$\mathbf{C}^T = \begin{pmatrix} b_1 \\ b_2 \\ \vdots \\ b_{n-1} \\ b_n \end{pmatrix} \tag{4.22}$$

then $\{\mathbf{A}, \mathbf{B}, \mathbf{C}\}$ is a minimal realization for $z(s)$. This is equivalent to $[\mathbf{A}, \mathbf{B}]$ being completely controllable and $[\mathbf{A}, \mathbf{C}^T]$ completely observable.

Finding a minimal realization corresponding to a multiport impedance matrix $\mathbf{Z}(s)$ is more involved and there are many procedures to find one. We will follow a physically motivated approach to find a minimal realization. The fitted impedance $\mathbf{Z}(s)$ in Eq. (3.1) contains most of the time numerical noise which makes residue matrices full rank. This is generically unphysical since a full rank residue matrix would correspond to a degenerate mode at a finite frequency. Finding a minimal representation for such an impedance would introduce unphysical degrees of freedom. To cure this problem we will apply the "compacting" technique described in [115] to reduce the rank of residue matrices and to obtain a minimal realization for our models.

Model-order reduction techniques are also used to reduce the dimension of non-minimal realizations. In applying order reduction procedures one should make sure that the passivity and reciprocity of the system is preserved [114, 116].

4.2.2 Positive-Real Property in State-Space terms

Here we state PR conditions given in Chapter (3.2.1) for a one-port impedance function in the state-space language for a multiport impedance $\mathbf{Z}(s)$.

Positive Real Lemma

Given an $m \times m$ impedance matrix $\mathbf{Z}(s)$ corresponding to an m-port network with $\mathbf{Z}(\infty) < \infty$ and with a minimal realization $\{\mathbf{A}, \mathbf{B}, \mathbf{C}, \mathbf{D}\}$. $\mathbf{Z}(s)$ is positive real if and only if there exist real matrices $\mathbf{P}$, $\mathbf{L}$ and $\mathbf{W}_0$ with $\mathbf{P}$ being positive definite symmetric satisfying

$$\mathbf{PA} + \mathbf{A^T P} = -\mathbf{L L^T} \tag{4.23}$$

$$\mathbf{PB} = \mathbf{C^T} - \mathbf{L W_0} \tag{4.24}$$

$$\mathbf{W_0^T W_0} = \mathbf{D} + \mathbf{D^T} \tag{4.25}$$

The Positive Real Lemma stated above goes also under the name "Kalman – Yakubovich – Popov Lemma" in control theory literature which refers to names involved in its development [117, 118, 119, 120, 121]. For more details on Positive Real lemma see Chapter 5 of [111].

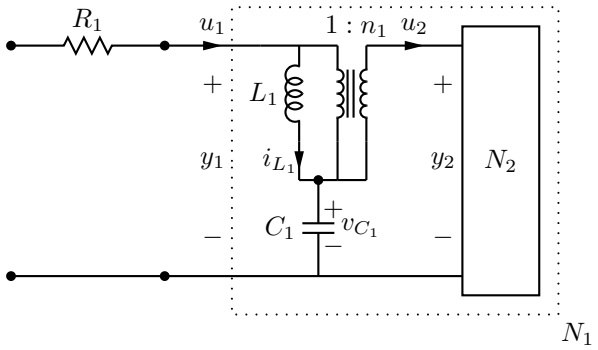

Figure 4.1: Brune circuit extraction in state-space

Most of the synthesis algorithms stated in state-space [111] are based on the determination of the matrix $\mathbf{P}$ which is usually done by solving a Riccati equation. The algorithm we present in the following will identify $\mathbf{P}$ in a recursive way which avoids numerical difficulties appearing in more direct methods presented in [111].

We will now present the Brune algorithm in state-space terms as described in [122].

4.2.3 Brune's algorithm in state-space terms (one-port case)

Here we assume that we have a one-port positive real impedance function $z(s)$ with the minimal realization $\{\mathbf{A}, \mathbf{B}, \mathbf{C}, D\}$ (We note that $\mathbf{D} = D$ is a scalar in this case). As shown in Fig. (4.1) Brune's algorithm in state-space starts with the extraction of the series resistance R_1. This step is identical to the step 2 in Chapter (3.2.2) except that the real part of the impedance is computed using the state-space matrices $\{\mathbf{A}, \mathbf{B}, \mathbf{C}, D\}$. Using Eq. (4.3) we can evaluate the real part of the impedance over the imaginary axis as follows

$$\begin{aligned} Re[z(j\omega)] &= \frac{1}{2}\left(z(j\omega) + z(-j\omega)\right) \\ &= D + \frac{1}{2}\mathbf{C}\left(j\omega\mathbf{I} - \mathbf{A}\right)^{-1}\mathbf{B} + \frac{1}{2}\mathbf{C}\left(-j\omega\mathbf{I} - \mathbf{A}\right)^{-1}\mathbf{B} \end{aligned} \tag{4.26}$$

Then the extracted resistance R_1 is given by

$$R_1 = \min_{\omega} Re[z(j\omega)] \tag{4.27}$$

for some frequency ω_0 with

$$Re[z(j\omega_0)] = R_1 \tag{4.28}$$

Let the network N_2 in Fig. (4.1) be described by the state-space equations

$$\dot{\mathbf{x}}_2 = \mathbf{A}_2\mathbf{x}_2 + \mathbf{B}_2\mathbf{u}_2 \tag{4.29}$$
$$\mathbf{y}_2 = \mathbf{C}_2\mathbf{x}_2 + D_2\mathbf{u}_2 \tag{4.30}$$

so that the realization $\{\mathbf{A}_2, \mathbf{B}_2, \mathbf{C}_2, D_2\}$ corresponds to the impedance $z_2(s) = D_2 + \mathbf{C}_2(s\mathbf{I} - \mathbf{A}_2)^{-1}\mathbf{B}_2$ seen at the terminals of the network N_2 (D_2 is a scalar).

Then the state-space equations for the network N_1 are given by

$$\begin{pmatrix} \dot{\mathbf{x}}_2 \\ \dot{x}_{C_1} \\ \dot{x}_{L_1} \end{pmatrix} = \begin{pmatrix} \mathbf{A}_2 & 0 & -\frac{\mathbf{B}_2}{n_1\sqrt{L_1}} \\ 0 & 0 & \frac{1}{n_1\sqrt{L_1C_1}} \\ \frac{\mathbf{C}_2}{n_1\sqrt{L_1}} & -\frac{1}{n_1\sqrt{L_1C_1}} & -\frac{D_2}{n_1^2L_1} \end{pmatrix} \begin{pmatrix} \mathbf{x}_2 \\ x_{C_1} \\ x_{L_1} \end{pmatrix} + \begin{pmatrix} \frac{\mathbf{B}_2}{n_1} \\ \frac{(1-1/n_1)}{\sqrt{C_1}} \\ \frac{D_2}{n_1^2\sqrt{L_1}} \end{pmatrix} \mathbf{u}_1$$
$$\mathbf{y}_1 = \begin{pmatrix} \frac{\mathbf{C}_2}{n_1} & \frac{(1-1/n_1)}{\sqrt{C_1}} & -\frac{D_2}{n_1^2\sqrt{L_1}} \end{pmatrix} \begin{pmatrix} \mathbf{x}_2 \\ x_{C_1} \\ x_{L_1} \end{pmatrix} + \frac{D_2}{n_1^2}\mathbf{u}_1 \tag{4.31}$$

where $x_{C_1} = \sqrt{C_1}v_{C_1}$ and $x_{L_1} = \sqrt{L_1}i_{L_1}$. Hence the state-space equations for the network N_1 are of the form

$$\dot{\mathbf{x}}_1 = \mathbf{A}_1\mathbf{x}_1 + \mathbf{B}_1\mathbf{u}_1 \tag{4.32}$$
$$\mathbf{y}_1 = \mathbf{C}_1\mathbf{x}_1 + D_1\mathbf{u}_1 \tag{4.33}$$

with

$$\mathbf{x}_1 = \begin{pmatrix} \mathbf{x}_2^T & x_{C_1} & x_{L_1} \end{pmatrix}^T \tag{4.34}$$

$$\mathbf{A}_1 = \begin{pmatrix} \mathbf{A}_2 & 0 & -\frac{\mathbf{B}_2}{n_1\sqrt{L_1}} \\ 0 & 0 & \frac{1}{n_1\sqrt{L_1C_1}} \\ \frac{\mathbf{C}_2}{n_1\sqrt{L_1}} & -\frac{1}{n_1\sqrt{L_1C_1}} & -\frac{D_2}{n_1^2L_1} \end{pmatrix} \tag{4.35}$$

$$\mathbf{B}_1 = \begin{pmatrix} \frac{\mathbf{B}_2}{n_1} \\ \frac{(1-1/n_1)}{\sqrt{C_1}} \\ \frac{D_2}{n_1^2\sqrt{L_1}} \end{pmatrix} \tag{4.36}$$

$$\mathbf{C}_1 = \begin{pmatrix} \frac{\mathbf{C}_2}{n_1} & \frac{(1-1/n_1)}{\sqrt{C_1}} & -\frac{D_2}{n_1^2\sqrt{L_1}} \end{pmatrix} \tag{4.37}$$

$$D_1 = \frac{D_2}{n_1^2} \tag{4.38}$$

The realization $\{\mathbf{A}_1, \mathbf{B}_1, \mathbf{C}_1, D_1\}$ then corresponds to the impedance function $z_1(s) = D_1 + \mathbf{C}_1 (s\mathbf{I} - \mathbf{A}_1)^{-1} \mathbf{B}_1$ seen at the terminals of the network N_1 (D_1 is a scalar) which is related to $z(s)$ by

$$z_1(s) = z(s) - R_1 \tag{4.39}$$

We note that $\mathrm{Re}[z_1(j\omega_0)] = 0$.

The following lemma stated in [122] shows that if $z_1(j\omega_0) + z_1(-j\omega_0) = 0$ is satisfied for some $\omega_0 > 0$ for a positive-real impedance function $z_1(s)$ with a minimal realization $\{\mathbf{A}_a, \mathbf{B}_a, \mathbf{C}_a, D_a\}$ then there exists a coordinate transformation $\mathbf{T}$ which would give an equivalent state-state description $\{\mathbf{A}_1, \mathbf{B}_1, \mathbf{C}_1, D_1\}$ for the impedance $z_1(s)$ in the form given in Eqs. (4.32-4.38) with

$$\begin{aligned} \mathbf{A}_1 &= \mathbf{T}\mathbf{A}_a\mathbf{T}^{-1} && (4.40)\\ \mathbf{B}_1 &= \mathbf{T}\mathbf{B}_a && (4.41)\\ \mathbf{C}_1 &= \mathbf{C}_a\mathbf{T}^{-1} && (4.42)\\ D_1 &= D_a && (4.43) \end{aligned}$$

See Chapter (4.2) for why $\{\mathbf{A}_1, \mathbf{B}_1, \mathbf{C}_1, D_1\}$ is an equivalent realization for the same impedance $z_1(s)$.

An explicit procedure is presented in [122] to compute $\mathbf{T}$. We now state the lemma and describe the algorithm to compute $\mathbf{T}$.

The Fundamental Lemma (one-port case)

Let $z_1(s)$ be a positive-real impedance function with the minimal realization $\{\mathbf{A}_a, \mathbf{B}_a, \mathbf{C}_a, D_a\}$ satisfying $z_1(j\omega_0) + z_1(-j\omega_0) = 0$ for some finite frequency ω_0 (with $j\omega_0$ not being an eigenvalue of $\mathbf{A}_a$). Then there exists a coordinate transformation matrix $\mathbf{T}$ such that $\mathbf{A}_1 = \mathbf{T}\mathbf{A}_a\mathbf{T}^{-1}$, $\mathbf{B}_1 = \mathbf{T}\mathbf{B}_a$, $\mathbf{C}_1 = \mathbf{C}_a\mathbf{T}^{-1}$ and $D_1 = D_a$ are of the form given in Eqs. (4.32-4.38).

Now we show how to construct $\mathbf{T}$.

1) Construct a nonsingular matrix $\mathbf{T}_a$ with the last two columns of $\mathbf{T}_a^{-1}$ being $(\omega_0^2\mathbf{I} + \mathbf{A}_a^2)^{-1}\mathbf{B}_a$ and $-\mathbf{A}_a(\omega_0^2\mathbf{I} + \mathbf{A}_a^2)^{-1}\mathbf{B}_a$.

2) Set $\mathbf{A}_b = \mathbf{T}_a\mathbf{A}_a\mathbf{T}_a^{-1}$, $\mathbf{B}_b = \mathbf{T}_a\mathbf{B}_a$ and $\mathbf{C}_b = \mathbf{C}_a\mathbf{T}_a^{-1}$ and compute

$$\begin{pmatrix} \mathbf{C}_b(\omega_0^2\mathbf{I} + \mathbf{A}_b^2)^{-1} \\ \mathbf{C}_b(\omega_0^2\mathbf{I} + \mathbf{A}_b^2)^{-1}\mathbf{A}_b \end{pmatrix} = \begin{pmatrix} \mathbf{K}_{12} & \mathbf{K}_{22} \end{pmatrix} \tag{4.44}$$

where $\mathbf{K}_{22}$ is a 2×2 matrix. Define

$$\mathbf{T}_b = \begin{pmatrix} \mathbf{I} & \mathbf{0} \\ \mathbf{K}_{22}^{-1}\mathbf{K}_{12} & \mathbf{I} \end{pmatrix} \tag{4.45}$$

3) Set $\mathbf{A}_c = \mathbf{T}_b\mathbf{A}_b\mathbf{T}_b^{-1}$, $\mathbf{B}_c = \mathbf{T}_b\mathbf{B}_b$ and $\mathbf{C}_c = \mathbf{C}_b\mathbf{T}_b^{-1}$ then

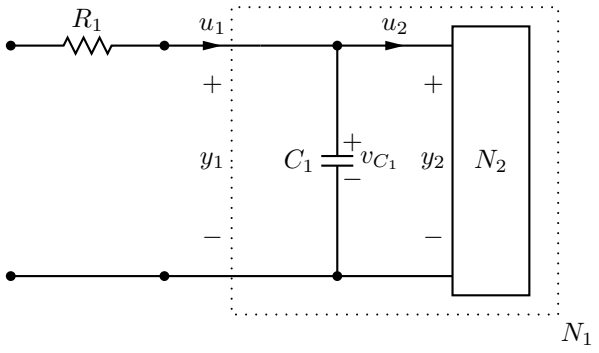

Figure 4.2: The capacitive degenerate Brune stage corresponding to the extraction of the resistor R_1 in Eq. (4.27) at inifinite frequency $\omega_0 = \infty$.

$$\begin{pmatrix} \mathbf{C}_c \left(\omega_0^2 \mathbf{I} + \mathbf{A}_c^2\right)^{-1} \\ \mathbf{C}_c \left(\omega_0^2 \mathbf{I} + \mathbf{A}_c^2\right)^{-1} \mathbf{A}_c \end{pmatrix} = \begin{pmatrix} 0 & \cdots & 0 & \alpha^2 & 0 \\ 0 & \cdots & 0 & 0 & \beta^2 \end{pmatrix} \tag{4.46}$$

for non-zero α, β. Define

$$\mathbf{T}_c = \begin{pmatrix} \mathbf{I} & 0 & 0 \\ 0 & \alpha & 0 \\ 0 & 0 & \beta \end{pmatrix} \tag{4.47}$$

Then $\mathbf{T} = \mathbf{T}_c \mathbf{T}_b \mathbf{T}_a$.

4.2.3.1 The Capacitive Degenerate Case

It is possible that the frequency ω_0 in Eq. (4.28) where the minimum in Eq. (4.27) is reached occurs at infinity $\omega_0 = \infty$. In such a case we need to extract a capacitive degenerate stage which doesn't involve the inductive circuit as shown in Fig. (4.2). Such a stage corresponds to the limit of $L_k' \to 0$ and $n_k \to \infty$. (The case $\omega_0 = 0$ requires the extraction of an inductive degenerate stage which won't be treated here).

Let the network N_2 in Fig. (4.1) be described again by the state-space equations

$$\dot{\mathbf{x}}_2 = \mathbf{A}_2 \mathbf{x}_2 + \mathbf{B}_2 \mathbf{u}_2 \tag{4.48}$$

$$\mathbf{y}_2 = \mathbf{C}_2 \mathbf{x}_2 + D_2 \mathbf{u}_2 \tag{4.49}$$

for some real matrices $\{\mathbf{A}_2, \mathbf{B}_2, \mathbf{C}_2, D_2\}$ so that the realization $\{\mathbf{A}_2, \mathbf{B}_2, \mathbf{C}_2, D_2\}$ corresponds to the impedance $z_2(s) = D_2 + \mathbf{C}_2 \left(s\mathbf{I} - \mathbf{A}_2\right)^{-1} \mathbf{B}_2$ seen at the terminals of the network N_2.

Then the state-space equations for the network N_1 are given by

$$\begin{pmatrix} \dot{\mathbf{x}}_2 \\ \dot{x}_{C_1} \end{pmatrix} = \begin{pmatrix} \mathbf{A}_2 - \frac{\mathbf{B}_2\mathbf{C}_2}{D_2} & \frac{\mathbf{B}_2}{D_2\sqrt{C_1}} \\ \frac{\mathbf{C}_2}{D_2\sqrt{C_1}} & -\frac{1}{D_2 C_1} \end{pmatrix} \begin{pmatrix} \mathbf{x}_2 \\ x_{C_1} \end{pmatrix} + \begin{pmatrix} 0 \\ \frac{1}{\sqrt{C_1}} \end{pmatrix} \mathbf{u}_1 \quad (4.50)$$

$$\mathbf{y}_1 = \begin{pmatrix} 0 & \frac{1}{\sqrt{C_1}} \end{pmatrix} \begin{pmatrix} \mathbf{x}_2 \\ x_{C_1} \end{pmatrix} \quad (4.51)$$

where $x_{C_1} = \sqrt{C_1} v_{C_1}$ and D_2 is a scalar in the one-port case. Hence the state-space equations for the network N_1 are of the form

$$\dot{\mathbf{x}}_1 = \mathbf{A}_1\mathbf{x}_1 + \mathbf{B}_1\mathbf{u}_1 \quad (4.52)$$

$$\mathbf{y}_1 = \mathbf{C}_1\mathbf{x}_1 + D_1\mathbf{u}_1 \quad (4.53)$$

with

$$\mathbf{x}_1 = \begin{pmatrix} \mathbf{x}_2^T & x_{C_1} \end{pmatrix}^T \quad (4.54)$$

$$\mathbf{A}_1 = \begin{pmatrix} \mathbf{A}_2 - \frac{\mathbf{B}_2\mathbf{C}_2}{D_2} & \frac{\mathbf{B}_2}{D_2\sqrt{C_1}} \\ \frac{\mathbf{C}_2}{D_2\sqrt{C_1}} & -\frac{1}{D_2 C_1} \end{pmatrix} \quad (4.55)$$

$$\mathbf{B}_1 = \begin{pmatrix} 0 \\ \frac{1}{\sqrt{C_1}} \end{pmatrix} \quad (4.56)$$

$$\mathbf{C}_1 = \begin{pmatrix} 0 & \frac{1}{\sqrt{C_1}} \end{pmatrix} \quad (4.57)$$

$$D_1 = 0 \quad (4.58)$$

The realization $\{\mathbf{A}_1, \mathbf{B}_1, \mathbf{C}_1, D_1\}$ then corresponds to the impedance function $z_1(s)$ seen at the terminals of the network N_1 which is related to $z(s)$ by

$$z_1(s) = z(s) - R_1 \quad (4.59)$$

In such a degenerate case we should also modify *the Fundamental Lemma* as follows:

The Fundamental Lemma (one-port capacitive degenerate case)

Let $z_1(s)$ be a positive-real impedance function with the minimal realization $\{\mathbf{A}_a, \mathbf{B}_a, \mathbf{C}_a, D_a\}$ satisfying $z_1(j\omega_0) + z_1(-j\omega_0) = 0$ for $\omega_0 = \infty$. Then there exists a coordinate transformation matrix $\mathbf{T}$ such that $\mathbf{A}_1 = \mathbf{T}\mathbf{A}_a\mathbf{T}^{-1}$, $\mathbf{B}_1 = \mathbf{T}\mathbf{B}_a$, $\mathbf{C}_1 = \mathbf{C}_a\mathbf{T}^{-1}$ and $D_1 = D_a = 0$ are of the form given in Eqs. (4.52-4.58).

Now we show how to construct $\mathbf{T}$.

1) Construct a nonsingular matrix $\mathbf{T}_a$ with the last column of $\mathbf{T}_a^{-1}$ being $\mathbf{B}_a$.
2) Set $\mathbf{A}_b = \mathbf{T}_a\mathbf{A}_a\mathbf{T}_a^{-1}$, $\mathbf{B}_b = \mathbf{T}_a\mathbf{B}_a$ and $\mathbf{C}_b = \mathbf{C}_a\mathbf{T}_a^{-1}$ and make the partitioning

$$\mathbf{C}_b = \begin{pmatrix} \mathbf{K}_{12} & \mathbf{K}_{22} \end{pmatrix} \tag{4.60}$$

where $\mathbf{K}_{22}$ is a scalar. Define

$$\mathbf{T}_b = \begin{pmatrix} \mathbf{I} & 0 \\ \mathbf{K}_{22}^{-1}\mathbf{K}_{12} & \mathbf{I} \end{pmatrix} \tag{4.61}$$

3) Set $\mathbf{A}_c = \mathbf{T}_b\mathbf{A}_b\mathbf{T}_b^{-1}$, $\mathbf{B}_c = \mathbf{T}_b\mathbf{B}_b$ and $\mathbf{C}_c = \mathbf{C}_b\mathbf{T}_b^{-1}$ then

$$\mathbf{C}_c = \begin{pmatrix} 0 & \cdots & 0 & \alpha^2 \end{pmatrix} \tag{4.62}$$

for a non-zero α. Define

$$\mathbf{T}_c = \begin{pmatrix} \mathbf{I} & 0 \\ 0 & \alpha \end{pmatrix} \tag{4.63}$$

Then $\mathbf{T} = \mathbf{T}_c\mathbf{T}_b\mathbf{T}_a$.

4.3 Quantization of the one-port state-space Brune circuit

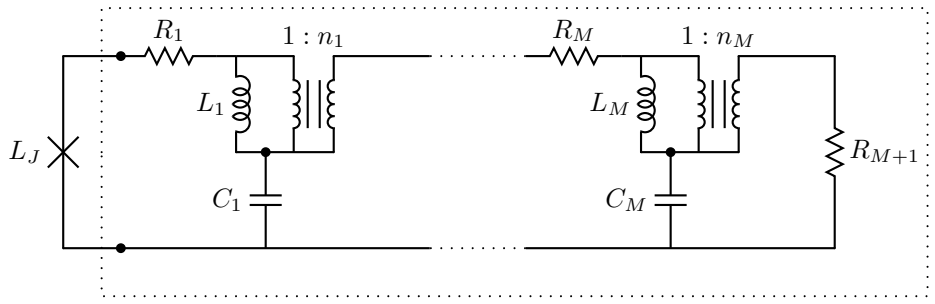

Figure 4.3: Brune circuit obtained from the state-space Brune algorithm is shown in the dotted box. We note that the coupled inductors at each stage of the classical Brune circuit in Fig. (3.9) are replaced by ordinary inductors shunting ideal transformers.

We call "the state-space Brune circuit" the circuit obtained by the application of the state-space Brune algorithm described in the previous section. An M stage state-space Brune circuit is shown in the dotted box in Fig. (4.3). We note that the coupled inductors at each stage of the classical Brune circuit in Fig. (3.9) are replaced by ordinary inductors shunting ideal transformers in Fig. (4.3). To treat the ideal transformers in the formalism of [18] we will introduce a new technique which will eliminate them by generating effective loop matrices involving turns ratios in their entries. We will see how this technique will simplify significantly the analysis of the one-port Brune circuit presented in the previous section. It will allow us to skip the transformation defined in Eq. (3.17). We will however see the full power of this technique in the next chapter when we will use it to quantize the multiport Brune circuit. Before starting to analyze this circuit we need to modify it as we did in Chapter (3.3.1).

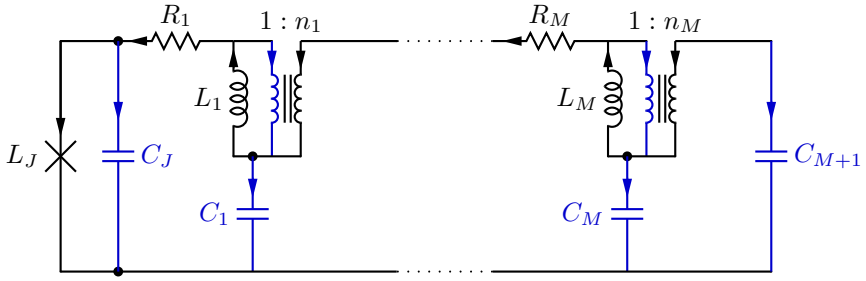

Figure 4.4: Modified state-space Brune circuit. Tree branches are shown in black and chord branches are shown in blue. Formal capacitance C_{M+1} is introduced for a technical reason: with the substitution $C_{M+1} = \frac{1}{i\omega R_{M+1}}$ we are able to compute dissipation rate due to R_{M+1} in the formalism of [17]. After the coordinate transformation (see below) we take $C_J \to 0$ limit.

An augmented form of the state-space Brune circuit is shown in Fig. (4.4). We modified the state-space Brune circuit in the same way as we did the original Brune circuit in Section (3.3.1). We repeat the modifications here for completeness. The last resistor R_{M+1} is again replaced with a capacitor C_{M+1} which is included in our analysis later through the substitution $C_{M+1} \leftarrow 1/(i\omega R_{M+1})$. Its contribution to the dissipation rate will be computed referring to the equation of motion Eq. (61) in [17].

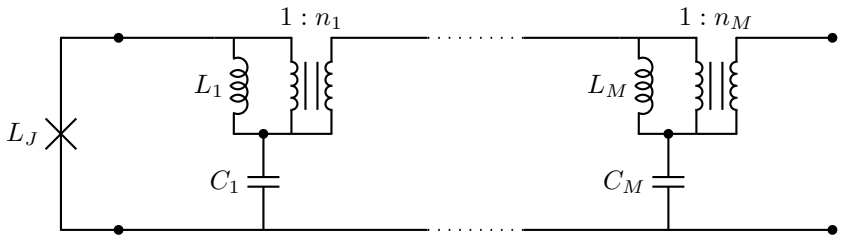

Figure 4.5: Lossless part of the state-space Brune circuit. It is this circuit that corresponds to the system Hamiltonian derived below. As discussed above, we take the limit $C_J \to 0$ so that this element is removed. The lossless circuit is obtained from Fig. (4.4) by taking R_1, R_2, ...$R_M \to 0$ and $R_{M+1} \to \infty$. It is these different limiting treatments that require the descriptions of $R_1 - R_M$ follow the low-impedance treatment as in [18], while the description of R_{M+1} needs the high-impedance treatment as in [17].

The lossless part of the state-space Brune circuit which corresponds to the system Hamiltonian derived below is shown in Fig. (4.5). As shown in Fig. (4.6) in

the special case of unity turns ratio, this circuit is exactly the (dual) lossless Foster form. We again add a formal capacitance C_J shunting the Josephson junction. This is required for a non-singular capacitance matrix if there are no degenerate stages.

Figure 4.6: Circuit identity showing that inductor-ideal transformer pairs appearing in state-space Brune stages simplify in the case of turns ratio equal to one; in this case Fig. (4.5) becomes identical to one of the classic lossless Foster canonical forms in Fig. (3.1).

We now show how to treat ideal transformers by extending the loop analysis in [18]. Kirchhoff's laws are given by Eqs. (4-5) in [18]

$$\mathbf{F}\mathbf{I}_{\text{ch}} = -\mathbf{I}_{\text{tr}} \tag{4.64}$$

$$\mathbf{F}^{\text{T}}\mathbf{V}_{\text{tr}} = \mathbf{V}_{\text{ch}} \tag{4.65}$$

where we have assumed that there is no flux bias. $\mathbf{I}_{\text{tr}}$ and $\mathbf{I}_{\text{ch}}$ are the tree and chord branch current vectors respectively partitioned as follows

$$\mathbf{I}_{\text{tr}} = \left(I_J, \mathbf{I}_L, \mathbf{I}_Z, \mathbf{I}_T^{(tr)}\right) \tag{4.66}$$

$$\mathbf{I}_{\text{ch}} = \left(\mathbf{I}_C, \mathbf{I}_T^{(ch)}\right) \tag{4.67}$$

Here labels J, L, Z, C, T correspond to Josephson junction, inductor, resistor, capacitor and ideal transformer branches, respectively. $\mathbf{I}_T^{(tr)}$ and $\mathbf{I}_T^{(ch)}$ are the current vectors for the ideal transformer branches in the tree and chords respectively. We also partition loop matrix $\mathbf{F}$ according to the partitioning of current vectors

$$\mathbf{F} = \begin{pmatrix} \mathbf{F}_{JC} & \mathbf{F}_{JT} \\ \mathbf{F}_{LC} & \mathbf{F}_{LT} \\ \mathbf{F}_{ZC} & \mathbf{F}_{ZT} \\ \mathbf{F}_{TC} & \mathbf{F}_{TT} \end{pmatrix} \tag{4.68}$$

We will eliminate ideal transformer branches from Kirchhoff laws in Eqs. (4.64)-(4.65) to get an effective loop matrices $\mathbf{F}^{eff}$ and $\left(\mathbf{F}^{T}\right)^{eff}$ such that we have a new set of effective Kirchhoff relations

$$\mathbf{F}^{eff}\mathbf{I}_{\text{ch}}^{eff} = -\mathbf{I}_{\text{tr}}^{eff} \tag{4.69}$$

$$\left(\mathbf{F}^{T}\right)^{eff}\mathbf{V}_{\text{tr}}^{eff} = \mathbf{V}_{\text{ch}}^{eff} \tag{4.70}$$

where

$$\begin{aligned}\mathbf{I}_{\text{tr}}^{eff} &= (I_J, \mathbf{I}_L, \mathbf{I}_Z)\\ \mathbf{I}_{\text{ch}}^{eff} &= \mathbf{I}_C\end{aligned}$$

and

$$\mathbf{F}^{eff} = \begin{pmatrix}\mathbf{F}_{JC}^{eff}\\ \mathbf{F}_{LC}^{eff}\\ \mathbf{F}_{ZC}^{eff}\end{pmatrix} \tag{4.71}$$

$$\left(\mathbf{F}^{T}\right)^{eff} = \begin{pmatrix}\left(\mathbf{F}_{JC}^{T}\right)^{eff} & \left(\mathbf{F}_{LC}^{T}\right)^{eff} & \left(\mathbf{F}_{ZC}^{T}\right)^{eff}\end{pmatrix} \tag{4.72}$$

In this section for simplicity reasons we will derive only the effective Kirchhoff's current law in Eq. (4.69) by computing $\mathbf{F}^{eff}$. We postpone the derivation of the effective Kirchhoff's voltage law and the computation of the matrix $\left(\mathbf{F}^{T}\right)^{eff}$ to the Appendix (6.5.1). However we note here that

$$\left(\mathbf{F}^{T}\right)^{eff} = \left(\mathbf{F}^{eff}\right)^{T} \tag{4.73}$$

should be verified to hold. This ensures the symmetry of various matrices computed in the formalisms of [17, 18] like the capacitance matrix $\mathcal{C}$ and the stiffness matrix M_0 for example.

Now we claim that $\mathbf{F}^{eff}$ in Eq. (4.71) is given by

$$\mathbf{F}_{JC}^{eff} = \begin{pmatrix}1 & 1 & \cdots & 1 & 1\end{pmatrix} \tag{4.74}$$

$$\mathbf{F}_{LC}^{eff} = \begin{pmatrix}1 & (1-n_1) & \cdots & (1-n_1) & (1-n_1)\\ & \ddots & \ddots & \vdots & \vdots\\ & & 1 & (1-n_{M-1}) & (1-n_{M-1})\\ \mathbf{0} & & & 1 & (1-n_M)\end{pmatrix} \tag{4.75}$$

$$\mathbf{F}_{ZC}^{eff} = \begin{pmatrix}1 & 1 & \cdots & 1 & 1\\ & 1 & \cdots & 1 & 1\\ & & \ddots & \vdots & \vdots\\ \mathbf{0} & & & 1 & 1\end{pmatrix} \tag{4.76}$$

where $\mathbf{F}_{JC}^{eff}$ is a row vector of length $(M+1)$, $\mathbf{F}_{LC}^{eff}$ and $\mathbf{F}_{ZC}^{eff}$ are $M \times (M+1)$ matrices. To see how the matrices in Eqs. (4.74)-(4.76) can be computed we first note the following

$$\mathbf{I}_T^{(tr)} = -\mathbf{F}_{TC}\mathbf{I}_C \tag{4.77}$$

with

$$\mathbf{F}_{TC} = \begin{pmatrix} 0 & 1 & 1 & \cdots & 1 \\ & 0 & 1 & \cdots & 1 \\ & & \ddots & \ddots & \vdots \\ \mathbf{0} & & & 0 & 1 \end{pmatrix} \tag{4.78}$$

where $\mathbf{F}_{TC}$ is a $M \times (M+1)$ matrix. We note that $\mathbf{F}_{TC}$ doesn't involve any turns ratios. Using the ideal transformer relations $\mathbf{I}_T^{(ch)} = -\mathbf{N}\mathbf{I}_T^{(tr)}$ with $\mathbf{N}$ being the diagonal matrix of turns ratios

$$\mathbf{N} = \begin{pmatrix} n_1 & & \mathbf{0} \\ & \ddots & \\ \mathbf{0} & & n_M \end{pmatrix} \tag{4.79}$$

and Eq. (4.77) we get

$$\mathbf{I}_T^{(ch)} = \mathbf{N}\mathbf{F}_{TC}\mathbf{I}_C \tag{4.80}$$

Inductor currents are given by

$$\mathbf{I}_L = -\mathbf{F}_{LC}\mathbf{I}_C - \mathbf{F}_{LT}\mathbf{I}_T^{(ch)} \tag{4.81}$$

where

$$\mathbf{F}_{LC} = \begin{pmatrix} 1 & 1 & \cdots & 1 & 1 \\ & 1 & \cdots & 1 & 1 \\ & & \ddots & \vdots & \vdots \\ \mathbf{0} & & & 1 & 1 \end{pmatrix} \tag{4.82}$$

and $\mathbf{F}_{LT} = -\mathbb{I}$. Using Eqs. (4.80) and (4.81) we get

$$\mathbf{I}_L = -\left(\mathbf{F}_{LC} - \mathbf{N}\mathbf{F}_{TC}\right)\mathbf{I}_C \tag{4.83}$$

which gives the effective loop matrix $\mathbf{F}_{LC}^{eff}$

$$\mathbf{F}_{LC}^{eff} = \mathbf{F}_{LC} - \mathbf{N}\mathbf{F}_{TC} \tag{4.84}$$

$$= \begin{pmatrix} 1 & (1-n_1) & \cdots & (1-n_1) & (1-n_1) \\ & \ddots & \ddots & \vdots & \vdots \\ & & 1 & (1-n_{M-1}) & (1-n_{M-1}) \\ \mathbf{0} & & & 1 & (1-n_M) \end{pmatrix} \tag{4.85}$$

We note that $\mathbf{F}_{LC}^{eff}$ is no longer a binary matrix as we have turns ratios appearing in its entries.

$\mathbf{F}_{JC}^{eff}$ is simply given by

$$\mathbf{F}_{JC}^{eff} = \mathbf{F}_{JC} \tag{4.86}$$

$$= \begin{pmatrix} 1 & 1 & \cdots & 1 & 1 \end{pmatrix} \tag{4.87}$$

Since the current through the Josephson junction depends only on chord capacitor currents

$$I_J = -\mathbf{F}_{JC}\mathbf{I}_C \tag{4.88}$$

Note that $\mathbf{F}_{JC}^{eff}$ does not depend on turns ratios. Similarly the currents through the resistors R_j for $1 \leq j \leq M$ depend only on chord capacitor currents

$$\mathbf{I}_Z = -\mathbf{F}_{ZC}\mathbf{I}_C$$

Hence

$$\mathbf{F}_{ZC}^{eff} = \mathbf{F}_{ZC} \tag{4.89}$$

$$= \begin{pmatrix} 1 & 1 & \cdots & 1 & 1 \\ & 1 & \cdots & 1 & 1 \\ & & \ddots & \vdots & \vdots \\ \mathbf{0} & & & 1 & 1 \end{pmatrix}$$

We compute the capacitance matrix in Eq. (22) of [18] as

$$\mathcal{C}_0 = \begin{pmatrix} C_J & \mathbf{0} \\ \mathbf{0} & \mathbf{0} \end{pmatrix} + \mathcal{F}_C^{eff}\mathbf{C}\left(\mathcal{F}_C^{eff}\right)^T \tag{4.90}$$

where $\mathbf{C}$ is the diagonal matrix of capacitances

$$\mathbf{C} = \begin{pmatrix} C_1 & & \mathbf{0} \\ & \ddots & \\ \mathbf{0} & & C_{M+1} \end{pmatrix} \tag{4.91}$$

and

$$\mathcal{F}_C^{eff} = \begin{pmatrix} \mathbf{F}_{JC}^{eff} \\ \mathbf{F}_{LC}^{eff} \end{pmatrix} \tag{4.92}$$

$\mathbf{L}_t$ in Eq. (15) of [18] is a diagonal matrix of inductances

$$\mathbf{L}_t = \begin{pmatrix} L_1 & & \mathbf{0} \\ & \ddots & \\ \mathbf{0} & & L_M \end{pmatrix} \tag{4.93}$$

With

$$\mathcal{G} = \begin{pmatrix} \mathbf{0} \\ 1_{M\times M} \end{pmatrix} \tag{4.94}$$

we get using Eq. (31) of [18]

$$M_0 = \mathcal{G}\mathbf{L}_t^{-1}\mathcal{G}^t \tag{4.95}$$

$$= \begin{pmatrix} 0 & \mathbf{0} \\ \mathbf{0} & \mathbf{L}_t^{-1} \end{pmatrix} \tag{4.96}$$

We skip the first transformation defined in (3.17) and the truncation afterwards since we are already in the low dimensional subspace with $(M+1)$ degrees of freedom. We again define a local transformation matrix T which makes the Lagrangian description (i.e., both $\mathcal{C}_0$ and M_0) of the system band-diagonal:

$$T = \begin{pmatrix} 1 & & & & \\ -1/(1-n_1) & -1/(1-n_1) & & \mathbf{0} & \\ & 1/(1-n_2) & 1/(1-n_2) & & \\ & & \ddots & \ddots & \\ & \mathbf{0} & & (-1)^M/(1-n_M) & (-1)^M/(1-n_M) \end{pmatrix} \tag{4.97}$$

Applying T to $\mathcal{C}_0$ and M_0 we get

$$\mathcal{C} = T^t \mathcal{C}_0 T \tag{4.98}$$

$$= \begin{pmatrix} C_J + n_1^2 C_1^{'} & n_1 C_1^{'} & & & \\ n_1 C_1^{'} & C_1^{'} + n_2^2 C_2^{'} & \ddots & 0 & \\ & \ddots & \ddots & & \\ & 0 & & C_{M-1}^{'} + n_M^2 C_M^{'} & n_M C_M^{'} \\ & & & n_M C_M^{'} & C_M^{'} + C_{M+1} \end{pmatrix} \tag{4.99}$$

$$\mathbf{M_0} = T^t M_0 T \tag{4.100}$$

$$= \begin{pmatrix} \frac{1}{L_1^{'}} & \frac{1}{L_1^{'}} & & & \\ \frac{1}{L_1^{'}} & \frac{1}{L_1^{'}} + \frac{1}{L_2^{'}} & \frac{1}{L_2^{'}} & 0 & \\ & \frac{1}{L_2^{'}} & \frac{1}{L_2^{'}} + \frac{1}{L_3^{'}} & \ddots & \\ & & \ddots & \ddots & \\ & 0 & & \frac{1}{L_{M-1}^{'}} + \frac{1}{L_M^{'}} & \frac{1}{L_M^{'}} \\ & & & \frac{1}{L_M^{'}} & \frac{1}{L_M^{'}} \end{pmatrix} \tag{4.101}$$

where $C_j^{'} = C_j / \left(1 - n_j\right)^2$, $L_j^{'} = L_j \left(1 - n_j\right)^2$.

A Lagrangian $\mathcal{L}_0$ (and equivalently a Hamiltonian $\mathcal{H}_\mathcal{S}$) can be written as

$$\mathcal{L}_0 = \frac{1}{2} \dot{\mathbf{\Phi}}^T \mathcal{C} \dot{\mathbf{\Phi}} - U\left(\mathbf{\Phi}\right), \; \mathcal{H}_\mathcal{S} = \frac{1}{2} \boldsymbol{Q}^T \mathcal{C}^{-1} \boldsymbol{Q} + U\left(\mathbf{\Phi}\right) \tag{4.102}$$

where

$$U\left(\mathbf{\Phi}\right) = -\left(\frac{\Phi_0}{2\pi}\right)^2 L_J^{-1} \cos\left(\varphi_J\right) + \frac{1}{2} \mathbf{\Phi}^T \mathbf{M_0} \mathbf{\Phi} \tag{4.103}$$

$\mathbf{\Phi}$ is the vector of transformed coordinates of length $(M+1)$ and $\Phi_1 = \left(\frac{\Phi_0}{2\pi}\right) \varphi_J$.

4.3.1 Dissipation Analysis

To compute relaxation rates $1/T_1$ for each resistor we will follow the same treatment of the Section (3.3.2). That is we will again interpret the equation of motion in Eq. (29) of [18] as an equation of motion in Eq. (61) of [17]. This allows us to make the following identifications as in Section (3.3.2)

$$\mathbf{M}_d\left(\omega\right) = \omega^2 \mathcal{C}_Z \tag{4.104}$$

$$K(\omega) = \omega^2 \bar{\mathbf{C}}_Z(\omega) \tag{4.105}$$

$\mathbf{M}_d$ and $K(\omega)$ are given in Eqs. (72-75) of [17]. Then coupling vectors $\bar{\mathbf{m}}$ are identical in both formalisms [17, 18] which can be computed using Eq. (27) of [18] with effective loop matrices computed in the previous section in Eqs. (4.89) and (4.92)

$$\bar{\mathbf{m}} = \mathcal{F}_C^{eff} \mathbf{C} \left(\mathbf{F}_{ZC}^{eff} \right)^T \tag{4.106}$$

We note that $\mathbf{F}_{ZC}^{eff}$ is independent of ideal transformer turns ratios. We treat each resistor separately. Hence for the resistor R_j we will use only the j^{th} row of the $\mathbf{F}_{ZC}^{eff}$ matrix in the formula Eq. (4.106). We apply again Eq. (124) of [17] as in Section (3.3.2) to compute the contribution to the relaxation rate from the resistor R_j $(1 \leq j \leq M+1)$:

$$\frac{1}{T_{1,j}} = \frac{4}{\hbar} \left| \langle 0 \left| \bar{\mathbf{m}}_j \cdot \mathbf{\Phi} \right| 1 \rangle \right|^2 J_j(\omega_{01}) \coth\left(\frac{\hbar \omega_{01}}{2 k_B T} \right) \tag{4.107}$$

where $|0,1\rangle$ are the qubit eigenlevels of the system Hamiltonian. As noted previously the vector $\bar{\mathbf{m}}_j$ (of length $(M+1)$) describes the coupling of the system to the environment representing resistor R_j. Note again that our use of the non-normalized coupling vector $\bar{\mathbf{m}}_j$ and the flux vector $\mathbf{\Phi}$ implies removal of the factor $\mu \left(\frac{\Phi_0}{2\pi} \right)^2$ from the definition of the spectral function of the bath J in Eq. (93) of [17] (See Eqs. (4.112) and (4.115) below).

For $1 \leq j \leq M$, using Eqs. (26-28) in [18] we compute

$$\bar{\mathbf{m}}_j = \begin{pmatrix} 0 \\ \vdots \\ 0 \\ j^{th} entry \rightarrow \frac{(-1)^j n_j C_j}{(1-n_j)} \\ \frac{(-1)^{j+1} n_{j+1} C_{j+1}}{(1-n_{j+1})} + \frac{(-1)^j C_j}{(1-n_j)} \\ \vdots \\ \frac{(-1)^M n_M C_M}{(1-n_M)} + \frac{(-1)^{M-1} C_{M-1}}{(1-n_{M-1})} \\ \frac{(-1)^M C_M}{(1-n_M)} \end{pmatrix} \tag{4.108}$$

where $\bar{\mathbf{m}}_j$ are vectors of length $(M+1)$ and

$$\bar{\mathbf{C}}_{Z,j}(\omega) = -\frac{i\omega R_j}{1 + i\omega R_j \left(\sum_{k=j}^{M} C_k \right)} \tag{4.109}$$

We then have

$$K_j(\omega) = \omega^2 \bar{\mathbf{C}}_{Z,j}(\omega) \tag{4.110}$$

$$= \frac{i\omega^3 R_j}{1 + i\omega R_j \left(\sum_{k=j}^{M} C_k \right)} \tag{4.111}$$

Hence we obtain

$$J_j = Im\left[K_j(\omega)\right] \tag{4.112}$$

$$= \frac{\omega^3 R_j}{1 + \omega^2 R_j^2 \left(\sum_{k=j}^{M} C_k \right)^2} \tag{4.113}$$

We treat the last resistor R_{M+1} in the same way as in Section (3.3.2), i.e. we replace C_{M+1} in the last row of capacitance matrix by $1/(i\omega R_{M+1})$ and the discussion in Section (3.3.2) applies again. We get the following dissipation matrix for resistor R_{M+1}

$$\mathbf{M}_d = K_{M+1}(\omega)\, \bar{\mathbf{m}}_{M+1} \bar{\mathbf{m}}_{M+1}^T, \tag{4.114}$$

where $K_{M+1}(\omega) = \frac{i\omega}{R_{M+1}}$ and $\bar{\mathbf{m}}_{M+1} = \begin{pmatrix} 0 \\ \vdots \\ 0 \\ 1 \end{pmatrix}$ is a vector with $(M+1)$ rows. We then have

$$J_{M+1}(\omega) = Im\left[K_{M+1}(\omega)\right] = \frac{\omega}{R_{M+1}}, \tag{4.115}$$

4.3.2 Degenerate case

Here again we consider only a single capacitive degenerate stage. Such a case has appeared in the example circuit we studied as listed in Table 3.2. We consider a degenerate case appearing at k^{th} stage. As noted in Section (4.2.3.1) such a stage corresponds to the limit of $L'_k \to 0$ and $n_k \to \infty$. In case of such degeneracy we remove the $(k+1)^{th}$ row in the $\mathcal{F}_C^{eff}$ matrix in Eq. (4.75):

$$\mathcal{F}_C^{eff} = \begin{pmatrix} 1 & 1 & \cdots & 1 & 1 & \cdots & 1 & 1 \\ 1 & (1-n_1) & \cdots & (1-n_1) & (1-n_1) & \cdots & (1-n_1) & (1-n_1) \\ & \ddots & \ddots & \vdots & \vdots & & \vdots & \vdots \\ & & 1 & (1-n_{k-1}) & (1-n_{k-1}) & \cdots & (1-n_{k-1}) & (1-n_{k-1}) \\ & & & 1 & (1-n_{k+1}) & \cdots & (1-n_{k+1}) & (1-n_{k+1}) \\ & & & & \ddots & \ddots & \vdots & \vdots \\ & \mathbf{0} & & & & 1 & (1-n_{M-1}) & (1-n_{M-1}) \\ & & & & & & 1 & (1-n_M) \end{pmatrix} \tag{4.116}$$

Using again Eqs. (22) and (31) of [18] respectively we obtain

$$\mathcal{C} = \begin{pmatrix} C_J + C_1' & n_1 C_1' & & & & & & \\ n_1 C_1' & n_1^2 C_1' + C_2' & \ddots & & & & & \\ & \ddots & \ddots & & & & & \\ & & & n_{k-1}^2 C_{k-1}' + (C_{k+1}' + C_k') & n_{k+1} C_{k+1}' & & & \\ & & & n_{k+1} C_{k+1}' & n_{k+1}^2 C_{k+1}' + C_{k+2}' & \ddots & & \\ & & & & \ddots & \ddots & & \\ & & \mathbf{0} & & & & n_{M-1}^2 C_{M-1}' + C_M' & n_M C_M' \\ & & & & & & n_M C_M' & n_M^2 C_M' + C_{M+1} \end{pmatrix} \tag{4.117}$$

$$\mathbf{M_0} = \begin{pmatrix} \frac{1}{L_1'} & \frac{1}{L_1'} & & & & & & \\ \frac{1}{L_1'} & \frac{1}{L_1'} + \frac{1}{L_2'} & \frac{1}{L_2'} & & & & & \\ & \frac{1}{L_2'} & \frac{1}{L_2'} + \frac{1}{L_3'} & \ddots & & & & \\ & & \ddots & \ddots & & & & \\ & & & & \frac{1}{L_{k-1}'} + \frac{1}{L_{k+1}'} & \frac{1}{L_{k+1}'} & & \\ & & & & \frac{1}{L_{k+1}'} & \frac{1}{L_{k+1}'} + \frac{1}{L_{k+2}'} & \ddots & \\ & & \mathbf{0} & & & \ddots & \ddots & \\ & & & & & & \frac{1}{L_{M-1}'} + \frac{1}{L_M'} & \frac{1}{L_M'} \\ & & & & & & \frac{1}{L_M'} & \frac{1}{L_M'} \end{pmatrix} \tag{4.118}$$

Note that the matrices above are of size $M \times M$.

In case of degeneracy $\bar{\mathbf{m}}$ vectors are computed again using the Eqs. (26-28) in [18]. We define some auxiliary vectors

$$\bar{\mathbf{m}}_a(j) = \begin{pmatrix} 0 \\ \vdots \\ 0 \\ j^{th}\ row \longrightarrow (-1)^j \frac{n_j C_j}{(1-n_j)} \\ \vdots \\ (-1)^{k-1} \frac{n_{k-1} C_{k-1}}{(1-n_{k-1})} \\ (-1)^k \frac{n_{k+1} C_{k+1}}{(1-n_{k+1})} \\ \vdots \\ (-1)^{M-1} \frac{n_M C_M}{(1-n_M)} \\ 0 \end{pmatrix} \tag{4.119}$$

$$\bar{\mathbf{m}}_b(j) = \begin{pmatrix} 0 \\ \vdots \\ 0 \\ (j+1)^{th}\ row \longrightarrow (-1)^j \frac{C_j}{(1-n_j)} \\ \vdots \\ (-1)^{k-1} \frac{C_{k-1}}{(1-n_{k-1})} \\ (-1)^k \frac{C_{k+1}}{(1-n_{k+1})} \\ \vdots \\ (-1)^{M-1} \frac{C_M}{(1-n_M)} \end{pmatrix} \tag{4.120}$$

$$\bar{\mathbf{m}}_{C_k} = \begin{pmatrix} 0 & \cdots & 0 & C_k & 0 & \cdots & 0 \end{pmatrix}^t \tag{4.121}$$

where C_k is in k^{th} row. Now we can write coupling vector $\bar{\mathbf{m}}_j$ to the bath of the resistor R_j as a function of the vectors defined in Eqs. (4.119), (4.120), (4.121) above as

$$\bar{\mathbf{m}}_j = \bar{\mathbf{m}}_a(j) + \bar{\mathbf{m}}_b(j) + \bar{\mathbf{m}}_{C_k}, \qquad if\ j \leq k \tag{4.122}$$

$$= \bar{\mathbf{m}}_a(j) + \bar{\mathbf{m}}_b(j), \qquad if\ j > k \tag{4.123}$$

Note that vectors above are all of length M. Spectral densities $J_i(\omega)$ are the same as in the non-degenerate case (Eqs. (4.112),(4.115)) for all resistors. Note also that dissipation treatment for the last resistor R_{M+1} is unaffected since C_{M+1} is untouched in Eq. (4.117).

CHAPTER 5

Multiport Brune Quantization

5.1 Introduction

In this chapter our aim is to introduce multiport state-space generalization of the Brune's impedance synthesis method. We will call the circuit obtained by this method the "Multiport Brune Circuit". We will then apply the multiport generalization of the effective Kirchhoff technique introduced in the previous chapter to quantize the multiport Brune circuit. However it is instructive to review first multiport network synthesis theory and discuss the properties of the synthesized multiport circuits.

5.2 A Survey of Multiport Network Synthesis

5.2.1 Lossless Synthesis

The simplest scenario for the multiport synthesis is the case of a lossless $(n \times n)$ impedance matrix $\mathbf{Z}(s)$. Such a case can be seen as the multiport generalization of the Foster's theorem. In that case the para-Hermitian part $\mathbf{Z}_{PH}(s)$ of the impedance matrix vanishes $\mathbf{Z}_{PH}(s) = \frac{1}{2}\left[\mathbf{Z}(s) + \mathbf{Z}^T(-s)\right] = 0$ and one can make a partial fraction expansion of $\mathbf{Z}(s)$ as

$$\mathbf{Z}(s) = \mathbf{B}_\infty + \mathbf{A}_\infty s + \mathbf{A}_0 s^{-1} + \sum_{i=1}^{M} \frac{\mathbf{A}_i s + \mathbf{B}_i}{s^2 + \omega_i^2} \tag{5.1}$$

where each term is LPR(lossless, positive-real), $\mathbf{A}_i$ is a $(n \times n)$ symmetric positive semidefinite matrix $i = 0, 1, \ldots, M, \infty$ and $\mathbf{B}_i$ is $(n \times n)$ skew-symmetric matrix for $i = 1, \ldots, M, \infty$. As shown in [70] each individual term in the expansion in Eq. (5.1) can be synthesized independent of the other terms and $\mathbf{Z}(s)$ is realized by the series connection of circuits corresponding to each term. Matrices $\mathbf{A}_i$ and $\mathbf{B}_i$ are related to the residue matrices $\mathbf{K}_i$ by the following relations

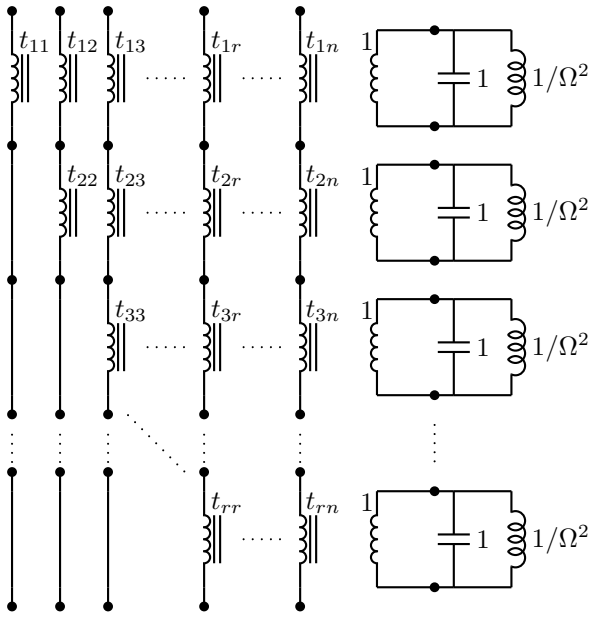

Figure 5.1: The canonical Cauer form [123, 124] for the term $\mathbf{Z}_i(s) = \frac{\mathbf{A}_i s}{s^2+\omega_i^2}$ in the reciprocal case of $\mathbf{B}_i = 0$. On the left is a Belevitch transformer with n open-circuited ports on the left and r ports on the right shunted by parallel LC circuits with resonance frequency $\Omega = \omega_i$, where r being the rank of the matrix $\mathbf{A}_i$.

$$\begin{cases} \mathbf{A}_i = \mathbf{K}_i + \mathbf{K}_i^T & i = 0, 1, \ldots, M, \infty \\ \mathbf{B}_i = j\omega_i \left[\mathbf{K}_i - \mathbf{K}_i^T\right] & i = 1, \ldots, M \end{cases} \tag{5.2}$$

The synthesis of the circuits corresponding to the terms $\mathbf{A}_0$, $\mathbf{A}_\infty$ and $\mathbf{B}_\infty$ are relatively easy and we refer the reader to Chapter (7.2) of [70] for the details. Here we will focus on the terms $\mathbf{Z}_i(s) = \frac{\mathbf{A}_i s + \mathbf{B}_i}{s^2+\omega_i^2}$ at finite frequencies ω_i for $i = 1, \ldots, M$.

In the reciprocal case of $\mathbf{B}_i = 0$ we have the *canonical* Cauer realization [123, 124] shown in Fig. (5.1) for the term $\mathbf{Z}_i(s) = \frac{\mathbf{A}_i s}{s^2+\omega_i^2}$. On the left side in Fig. (5.1) we see a new type of circuit element: the "Belevitch Transformer" [125]. The Belevitch transformer in Fig. (5.1) is a multiport device with n open-circuited ports on the left and r ports shunted by parallel LC circuits of resonant frequency $\Omega = \omega_i$ on the right, with r being the rank of the matrix $\mathbf{A}_i$. The Cauer realization is canonical in the sense that $r = k$ where $k = rank[\mathbf{K}_i]$ and a minimum number of $2k$ reactive elements are used in the circuit of Fig. (5.1) (see [70], p. 215 for a proof).

A generic multiport Belevitch transformer with N ports on the left and M ports

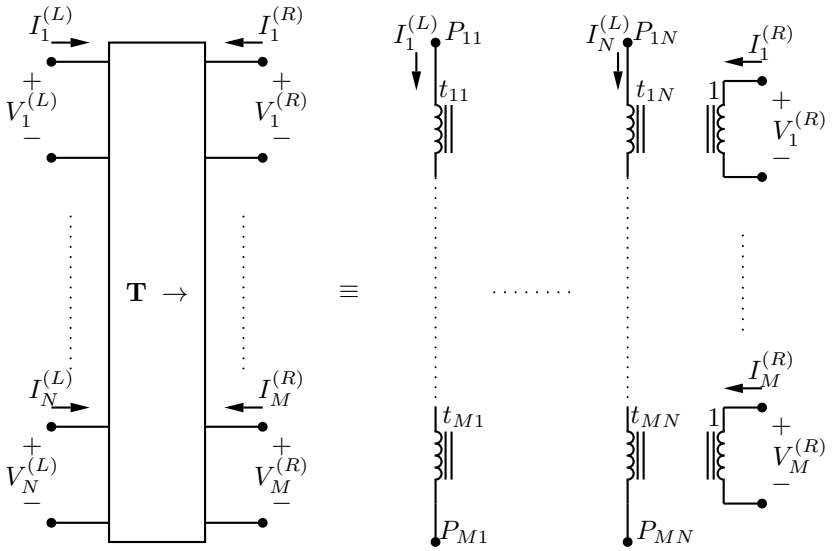

Figure 5.2: The Belevitch Transformer with N ports on the left and M ports on the right. On the right side we see the detailed circuit representation of this device. There is a turns ratio matrix $\mathbf{T} = \begin{pmatrix} t_{11} & \cdots & t_{1N} \\ \vdots & \ddots & \vdots \\ t_{M1} & \cdots & t_{MN} \end{pmatrix}$ associated with the Belevitch transformer which relates currents and voltages on both side of the device as given in Eqs. (5.8) and (5.9). The arrow in the box is used to refer to the asymmetrical character of the Belevitch transformer.

on the right is shown in Fig. (5.2) on the left. The detailed circuit representation of the Belevitch transformer $\mathbf{T}$ is shown on the right of Fig. (5.2) which defines a $M \times N$ matrix for $\mathbf{T}$

$$\mathbf{T} = \begin{pmatrix} t_{11} & \cdots & t_{1N} \\ \vdots & \ddots & \vdots \\ t_{M1} & \cdots & t_{MN} \end{pmatrix} \tag{5.3}$$

Let the current vectors $\mathbf{I}^{(L)}$ and $\mathbf{I}^{(R)}$ be the vectors holding the currents at the ports on the left side and the right side of the Belevitch transformer $\mathbf{T}$, respectively, i.e.

$$\mathbf{I}^{(L)} = \left(I_1^{(L)}, \ldots, I_N^{(L)}\right)^T \tag{5.4}$$

$$\mathbf{I}^{(R)} = \left(I_1^{(R)}, \ldots, I_M^{(R)}\right)^T \tag{5.5}$$

and let the vectors $\mathbf{V}^{(L)}$ and $\mathbf{V}^{(R)}$ be the vectors holding the voltages at the ports on the left side and the right side of the Belevitch transformer $\mathbf{T}$, respectively, i.e.

$$\mathbf{V}^{(L)} = \left(V_1^{(L)}, \ldots, V_N^{(L)}\right)^T \tag{5.6}$$

$$\mathbf{V}^{(R)} = \left(V_1^{(R)}, \ldots, V_M^{(R)}\right)^T \tag{5.7}$$

then we can write the Belevitch transformer relations as

$$\mathbf{I}^{(R)} = -\mathbf{T}\mathbf{I}^{(L)} \tag{5.8}$$

$$\mathbf{V}^{(L)} = \mathbf{T}^T\mathbf{V}^{(R)} \tag{5.9}$$

One should recognize the asymmetrical character of the Belevitch transformer which we noted by putting an arrow in the box representing the Belevitch transformer in Fig. (5.2). However in Chapters (5.3), (5.4) and (5.5) we will use the Belevitch transformer in Fig. (5.2) in a reflected form as shown in Fig. (5.3).

The current and voltage relations for the reflected Belevitch transformer in Fig. (5.3) are given by

$$\mathbf{I}^{(L)} = \mathbf{T}\mathbf{I}^{(R)} \tag{5.10}$$

$$\mathbf{V}^{(R)} = \mathbf{T}^T\mathbf{V}^{(L)} \tag{5.11}$$

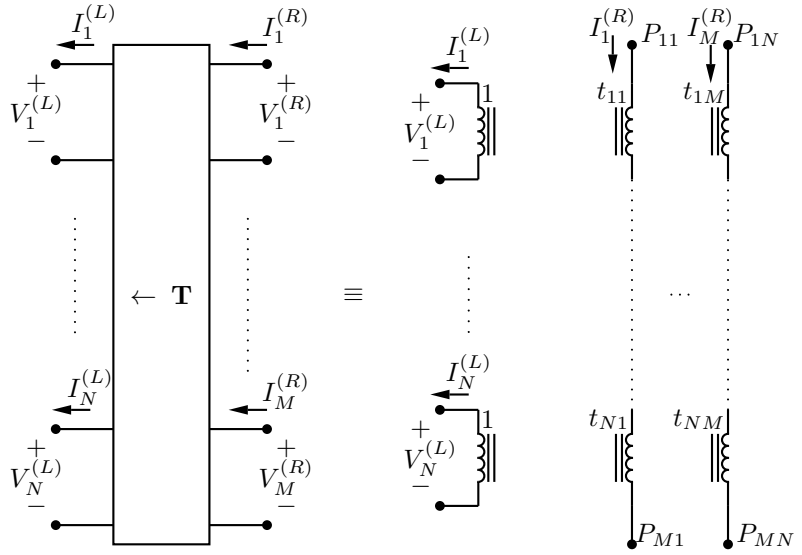

Figure 5.3: The Belevitch transformer in reflected form as used in Chapters (5.3), (5.4) and (5.5). The current and voltage relations for this transformer are given in Eqs. (5.10), (5.11).

It is interesting to note the similarity of the Belevitch transformer relations in Eqs. (5.8) and (5.9) to the Kirchhoff's laws given in terms of the loop matrix $\mathbf{F}$ in Eqs. (4.64) and (4.65) given in Chapter (4.3).

Now going back to the canonical circuit of Cauer in Fig. (5.1) the impedance matrix seen by the Belevitch transformer looking to the right is the impedance matrix of the parallel LC resonators

$$\mathbf{Z}_{LC}(s) = \frac{s}{s^2+\Omega^2}\mathbf{I}_{M\times M} \tag{5.12}$$

where $Z_{LC}(s) = \frac{s}{s^2+\Omega^2}$ is the impedance of a single LC resonator in Fig. (5.1). Noting

$$\mathbf{V}^{(R)} = -\mathbf{Z}_{LC}(s)\,\mathbf{I}^{(R)} \tag{5.13}$$

and using Eqs. (5.8) and (5.9) we get

$$\begin{aligned} \mathbf{V}^{(L)} &= \mathbf{T}^T\mathbf{Z}_{LC}\mathbf{T}\mathbf{I}^{(L)} && (5.14)\\ &= \frac{s}{s^2+\Omega^2}\mathbf{T}^T\mathbf{T}\mathbf{I}^{(L)} && (5.15) \end{aligned}$$

from which we conclude

$$\mathbf{Z}_i(s) = \frac{s}{s^2+\Omega^2}\mathbf{T}^T\mathbf{T} \tag{5.16}$$

and

$$\mathbf{A}_i = \mathbf{T}^T\mathbf{T} \tag{5.17}$$

We observe that $\mathbf{T}$ can be chosen to be the Cholesky decomposition of the symmetric positive semidefinite matrix $\mathbf{A}_i$.

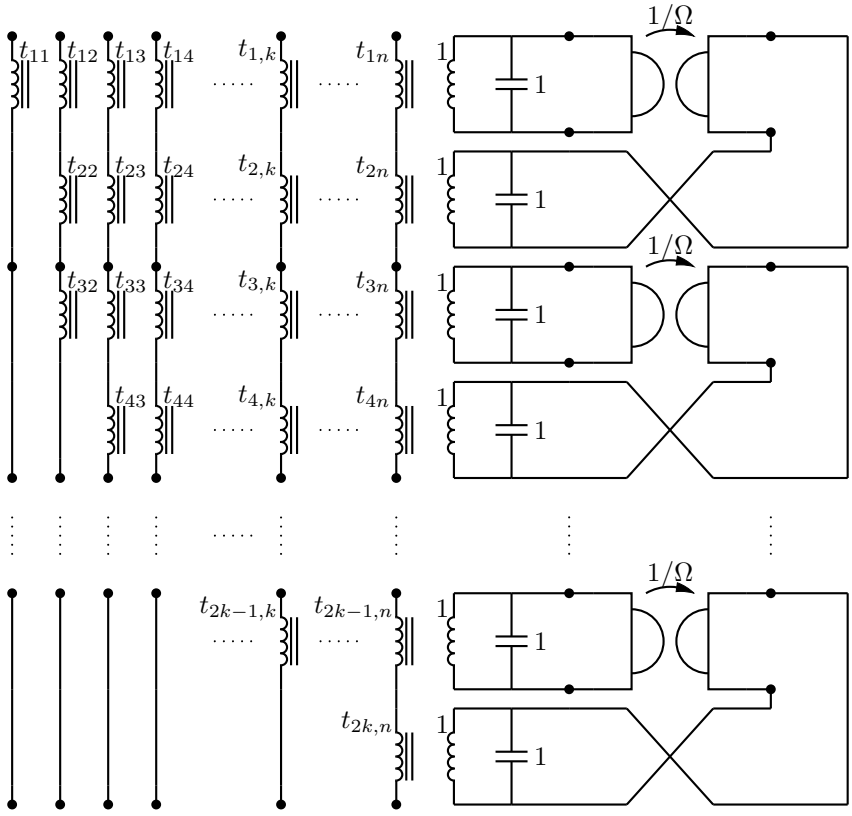

Figure 5.4: The circuit corresponding to the term $\frac{\mathbf{A}_i s+\mathbf{B}_i}{s^2+\omega_i^2}$ (with $\Omega = \omega_i$) in the partial fraction expansion of $\mathbf{Z}(s)$ in Eq. (5.1). On the left we see a $(n \times 2k)$-port Belevitch transformer (for the definition of the Belevitch transformer see Fig. (5.2)), k being the rank of the residue matrix $\mathbf{K}_i$. The n ports on the left are the ports of the $(n \times n)$ impedance matrix $\mathbf{Z}(s)$. The $2k$ ports on the right are shunted by circuits consisting of gyrators shunted by capacitors on both of their ports. See Fig. (5.5) for the choice of current directions and voltage polarities for the gyrator.

In Fig. (5.4) we show the circuit corresponding to the term $\mathbf{Z}_i(s) = \frac{\mathbf{A}_i s + \mathbf{B}_i}{s^2+\omega_i^2}$ for the case when $\mathbf{B}_i \neq 0$. For details about the algorithm to synthesize such a circuit we refer the reader to Chapter 7.2 of [70] where it is also noted that the circuit in Fig. (5.4) reduces to the Cauer realization in Fig. (5.1) when $\mathbf{B}_i = 0$. Here we note that the circuit in Fig. (5.4) is *canonical* in the sense that the number of reactive elements which is the number of capacitors in this case is equal to $2k$ where $k = rank\,[\mathbf{K}_i]$, $\mathbf{K}_i$ being the residue matrix defined in Eq. (5.2) (see [70], p. 215).

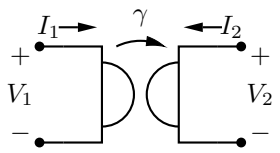

Figure 5.5: Circuit symbol and choice of current directions and voltage polarities for the gyrator.

In Fig. (5.4) appears a new type of circuit element: the gyrator. It was proposed first by Tellegen in [126] as a new kind of circuit element. The gyrator is a two-port circuit element which provides the non-reciprocity required for the most general non-reciprocal multiport impedance response. The two-port circuit symbol for the gyrator is shown in Fig. (5.5) with following voltage-current relations

$$\begin{pmatrix} V_1 \\ V_2 \end{pmatrix} = \begin{pmatrix} 0 & \gamma \\ -\gamma & 0 \end{pmatrix} \begin{pmatrix} I_1 \\ I_2 \end{pmatrix} \tag{5.18}$$

In Fig. (5.6) we show an important circuit equivalence which also explains the absence of inductors in the canonical circuit in Fig. (5.4).

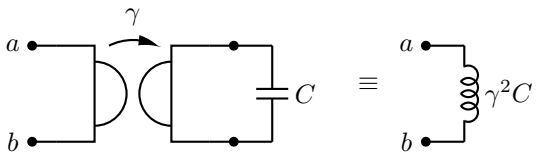

Figure 5.6: Circuit equivalence showing how to obtain an inductor of inductance $L = \gamma^2 C$ by terminating a gyrator with a capacitance C. This equivalence explains the absence of the inductors in the canonical circuit in Fig. (5.4).

For lossless circuits see [127] for a synthesis method in state-space which is minimal in both the number of reactances and the number of gyrators. The minimum number of gyrators that a synthesis can achieve for an impedance $\mathbf{Z}(s)$ (lossy or lossless) is given by *half* of the normal rank of $\left(\mathbf{Z}^T(s) - \mathbf{Z}(s)\right)$ (normal rank is equal to the rank of the matrix with the variable s taken as indeterminate). In Appendix (6.4) we discuss the quantization of circuits involving gyrators for a subclass of circuits where each gyrator is shunted by a capacitor at each of its ports.

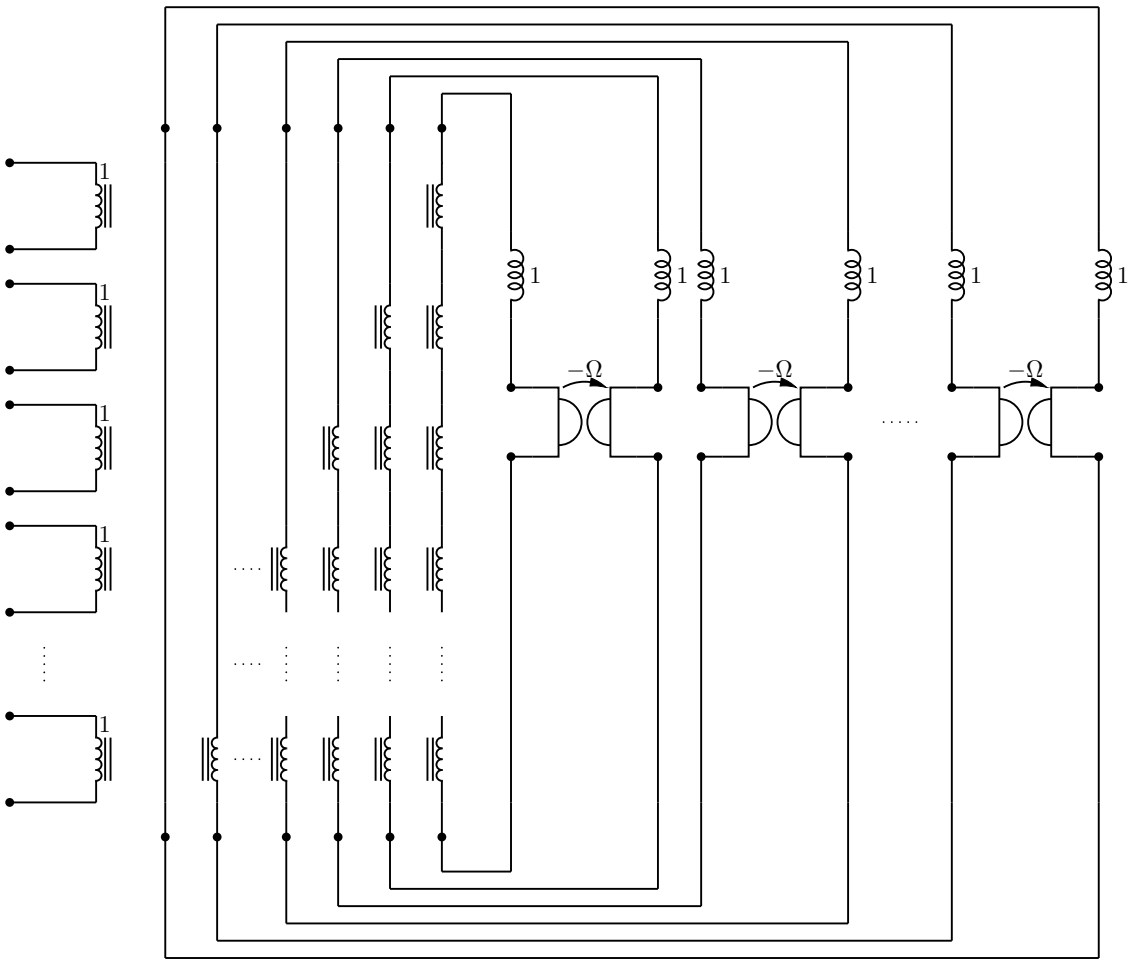

Figure 5.7: The curious circuit for the canonical realization for the term $\mathbf{Y}_i(s) = \frac{\mathbf{C}_i s + \mathbf{D}_i}{s^2+\omega_i^2}$. We call this circuit the *multiport second Foster form* by analogy with the circuit in Fig. (3.2).

The partial fraction expansion for a lossless admittance $\mathbf{Y}(s)$ has the same form as the lossless impedance $\mathbf{Z}(s)$ in Eq. (5.1)

$$\mathbf{Y}(s) = \mathbf{D}_\infty + \mathbf{C}_\infty s + \mathbf{C}_0 s^{-1} + \sum_{i=1}^{M} \frac{\mathbf{C}_i s + \mathbf{D}_i}{s^2 + \omega_i^2} \tag{5.19}$$

For completeness we show the circuit corresponding to the term $\mathbf{Y}_i(s) = \frac{\mathbf{C}_i s + \mathbf{D}_i}{s^2 + \omega_i^2}$ in Fig. (5.7). By analogy with the circuits in Figs. (3.1), (3.2) in Chapter (3.2) we can call the circuit in Fig. (5.4) the *multiport first Foster form* and the circuit in Fig. (5.7) the *multiport second Foster form.*

5.2.2 The Bayard Synthesis

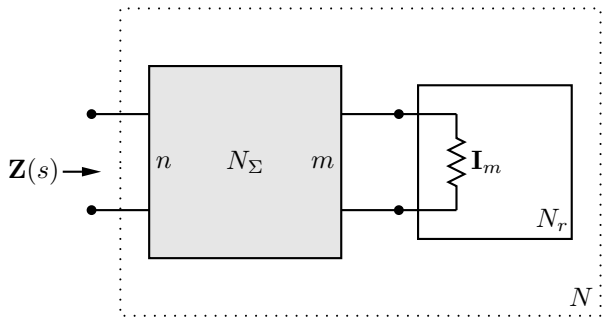

Figure 5.8: Resistance extraction procedure of the Bayard's method. The extracted resistances shunt the purely reactive subnetwork N_Σ.

In this section we discuss beriefly one of the simplest multiport lossy impedance synthesis methods, the Bayard synthesis [128] (see also [129, 130, 131]) as described in [70]. The Bayard synthesis is based on a resistance extraction to isolate a purely reactive subnetwork N_Σ as shown in Fig. (5.8). The Bayard synthesis is originally a classical synthesis method in the sense that it is based on the factorization of rational matrices in Laplace domain as we will see below. However the idea of partitioning of the full network into reactive, resistive and nondynamic subnetworks is extensively used in state-space synthesis methods. We will give an example of such a state-space method in Chapter (5.2.3) below; see [111] for other methods in state-space using similar partitioning approaches.

If we assume the following partitioning for the lossless impedance matrix $\mathbf{Z}_\Sigma(s)$ for the subnetwork N_Σ

$$\mathbf{Z}_\Sigma(s) = \begin{pmatrix} \mathbf{U}(s) & \mathbf{V}(s) \\ -\mathbf{V}^T(-s) & \mathbf{W}(s) \end{pmatrix} \tag{5.20}$$

such that $\mathbf{Z}_{\Sigma}^{T}(-s) = -\mathbf{Z}_{\Sigma}(s)$ where $\mathbf{U}(s)$, $\mathbf{V}(s)$ and $\mathbf{W}(s)$ are $(n \times n)$, $(n \times m)$ and $(m \times m)$ matrices respectively, then by multiport circuit composition rules we can write

$$\mathbf{Z}(s) = \mathbf{U}(s) + \mathbf{V}(s)\left(\mathbf{W}(s) + \mathbf{I}_m\right)^{-1}\mathbf{V}^{T}(-s) \tag{5.21}$$

Bayard's synthesis starts by the factorization of the para-Hermitian part $\mathbf{Z}_{PH}(s)$ of the impedance matrix $\mathbf{Z}(s)$

$$\begin{aligned} \mathbf{Z}_{PH}(s) &= \frac{1}{2}\left[\mathbf{Z}(s) + \mathbf{Z}^{T}(-s)\right] && (5.22)\\ &= \mathbf{N}(s)\left(d(s)\,\mathbf{L}(s)\right)^{-1}\left(d(-s)\,\mathbf{L}(-s)\right)^{-1}\mathbf{N}^{T}(-s) && (5.23) \end{aligned}$$

where $d(s)\,d(-s)$ is the least common denominator of $\mathbf{Z}_{PH}$ with $d(s)$ being a monic Hurwitz polynomial, $\mathbf{N}(s)$ is a $n \times \rho$ real polynomial matrix and $\mathbf{L}(s)$ is a $\rho \times \rho$ diagonal matrix of real Hurwitz polynomials with $\rho = rank\left[\mathbf{Z}_{PH}\right]$.

Then one follows one of the two cases below:

Case 1

$$\begin{aligned} W(s) &= \mathrm{Ev}\left[d(s)\,\mathbf{L}(s)\right] && (5.24)\\ Y(s) &= \mathrm{Od}\left[d(s)\,\mathbf{L}(s)\right] && (5.25) \end{aligned}$$

Case 2

$$\begin{aligned} W(s) &= \mathrm{Od}\left[d(s)\,\mathbf{L}(s)\right] && (5.26)\\ Y(s) &= \mathrm{Ev}\left[d(s)\,\mathbf{L}(s)\right] && (5.27) \end{aligned}$$

and form

$$\begin{aligned} \mathbf{V}(s) &= \mathbf{N}(s)\left(\mathrm{Od}\left[d(s)\,\mathbf{L}(s)\right]\right)^{-1} && (5.28)\\ \mathbf{W}(s) &= \mathrm{Ev}\left[d(s)\,\mathbf{L}(s)\right]\left(\mathrm{Od}\left[d(s)\,\mathbf{L}(s)\right]\right)^{-1} && (5.29) \end{aligned}$$

for *Case 1* or

$$\begin{aligned} \mathbf{V}(s) &= \mathbf{N}(s)\left(\mathrm{Ev}\left[d(s)\,\mathbf{L}(s)\right]\right)^{-1} && (5.30)\\ \mathbf{W}(s) &= \mathrm{Od}\left[d(s)\,\mathbf{L}(s)\right]\left(\mathrm{Ev}\left[d(s)\,\mathbf{L}(s)\right]\right)^{-1} && (5.31) \end{aligned}$$

for *Case 2*. Form also $\mathbf{U}(s)$ for both cases as

$$\mathbf{U}(s) = \mathbf{Z}(s) - \mathbf{V}(s)\left(\mathbf{W}(s) + \mathbf{I}_\rho\right)^{-1}\mathbf{V}^T(-s) \tag{5.32}$$

Now one can synthesize $\mathbf{Z}_\Sigma(s)$ in Eq. (5.20) using the lossless synthesis methods of the previous section and terminate the last ρ ports by unit resistors as shown in Fig. (5.8). The most important property of the Bayard's synthesis is that it achieves the synthesis by using the minimum number of resistors given by the rank of $\mathbf{Z}_{PH}$. However the number of reactive elements used is non-minimal which makes a quantum analysis problematic with this method. One reason for that is numerical difficulty since one then needs to solve a Schrodinger equation in non-minimal dimensions. Another aspect of the method is that if one follows the *Case 2* above one may end up with a circuit containing gyrators even though $\mathbf{Z}(s)$ is symmetric(reciprocal). *Case 1* however will always produce reciprocal circuits for symmetric impedances $\mathbf{Z}(s)$.

5.2.3 State-space Reactance Extraction Synthesis

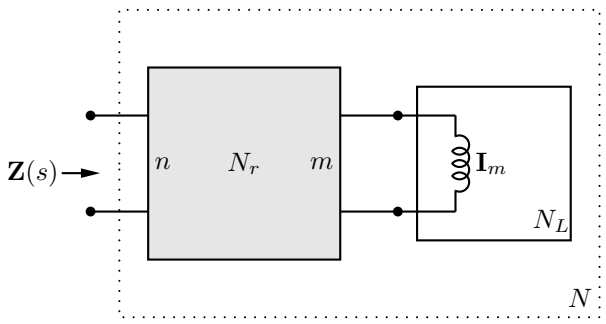

Figure 5.9: State-space reactance extraction. A purely reactive subnetwork N_L consisting of unit inductors is extracted to isolate a nondynamic subnetwork N_r.

In this section we will present a canonical multiport synthesis method in the state-space [111]. The method is based on the extraction of reactances and isolating a nondynamic subnetwork N_r as shown in Fig. (5.9), where the subnetwork N_L is the subnetwork of unit inductances shunting the nondynamic subnetwork N_r. The absence of capacitors in the subnetwork N_L can be understood by observing the equivalence of the circuits shown in Fig. (5.10). Using this equivalence any extracted capacitor in the subnetwork N_L can be converted to an inductor shunting one port of a gyrator as shown in Fig. (5.10) and the gyrator can be absorbed in the nondynamic subnetwork N_r. In addition to gyrators N_r might contain resistors, and ideal transformers.

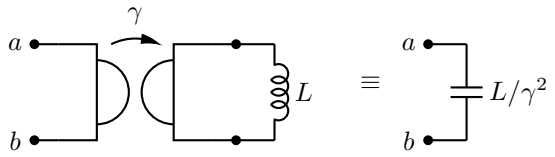

Figure 5.10: Equivalence of an inductor shunting a gyrator to a capacitor. The ratio of the inductance to the capacitance is γ^2 where γ is the gyration ratio. This circuit equivalence explains the lack of capacitors in the reactive subnetwork N_L in Fig. (5.9).

If we partition the constant impedance matrix $\mathbf{Z}_{N_r}$ of the subnetwork N_r according to its n ports on the left and m ports on the right as

$$\mathbf{Z}_{N_r} = \begin{pmatrix} \mathbf{Z}_{11}^{(N_r)} & \mathbf{Z}_{12}^{(N_r)} \\ \mathbf{Z}_{21}^{(N_r)} & \mathbf{Z}_{22}^{(N_r)} \end{pmatrix} \tag{5.33}$$

then by multiport impedance cascading formulas we can write the impedance $\mathbf{Z}(s)$ of the full network N in Fig. (5.9) as

$$\mathbf{Z}(s) = \mathbf{Z}_{11}^{(N_r)} - \mathbf{Z}_{12}^{(N_r)} \left(s\mathbf{I}_m + \mathbf{Z}_{22}^{(N_r)} \right)^{-1} \mathbf{Z}_{21}^{(N_r)} \tag{5.34}$$

But we know from Eq. (4.3) that given a state-space realization $\{\mathbf{A}, \mathbf{B}, \mathbf{C}, \mathbf{D}\}$ for the impedance $\mathbf{Z}(s)$ we have

$$\mathbf{Z}(s) = \mathbf{D} + \mathbf{C}(s\mathbf{I} - \mathbf{A})^{-1}\mathbf{B} \tag{5.35}$$

Comparing Eqs. (5.34) and (5.35) above we identify

$$\mathbf{Z}_{11}^{(N_r)} = \mathbf{D} \tag{5.36}$$
$$\mathbf{Z}_{12}^{(N_r)} = -\mathbf{C} \tag{5.37}$$
$$\mathbf{Z}_{21}^{(N_r)} = \mathbf{B} \tag{5.38}$$
$$\mathbf{Z}_{22}^{(N_r)} = -\mathbf{A} \tag{5.39}$$

that is

$$\mathbf{Z}_{N_r} = \begin{pmatrix} \mathbf{D} & -\mathbf{C} \\ \mathbf{B} & -\mathbf{A} \end{pmatrix} \tag{5.40}$$

As we see in Eq. (5.40) there is natural connection between the submatrices of the impedance matrix $\mathbf{Z}_{N_r}$ for the nondynamic subnetwork N_r and the state-space

description $\{\mathbf{A}, \mathbf{B}, \mathbf{C}, \mathbf{D}\}$ for $\mathbf{Z}(s)$. However before claiming that we achieved a synthesis for N_r (and hence for $\mathbf{Z}$) we need to check that $\mathbf{Z}_{N_r}$ is positive-real. Since N_r is nondynamic $\mathbf{Z}_{N_r}$ is a constant matrix in which case the positive-real condition we need to satisfy simplifies to

$$\mathbf{Z}_{N_r} + \mathbf{Z}_{N_r}^T \geq 0 \tag{5.41}$$

$\mathbf{Z}_{N_r}$ defined in Eq. (5.40) doesn't necessarily satisfy Eq. (5.41). However as we show below one can find another equivalent representation $\{\mathbf{A}_a, \mathbf{B}_a, \mathbf{C}_a, \mathbf{D}_a\}$ for $\mathbf{Z}(s)$ such that

$$\mathbf{Z}(s) = \mathbf{D}_a + \mathbf{C}_a (s\mathbf{I} - \mathbf{A}_a)^{-1} \mathbf{B}_a \tag{5.42}$$

and if we re-define $\mathbf{Z}_{N_r}$ in Eq. (5.40) as

$$\mathbf{Z}_{N_r} = \begin{pmatrix} \mathbf{D}_a & -\mathbf{C}_a \\ \mathbf{B}_a & -\mathbf{A}_a \end{pmatrix} \tag{5.43}$$

then $\mathbf{Z}_{N_r}$ satisfy the positive-real condition in Eq. (5.41).

To show this we need Theorem 9.1.1 in [111] which states that given a minimal realization $\{\mathbf{A}, \mathbf{B}, \mathbf{C}, \mathbf{D}\}$ for a positive-real $\mathbf{Z}(s)$ it possible to find a transformation $\mathbf{T}$ such that $\{\mathbf{A}_a, \mathbf{B}_a, \mathbf{C}_a, \mathbf{D}_a\}$ is a minimal realization for $\mathbf{Z}(s)$ with

$$\begin{aligned} \mathbf{A}_a &= \mathbf{T}\mathbf{A}\mathbf{T}^{-1} && (5.44)\\ \mathbf{B}_a &= \mathbf{T}\mathbf{B} && (5.45)\\ \mathbf{C}_a &= \mathbf{C}\mathbf{T}^{-1} && (5.46)\\ \mathbf{D}_a &= \mathbf{D} && (5.47) \end{aligned}$$

and there exists matrices $\mathbf{L}$ and $\mathbf{W}_0$ such that

$$\begin{aligned} \mathbf{A}_a + \mathbf{A}_a^T &= -\mathbf{L}\mathbf{L}^T && (5.48)\\ \mathbf{B}_a &= \mathbf{C}_a^T - \mathbf{L}\mathbf{W}_0 && (5.49)\\ \mathbf{D}_a + \mathbf{D}_a^T &= \mathbf{W}_0^T\mathbf{W}_0 && (5.50) \end{aligned}$$

The matrix $\mathbf{T}$ is a non-singular matrix satisfying $\mathbf{T}^T\mathbf{T} = \mathbf{P}$ where $\mathbf{P}$ is the symmetric positive definite solution of the positive real lemma Eqs. (4.23)-(4.25) for the realization $\{\mathbf{A}, \mathbf{B}, \mathbf{C}, \mathbf{D}\}$. We already know from Chapter (4.2) that such a non-singular transformation keeps the impedance unchanged.

Hence we can write using Eq. (5.43)

$$\mathbf{Z}_{N_r} + \mathbf{Z}_{N_r}^T = \begin{pmatrix} \mathbf{D}_a + \mathbf{D}_a^T & \left(\mathbf{B}_a - \mathbf{C}_a^T\right)^T \\ \left(\mathbf{B}_a - \mathbf{C}_a^T\right) & -\left(\mathbf{A}_a + \mathbf{A}_a^T\right) \end{pmatrix} \tag{5.51}$$

$$= \begin{pmatrix} \mathbf{W}_0^T\mathbf{W}_0 & -\mathbf{W}_0^T\mathbf{L}^T \\ -\mathbf{L}\mathbf{W}_0 & \mathbf{L}\mathbf{L}^T \end{pmatrix} \tag{5.52}$$

$$= \begin{pmatrix} \mathbf{W}_0^T \\ -\mathbf{L} \end{pmatrix} \begin{pmatrix} \mathbf{W}_0 & \mathbf{L}^T \end{pmatrix} \tag{5.53}$$

$$\geq 0 \tag{5.54}$$

where in Eq. (5.52) in the second line above we used Eqs. (5.48)-(5.50). Therefore $\mathbf{Z}_{N_r}$ defined in Eq. (5.43) satisfies Eq. (5.41). We refer the reader to p. 373 of [111] for the details of the synthesis of the impedance $\mathbf{Z}_{N_r}$.

We note that the reactance extraction method described here is minimal in the number of reactive elements. One can also achieve the minimum number of resistors which is given by $rank\left[\mathbf{Z}(s) + \mathbf{Z}^T(-s)\right]$ simultaneously. We refer the reader to [111] for details. We should also mention that in the case of a symmetric $\mathbf{Z}(s)$ the reactance extraction method above will possibly produce a synthesis with gyrators in the subnetwork N_r. However there exists a reciprocal state-space reactance extraction synthesis method that generates a gyrators-less circuit for a symmetric $\mathbf{Z}(s)$; for details see [111], Chapter 10.3.

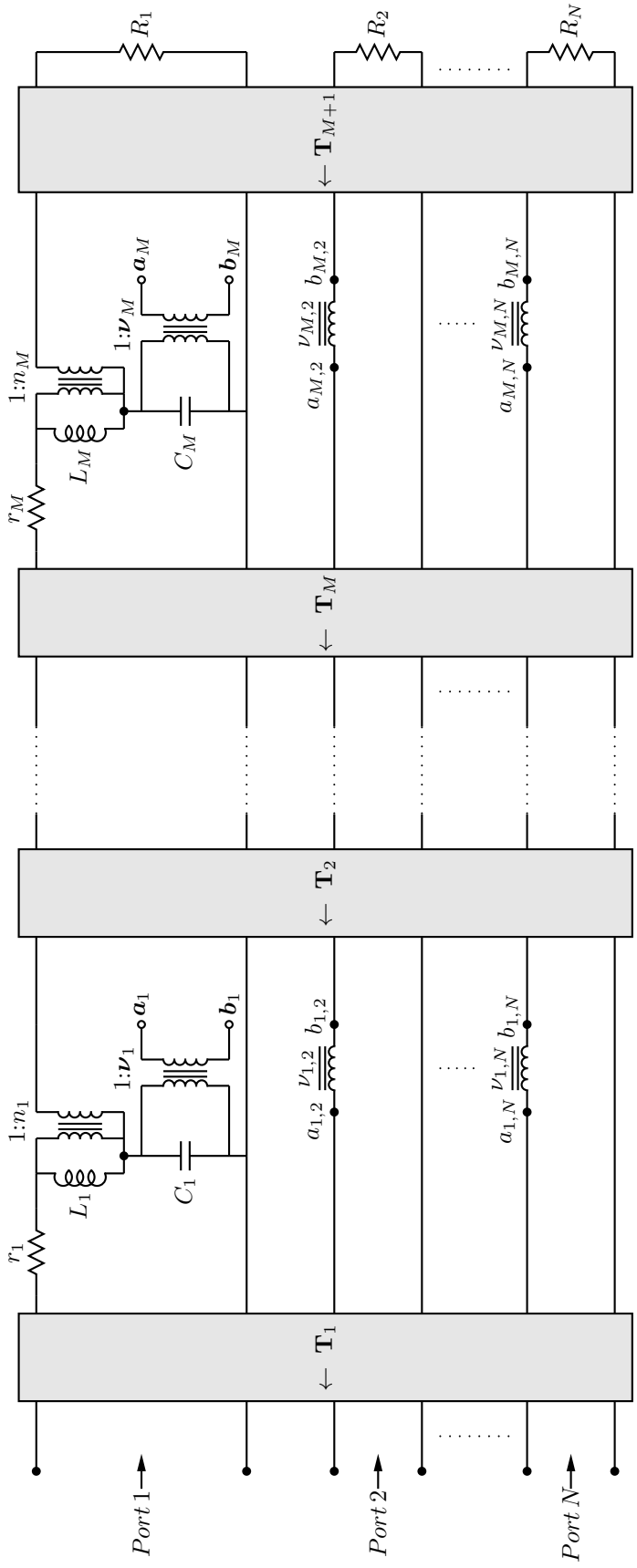

Figure 5.11: The multiport Brune Circuit

5.3 Multiport Brune's method

The multiport Brune circuit is shown in Fig. (5.11). This circuit is obtained by applying the multiport Brune's method [122] in state-space which we describe below. There is also a classical generalization of the one-port Brune's method to multiport responses (including non-reciprocal ones) which is described in Chapter 8.3 of [70] (for more details on the multiport circuit structures obtained see [132, 133]). Generalization of Brune's method to multiport responses was first given by Oono [134] (see also Chapter 8.4 of [70]) in the reciprocal case. Other approaches which generalize Brune's method and which differ in the way they extract resistors in the reciprocal case are [135, 136, 137, 138] and in the non-reciprocal case [139].

The circuit in Fig. (5.11) consists of N ports and M stages. On the far left we have N terminal pairs corresponding to the ports. Each stage starts with the extraction of a Belevitch transformer $\mathbf{T}_k$. Each $\mathbf{T}_k$ is a $2N$-port transformer with N ports on the left and N ports on the right. The circuit representation of the Belevitch transformer is shown in Fig. (5.3). The multiport Belevitch tranformer $\mathbf{T}_k$ is followed by a resistor r_k extracted only at the first port. We will describe below how to extract Belevitch transformers and resistors. After the resistor extraction we have the reactive part of the multiport Brune stage. We observe that the part of each Brune stage that comes after the Belevitch transformer at the first port is almost identical to the one-port Brune stage. We see however an additional transformer $\boldsymbol{\nu}_k$ coupling the reactive circuit in the first port to the remaining ports. $\boldsymbol{\nu}_k$ is a multiport transformer with the primary winding connected in parallel across the terminals of the capacitor C_k at stage k. Each of the secondary windings are connected in series between terminals of the Belevitch transformers at the remaining ports. The last stage consists of the Belevitch transformer $\mathbf{T}_{M+1}$ shunted by the resistors $R_1, \ldots, R_N$.

5.4 Multiport Brune Algorithm

In this section we will describe multiport generalization of the Brune's synthesis algorithm described in state-space in Chapter (4.2.3) for one-port networks. Fig. (5.12) illustrates extraction of a multiport Brune stage. Since the algorithm is recursive we will describe it only on the first stage. At each stage the degree of the network is reduced by two hence the algorithm terminates once a constant multiport impedance is reached as in the one-port case.

We will only focus on the reciprocal response case, that is when $\mathbf{Z} = \mathbf{Z}^T$. We will show later how the gyrators appear in the multiport Brune circuit in case of a non-reciprocal impedance.

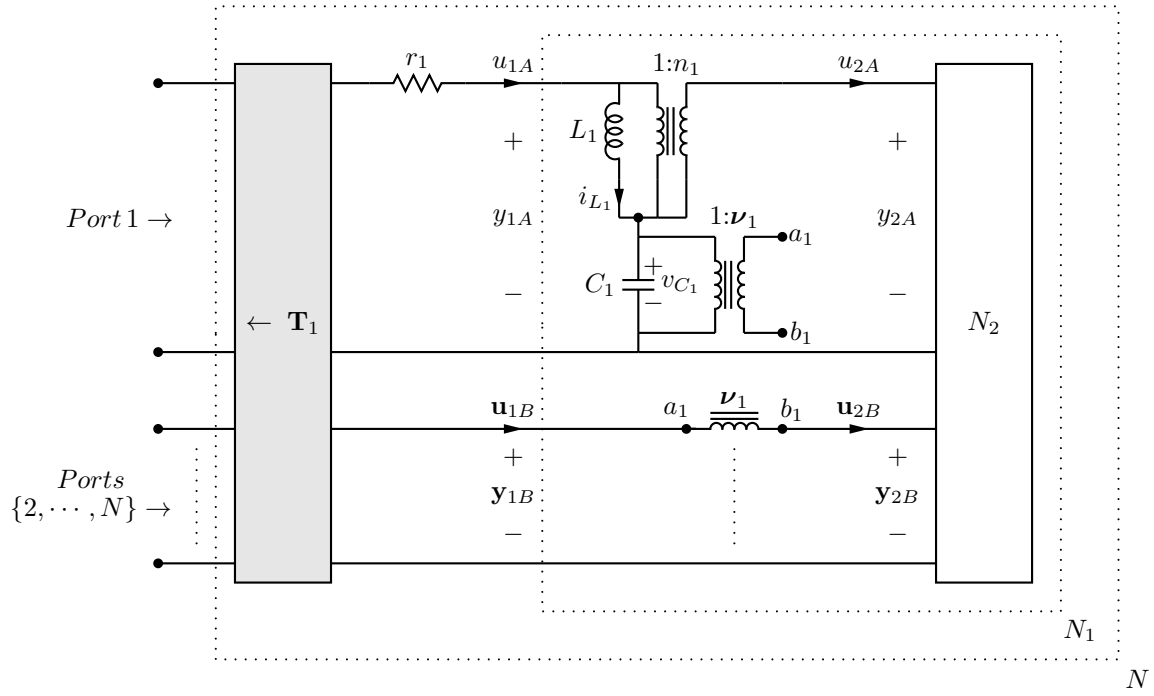

Figure 5.12: Multiport Brune circuit extraction step. The extraction starts with the Belevitch transformer $\mathbf{T}_1$. The circuit that follows $\mathbf{T}_1$ is almost identical to the one-port Brune stage in Fig. (4.1) except the multiport transformer $\boldsymbol{\nu}_1$ coupling the first port to the remaining ones.

The synthesis of a multiport Brune stage starts with the extraction of the multiport Belevitch transformer $\mathbf{T}_1$ together with the resistor r_1 at the first port. Let the impedance matrices seen at the ports of the networks labeled N and N_1 in Fig. (5.12) be $\mathbf{Z}$ and $\mathbf{Z}_1$ respectively. Assuming that $\mathbf{Z}$ is positive-real the aim of the resistance and Belevitch transformer extraction is to get $\mathbf{Z}_1$ PR together with $Re\left[\mathbf{Z}_{1,11}\left(j\omega_1\right)\right] = 0$ for some frequency ω_1 where $\mathbf{Z}_{1,11}$ is the $(1,1)$ entry of the impedance $\mathbf{Z}_1$. As we will see below those are necessary and sufficient conditions for the multiport Brune algorithm.

5.4.1 Resistance Extraction

The most direct way to get $Re\left[\mathbf{Z}_{1,11}\left(j\omega_1\right)\right] = 0$ is to first make an eigenvalue decomposition for the Hermitian part $\mathbf{Z}_H$ of $\mathbf{Z}$ at each frequency ω

$$\mathbf{Z}_H\left(j\omega\right) = U\left(\omega\right) S\left(\omega\right) U^T\left(\omega\right) \tag{5.55}$$

where

$$\mathbf{Z}_H\left(j\omega\right) = \frac{1}{2}\left(\mathbf{Z}\left(j\omega\right) + \mathbf{Z}^T\left(-j\omega\right)\right) \tag{5.56}$$

$S\left(\omega\right)$ can be assumed to be the diagonal matrix having the eigenvalues $\alpha_j\left(\omega\right)$'s for $1 \leq j \leq N$ on its diagonal in increasing order ($\alpha_j\left(\omega\right) \geq 0$ since $\mathbf{Z}_H\left(j\omega\right)$ is positive semi-definite):

$$S\left(\omega\right) = \begin{pmatrix} \alpha_1\left(\omega\right) & & \mathbf{0} \\ & \ddots & \\ \mathbf{0} & & \alpha_N\left(\omega\right) \end{pmatrix} \tag{5.57}$$

and $U\left(\omega\right)$ can be chosen to be orthogonal.

If we then choose the following value for the extracted resistor r_1

$$r_1 = \min_{0 \leq \omega \leq \infty} \alpha_1\left(\omega\right) \tag{5.58}$$

with ω_1 being the frequency at which the minimum in Eq. (5.58) occurs

$$\alpha_1\left(\omega_1\right) = r_1 \tag{5.59}$$

We have $Re\left[\mathbf{Z}_{1,11}\left(j\omega_1\right)\right] = 0$ with

$$\mathbf{Z}_1 = U^T\left(\omega_1\right)\mathbf{Z}U\left(\omega_1\right) - r_1 \begin{pmatrix} 1 & & \mathbf{0} \\ & 0 & \\ & & \ddots \\ \mathbf{0} & & 0 \end{pmatrix} \tag{5.60}$$

One then needs to choose the turns-ratio matrix $\mathbf{T}_1$ as

$$\mathbf{T}_1 = U(\omega_1) \tag{5.61}$$

One can also imagine extracting first the resistor and then the Belevitch transformer. The value of the resistor r_1 in Fig. (5.12) in that case can be computed using the following formula [140]

$$r_1 = \min_{0 \leq \omega \leq \infty} \boldsymbol{\Delta}(\omega) / \boldsymbol{\Delta}_{11}(\omega) \tag{5.62}$$

where $\boldsymbol{\Delta}(\omega)$ is the determinant and $\boldsymbol{\Delta}_{11}(\omega)$ is the $(1,1)$ minor of $\mathbf{Z}_H(j\omega)$.

Let ω_0 be the frequency at which the minimum in Eq. (5.62) occurs such that

$$r_1 = \boldsymbol{\Delta}(\omega_0) / \boldsymbol{\Delta}_{11}(\omega_0) \tag{5.63}$$

Then the Belevitch transformer matrix $\mathbf{T}_1$ in Fig. (5.12) is given by the matrix that simultaneously diagonalizes [141] $\mathbf{Z}_H(j\omega_0)$ and $\begin{pmatrix} 1 & & \mathbf{0} \\ & 0 & \\ & \ddots & \\ \mathbf{0} & & 0 \end{pmatrix}$ such that

$$\mathbf{Z}_H(j\omega_0) = \mathbf{T}_1 \mathbf{D} \mathbf{T}_1^T \tag{5.64}$$

where $\mathbf{D}$ is a diagonal matrix with $\mathbf{D}(1,1) = r_1$. $\mathbf{T}_1$ in that case can be found using the Gauss diagonalization procedure.

The formula given in Eq. (5.62) is nice in the sense that it doesn't require an eigenvalue decomposition for each frequency ω, $0 \leq \omega \leq \infty$. However the Belevitch transformer matrix $\mathbf{T}_1$ obtained by the above method is in general non-orthogonal.

5.4.2 Extraction of the reactive part of the multiport Brune stage

Let the subnetwork N_2 in Fig. (5.12) be described by the following state space equations

$$\dot{\mathbf{x}}_2 = \mathbf{A}_2 \mathbf{x}_2 + \mathbf{B}_2 \mathbf{u}_2 \tag{5.65}$$

$$\mathbf{y}_2 = \mathbf{C}_2 \mathbf{x}_2 + \mathbf{D}_2 \mathbf{u}_2 \tag{5.66}$$

where

$$\mathbf{B}_2 = \begin{pmatrix} \mathbf{B}_{2A} & \mathbf{B}_{2B} \end{pmatrix} \tag{5.67}$$

$$\mathbf{C}_2 = \begin{pmatrix} \mathbf{C}_{2A} \\ \mathbf{C}_{2B} \end{pmatrix} \tag{5.68}$$

$$\mathbf{D}_2 = \begin{pmatrix} D_{2AA} & \mathbf{D}_{2AB} \\ \mathbf{D}_{2BA} & \mathbf{D}_{2BB} \end{pmatrix} \tag{5.69}$$

and

$$\mathbf{u}_2 = \begin{pmatrix} u_{2A} \\ \mathbf{u}_{2B} \end{pmatrix} \tag{5.70}$$

$$\mathbf{y}_2 = \begin{pmatrix} y_{2A} \\ \mathbf{y}_{2B} \end{pmatrix} \tag{5.71}$$

where u_{2A} is the current into the first port of the subnetwork N_2 in Fig. (5.12) and $\mathbf{u}_{2B}$ is the vector holding the currents at the remaining ports (ports $2-N$) of the subnetwork N_2. Similarly y_{2A} is the voltage across the first port of the subnetwork N_2 and $\mathbf{y}_{2B}$ is the vector holding the voltages across the remaining ports (ports $2-N$) of the subnetwork N_2. $\{\mathbf{A}_2, \mathbf{B}_2, \mathbf{C}_2, \mathbf{D}_2\}$ is a state-space realization for the impedance $\mathbf{Z}_2(s)$ seen at the ports of the network N_2.

Then the network N_1 is described by the the following equations

$$\begin{pmatrix} \dot{\mathbf{x}}_2 \\ \dot{x}_{C_1} \\ \dot{x}_{L_1} \end{pmatrix} = \begin{pmatrix} \mathbf{A}_2 & 0 & -\frac{\mathbf{B}_{2A}}{n_1\sqrt{L_1}} \\ 0 & 0 & \frac{1}{n_1\sqrt{L_1 C_1}} \\ \frac{\mathbf{C}_{2A}}{n_1\sqrt{L_1}} & -\frac{1}{n_1\sqrt{L_1 C_1}} & -\frac{D_{2AA}}{n_1^2 L_1} \end{pmatrix} \begin{pmatrix} \mathbf{x}_2 \\ x_{C_1} \\ x_{L_1} \end{pmatrix} + \begin{pmatrix} \mathbf{B}_{2A}/n_1 & \mathbf{B}_{2B} \\ \frac{1-1/n_1}{\sqrt{C_1}} & \frac{\boldsymbol{\nu}_1^T}{\sqrt{C_1}} \\ \frac{D_{2AA}}{n_1^2\sqrt{L_1}} & \frac{\mathbf{D}_{2AB}}{n_1\sqrt{L_1}} \end{pmatrix} \begin{pmatrix} u_{1A} \\ \mathbf{u}_{1B} \end{pmatrix} \tag{5.72}$$

$$\begin{pmatrix} y_{1A} \\ \mathbf{y}_{1B} \end{pmatrix} = \begin{pmatrix} \frac{\mathbf{C}_{2A}}{n_1} & \frac{1-1/n_1}{\sqrt{C_1}} & -\frac{D_{2AA}}{n_1^2\sqrt{L_1}} \\ \mathbf{C}_{2B} & \frac{\boldsymbol{\nu}_1}{\sqrt{C_1}} & -\frac{\mathbf{D}_{2BA}}{n_1\sqrt{L_1}} \end{pmatrix} \begin{pmatrix} \mathbf{x}_2 \\ x_{C_1} \\ x_{L_1} \end{pmatrix} + \begin{pmatrix} D_{2AA}/n_1^2 & \mathbf{D}_{2AB}/n_1 \\ \mathbf{D}_{2BA}/n_1 & \mathbf{D}_{2BB} \end{pmatrix} \begin{pmatrix} u_{1A} \\ \mathbf{u}_{1B} \end{pmatrix} \tag{5.73}$$

from which we identify

$$\mathbf{A}_1 = \begin{pmatrix} \mathbf{A}_2 & 0 & -\frac{\mathbf{B}_{2A}}{n_1\sqrt{L_1}} \\ 0 & 0 & \frac{1}{n_1\sqrt{L_1 C_1}} \\ \frac{\mathbf{C}_{2A}}{n_1\sqrt{L_1}} & -\frac{1}{n_1\sqrt{L_1 C_1}} & -\frac{D_{2AA}}{n_1^2 L_1} \end{pmatrix} \tag{5.74}$$

$$\mathbf{B}_1 = \begin{pmatrix} \mathbf{B}_{2A}/n_1 & \mathbf{B}_{2B} \\ \frac{1-1/n_1}{\sqrt{C_1}} & \frac{\boldsymbol{\nu}_1^T}{\sqrt{C_1}} \\ \frac{D_{2AA}}{n_1^2\sqrt{L_1}} & \frac{\mathbf{D}_{2AB}}{n_1\sqrt{L_1}} \end{pmatrix} \tag{5.75}$$

$$\mathbf{C}_1 = \begin{pmatrix} \frac{\mathbf{C}_{2A}}{n_1} & \frac{1-1/n_1}{\sqrt{C_1}} & -\frac{D_{2AA}}{n_1^2\sqrt{L_1}} \\ \mathbf{C}_{2B} & \frac{\boldsymbol{\nu}_1}{\sqrt{C_1}} & -\frac{\mathbf{D}_{2BA}}{n_1\sqrt{L_1}} \end{pmatrix} \tag{5.76}$$

$$\mathbf{D}_1 = \begin{pmatrix} D_{2AA}/n_1^2 & \mathbf{D}_{2AB}/n_1 \\ \mathbf{D}_{2BA}/n_1 & \mathbf{D}_{2BB} \end{pmatrix} \tag{5.77}$$

and

$$\mathbf{x}_1 = \begin{pmatrix} \mathbf{x}_2 \\ x_{C_1} \\ x_{L_1} \end{pmatrix} \tag{5.78}$$

where $x_{C_1} = \sqrt{C_1} v_{C_1}$, $x_{L_1} = \sqrt{L_1} i_{L_1}$ and $\boldsymbol{\nu}_1 = (\nu_{12}, \ldots, \nu_{1N})^T$; u_{1A} is the current into the first port of the subnetwork N_1 in Fig. (5.12) and $\mathbf{u}_{1B}$ is the vector holding the currents at the remaining ports (ports $2-N$) of the subnetwork N_1. Similarly y_{1A} is the voltage across the first port of the subnetwork N_1 and $\mathbf{y}_{1B}$ is the vector holding the voltages across the remaining ports (ports $2-N$) of the subnetwork N_1. $\{\mathbf{A}_1, \mathbf{B}_1, \mathbf{C}_1, \mathbf{D}_1\}$ is then a realization for the impedance $\mathbf{Z}_1(s)$ seen at the ports of the network N_1.

Now we will state the multiport version of the fundamental lemma stated in Section (4.2.3) to show how to transform state-space equations given for a minimal realization of the impedance $\mathbf{Z}_1$ into the form in Eqs. (5.72) and (5.73). For details refer to [122].

The Multiport Synthesis Lemma

Let $\{\mathbf{A}_a, \mathbf{B}_a, \mathbf{C}_a, \mathbf{D}_a\}$ be a minimal realization corresponding to the positive-real impedance $\mathbf{Z}_1(s)$ satisfying $\mathbf{Z}_{1,11}(j\omega_0) + \mathbf{Z}_{1,11}(-j\omega_0) = 0$ for some frequency ω_0, $\mathbf{Z}_{1,11}$ is the $(1,1)$ entry of the impedance matrix $\mathbf{Z}_1$ (We also assume that $j\omega_0$ is not an eigenvalue of $\mathbf{A}_a$). Then there exists a coordinate transformation matrix $\mathbf{T}$ such that $\mathbf{A}_1 = \mathbf{T}\mathbf{A}_a\mathbf{T}^{-1}$, $\mathbf{B}_1 = \mathbf{T}\mathbf{B}_a$, $\mathbf{C}_1 = \mathbf{C}_a\mathbf{T}^{-1}$ and $\mathbf{D}_1 = \mathbf{D}_a$ are of the form given in Eqs. (5.74-5.77).

To compute $\mathbf{T}$ we will follow the algorithm described in *Fundamental Lemma* in Section (4.2.3). Before applying the algorithm we set

$$\mathbf{b}_a = \mathbf{B}_a\mathbf{e}_1 \tag{5.79}$$

$$\mathbf{c}_a^T = \mathbf{C}_a^T\mathbf{e}_1 \tag{5.80}$$

and apply the one-port algorithm described in the *Fundamental Lemma* in Chapter (4.2.3) to the set $\{\mathbf{A}_a, \mathbf{b}_a, \mathbf{c}_a, \mathbf{D}_a\}$ where $\mathbf{e}_1 = \begin{pmatrix} 1 & 0 & \ldots & 0 \end{pmatrix}^T$; that is we apply the one-port algorithm by picking up the first columns of $\mathbf{B}_a$ and $\mathbf{C}_a^T$ matrices.

To see why $\{\mathbf{A}_1, \mathbf{B}_1, \mathbf{C}_1, \mathbf{D}_1\}$ is an equivalent realization for the impedance $\mathbf{Z}_1(s)$ see Chapter (4.2) or Theorem (3.3.9) in [111].

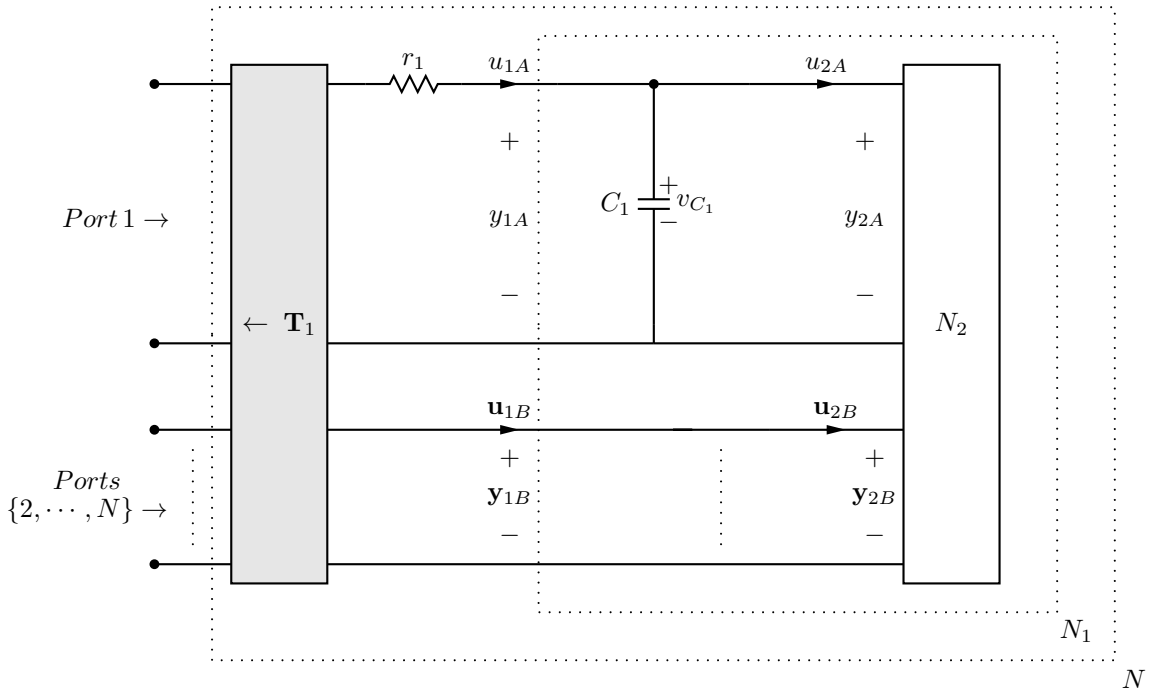

Figure 5.13: Extraction of the multiport capacitive denegenerate stage in the multiport Brune circuit when $\omega_1 = \infty$ in Eq. (5.59). We observe that the $\boldsymbol{\nu}$-type transformer is not necessary in that case.

5.4.2.1 The Multiport Capacitive Degenerate Stage

Similar to our discussion in Chapter (4.2.3.1) it is possible that the minimum in Eq. (5.59) occurs at infinity, $\omega_1 = \infty$. Such a case needs the extraction of the degenerate reactive stage shown in Fig. (5.13). As in the one-port case the reactive Brune stage doesn't involve any inductive part. Note also that we don't have the $\boldsymbol{\nu}$-type transformer coupling the first port to the remaining ports.

To synthesize such a stage we need to modify our treatment in Chapter (5.4.2). Assuming that the subnetwork N_2 in Fig. (5.13) is described by Eqs. (5.65)-(5.71), the network N_1 is described by

$$\begin{pmatrix} \dot{\mathbf{x}}_2 \\ \dot{x}_{C_1} \end{pmatrix} = \begin{pmatrix} \mathbf{A}_2 - \frac{\mathbf{B}_{2A}\mathbf{C}_{2A}}{D_{2AA}} & \frac{\mathbf{B}_{2A}}{D_{2AA}\sqrt{C_1}} \\ \frac{\mathbf{C}_{2A}}{D_{2AA}\sqrt{C_1}} & -\frac{1}{D_{2AA}C_1} \end{pmatrix} \begin{pmatrix} \mathbf{x}_2 \\ x_{C_1} \end{pmatrix} + \begin{pmatrix} 0 & \mathbf{B}_{2B} - \frac{\mathbf{B}_{2A}\mathbf{D}_{2AB}}{D_{2AA}} \\ \frac{1}{\sqrt{C_1}} & \frac{\mathbf{D}_{1AB}}{D_{2AA}\sqrt{C_1}} \end{pmatrix} \begin{pmatrix} u_{1A} \\ \mathbf{u}_{1B} \end{pmatrix} \tag{5.81}$$

$$\begin{pmatrix} y_{1A} \\ \mathbf{y}_{1B} \end{pmatrix} = \begin{pmatrix} 0 & \frac{1}{\sqrt{C_1}} \\ \mathbf{C}_{2B} - \frac{\mathbf{D}_{2BA}\mathbf{C}_{2A}}{D_{2AA}} & \frac{\mathbf{D}_{2BA}}{D_{2AA}\sqrt{C_1}} \end{pmatrix} \begin{pmatrix} \mathbf{x}_2 \\ x_{C_1} \end{pmatrix} + \begin{pmatrix} 0 & 0 \\ 0 & \mathbf{D}_{2BB} - \frac{\mathbf{D}_{2BA}\mathbf{D}_{2AB}}{D_{2AA}} \end{pmatrix} \begin{pmatrix} u_{1A} \\ \mathbf{u}_{1B} \end{pmatrix} \tag{5.82}$$

from which we identify

$$\mathbf{A}_1 = \begin{pmatrix} \mathbf{A}_2 - \frac{\mathbf{B}_{2A}\mathbf{C}_{2A}}{D_{2AA}} & \frac{\mathbf{B}_{2A}}{D_{2AA}\sqrt{C_1}} \\ \frac{\mathbf{C}_{2A}}{D_{2AA}\sqrt{C_1}} & -\frac{1}{D_{2AA}C_1} \end{pmatrix} \tag{5.83}$$

$$\mathbf{B}_1 = \begin{pmatrix} 0 & \mathbf{B}_{2B} - \frac{\mathbf{B}_{2A}\mathbf{D}_{2AB}}{D_{2AA}} \\ \frac{1}{\sqrt{C_1}} & \frac{\mathbf{D}_{1AB}}{D_{2AA}\sqrt{C_1}} \end{pmatrix} \tag{5.84}$$

$$\mathbf{C}_1 = \begin{pmatrix} 0 & \frac{1}{\sqrt{C_1}} \\ \mathbf{C}_{2B} - \frac{\mathbf{D}_{2BA}\mathbf{C}_{2A}}{D_{2AA}} & \frac{\mathbf{D}_{2BA}}{D_{2AA}\sqrt{C_1}} \end{pmatrix} \tag{5.85}$$

$$\mathbf{D}_1 = \begin{pmatrix} 0 & 0 \\ 0 & \mathbf{D}_{2BB} - \frac{\mathbf{D}_{2BA}\mathbf{D}_{2AB}}{D_{2AA}} \end{pmatrix} \tag{5.86}$$

and

$$\mathbf{x}_1 = \begin{pmatrix} \mathbf{x}_2 \\ x_{C_1} \end{pmatrix} \tag{5.87}$$

where $x_{C_1} = \sqrt{C_1} v_{C_1}$; u_{1A} is the current into the first port of the subnetwork N_1 in Fig. (5.12) and $\mathbf{u}_{1B}$ is the vector holding the currents at the remaining ports (ports $2 - N$) of the subnetwork N_1. Similarly y_{1A} is the voltage across the first port of the subnetwork N_1 and $\mathbf{y}_{1B}$ is the vector holding the voltages across the remaining ports (ports $2 - N$) of the subnetwork N_1. $\{\mathbf{A}_1, \mathbf{B}_1, \mathbf{C}_1, \mathbf{D}_1\}$ is then a realization for the impedance $\mathbf{Z}_1(s)$ seen at the ports of the network N_1.

One needs to modify also the *Multiport Synthesis Lemma* as follows:

The Multiport Synthesis Lemma (multi-port capacitive degenerate case)

Let $\{\mathbf{A}_a, \mathbf{B}_a, \mathbf{C}_a, \mathbf{D}_a\}$ be a minimal realization corresponding to the positive-real impedance $\mathbf{Z}_1(s)$ satisfying $\mathbf{Z}_{1,11}(j\omega_0) + \mathbf{Z}_{1,11}(-j\omega_0) = 0$ for some $\omega_0 = \infty$, $\mathbf{Z}_{1,11}$ is the $(1,1)$ entry of the impedance matrix $\mathbf{Z}_1$. Then there exists a coordinate transformation matrix $\mathbf{T}$ such that $\mathbf{A}_1 = \mathbf{T}\mathbf{A}_a\mathbf{T}^{-1}$, $\mathbf{B}_1 = \mathbf{T}\mathbf{B}_a$, $\mathbf{C}_1 = \mathbf{C}_a\mathbf{T}^{-1}$ and $\mathbf{D}_1 = \mathbf{D}_a$ are of the form given in Eqs. ((5.83)-(5.86)).

To compute $\mathbf{T}$ we will follow the algorithm described in *The Fundamental Lemma (one-port capacitive degenerate case)* in Section (4.2.3.1). Before applying the algorithm we set

$$\mathbf{b}_a = \mathbf{B}_a \mathbf{e}_1 \tag{5.88}$$
$$\mathbf{c}_a^T = \mathbf{C}_a^T \mathbf{e}_1 \tag{5.89}$$

and apply the one-port algorithm described in *The Fundamental Lemma (one-port capacitive degenerate case)* in Chapter (4.2.3.1) to the set $\{\mathbf{A}_a, \mathbf{b}_a, \mathbf{c}_a, \mathbf{D}_a\}$ where $\mathbf{e}_1 = \begin{pmatrix} 1 & 0 & \dots & 0 \end{pmatrix}^T$; that is we apply the one-port algorithm by picking up the first columns of $\mathbf{B}_a$ and $\mathbf{C}_a^T$ matrices.

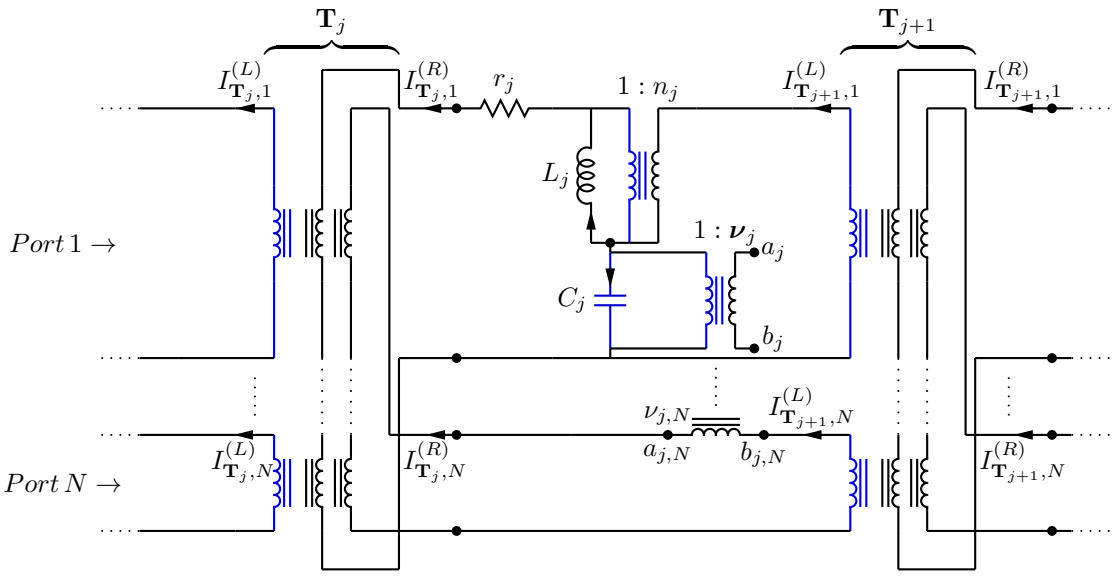

Figure 5.14: Multiport Brune stage. Tree branches are shown in black and chord branches are shown in blue. Note that the Belevitch transformers $\mathbf{T}_j$ and $\mathbf{T}_{j+1}$ are reflected compared to the Fig. (5.2).

5.5 Quantization of the multiport Brune circuit

The multiport Brune circuit contains ideal transformers. In this section we show that one can eliminate transformer branch variables and write a set of effective Kirchhoff relations for the rest of the branch currents and voltages. The effective Kirchhoff relations are given by the loop matrix $\mathbf{F}^{eff}$ involving turn ratios which we define below. The treatment here is similar to the analysis done in Chapter (4.3) for the one-port state-space Brune circuit. However as we will see the addition of Belevitch transformers and $\boldsymbol{\nu}$-type transformers makes the analysis more involved. We note that we replace the shunt resistors R_j's in the last stage by capacitors C_{R_j}'s for $1 \leq j \leq N$ as shown in Fig. (5.17) to do the dissipation analysis as discussed in detail in Appendix (6.2.2).

We will follow the same approach of Chapter (4.3). We write again the Kirchhoff's laws (Eqs. (6.38), (6.39)) for the multiport Brune circuit in Fig. (5.11) whose j^{th} stage is shown in detail in Fig. (5.14)

$$\mathbf{F}\mathbf{I}_{\text{ch}} = -\mathbf{I}_{\text{tr}} \tag{5.90}$$

$$\mathbf{F}^{\text{T}}\mathbf{V}_{\text{tr}} = \mathbf{V}_{\text{ch}} \tag{5.91}$$

where we have again assumed that there is no external flux bias. We note that the

relations in Eqs. (5.90) and (5.91) are derived from a graph theoretical analysis [18] of the multiport Brune network.

$\mathbf{I}_{\rm tr}$ and $\mathbf{I}_{\rm ch}$ are the tree and chord branch current vectors in Fig. (5.11) respectively partitioned as follows

$$\mathbf{I}_{\rm tr} = \left(\mathbf{I}_J, \mathbf{I}_L, \mathbf{I}_Z, \mathbf{I}_T^{(tr)}\right) \tag{5.92}$$

$$\mathbf{I}_{\rm ch} = \left(\mathbf{I}_C, \mathbf{I}_T^{(ch)}\right) \tag{5.93}$$

and tree and chord branches' voltages are partitioned respectively as

$$\mathbf{V}_{\rm tr} = \left(\mathbf{V}_J, \mathbf{V}_L, \mathbf{V}_Z, \mathbf{V}_T^{(tr)}\right) \tag{5.94}$$

$$\mathbf{V}_{\rm ch} = \left(\mathbf{V}_C, \mathbf{V}_T^{(ch)}\right) \tag{5.95}$$

Here labels J, L, Z, C, T correspond to Josephson junction, inductor, resistor, capacitor and ideal transformer branches, respectively.

Our aim here is to write an effective set of Kirchhoff relations as

$$\mathbf{F}^{eff}\mathbf{I}_{\rm ch}^{eff} = -\mathbf{I}_{\rm tr}^{eff} \tag{5.96}$$

$$\left(\mathbf{F}^T\right)^{eff}\mathbf{V}_{\rm tr}^{eff} = \mathbf{V}_{\rm ch}^{eff} \tag{5.97}$$

where transformer branches are eliminated such that

$$\begin{aligned}
\mathbf{I}_{\rm tr}^{eff} &= (\mathbf{I}_J, \mathbf{I}_L, \mathbf{I}_Z) && (5.98)\\
\mathbf{I}_{\rm ch}^{eff} &= \mathbf{I}_C && (5.99)\\
\mathbf{V}_{\rm tr}^{eff} &= (\mathbf{V}_J, \mathbf{V}_L, \mathbf{V}_Z) && (5.100)\\
\mathbf{V}_{\rm ch}^{eff} &= \mathbf{V}_C && (5.101)
\end{aligned}$$

Here we will do this effective loop matrix analysis for the Kirchhoff's current law to get the matrix $\mathbf{F}^{eff}$ in Eq. (5.96). It is important to note that one should also do a similar analysis for the Kirchhoff's voltage law to get an effective $\left(\mathbf{F}^T\right)^{eff}$ in Eq. (5.97) and verify that

$$\left(\mathbf{F}^T\right)^{eff} = \left(\mathbf{F}^{eff}\right)^T \tag{5.102}$$

holds. This we do in the Appendix (6.5.2). Eq. (5.102) is important to keep the various matrices of interest like the capacitance $\mathcal{C}$ and stiffness $\mathbf{M}_0$ matrices symmetric.

To show how one can find such a $\mathbf{F}^{eff}$ matrix we will further partition transformer current vectors $\mathbf{I}_T^{(tr)}$ and $\mathbf{I}_T^{(ch)}$ in Eqs. (5.92) and (5.93). We first note that left branches of all transformers in the circuit in Fig. (5.14) are chord branches (colored in blue) and that right branches of all transformers are in the tree (shown in black in Fig. (5.14)). Hence we can write

$$\mathbf{I}_T^{(tr)} = \left(\mathbf{I}_n^{(R)}, \mathbf{I}_{\mathbf{T}}^{(R)}, \mathbf{I}_{\boldsymbol{\nu}}^{(R)}\right) \tag{5.103}$$

$$\mathbf{I}_T^{(ch)} = \left(\mathbf{I}_n^{(L)}, \mathbf{I}_{\mathbf{T}}^{(L)}, \mathbf{I}_{\boldsymbol{\nu}}^{(L)}\right) \tag{5.104}$$

where

$$\mathbf{I}_n^{(R)} = \left(I_{n_1}^{(R)}, \ldots, I_{n_M}^{(R)}\right) \tag{5.105}$$

$$\mathbf{I}_{\mathbf{T}}^{(R)} = \left(\mathbf{I}_{\mathbf{T}_1}^{(R)}, \ldots, \mathbf{I}_{\mathbf{T}_{M+1}}^{(R)}\right) \tag{5.106}$$

$$\mathbf{I}_{\boldsymbol{\nu}}^{(R)} = \left(\mathbf{I}_{\boldsymbol{\nu}_1}^{(R)}, \ldots, \mathbf{I}_{\boldsymbol{\nu}_M}^{(R)}\right) \tag{5.107}$$

and

$$\mathbf{I}_n^{(L)} = \left(I_{n_1}^{(L)}, \ldots, I_{n_M}^{(L)}\right) \tag{5.108}$$

$$\mathbf{I}_{\mathbf{T}}^{(L)} = \left(\mathbf{I}_{\mathbf{T}_1}^{(L)}, \ldots, \mathbf{I}_{\mathbf{T}_{M+1}}^{(L)}\right) \tag{5.109}$$

$$\mathbf{I}_{\boldsymbol{\nu}}^{(L)} = \left(I_{\boldsymbol{\nu}_1}^{(L)}, \ldots, I_{\boldsymbol{\nu}_M}^{(L)}\right) \tag{5.110}$$

with

$$\mathbf{I}_{\mathbf{T}_j}^{(L)(R)} = \begin{pmatrix} I_{\mathbf{T}_j,1}^{(L)(R)} \\ \vdots \\ I_{\mathbf{T}_j,N}^{(L)(R)} \end{pmatrix} \tag{5.111}$$

$$\mathbf{I}_{\boldsymbol{\nu}_j}^{(R)} = \begin{pmatrix} I_{\boldsymbol{\nu}_j,2}^{(R)} \\ \vdots \\ I_{\boldsymbol{\nu}_j,N}^{(R)} \end{pmatrix} \tag{5.112}$$

where $\mathbf{I}_{\mathbf{T}_j}^{(L)(R)}$ are vectors of length N for $1 \leq j \leq M+1$ and $\mathbf{I}_{\boldsymbol{\nu}_j}^{(R)}$ are vectors of length $(N-1)$ for $1 \leq j \leq M$.

Before moving further in the analysis we beriefly review the relations between the currents through left and right branches of the three different types of transformers

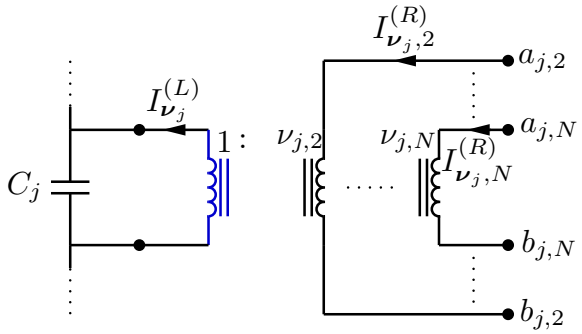

Figure 5.15: $\boldsymbol{\nu}$-type transformer circuit at j^{th} multiport Brune stage in Fig. (5.14). We also show the connection of the transformer to the capacitor C_j to make the correpondence to the Fig. (5.14) more clear.

in the multiport Brune circuit. We also give voltage relations for completeness although we don't need them for the analysis in this section. However we will refer to the voltage relations in the Appendix (6.5.2).

$\mathbf{I}^{(L)(R)}_{\mathbf{T}_j}$ is the vector of currents through the left(right) branches of the Belevitch multiport transformer appearing at the j^{th} multiport Brune stage, $1 \leq j \leq M+1$ as shown in Fig. (5.14). Hence by Eqs. (5.10) and (5.11) we have

$$\mathbf{I}^{(L)}_{\mathbf{T}_j} = \mathbf{T}_j \mathbf{I}^{(R)}_{\mathbf{T}_j} \tag{5.113}$$

$$\mathbf{V}^{(R)}_{\mathbf{T}_j} = \mathbf{T}^T_j \mathbf{V}^{(L)}_{\mathbf{T}_j} \tag{5.114}$$

where $\mathbf{V}^{(L)(R)}_{\mathbf{T}_j}$ is the vector of voltages across the left(right) branches of the Belevitch multiport transformer appearing at the j^{th} multiport Brune stage, $1 \leq j \leq M+1$ in Fig. (5.14).

The turns ratio vector of the $\boldsymbol{\nu}$-type transformer $\boldsymbol{\nu}_j$ at the j^{th} multiport Brune stage is given by

$$\boldsymbol{\nu}_j = \begin{pmatrix} \nu_{j,2} \\ \vdots \\ \nu_{j,N} \end{pmatrix} \tag{5.115}$$

The detailed circuit representation of the $\boldsymbol{\nu}$-type transformer at the j^{th} stage is given in Fig. (5.15). The current on the left branch is related to the currents on the right branches by

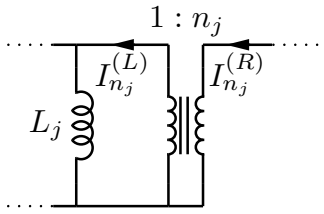

Figure 5.16: Conventions for the direction of currents for the n-type transformer of j^{th} stage in the multiport Brune circuit in Fig. (5.14). The inductive branch L_j is shown for orientation purposes with Fig. (5.14).

$$I^{(L)}_{\boldsymbol{\nu}_j} = \boldsymbol{\nu}_j^T \begin{pmatrix} I^{(R)}_{\boldsymbol{\nu}_j,2} \\ \vdots \\ I^{(R)}_{\boldsymbol{\nu}_j,N} \end{pmatrix} \tag{5.116}$$

and the voltages across the right branches of the $\boldsymbol{\nu}$-type transformer are related to the voltage across its left branch by the following formula

$$\begin{pmatrix} V^{(R)}_{\boldsymbol{\nu}_j,2} \\ \vdots \\ V^{(R)}_{\boldsymbol{\nu}_j,N} \end{pmatrix} = \boldsymbol{\nu}_j V^{(L)}_{\boldsymbol{\nu}_j} \tag{5.117}$$

The detailed circuit diagram with current direction conventions for the n-type transformer is shown in Fig. (5.16). For this type of transformer the relations between currents and voltages are given by

$$I^{(L)}_{n_j} = n_j I^{(R)}_{n_j} \tag{5.118}$$

$$V^{(R)}_{n_j} = n_j V^{(L)}_{n_j} \tag{5.119}$$

Now we can begin our analysis. We will proceed from the last(rightmost) stage to the first(leftmost) in Fig. (5.11) by relating the currents of consecutive stages.

Starting at the last stage we have (see Fig. (5.17))

$$\mathbf{I}^{(R)}_{\mathbf{T}_{M+1}} = -\mathbf{I}_{C_R} \tag{5.120}$$

where $\mathbf{I}_{C_R}$ are the currents through the capacitors(substituted for the shunt resistors) of the last stage.

The currents of inter-stage transformers are given by Eq. (5.113)

$$\mathbf{I}^{(L)}_{\mathbf{T}_j} = \mathbf{T}_j \mathbf{I}^{(R)}_{\mathbf{T}_j} \tag{5.121}$$

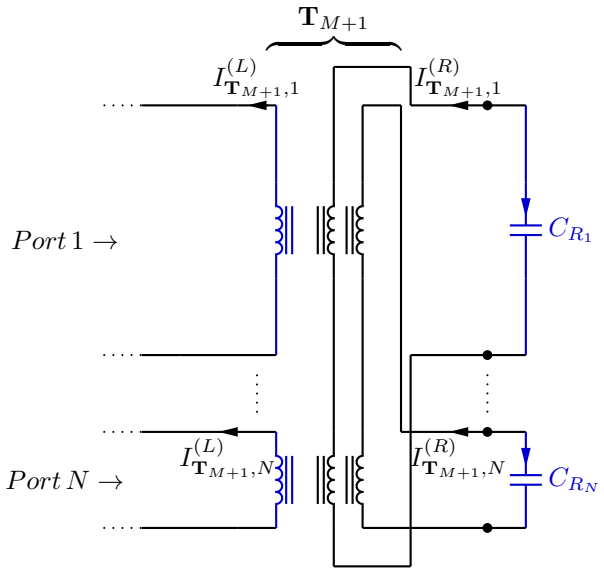

Figure 5.17: Last stage of the multiport Brune circuit. Tree branches are shown in black and chord branches are shown in blue.

for $1 \leq j \leq M+1$, where $\mathbf{T}_j$ is the $(N \times N)$ Belevitch transformer matrix of the j^{th} stage. The currents of consecutive inter-stage transformers are related by

$$\mathbf{I}^{(R)}_{\mathbf{T}_j} = -\mathbf{e}_1 I_{C_j} + \mathbf{A}_j \mathbf{I}^{(L)}_{\mathbf{T}_{j+1}} \tag{5.122}$$

for $1 \leq j \leq M$, where

$$\mathbf{A}_j = \begin{pmatrix} 1 & -\nu_{j,2} & \cdots & -\nu_{j,N} \\ & 1 & \mathbf{0} & \\ & \mathbf{0} & \ddots & \\ & & & 1 \end{pmatrix} \tag{5.123}$$

$\mathbf{A}_j$ is a $(N \times N)$ matrix and $\mathbf{e}_1$ is the unit vector $\mathbf{e}_1 = (1, 0, \ldots, 0)^T$ of length N. We note that in the case of a degenerate stage as in Fig. (5.13) for the j^{th} stage we have $\nu_{j,k} = 0$ for $2 \leq k \leq N$, hence $\mathbf{A}_j$ is the identity matrix in such a case.

The current I_{L_j} through the inductor L_j at the j^{th} multiport Brune stage can be written

$$I_{L_j} = -I_{C_j} + \boldsymbol{\upsilon}_j \mathbf{I}^{(L)}_{\mathbf{T}_{j+1}} \tag{5.124}$$

where $\boldsymbol{\upsilon}_j$ is a row vector of length N :

$$\boldsymbol{\upsilon}_j = \begin{pmatrix} (1-n_j) & -\nu_{j2} & \cdots & -\nu_{j,N} \end{pmatrix} \tag{5.125}$$

Using the Eqs. (5.120), (5.121), (5.122) and (5.124) we can iterate over the index j backwards starting at $j = M + 1$:

$$\begin{aligned}
\mathbf{I}^{(L)}_{\mathbf{T}_{M+1}} &= \mathbf{T}_{M+1}\mathbf{I}^{(R)}_{\mathbf{T}_{M+1}} = -\mathbf{T}_{M+1}\mathbf{I}_{C_R} \\
I_{L_M} &= -I_{C_M} + \boldsymbol{\upsilon}_M \mathbf{I}^{(L)}_{\mathbf{T}_{M+1}} = -I_{C_M} - \boldsymbol{\upsilon}_M \mathbf{T}_{M+1}\mathbf{I}_{C_R} \\
\mathbf{I}^{(R)}_{\mathbf{T}_M} &= -\mathbf{e}_1 I_{C_M} + \mathbf{A}_M \mathbf{I}^{(L)}_{\mathbf{T}_{M+1}} = -\mathbf{e}_1 I_{C_M} - \mathbf{A}_M \mathbf{T}_{M+1}\mathbf{I}_{C_R} \\
\mathbf{I}^{(L)}_{\mathbf{T}_M} &= \mathbf{T}_M \mathbf{I}^{(R)}_{\mathbf{T}_M} = -\mathbf{T}_M \mathbf{e}_1 I_{C_M} - \mathbf{T}_M \mathbf{A}_M \mathbf{T}_{M+1}\mathbf{I}_{C_R} \\
I_{L_{M-1}} &= -I_{C_{M-1}} + \boldsymbol{\upsilon}_{M-1}\mathbf{I}^{(L)}_{\mathbf{T}_M} = -I_{C_{M-1}} - \boldsymbol{\upsilon}_{M-1}\mathbf{T}_M \mathbf{e}_1 I_{C_M} - \boldsymbol{\upsilon}_{M-1}\mathbf{T}_M \mathbf{A}_M \mathbf{T}_{M+1}\mathbf{I}_{C_R} \\
\mathbf{I}^{(R)}_{\mathbf{T}_{M-1}} &= -\mathbf{e}_1 I_{C_{M-1}} + \mathbf{A}_{M-1}\mathbf{I}^{(L)}_{\mathbf{T}_M} = -\mathbf{e}_1 I_{C_{M-1}} - \mathbf{A}_{M-1}\mathbf{T}_M \mathbf{e}_1 I_{C_M} - \mathbf{A}_{M-1}\mathbf{T}_M \mathbf{A}_M \mathbf{T}_{M+1}\mathbf{I}_{C_R} \\
\mathbf{I}^{(L)}_{\mathbf{T}_{M-1}} &= \mathbf{T}_{M-1}\mathbf{I}^{(R)}_{\mathbf{T}_{M-1}} \\
&= -\mathbf{T}_{M-1}\mathbf{e}_1 I_{C_{M-1}} - \mathbf{T}_{M-1}\mathbf{A}_{M-1}\mathbf{T}_M \mathbf{e}_1 I_{C_M} - \mathbf{T}_{M-1}\mathbf{A}_{M-1}\mathbf{T}_M \mathbf{A}_M \mathbf{T}_{M+1}\mathbf{I}_{C_R} \\
I_{L_{M-2}} &= -I_{C_{M-2}} + \boldsymbol{\upsilon}_{M-2}\mathbf{I}^{(L)}_{\mathbf{T}_{M-1}} \\
&= -I_{C_{M-2}} - \boldsymbol{\upsilon}_{M-2}\mathbf{T}_{M-1}\mathbf{e}_1 I_{C_{M-1}} - \boldsymbol{\upsilon}_{M-2}\mathbf{T}_{M-1}\mathbf{A}_{M-1}\mathbf{T}_M \mathbf{e}_1 I_{C_M} + \\
&\quad -\boldsymbol{\upsilon}_{M-2}\mathbf{T}_{M-1}\mathbf{A}_{M-1}\mathbf{T}_M \mathbf{A}_M \mathbf{T}_{M+1}\mathbf{I}_{C_R} \qquad (5.126) \\
\vdots \quad \vdots &\quad \vdots
\end{aligned}$$

Hence we conclude that one can write

$$\mathbf{I}_L = -\mathbf{F}^{eff}_{LC}\mathbf{I}_C \qquad (5.127)$$

with for $1 \leq j \leq M$:

$$\begin{cases}
\mathbf{F}^{eff}_{LC}(j,k) = 0 & for\ k < j \\
\mathbf{F}^{eff}_{LC}(j,k) = 1 & for\ k = j \\
\mathbf{F}^{eff}_{LC}(j,k) = \boldsymbol{\upsilon}_j \mathbf{T}_{j+1}\mathbf{e}_1 & for\ k = j+1,\ and\ j < M \\
\mathbf{F}^{eff}_{LC}(j,k) = \boldsymbol{\upsilon}_j \mathbf{T}_{j+1}\mathbf{A}_{j+1}\ldots\mathbf{T}_{k-1}\mathbf{A}_{k-1}\mathbf{T}_k\mathbf{e}_1 & for\ j+2 \leq k \leq M \\
\mathbf{F}^{eff}_{LC}(j,k) = \boldsymbol{\upsilon}_j \mathbf{T}_{j+1}\mathbf{A}_{j+1}\ldots\mathbf{T}_M\mathbf{A}_M\mathbf{T}_{M+1}\mathbf{e}_{k-M} & for\ j < M\ and\ M+1 \leq k \leq M+N \\
\mathbf{F}^{eff}_{LC}(j,k) = \boldsymbol{\upsilon}_M \mathbf{T}_{M+1}\mathbf{e}_{k-M} & for\ j = M\ and\ M+1 \leq k \leq M+N
\end{cases} \qquad (5.128)$$

where $\mathbf{e}_k$ is the unit vector of length N non-zero only at its k^{th} entry such that $\mathbf{e}_k(j) = 0$ for $j \neq k$ and $\mathbf{e}_k(k) = 1$. We assumed the following ordering for the capacitors

$$\{C_1, \ldots, C_M, C_{R_1}, \ldots, C_{R_N}\} \qquad (5.129)$$

To compute $\mathbf{F}^{eff}_{ZC}$ we note the following

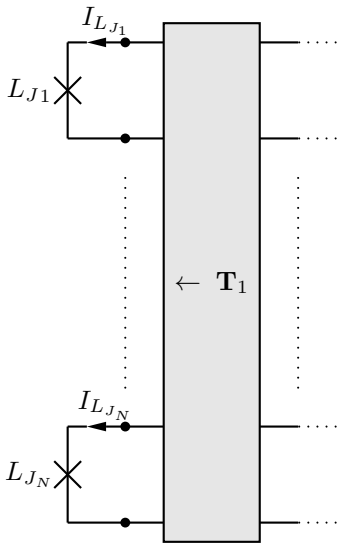

Figure 5.18: To compute $\mathbf{F}_{JC}^{eff}$, for simplicity, we assume that all the ports of the multiport Brune circuit are shunted by Josephson junctions $L_{J_1}, \ldots, L_{J_N}$.

$$I_{r_j} = I_{\mathbf{T}_j,1}^{(R)} \tag{5.130}$$

$$= \mathbf{e}_1^T \mathbf{I}_{\mathbf{T}_j}^{(R)} \tag{5.131}$$

for $1 \leq j \leq M$.

Referring back to the iteration in Eqs. (5.126) and using Eq. (5.131) we can write

$$\mathbf{I}_Z = -\mathbf{F}_{ZC}^{eff} \mathbf{I}_C \tag{5.132}$$

with for $1 \leq j \leq M$:

$$\begin{cases} \mathbf{F}_{ZC}^{eff}(j,k) = 0 & for\ k < j \\ \mathbf{F}_{ZC}^{eff}(j,k) = 1 & for\ k = j \\ \mathbf{F}_{ZC}^{eff}(j,k) = \mathbf{e}_1^T \mathbf{A}_j \mathbf{T}_{j+1} \ldots \mathbf{T}_{k-1} \mathbf{A}_{k-1} \mathbf{T}_k \mathbf{e}_1 & for\ j+1 \leq k \leq M \\ \mathbf{F}_{ZC}^{eff}(j,k) = \mathbf{e}_1^T \mathbf{A}_j \mathbf{T}_{j+1} \ldots \mathbf{T}_M \mathbf{A}_M \mathbf{T}_{M+1} \mathbf{e}_{k-M} & for\ M+1 \leq k \leq M+N \end{cases} \tag{5.133}$$

To compute $\mathbf{F}_{JC}^{eff}$ we will assume for simplicity that all the ports are shunted by Josephson junctions as shown in Fig. (5.18) so that all the junctions belong to the

spanning tree. Later we will allow for resistors and voltage sources shunting the ports of the multiport Brune network. We note the following

$$\mathbf{I}_J = \mathbf{I}_{\mathbf{T}_1}^{(L)} \tag{5.134}$$

Hence referring back to the iteration in Eq. (5.126) we deduce using Eq. (5.134)

$$\begin{aligned} \mathbf{I}_J &= \mathbf{I}_{\mathbf{T}_1}^{(L)} \\ &= -\mathbf{T}_1\mathbf{e}_1 I_{C_1} - \mathbf{T}_1\mathbf{A}_1\mathbf{T}_2\mathbf{e}_1 I_{C_2} \ldots - \mathbf{T}_1\mathbf{A}_1 \ldots \mathbf{T}_{M-1}\mathbf{A}_{M-1}\mathbf{T}_M\mathbf{e}_1 I_{C_M} + \\ &\quad -\mathbf{T}_1\mathbf{A}_1 \ldots \mathbf{T}_M\mathbf{A}_M\mathbf{T}_{M+1}\mathbf{I}_{C_R} \end{aligned} \tag{5.135}$$

Hence for $1 \leq j \leq N$

$$\begin{cases} \mathbf{F}_{JC}^{eff}(j,k) = \mathbf{e}_j^T\mathbf{T}_1\mathbf{e}_1 & for\ k = 1 \\ \mathbf{F}_{JC}^{eff}(j,k) = \mathbf{e}_j^T\mathbf{T}_1\mathbf{A}_1 \ldots \mathbf{T}_{k-1}\mathbf{A}_{k-1}\mathbf{T}_k\mathbf{e}_1 & for\ 1 < k \leq M \\ \mathbf{F}_{JC}^{eff}(j,k) = \mathbf{e}_j^T\mathbf{T}_1\mathbf{A}_1 \ldots \mathbf{T}_M\mathbf{A}_M\mathbf{T}_{M+1}\mathbf{e}_{k-M} & for\ M+1 \leq k \leq M+N \end{cases} \tag{5.136}$$

where $\mathbf{F}_{JC}^{eff}$ is defined by

$$\mathbf{I}_J = -\mathbf{F}_{JC}^{eff}\mathbf{I}_C \tag{5.137}$$

Now that we derived effective loop matrices we will follow the Appendix (6.2.1) and (6.2.2) to compute Hamiltonian matrices and to do dissipation analysis due to the resistors in the multiport Brune circuit. We will repeat here some of the definitions - which will be used with the effective loop matrices- of the Appendix (6.2.1) for convenience.

With the effective loop matrix

$$\mathcal{F}_C^{eff} = \begin{pmatrix} \mathbf{F}_{JC}^{eff} \\ \mathbf{F}_{LC}^{eff} \end{pmatrix} \tag{5.138}$$

we can compute the capacitance matrix $\mathcal{C}$ defined in Eq. (6.46)

$$\mathcal{C} = \begin{pmatrix} \mathbf{C}_J & \mathbf{0} \\ \mathbf{0} & \mathbf{0} \end{pmatrix} + \mathcal{F}_C^{eff}\mathbf{C}\left(\mathcal{F}_C^{eff}\right)^T \tag{5.139}$$

where we have the following partitioning to identify the submatrices $\mathbf{C}_0$ and $\mathbf{C}_R$ corresponding to ordinary capacitances and capacitances to be replaced by shunt resistors in the last stage of the multiport Brune circuit, respectively

$$\mathbf{C} = \begin{pmatrix} \mathbf{C}_0 & \mathbf{0} \\ \mathbf{0} & \mathbf{C}_R \end{pmatrix} \tag{5.140}$$

with

$$\mathbf{C}_0 = \begin{pmatrix} C_1 & & \mathbf{0} \\ & \ddots & \\ \mathbf{0} & & C_M \end{pmatrix} \tag{5.141}$$

and

$$\mathbf{C}_R = \begin{pmatrix} C_{R_1} & & \mathbf{0} \\ & \ddots & \\ \mathbf{0} & & C_{R_N} \end{pmatrix} \tag{5.142}$$

and the matrix $\mathbf{C}_J$ in Eq. (5.139) for the Josephson junction capacitances is

$$\mathbf{C}_J = \begin{pmatrix} C_{J_1} & & \mathbf{0} \\ & \ddots & \\ \mathbf{0} & & C_{J_N} \end{pmatrix} \tag{5.143}$$

Partitioning also $\mathcal{F}_C^{eff}$ according to the partitioning in Eq. (5.140) as in Eq. (6.72)

$$\mathcal{F}_C^{eff} = \begin{pmatrix} \mathcal{F}_{C_0}^{eff} & \mathcal{F}_{C_R}^{eff} \end{pmatrix} \tag{5.144}$$

we can decompose $\mathcal{C}$ in Eq. (5.139) as in Eq. (6.75)

$$\begin{aligned} \mathcal{C} &= \begin{pmatrix} \mathbf{C}_J & \mathbf{0} \\ \mathbf{0} & \mathbf{0} \end{pmatrix} + \mathcal{F}_C^{eff} \mathbf{C} \left(\mathcal{F}_C^{eff} \right)^T && (5.145) \\ &= \mathcal{C}_0 + \mathcal{C}_R && (5.146) \end{aligned}$$

where we defined as we did in Eqs. (6.76) and (6.77)

$$\begin{aligned} \mathcal{C}_0 &= \begin{pmatrix} \mathbf{C}_J & \mathbf{0} \\ \mathbf{0} & \mathbf{0} \end{pmatrix} + \mathcal{F}_{C_0}^{eff} \mathbf{C}_0 \left(\mathcal{F}_{C_0}^{eff} \right)^T && (5.147) \\ \mathcal{C}_R &= \mathcal{F}_{C_R}^{eff} \mathbf{C}_R \left(\mathcal{F}_{C_R}^{eff} \right)^T && (5.148) \end{aligned}$$

$\mathcal{C}_0$ is the capacitance matrix that appears in the system Lagrangian and Hamiltonian for the multiport Brune circuit whereas $\mathcal{C}_R$ is a dissipative term which we will treat later below by making the substitution $\mathbf{C}_R \leftarrow (i\omega)^{-1} \mathbf{R}^{-1}$ as described in Eq. (6.70) for the shunt resistors in the last stage.

$\mathbf{L}_t^{-1}$ and $\mathcal{G}$ matrices defined in Eqs. (6.66), (6.67) are simply

$$\mathbf{L}_t^{-1} = \begin{pmatrix} 1/L_1 & & \mathbf{0} \\ & \ddots & \\ \mathbf{0} & & 1/L_M \end{pmatrix} \tag{5.149}$$

$$\mathcal{G} = \begin{pmatrix} \mathbf{0} \\ \mathbf{I}_L \end{pmatrix} \tag{5.150}$$

since there are no chord inductors in the circuit. Hence we have by Eq. (6.64)

$$\mathbf{M}_0 = \mathcal{G}\mathbf{L}_t^{-1}\mathcal{G}^T \tag{5.151}$$

$$= \begin{pmatrix} \mathbf{0}_J & & \mathbf{0} \\ & 1/L_1 & \\ & \ddots & \\ \mathbf{0} & & 1/L_M \end{pmatrix} \tag{5.152}$$

where $\mathbf{0}_J$ is a $N_J \times N_J$ zero matrix. Here since we assumed that all ports are shunted by Josephson junctions $N_J = N$.

Using the Eq. (6.127) we have the following Hamiltonian for the multiport Brune circuit

$$\mathcal{H}_{\mathcal{S}} = \frac{1}{2}\boldsymbol{Q}^T\mathcal{C}_0^{-1}\boldsymbol{Q} + U(\boldsymbol{\Phi}) \tag{5.153}$$

where

$$U(\boldsymbol{\Phi}) = -\left(\frac{\Phi_0}{2\pi}\right)^2 \mathbf{L}_J^{-1}\cos(\boldsymbol{\varphi}_J) + \frac{1}{2}\boldsymbol{\Phi}^T\mathbf{M_0}\boldsymbol{\Phi} \tag{5.154}$$

To treat the dissipation we first note that the diagonal tree impedance matrix

$$\mathbf{Z} = \begin{pmatrix} r_1 & & \mathbf{0} \\ & \ddots & \\ \mathbf{0} & & r_M \end{pmatrix} \tag{5.155}$$

consists of in-series resistances $r_1, \ldots, r_M$ of the multiport Brune circuit in Fig. (5.11). However, as we noted in Appendix (6.2.2) we will treat each in-series resistor r_j separately for $1 \leq j \leq M$. So instead of using the full $\mathbf{F}_{ZC}^{eff}$ matrix defined in Eq. (5.133) we will use its rows $\mathbf{F}_{r_j,C_0}^{eff}$'s corresponding to the in-series resistors r_j's for $1 \leq j \leq M$, in our dissipation treatment below.

We compute the coupling $\bar{\mathbf{m}}_j$ of the bath due to the resistor r_j for $1 \leq j \leq M$ to the circuit degrees of freedom using Eq. (6.101) with the effective row vector

$\mathbf{F}^{eff}_{r_j,C_0}$ (since we treat resistors one at a time $\mathbf{F}^{eff}_{r_j,C_0}$ is the j^{th} row of the matrix $\mathbf{F}^{eff}_{ZC_0}$ defined in Eq. (6.92) corresponding to the resistor r_j)

$$\bar{\mathbf{m}}_j = \mathcal{F}^{eff}_{C_0}\mathbf{C}_0\left(\mathbf{F}^{eff}_{r_j,C_0}\right)^T \tag{5.156}$$

$$= \begin{pmatrix} \bar{\mathbf{m}}_{j,J} \\ \bar{\mathbf{m}}_{j,L} \end{pmatrix} \tag{5.157}$$

and using Eq. (6.113)

$$\bar{\mathbf{C}}_{Z,r_j}(\omega) = -i\omega r_j\left[1 + i\omega r_j \mathbf{F}^{eff}_{r_j,C_0}\mathbf{C}_0\left(\mathbf{F}^{eff}_{r_j,C_0}\right)^T\right]^{-1} \tag{5.158}$$

which is related to the kernel as derived in Eq. (6.111) (we note that $\bar{\mathbf{C}}_{Z,r_j}(\omega)$ is a scalar)

$$K_j(\omega) = -\omega^2\bar{\mathbf{C}}_{Z,r_j}(\omega) \tag{5.159}$$

and the spectrum of the bath due to the resistor r_j is given by Eq. (6.114)

$$J_j(\omega) = Im\left[K_j(\omega)\right] \tag{5.160}$$

$$= \frac{\omega^3 r_j}{1 + \omega^2 r_j^2\left[\mathbf{F}^{eff}_{r_j,C_0}\mathbf{C}_0\left(\mathbf{F}^{eff}_{r_j,C_0}\right)^T\right]^2} \tag{5.161}$$

The contribution of the resistor r_j to the relaxation rate is given by the formula in Eq. (6.115)

$$\frac{1}{T_{1,r_j}} = \frac{4}{\hbar}\left|\langle 0\left|\bar{\mathbf{m}}_j\cdot\mathbf{\Phi}\right|1\rangle\right|^2 J_j(\omega_{01})\coth\left(\frac{\hbar\omega_{01}}{2k_BT}\right) \tag{5.162}$$

where ω_{01} is the qubit frequency.

To compute the dissipative contribution of the resistors $\{R_1,\ldots,R_N\}$ shunting the last stage we make the substitution $\mathbf{C}_R \leftarrow (i\omega)^{-1}\mathbf{R}^{-1}$ done in Eq. (6.70) to get the resistance matrix defined in Eq. (6.81)

$$\mathcal{R}^{-1} = \mathcal{F}^{eff}_{C_R}\mathbf{R}^{-1}\left(\mathcal{F}^{eff}_{C_R}\right)^T \tag{5.163}$$

where $\mathbf{R}$ is defined as

$$\mathbf{R} = \begin{pmatrix} R_1 & & \mathbf{0} \\ & \ddots & \\ \mathbf{0} & & R_N \end{pmatrix} \tag{5.164}$$

We again treat the shunt resistors $\{R_1, \ldots, R_N\}$ one at a time, that is, to compute the contribution of the resistor R_j to the relaxation rate we set $R_k = \infty$ for $1 \leq k \leq N$ and $k \neq j$ and we short circuit in series resistors by setting $r_k = 0$ for $1 \leq k \leq M$. The coupling vector $\bar{\mathbf{m}}_{R_j}$ which couples the bath due to R_j to the circuit degrees of freedom is given in Eq. (6.87) as

$$\bar{\mathbf{m}}_{R_j} = \mathcal{F}^{eff}_{R_j, C_R} \tag{5.165}$$

where $\mathcal{F}^{eff}_{R_j, C_R}$ is the j^{th} column of the matrix $\mathcal{F}^{eff}_{C_R}$ and the dissipation kernel due to R_j is given in Eq. (6.88) as

$$K_{R_j}(\omega) = \frac{i\omega}{R_j} \tag{5.166}$$

and the spectral density J_{R_j} of the bath due to R_j is given by Eq. (6.89)

$$\begin{aligned} J_{R_j}(\omega) &= \mathrm{Im}\left[K_{R_j}(\omega)\right] && (5.167)\\ &= \frac{\omega}{R_j} && (5.168) \end{aligned}$$

Hence by Eq. (6.91) we compute the contribution of the resistor R_j to the relaxation rate as

$$\frac{1}{T_{1,R_j}} = \frac{4}{\hbar} \left|\left\langle 0 \left| \bar{\mathbf{m}}_{R_j} \cdot \mathbf{\Phi} \right| 1 \right\rangle\right|^2 J_{R_j}(\omega_{01}) \coth\left(\frac{\hbar\omega_{01}}{2k_B T}\right) \tag{5.169}$$

5.5.1 Resistors shunting the ports

One can also think of shunting some of the ports in Fig. (5.18) by resistors. For simplicity let's assume that we shunt only the j^{th} port of the multiport Brune circuit by a resistor R^x_j and the rest of the ports by Josephson junctions as shown in Fig. (5.19). The branch of the resistor R^x_j belongs to the spanning tree hence its treatment will be similar to the treatment of the in-series resistors r_j in the previous section. We will derive an effective loop row-vector $\mathbf{F}^{eff}_{R^x_j, C}$ corresponding to R^x_j. Before doing this we note that the j^{th} row of the effective loop matrix $\mathbf{F}^{eff}_{JC}$ derived in Eq. (5.136) above needs to be dropped since we replaced the j^{th} Josephson junction in Fig. (5.18) by the resistor R^x_j.

We first note the following

$$I_{R^x_j} = I^{(L)}_{\mathbf{T}_1, j} \tag{5.170}$$

Hence from the iteration in Eq. (5.126) we conclude

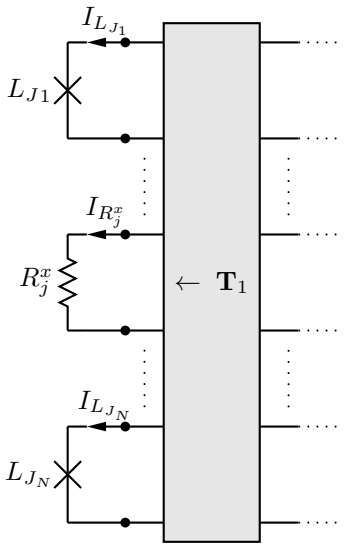

Figure 5.19: The multiport Brune circuit shunted by a resistor at its j^{th} port and by Josephson junctions at the remaining ports.

$$\begin{aligned} I_{R_j^x} &= \mathbf{e}_j^T \mathbf{I}_{\mathbf{T}_1}^{(L)} \\ &= -\mathbf{e}_j^T \mathbf{T}_1 \mathbf{e}_1 I_{C_1} - \mathbf{e}_j^T \mathbf{T}_1 \mathbf{A}_1 \mathbf{T}_2 \mathbf{e}_1 I_{C_2} \ldots - \mathbf{e}_j^T \mathbf{T}_1 \mathbf{A}_1 \ldots \mathbf{T}_{M-1} \mathbf{A}_{M-1} \mathbf{T}_M \mathbf{e}_1 I_{C_M} + \\ &\quad -\mathbf{e}_j^T \mathbf{T}_1 \mathbf{A}_1 \ldots \mathbf{T}_M \mathbf{A}_M \mathbf{T}_{M+1} \mathbf{I}_{C_R} \end{aligned} \tag{5.171}$$

From which we conclude that

$$I_{R_j^x} = -\mathbf{F}_{R_j^x,C}^{eff} \mathbf{I}_C$$

where $\mathbf{F}_{R_j^x,C}^{eff}$ is a row vector of length $(M+N)$ with

$$\begin{cases} \mathbf{F}_{R_j^x,C}^{eff}(k) = \mathbf{e}_j^T \mathbf{T}_1 \mathbf{e}_1 & for\ k = 1 \\ \mathbf{F}_{R_j^x,C}^{eff}(k) = \mathbf{e}_j^T \mathbf{T}_1 \mathbf{A}_1 \ldots \mathbf{T}_{k-1} \mathbf{A}_{k-1} \mathbf{T}_k \mathbf{e}_1 & for\ 1 < k \leq M \\ \mathbf{F}_{R_j^x,C}^{eff}(k) = \mathbf{e}_j^T \mathbf{T}_1 \mathbf{A}_1 \ldots \mathbf{T}_M \mathbf{A}_M \mathbf{T}_{M+1} \mathbf{e}_k & for\ M+1 \leq k \leq M+N \end{cases} \tag{5.172}$$

So one then needs to append $\mathbf{F}_{R_j^x,C}^{eff}$ to $\mathbf{F}_{ZC}^{eff}$ defined in Eq. (5.133) as its last row. Also R_j^x will appear at the last diagonal entry of the tree impedance matrix $\mathbf{Z}$ defined in Eq. (5.155)

$$\mathbf{Z} = \begin{pmatrix} r_1 & & \mathbf{0} \\ & \ddots & \\ & & r_M \\ \mathbf{0} & & R_j^x \end{pmatrix} \tag{5.173}$$

To compute the contribution of R_j^x to the dissipation rate we follow the same procedure done for the resistors r_j, $1 \leq j \leq M$ in Eqs. (5.156)-(5.162) above and compute the coupling $\bar{\mathbf{m}}_{R_j^x}$ of the bath due to the resistor R_j^x to the circuit degrees of freedom using Eq. (6.101) with the effective matrix $\mathbf{F}^{eff}_{R_j^x,C_0}$

$$\begin{aligned} \bar{\mathbf{m}}_{R_j^x} &= \mathcal{F}^{eff}_{C_0} \mathbf{C}_0 \left(\mathbf{F}^{eff}_{R_j^x,C_0}\right)^T && (5.174) \\ &= \begin{pmatrix} \bar{\mathbf{m}}_{j,J} \\ \bar{\mathbf{m}}_{j,L} \end{pmatrix} && (5.175) \end{aligned}$$

where we assume the following partitioning for $\mathbf{F}^{eff}_{R_j^x,C}$

$$\mathbf{F}^{eff}_{R_j^x,C} = \begin{pmatrix} \mathbf{F}^{eff}_{R_j^x,C_0} & \mathbf{F}^{eff}_{R_j^x,C_R} \end{pmatrix} \tag{5.176}$$

where $\mathbf{F}^{eff}_{R_j^x,C_0}$ and $\mathbf{F}^{eff}_{R_j^x,C_R}$ are row vectors of length M and N, respectively.

Using Eq. (6.113)

$$\bar{\mathbf{C}}_{Z,R_j^x}(\omega) = -i\omega R_j^x \left[1 + i\omega R_j^x \mathbf{F}^{eff}_{R_j^x,C_0} \mathbf{C}_0 \left(\mathbf{F}^{eff}_{R_j^x,C_0}\right)^T\right]^{-1} \tag{5.177}$$

which is related to the kernel as derived in Eq. (6.111)

$$K_{R_j^x}(\omega) = -\omega^2 \bar{\mathbf{C}}_{Z,R_j^x}(\omega) \tag{5.178}$$

and the spectrum of the bath due to the resistor R_j^x is given by Eq. (6.114)

$$\begin{aligned} J_{R_j^x} &= Im\left[K_{R_j^x}(\omega)\right] && (5.179) \\ &= \frac{\omega^3 R_j^x}{1 + \omega^2 \left(R_j^x\right)^2 \left[\mathbf{F}^{eff}_{R_j^x,C_0} \mathbf{C}_0 \left(\mathbf{F}^{eff}_{R_j^x,C_0}\right)^T\right]^2} && (5.180) \end{aligned}$$

And by Eq. (6.115) the contribution of R_j^x to the loss rate

$$\frac{1}{T_{1,R_j^x}} = \frac{4}{\hbar} \left|\left\langle 0 \left| \bar{\mathbf{m}}_{R_j^x} \cdot \mathbf{\Phi} \right| 1 \right\rangle\right|^2 J_{R_j^x}(\omega_{01}) \coth\left(\frac{\hbar\omega_{01}}{2k_B T}\right)$$

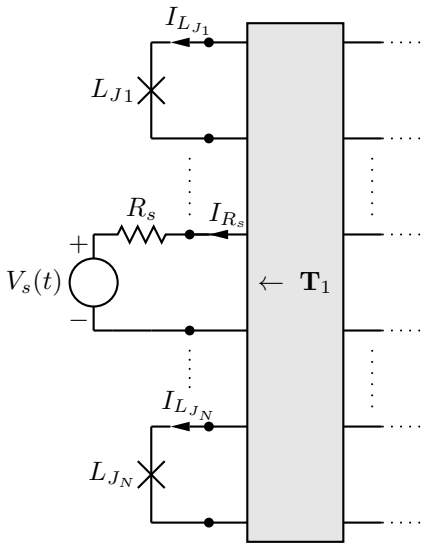

Figure 5.20: Voltage source $V_s(t)$ in series with a resistance R_s shunting the j^{th} port of the multiport Brune circuit.

If we have several resistors shunting the multiport Brune circuit the analysis is straightforward. One then needs to drop the rows in the $\mathbf{F}_{JC}^{eff}$ matrix corresponding to the ports shunted by resistors and repeat the dissipation analysis above for each R_j^x. A full $\mathbf{F}_{ZC}^{eff}$ is obtained by appending the rows $\mathbf{F}_{R_j^x,C}^{eff}$ corresponding to each R_j^x which are appended to $\mathbf{Z}$.

5.5.2 Voltage sources shunting the ports

Now we consider shunting one of the ports by a possibly time-dependent voltage source $V_s(t)$ as shown in Fig. (5.20). We also assume that the voltage source has an in series resistance R_s. Assuming also that V_s and R_s shunt the j^{th} port the treatment of the resistor R_s follows the same analysis we did above for the resistor R_j^x. To treat the voltage source we first note the following

$$I_{V_s} = I_{R_s} = I_{\mathbf{T}_1,j}^{(L)} \tag{5.181}$$

Hence with the same loop analysis we did for the resistor R_j^x above we can derive an effective loop matrix $\mathbf{F}_{V_s,C}^{eff}$ such that

$$I_{V_s} = -\mathbf{F}_{V_s,C}^{eff}\mathbf{I}_C \tag{5.182}$$

where $\mathbf{F}_{V_s,C}^{eff} = \mathbf{F}_{R_j^x,C}^{eff}$ with $\mathbf{F}_{R_j^x,C}^{eff}$ being defined in Eq. (5.172).

Now $\mathbf{F}^{eff}_{V_s,C}$ will appear as one of the rows of the $\mathbf{F}_{VC}$ matrix. One can then use $\mathbf{F}_{VC}$ to first compute $\bar{\mathbf{m}}_V$ defined in Eq. (6.53) and then the coupling vectors $\mathbf{C}_V$ and $\mathcal{C}_V$ defined in Eqs. (6.47) and (6.58), respectively, in Appendix (6.2.1). Making the substitution $\mathbf{C}_R \leftarrow (i\omega)^{-1}\mathbf{R}^{-1}$ in Eq. (6.70) and following the analysis at the end of Appendix (6.2.1) we get the following Hamiltonian derived in Eq. (6.127) for the multiport Brune circuit shunted by the voltage source at one of its ports

$$\mathcal{H}_S = \frac{1}{2}\left(\mathbf{Q} - \left(\mathbf{C}_{V,0} + \mathcal{C}_{V,R}\left(t\right)\right) * \mathbf{V}_V\left(t\right)\right)^T \mathcal{C}_0^{-1}\left(\mathbf{Q} - \left(\mathbf{C}_{V,0} + \mathcal{C}_{V,R}\left(t\right)\right) * \mathbf{V}_V\left(t\right)\right) + U\left(\mathbf{\Phi}\right) \tag{5.183}$$

where the voltage source vector $\mathbf{V}_V\left(t\right)$ has $V_s\left(t\right)$ at its corresponding entry. The matrices $\mathbf{C}_{V,0}$ and $\mathcal{C}_{V,R}\left(t\right)$ are defined, respectively, in Eqs. (6.118) and (6.125) in Appendix (6.2.3) which we repeat here for convenience

$$\mathbf{C}_{V,0} = \mathcal{F}^{eff}_{C_0}\mathbf{C}_0\left(\mathbf{F}^{eff}_{VC_0}\right)^T \tag{5.184}$$

$$\mathcal{C}_{V,R}\left(\omega\right) = \mathbf{C}_{V,R}\left(\omega\right) + \mathcal{C}_V\left(\omega\right) \tag{5.185}$$

where in the definition of the frequency-independent coupling matrix $\mathbf{C}_{V,0}$ we assumed the following partitioning for $\mathbf{F}^{eff}_{VC}$ as in Eq. (6.116)

$$\mathbf{F}^{eff}_{VC} = \begin{pmatrix} \mathbf{F}^{eff}_{VC_0} & \mathbf{F}^{eff}_{VC_R} \end{pmatrix} \tag{5.186}$$

For the definitions of the matrices appearing $\mathbf{C}_{V,R}\left(\omega\right)$ and $\mathcal{C}_V\left(\omega\right)$ in Eq. (5.185) we refer the reader to Eqs. (6.119) and (6.124), respectively, in Appendix (6.2.3). We recall that effective loop matrices should be used in those definitions.

5.6 Example

Here we illustrate the method described in the previous section with a generic 2-port 1-stage Brune circuit.

5.6.1 2-port 1-stage generic Brune circuit

We consider a generic 2-port 1-stage Brune circuit shown in Fig. (5.21). The 2-port Brune circuit is shown in the dotted box. This 2-port Brune circuit is shunted by two Josephson junctions L_{J_1} and L_{J_2} at each of its ports. There is only one reactive stage which corresponds to a single pole at a finite frequency in the partial fraction expansion for the impedance fit in Eq. (3.1).

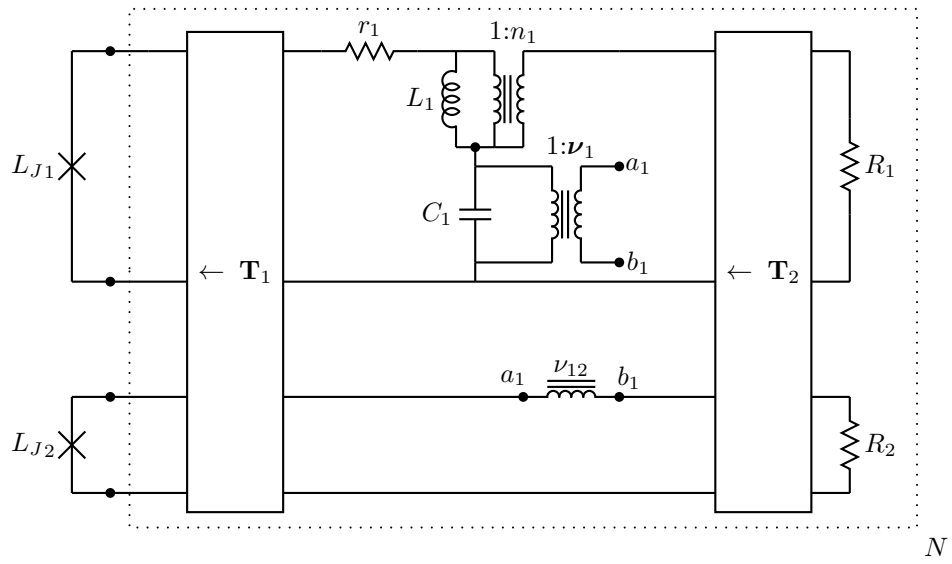

Figure 5.21: 2-port 1-stage multiport Brune circuit. The part of the circuit labeled N contained in the dotted box is the 2-port Brune circuit shunted by two Josephson junctions at each of its ports.

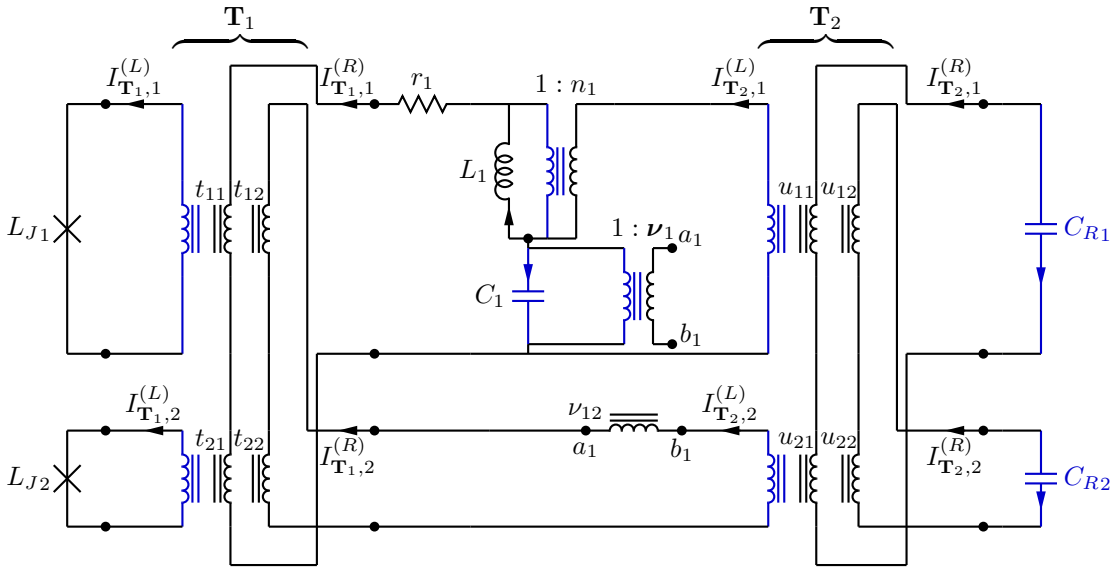

Figure 5.22: Modified 2-port Brune circuit. Chord branches are shown in blue, tree branches are shown in black.

First we need to replace the resistors R_1 and R_2 in the last stage by capacitors C_{R_1} and C_{R_2} as shown in Fig. (5.22). We will later make the substitutions $C_{R_1} \leftarrow \frac{1}{i\omega R_1}$ and $C_{R_2} \leftarrow \frac{1}{i\omega R_2}$ for the dissipation analysis.

There are three capacitors in the circuit in Fig. (5.22). All the capacitors are in chord branches. The currents through those capacitors are given by the vector

$$\mathbf{I}_C = \begin{pmatrix} I_{C_1} \\ I_{C_{R_1}} \\ I_{C_{R_2}} \end{pmatrix} \tag{5.187}$$

As described in the previous section we will eliminate transformer branches and write the currents through tree branches as functions of capacitor currents. This way we will compute effective loop matrices $\mathbf{F}_{JC}^{eff}$, $\mathbf{F}_{LC}^{eff}$ and $\mathbf{F}_{ZC}^{eff}$.

As we see in Fig. (5.22) the two Belevitch transformers $\mathbf{T}_1$ and $\mathbf{T}_2$ are given by the turns ratios matrices

$$\mathbf{T}_1 = \begin{pmatrix} t_{11} & t_{12} \\ t_{21} & t_{22} \end{pmatrix} \tag{5.188}$$

$$\mathbf{T}_2 = \begin{pmatrix} u_{11} & u_{12} \\ u_{21} & u_{22} \end{pmatrix} \tag{5.189}$$

We can now write

$$\begin{aligned} \mathbf{I}_{\mathbf{T}_2}^{(L)} &= \mathbf{T}_2 \mathbf{I}_{\mathbf{T}_2}^{(R)} = -\mathbf{T}_2 \mathbf{I}_{C_R} && (5.190) \\ &= -\begin{pmatrix} u_{11} & u_{12} \\ u_{21} & u_{22} \end{pmatrix} \begin{pmatrix} I_{C_{R_1}} \\ I_{C_{R_2}} \end{pmatrix} && (5.191) \end{aligned}$$

where we used $\mathbf{I}_{\mathbf{T}_2}^{(R)} = -\mathbf{I}_{C_R}$. The current I_{L_1} through the inductor L_1 is given by

$$\begin{aligned} I_{L_1} &= -I_{C_1} + \boldsymbol{\upsilon}_1 \mathbf{I}_{\mathbf{T}_2}^{(L)} && (5.192) \\ &= -I_{C_1} - \left((1-n_1), -\nu_{12}\right) \begin{pmatrix} u_{11} & u_{12} \\ u_{21} & u_{22} \end{pmatrix} \begin{pmatrix} I_{C_{R_1}} \\ I_{C_{R_2}} \end{pmatrix} && (5.193) \\ &= -I_{C_1} - \left((1-n_1)\, u_{11} - u_{21}\nu_{12},\, (1-n_1)\, u_{12} - u_{22}\nu_{12}\right) \begin{pmatrix} I_{C_{R_1}} \\ I_{C_{R_2}} \end{pmatrix} \end{aligned}$$

from which we identify

$$\mathbf{F}_{LC}^{eff} = \left(1,\, (1-n_1)\, u_{11} - u_{21}\nu_{12},\, (1-n_1)\, u_{12} - u_{22}\nu_{12}\right) \tag{5.194}$$

where $\mathbf{F}_{LC}^{eff}$ is defined by the relation

$$I_{L_1} = -\mathbf{F}_{LC}^{eff}\mathbf{I}_C \tag{5.195}$$

We now move to the transformer $\mathbf{T}_1$ and write

$$\begin{aligned}
\mathbf{I}_{\mathbf{T}_1}^{(R)} &= -I_{C_1}\mathbf{e}_1 + \mathbf{A}_1\mathbf{I}_{\mathbf{T}_2}^{(L)} && (5.196)\\
&= -I_{C_1}\begin{pmatrix} 1 \\ 0 \end{pmatrix} + \begin{pmatrix} 1 & -\nu_{12} \\ 0 & 1 \end{pmatrix}\mathbf{I}_{\mathbf{T}_2}^{(L)} && (5.197)\\
&= -I_{C_1}\begin{pmatrix} 1 \\ 0 \end{pmatrix} - \begin{pmatrix} 1 & -\nu_{12} \\ 0 & 1 \end{pmatrix}\begin{pmatrix} u_{11} & u_{12} \\ u_{21} & u_{22} \end{pmatrix}\begin{pmatrix} I_{C_{R_1}} \\ I_{C_{R_2}} \end{pmatrix} && (5.198)
\end{aligned}$$

and

$$\begin{aligned}
\mathbf{I}_{\mathbf{T}_1}^{(L)} &= \mathbf{T}_1\mathbf{I}_{\mathbf{T}_1}^{(R)} && (5.199)\\
&= -I_{C_1}\mathbf{T}_1\mathbf{e}_1 + \mathbf{T}_1\mathbf{A}_1\mathbf{I}_{\mathbf{T}_2}^{(L)} && (5.200)\\
&= -I_{C_1}\begin{pmatrix} t_{11} \\ t_{21} \end{pmatrix} - \begin{pmatrix} t_{11} & t_{12} \\ t_{21} & t_{22} \end{pmatrix}\begin{pmatrix} 1 & -\nu_{12} \\ 0 & 1 \end{pmatrix}\begin{pmatrix} u_{11} & u_{12} \\ u_{21} & u_{22} \end{pmatrix}\begin{pmatrix} I_{C_{R_1}} \\ I_{C_{R_2}} \end{pmatrix}\\
&= -I_{C_1}\begin{pmatrix} t_{11} \\ t_{21} \end{pmatrix} + && (5.201)\\
&\quad -\begin{pmatrix} t_{11}u_{11} + u_{21}\left(t_{12} - t_{11}\nu_{12}\right) & t_{11}u_{12} + u_{22}\left(t_{12} - t_{11}\nu_{12}\right) \\ t_{21}u_{11} + u_{21}\left(t_{22} - t_{21}\nu_{12}\right) & t_{21}u_{12} + u_{22}\left(t_{22} - t_{21}\nu_{12}\right) \end{pmatrix}\begin{pmatrix} I_{C_{R_1}} \\ I_{C_{R_2}} \end{pmatrix}
\end{aligned}$$

Using the relation $\mathbf{I}_J = \mathbf{I}_{\mathbf{T}_1}^{(L)}$ and the Eqs. (5.199)-(5.201) above we identify

$$\mathbf{F}_{JC}^{eff} = \begin{pmatrix} t_{11} & t_{11}u_{11} + u_{21}\left(t_{12} - t_{11}\nu_{12}\right) & t_{11}u_{12} + u_{22}\left(t_{12} - t_{11}\nu_{12}\right) \\ t_{21} & t_{21}u_{11} + u_{21}\left(t_{22} - t_{21}\nu_{12}\right) & t_{21}u_{12} + u_{22}\left(t_{22} - t_{21}\nu_{12}\right) \end{pmatrix} \tag{5.202}$$

where $\mathbf{F}_{JC}^{eff}$ is defined by the relation $\mathbf{I}_J = -\mathbf{F}_{JC}^{eff}\mathbf{I}_C$.

Using Eqs. (5.194), (5.202) and making the partitioning in Eq. (5.144) we get

$$\mathcal{F}_{C_0}^{eff} = \begin{pmatrix} t_{11} \\ t_{21} \\ 1 \end{pmatrix} \tag{5.203}$$

and hence by Eq. (5.147)

$$\begin{aligned}
\mathcal{C}_0 &= \begin{pmatrix} \mathbf{C}_J & \mathbf{0} \\ \mathbf{0} & \mathbf{0} \end{pmatrix} + \mathcal{F}_{C_0}^{eff}\mathbf{C}_0\left(\mathcal{F}_{C_0}^{eff}\right)^T && (5.204)\\
&= \begin{pmatrix} C_{J_1} + t_{11}^2 C_1 & t_{11}t_{21}C_1 & t_{11}C_1 \\ t_{21}t_{11}C_1 & C_{J_2} + t_{21}^2 C_1 & t_{21}C_1 \\ t_{11}C_1 & t_{21}C_1 & C_1 \end{pmatrix} && (5.205)
\end{aligned}$$

where we noted that $\mathbf{C}_0 = C_1$ and assumed that $\mathbf{C}_J = \begin{pmatrix} C_{J_1} & 0 \\ 0 & C_{J_2} \end{pmatrix}$. We also note that a non-zero $\mathbf{C}_J$ is necessary here to have a non-singular $\mathcal{C}_0$ matrix.

$\mathbf{M}_0$ is given by Eq. (5.152) as

$$\mathbf{M}_0 = \begin{pmatrix} 0 & 0 & 0 \\ 0 & 0 & 0 \\ 0 & 0 & \frac{1}{L_1} \end{pmatrix} \tag{5.206}$$

Noting also $I_{r_1} = I^{(R)}_{\mathbf{T}_1,1}$ we identify by Eq. (5.198)

$$\mathbf{F}^{eff}_{ZC} = \begin{pmatrix} 1 & u_{11} - u_{21}\nu_{12} & u_{12} - u_{22}\nu_{12} \end{pmatrix} \tag{5.207}$$

$\mathbf{F}^{eff}_{ZC}$ is defined by $I_{r_1} = -\mathbf{F}^{eff}_{ZC}\mathbf{I}_C$. We note

$$\mathbf{F}^{eff}_{r_1,C_0} = 1 \tag{5.208}$$

and using Eq. (5.156) and Eqs. (5.203), (5.208) we compute

$$\begin{aligned} \bar{\mathbf{m}}_1 &= \mathcal{F}^{eff}_{C_0}\mathbf{C}_0\left(\mathbf{F}^{eff}_{r_1,C_0}\right)^T && (5.209) \\ &= \begin{pmatrix} t_{11} \\ t_{21} \\ 1 \end{pmatrix} C_1 && (5.210) \end{aligned}$$

Using Eq. (5.158) and (5.208) we compute

$$\begin{aligned} \bar{\mathbf{C}}_{Z,r_1}(\omega) &= - i\omega r_1\left[1 + i\omega r_1 \mathbf{F}^{eff}_{r_1,C_0}\mathbf{C}_0\left(\mathbf{F}^{eff}_{r_1,C_0}\right)^T\right]^{-1} && (5.211) \\ &= -i\omega r_1\left[1 + i\omega r_1 C_1\right]^{-1} && (5.212) \end{aligned}$$

and by Eq. (5.159) we have

$$\begin{aligned} K_1(\omega) &= -\omega^2\bar{\mathbf{C}}_{Z,r_1}(\omega) && (5.213) \\ &= i\omega^2 r_1\left[1 + i\omega r_1 C_1\right]^{-1} && (5.214) \end{aligned}$$

hence by Eq. (5.161) we get the spectral density of the bath due to the resistor r_1 as

$$\begin{aligned} J_1(\omega) &= Im\left[K_1(\omega)\right] && (5.215) \\ &= \frac{r_1\omega^3}{1 + r_1^2 C_1^2\omega^4} && (5.216) \end{aligned}$$

Contribution of r_1 to the loss rate is computed then by using the formula in Eq. (5.162).

To do the dissipation analysis for the last two shunt resistors R_1 and R_2 we first note the following, using Eqs. (5.194), (5.202) and making the partitioning in Eq. (5.144)

$$\mathcal{F}_{C_R}^{eff} = \begin{pmatrix} t_{11}u_{11} + u_{21}\left(t_{12} - t_{11}\nu_{12}\right) & t_{11}u_{12} + u_{22}\left(t_{12} - t_{11}\nu_{12}\right) \\ t_{21}u_{11} + u_{21}\left(t_{22} - t_{21}\nu_{12}\right) & t_{21}u_{12} + u_{22}\left(t_{22} - t_{21}\nu_{12}\right) \\ \left(1 - n_1\right)u_{11} - u_{21}\nu_{12} & \left(1 - n_1\right)u_{12} - u_{22}\nu_{12} \end{pmatrix} \tag{5.217}$$

In Eq. (5.165) $\bar{\mathbf{m}}_{R_1}$ is defined as the first column of $\mathcal{F}_{C_R}^{eff}$ and $\bar{\mathbf{m}}_{R_2}$ is defined as the second column of $\mathcal{F}_{C_R}^{eff}$ so that

$$\bar{\mathbf{m}}_{R_1} = \begin{pmatrix} t_{11}u_{11} + u_{21}\left(t_{12} - t_{11}\nu_{12}\right) \\ t_{21}u_{11} + u_{21}\left(t_{22} - t_{21}\nu_{12}\right) \\ \left(1 - n_1\right)u_{11} - u_{21}\nu_{12} \end{pmatrix} \tag{5.218}$$

and

$$\bar{\mathbf{m}}_{R_2} = \begin{pmatrix} t_{11}u_{12} + u_{22}\left(t_{12} - t_{11}\nu_{12}\right) \\ t_{21}u_{12} + u_{22}\left(t_{22} - t_{21}\nu_{12}\right) \\ \left(1 - n_1\right)u_{12} - u_{22}\nu_{12} \end{pmatrix} \tag{5.219}$$

The spectral densities J_{R_1} and J_{R_2} of the baths due to the resistors R_1 and R_2, respectively, are given by the formula in Eq. (5.168) as

$$J_{R_1}\left(\omega\right) = \frac{\omega}{R_1} \tag{5.220}$$

and

$$J_{R_2}\left(\omega\right) = \frac{\omega}{R_2} \tag{5.221}$$

Contributions of the shunt resistors R_1 and R_2 to the loss rate are then computed using the formula in Eq. (5.169).

5.6.2 3-port data for the 3D-Transmon in Chapter (3.4)

Number of ports $N = 3$, number of stages $M = 12$. Three degenerate stages, namely stages $1, 11, 12$.

$$\mathbf{T}_1 \;=\; \begin{pmatrix} -1.0000 & -0.0001 & -0.0010 \\ 0.0008 & -0.7148 & -0.6993 \\ 0.0007 & 0.6993 & -0.7148 \end{pmatrix} \tag{5.222}$$

j	$r_j\,(\Omega)$	$L_j\,(nH)$	$C_j\,(nF)$	$t_j = 1/n_j$	$\boldsymbol{\nu}_{j,2}$	$\boldsymbol{\nu}_{j,3}$
$1*$	0.0923	0	1.1953×10^{-4}	0	0	0
2	0.0471	7.1890×10^{2}	2.4523×10^{-7}	0.9478	-0.0008	-0.0259
3	0.0973	2.7674	7.7198×10^{-4}	0.0986	-0.0002	0.2050
4	0.1063	2.7113	7.8675×10^{-4}	0.0971	0.0003	-0.0020
5	0.2136	3.0283×10^{3}	1.7701×10^{-7}	0.9915	0.0037	0.0018
6	20.7896	2.7344×10^{2}	1.0464×10^{-6}	0.7657	0.0002	0.3708
7	21.4619	2.7500×10^{2}	1.0416×10^{-6}	0.7508	0	-0.0222
8	26.6330	2.4557×10^{4}	6.2335×10^{-9}	0.9959	9.65×10^{-5}	-2.311×10^{-4}
9	4.7957	4.9851×10^{2}	2.0961×10^{-7}	0.8408	0.0002	0.0122
10	30.5600	4.6115×10^{2}	2.2697×10^{-7}	0.8409	0.0007	-0.0623
$11*$	84.5207	0	2.4178×10^{-7}	0	0	0
$12*$	88.4419	0	2.2673×10^{-7}	0	0	0

$R_1 = 1.0837 \times 10^{7}$, $R_2 = 1.1306 \times 10^{7}$, $R_3 = 7.7537 \times 10^{7}$

Table 5.1: 3-port Brune circuit parameter values for the dataset corresponding to the setup in Figs. (3.13) and (3.14) in Chapter (3.4). Stages marked with $*$ are capactive degenerate stages. We note that in degenerate stages there are no n-type and $\boldsymbol{\nu}$-type transformer couplings.

$$\mathbf{T}_2 = \begin{pmatrix} 0.8933 & -0.0132 & -0.4493 \\ -0.0132 & -0.9999 & 0.0032 \\ -0.4493 & 0.0030 & -0.8934 \end{pmatrix} \tag{5.223}$$

$$\mathbf{T}_3 = \begin{pmatrix} 0.4315 & 0.0060 & -0.9021 \\ 0.0127 & 0.9998 & 0.0127 \\ 0.9020 & -0.0169 & 0.4314 \end{pmatrix} \tag{5.224}$$

$$\mathbf{T}_4 = \begin{pmatrix} 0.0000 & -1.0000 & 0.0030 \\ 1.0000 & 0.0000 & 0.0000 \\ 0.0000 & 0.0030 & 1.0000 \end{pmatrix} \tag{5.225}$$

$$\mathbf{T}_5 = \begin{pmatrix} 0.0000 & 0.4254 & -0.9050 \\ 0.0403 & -0.9043 & -0.4250 \\ -0.9992 & -0.0365 & -0.0171 \end{pmatrix} \tag{5.226}$$

$$\mathbf{T}_6 = \begin{pmatrix} -0.0416 & 0.0024 & -0.9991 \\ 0.9299 & 0.3659 & -0.0378 \\ 0.3655 & -0.9306 & -0.0174 \end{pmatrix} \tag{5.227}$$

$$\mathbf{T}_7 = \begin{pmatrix} -0.0006 & -0.9994 & -0.0342 \\ 1.0000 & -0.0006 & -0.0000 \\ 0.0000 & -0.0342 & 0.9994 \end{pmatrix} \tag{5.228}$$

$$\mathbf{T}_8 = \begin{pmatrix} 0.9975 & 0.0341 & -0.0615 \\ -0.0308 & 0.9981 & 0.0538 \\ 0.0632 & -0.0517 & 0.9967 \end{pmatrix} \tag{5.229}$$

$$\mathbf{T}_9 = \begin{pmatrix} -0.9976 & 0.0011 & -0.0685 \\ 0.0032 & 0.9995 & -0.0299 \\ 0.0685 & -0.0301 & -0.9972 \end{pmatrix} \tag{5.230}$$

$$\mathbf{T}_{10} = \begin{pmatrix} -0.0011 & -0.9999 & -0.0109 \\ 1.0000 & -0.0011 & 0.0003 \\ -0.0003 & -0.0109 & 0.9999 \end{pmatrix} \tag{5.231}$$

$$\mathbf{T}_{11} = \begin{pmatrix} -0.9775 & -0.1067 & -0.1820 \\ -0.1088 & 0.9941 & 0.0015 \\ 0.1808 & 0.0212 & -0.9833 \end{pmatrix} \tag{5.232}$$

$$\mathbf{T}_{12} = \begin{pmatrix} -0.0081 & 0.9876 & -0.1566 \\ -1.0000 & -0.0080 & 0.0013 \\ 0 & 0.1566 & 0.9877 \end{pmatrix} \tag{5.233}$$

$$\mathbf{T}_{13} = \begin{pmatrix} -0.0978 & 0.9951 & -0.0116 \\ 0.9952 & 0.0978 & -0.0001 \\ 0.0011 & -0.0116 & -0.9999 \end{pmatrix} \tag{5.234}$$

We note that all the Belevitch transformer matrices above are orthogonal up to numerical noise.

5.7 Non-reciprocal Brune stage

The multiport Brune's Algorithm described in Chapter (5.3) produces reciprocal stages for a reciprocal impedance response $\mathbf{Z}(s)$. If the response is non-reciprocal the multiport Brune circuit extracted at each stage is slightly modified as shown in Fig. (5.23), [122]. In Fig. (5.23) we see that a multiport gyrator with a gyration vector $\boldsymbol{\gamma}$ is extracted right after the resistance r_1. The circuit symbol for this multiport gyrator is shown in Fig. (5.24). It has a single port on the left and $(N-1)$ ports on the right with the following constitutive relations, [122]:

$$\begin{pmatrix} V_1 \\ \mathbf{V}_2 \end{pmatrix} = \begin{pmatrix} 0 & -\boldsymbol{\gamma}^T \\ \boldsymbol{\gamma} & 0 \end{pmatrix} \begin{pmatrix} I_1 \\ \mathbf{I}_2 \end{pmatrix} \tag{5.235}$$

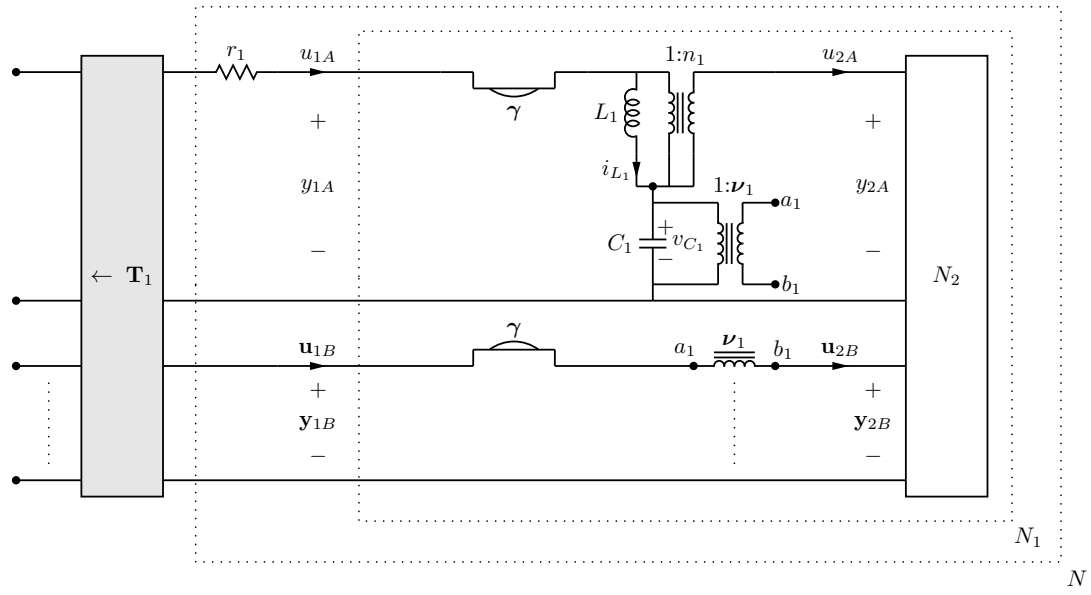

Figure 5.23: Multiport Brune stage circuit in the case of a non-reciprocal response. We observe the appearance of a multiport gyrator coupling the first port to the remaining ports with a gyration vector $\boldsymbol{\gamma}$ as shown in [122].

where V_1, I_1 are the voltage and the current of the left port and $\mathbf{V}_2$, $\mathbf{I}_2$ are vectors of length $(N-1)$ holding the voltages and currents of the ports on the right, respectively.

The network N_1 has the same time-evolution description as in Eq. (5.72). However the input-output relation is slightly different with the appearance of the gyration vector $\boldsymbol{\gamma}$ in the $\mathbf{D}_1$ matrix:

$$\mathbf{D}_1 = \begin{pmatrix} \mathbf{D}_{2AA}/n_1^2 & -\boldsymbol{\gamma}^T + \mathbf{D}_{2AB}/n_1 \\ \boldsymbol{\gamma} + \mathbf{D}_{2BA}/n_1 & \mathbf{D}_{2BB} \end{pmatrix} \tag{5.236}$$

That is $\boldsymbol{\gamma}$ is extracted by taking the anti-symmetric part of $\mathbf{D}_1$.

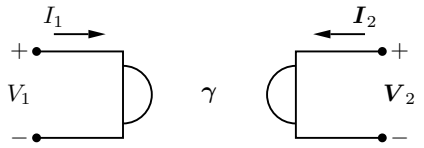

Figure 5.24: The multiport gyrator appearing in the non-reciprocal Brune stage in Fig. (5.23). The gyration ratios are given by the vector $\boldsymbol{\gamma}$.

We note that the quantization of the multiport Brune circuit with gyrators - in the most general non-reciprocal case - is an open problem.

CHAPTER 6

Appendix

6.1 Fidelity Analysis for the Direct Parity Measurement

In this Appendix we will compute fidelities between output signals for the case of a finite bandwidth probe.

We compute the fidelity between output signals corresponding to two different qubit states $|\mathbf{s}\rangle$ and $|\mathbf{s}'\rangle$. We first construct the creation operator $\hat{a}^\dagger_{pulse}$ corresponding to a finite bandwidth probe pulse as a linear combination of a densely spaced, discrete set of harmonic modes $\hat{a}^\dagger_{\omega_i}$ [90]:

$$\hat{a}^\dagger_{pulse} = \sum_i C_i \hat{a}^\dagger_{\omega_i} \tag{6.1}$$

with

$$C_i = \frac{\sqrt{\delta\omega} e^{-(\omega_i-\omega_p)^2/4W^2}}{(2\pi W^2)^{1/4}}, \tag{6.2}$$

where ω_p is the center frequency, W the bandwidth of the probe signal, ω_i is the frequency of mode i, and $\delta\omega$ is the difference between frequencies of successive modes. In the above expression the weight C_i of each term is chosen such that in the limit of a continuum of modes ($\delta\omega \to 0$) the unitarity constraint is satisfied [90]:

$$\sum |C_i|^2 \approx \frac{1}{\sqrt{2\pi W^2}} \int_{-\infty}^{\infty} d\omega e^{-(\omega-\omega_p)^2/2W^2} \tag{6.3}$$

$$= 1 + O(\delta\omega). \tag{6.4}$$

Now we define a coherent state of amplitude α for probe pulse:

$$|\alpha\rangle = e^{-|\alpha|^2/2} e^{\alpha \hat{a}^\dagger_{pulse}} |0\rangle . \tag{6.5}$$

If we define an amplitude α_i for mode i as follows:

$$\alpha_i \equiv \alpha C_i = \alpha \frac{\sqrt{\delta\omega} e^{-(\omega_i-\omega_p)^2/4W^2}}{(2\pi W^2)^{1/4}} \tag{6.6}$$

using the fact

$$\lim_{\delta\omega\to 0} \sum_i |\alpha_i|^2 = |\alpha|^2 \lim_{\delta\omega\to 0} \sum_i |C_i|^2 = |\alpha|^2 \tag{6.7}$$

we can rewrite the coherent probe state $|\alpha\rangle$ in Eq. (6.5) in the continuum modes limit as:

$$\begin{aligned}
|\alpha\rangle &= e^{-|\alpha|^2/2} e^{\alpha \hat{a}^\dagger_{pulse}} |0\rangle && (6.8)\\
&= e^{-\frac{1}{2}\sum_i |\alpha_i|^2} e^{\alpha \sum_i C_i \hat{a}^\dagger_{\omega_i}} |0\rangle && (6.9)\\
&= \prod_i e^{-|\alpha_i|^2/2} e^{\alpha_i \hat{a}^\dagger_{\omega_i}} |0\rangle && (6.10)\\
&= \prod_i |\alpha_i\rangle && (6.11)
\end{aligned}$$

where we have defined a coherent state for each mode i as

$$|\alpha_i\rangle = e^{-|\alpha_i|^2/2} e^{\alpha_i \hat{a}^\dagger_{\omega_i}} |0\rangle . \tag{6.12}$$

Now if the qubits are in state $|\mathbf{s}\rangle$ the coherent component $|\alpha_i\rangle$ of the input probe at frequency ω_i will get a phase shift of $\theta_{\mathbf{s}}(\omega_i)$ and go to the state $\left|\alpha_i e^{i\theta_{\mathbf{s}}(\omega_i)}\right\rangle$. If we call $|\beta_{\mathbf{s}}\rangle$ the state of the output signal when qubits are in state $|\mathbf{s}\rangle$ we can compute the fidelity

$$\begin{aligned}
\mathcal{F} &= \langle \beta_{\mathbf{s}} | \beta_{\mathbf{s}'} \rangle && (6.13)\\
&= \prod_i \left\langle \alpha_i e^{i\theta_{\mathbf{s}}(\omega_i)} | \alpha_i e^{i\theta_{\mathbf{s}'}(\omega_i)} \right\rangle && (6.14)\\
&= \prod_i \exp\left\{ - |\alpha_i|^2 \left(1 - e^{-i(\theta_{\mathbf{s}}(\omega_i) - \theta_{\mathbf{s}'}(\omega_i))}\right)\right\} && (6.15)\\
&= \exp\left\{ -\sum_i |\alpha_i|^2 \left(1 - e^{-i(\theta_{\mathbf{s}}(\omega_i) - \theta_{\mathbf{s}'}(\omega_i))}\right)\right\} . && (6.16)
\end{aligned}$$

Expanding the phases around the center frequency of the probe $\omega_i = \omega_p + \Delta\omega_i$

$$\theta_{\mathbf{s}}(\omega_i) = \theta_{\mathbf{s}}(\omega_p) + \theta'_{\mathbf{s}}(\omega_p)\,\Delta\omega_i + O\left((\Delta\omega_i)^2\right), \tag{6.17}$$

$$\theta_{\mathbf{s}'}(\omega_i) = \theta_{\mathbf{s}'}(\omega_p) + \theta'_{\mathbf{s}'}(\omega_p)\,\Delta\omega_i + O\left((\Delta\omega_i)^2\right). \tag{6.18}$$

Now, we consider the case when **s** and **s'** have the same parity. Then $\theta_{\mathbf{s}}(\omega_p) = \theta_{\mathbf{s}'}(\omega_p) \mod(2\pi)$, and we get to the first order in $\Delta\omega_i$

$$\mathcal{F} = \exp\left\{-\sum_i |\alpha_i|^2 (1 - e^{-ib\Delta\omega_i})\right\} \tag{6.19}$$

where we have defined

$$b \equiv \theta'_{\mathbf{s}}(\omega_p) - \theta'_{\mathbf{s}'}(\omega_p). \tag{6.20}$$

Using the expression for α_i in Eq. (6.6) and taking the limit of continuum of modes the sum in the exponent of the above expression becomes an integral

$$\mathcal{F} = \exp\left\{-\frac{|\alpha|^2}{\sqrt{2\pi W^2}}\int_{-\infty}^{\infty} d\omega e^{-(\omega-\omega_p)^2/2W^2}(1 - e^{-ib(\omega-\omega_p)})\right\} \tag{6.21}$$

$$= \exp\left\{-|\alpha|^2\left(1 - e^{-b^2W^2/2}\right)\right\}. \tag{6.22}$$

If $bW \ll 1$ then $1 - e^{-b^2W^2/2} \simeq \frac{b^2W^2}{2}$ so that

$$\mathcal{F} \simeq e^{-|\alpha|^2 b^2 W^2/2}. \tag{6.23}$$

If we further assume that $|\alpha|\, bW \ll 1$ we get

$$\mathcal{F} \simeq 1 - \frac{|\alpha|^2 b^2 W^2}{2}. \tag{6.24}$$

The fidelity between odd and even states is given by a simpler calculation:

$$\mathcal{F}_{even/odd} = \left\langle \alpha e^{i\theta_{\rm even}} | \alpha e^{i\theta_{\rm odd}} \right\rangle \tag{6.25}$$

$$= e^{-|\alpha|^2(1-\cos\Delta\theta)} \approx e^{-2|\alpha|^2}. \tag{6.26}$$

The final expression is a consequence of the fact that $\Delta\theta \approx \pi$.

Another case we look at, relevant for the alternative scheme of [35], is the case of matching linear dispersion (i.e. $b = 0$) but finite quadratic dispersion mismatch

$$b' \equiv \left.\frac{d^2\theta_{\mathbf{s}}(\omega)}{d\omega^2}\right|_{\omega_p} - \left.\frac{d^2\theta_{\mathbf{s}}(\omega)}{d\omega^2}\right|_{\omega_p}. \tag{6.27}$$

Then the fidelity, for the case of the same parity, is

$$\mathcal{F} = \left| \exp\left\{ -\sum_i |\alpha_i|^2 \left(1 - e^{-ib'(\Delta\omega_i)^2}\right) \right\} \right|. \tag{6.28}$$

Again in the limit of continuum of modes $\mathcal{F}$ becomes

$$\mathcal{F} = \left| \exp\left\{ -\frac{|\alpha|^2}{\sqrt{2\pi W^2}} \int_{-\infty}^{\infty} d\omega e^{-(\omega-\omega_p)^2/2W^2} \left(1 - e^{-ib'(\omega_i-\omega_p)^2}\right) \right\} \right| \tag{6.29}$$

$$= \left| \exp\left\{ -|\alpha|^2 \left(1 - \frac{1}{\sqrt{1+2ib'W^2}}\right) \right\} \right| \tag{6.30}$$

$$= \exp\left\{ Re\left[-|\alpha|^2 \left(1 - \frac{1}{\sqrt{1+2ib'W^2}}\right) \right] \right\} \tag{6.31}$$

$$= \exp\left\{ -|\alpha|^2 \left(1 - \sqrt{\frac{1+\sqrt{1+4b'^2W^4}}{2+8b'^2W^4}}\right) \right\} \tag{6.32}$$

$$\simeq 1 - \frac{3\,|\alpha|^2\, b'^2W^4}{2} + O\left(|\alpha|^4 \left(b'W^2\right)^4\right) \tag{6.33}$$

where we assumed that $b'W^2 \ll 1$ and $|\alpha|\, b'W^2 \ll 1$.

To get an estimate for the power of the measurement signal we assume that the signal contains $|\alpha|^2 = 5$ photons and that it has duration $T = 1\mu s$ so that the peak power P will roughly be $P = \frac{|\alpha|^2 \hbar\omega_p}{T} = -135\, dBm$.

6.2 Review of lumped element circuit quantization methods

In this chapter we will review two formalisms [17, 18] developed for the quantization of the lumped element superconducting circuits. We won't attempt to do a full review of each formalism. We will rather content ourselves with describing how to combine parts of each formalism for the purpose of quantizing Brune circuits. In the following we will refer to [17] as "BKD" and to [18] as "Burkard"; "KCL" stands for Kirchhoff's current law and "KVL" stands for Kirchhoff's voltage law.

Both methods derive classical equations of motions for the lumped element circuits and identify canonical variables. They both start with a graph theoretical analysis by choosing a spanning tree in the circuit to write KCL and KVL relations involving current and voltage variables in the circuit. We will follow the graph analysis done in Burkard. This will allow us to write an equation of motion and to identify the canonical degrees of freedom of the circuit. We will need to make slight modifications to the theory to be able to treat Brune circuits. Once we have the equation of motion, we will interpret it as an equation of motion of BKD to do a dissipation analysis and compute relaxation rates.

6.2.1 Derivation of the equation of motion by Burkard's method

The first step in Burkard is to find a spanning tree containing all the Josephson junctions, voltage sources and impedances in the circuit. One can also put linear inductors in the tree. However there should be no capacitors in the tree so that all capacitors are in the chord branches. Linear inductors are also allowed to be in the chord branches. Burkard assumes that there is no loop containing only Josephson junctions, voltage sources and impedances which is physically justified since in reality each loop would have a finite self-inductance.

With the choice of such a spanning tree we can partition the current and voltage vectors as follows

$$\mathbf{I}_{\text{tr}} = (\mathbf{I}_J, \mathbf{I}_L, \mathbf{I}_V, \mathbf{I}_Z) \tag{6.34}$$

$$\mathbf{V}_{\text{tr}} = (\mathbf{V}_J, \mathbf{V}_L, \mathbf{V}_V, \mathbf{V}_Z) \tag{6.35}$$

$$\mathbf{I}_{\text{ch}} = (\mathbf{I}_{C_J}, \mathbf{I}_C, \mathbf{I}_K) \tag{6.36}$$

$$\mathbf{V}_{\text{ch}} = (\mathbf{V}_{C_J}, \mathbf{V}_C, \mathbf{V}_K) \tag{6.37}$$

where $\mathbf{I}_{\text{tr}}$ and $\mathbf{I}_{\text{ch}}$ are the vectors holding the currents through the tree and chord branches and $\mathbf{V}_{\text{tr}}$ and $\mathbf{V}_{\text{ch}}$ are vectors holding the voltages across the tree and chord branches, respectively. Labels J, L, K, V, Z, C_J, C correspond to Josephson junctions, tree inductors, chord inductors, voltage sources, impedances, Josephson junction capacitances and ordinary capacitances, respectively. In terms of those loop variables Kirchhoff's laws can be written as

$$\mathbf{F}\mathbf{I}_{\text{ch}} = -\mathbf{I}_{\text{tr}} \tag{6.38}$$

$$\mathbf{F}^T\mathbf{V}_{\text{tr}} = \mathbf{V}_{\text{ch}} - \dot{\mathbf{\Phi}}_x \tag{6.39}$$

where we have introduced the loop matrix $\mathbf{F}$ defined in Eq. (3) of Burkard. $\mathbf{\Phi}_x = (\Phi_1, \ldots, \Phi_F)$ is the flux bias vector holding the external fluxes threading F fundamental loops of the circuit, each fundamental loop being defined by a chord branch. The loop matrix $\mathbf{F}$ can be partitioned as

$$\mathbf{F} = \begin{pmatrix} \mathbf{I} & \mathbf{F}_{JC} & \mathbf{F}_{JK} \\ \mathbf{0} & \mathbf{F}_{LC} & \mathbf{F}_{LK} \\ \mathbf{0} & \mathbf{F}_{VC} & \mathbf{F}_{VK} \\ \mathbf{0} & \mathbf{F}_{ZC} & \mathbf{F}_{ZK} \end{pmatrix} \tag{6.40}$$

The first column is due to Josephson junction capacitances C_J's shunting only the Josephson junctions.

Burkard further assumes that the voltage sources and the impedances are not inductively shunted in the sense that

$$\mathbf{F}_{VK} = \mathbf{F}_{ZK} = 0 \tag{6.41}$$

Then by writing KCL for Josephson junctions and tree inductors and KVL for chord capacitors Burkard derives the first-order equation of motion (Eq. (19) in Burkard - we fixed a sign typo)

$$\mathcal{C}\dot{\mathbf{\Phi}} = \mathbf{Q} - \mathbf{C}_V\mathbf{V}_V + \mathcal{F}_C\mathbf{C}_Z * \mathbf{V}_C \tag{6.42}$$

where the vector $\mathbf{\Phi}$ holds the flux degrees of freedom corresponding to the fluxes across the Josephson junctions (J) and tree inductor branches (L)

$$\mathbf{\Phi} = \begin{pmatrix} \mathbf{\Phi}_J \\ \mathbf{\Phi}_L \end{pmatrix} \tag{6.43}$$

with $\mathbf{\Phi}_J = \Phi_0\boldsymbol{\varphi}_J/2\pi$, $\boldsymbol{\varphi}_J$ being the vector of phases across the Josephson junctions. The canonical charge variables are given by the vector $\mathbf{Q}$

$$\mathbf{Q} = -\begin{pmatrix} \mathbf{Q}_J \\ \mathbf{Q}_L \end{pmatrix} - \mathcal{F}_K \mathbf{Q}_K \tag{6.44}$$

with

$$\mathcal{F}_K = \begin{pmatrix} \mathbf{F}_{JK} \\ \mathbf{F}_{LK} \end{pmatrix} \tag{6.45}$$

$$\mathcal{F}_C = \begin{pmatrix} \mathbf{F}_{JC} \\ \mathbf{F}_{LC} \end{pmatrix}$$

and the capacitance matrices in Eq. (6.42) are given by

$$\mathcal{C} = \begin{pmatrix} \mathbf{C}_J & \mathbf{0} \\ \mathbf{0} & \mathbf{0} \end{pmatrix} + \mathcal{F}_C \mathbf{C} \mathcal{F}_C^T \tag{6.46}$$

$$\mathbf{C}_V = \mathcal{F}_C \mathbf{C} \mathbf{F}_{VC}^T \tag{6.47}$$

$$\mathbf{C}_Z(\omega) = (i\omega)\, \mathbf{C} \mathbf{F}_{ZC}^T \mathbf{Z}(\omega)\, \mathbf{F}_{ZC} \mathbf{C} \tag{6.48}$$

where $\mathbf{C}$ is the diagonal matrix of ordinary capacitances in the circuit except Josephson junctions' capacitances such that

$$\mathbf{Q}_C = \mathbf{C} \mathbf{V}_C \tag{6.49}$$

The last term $\mathcal{F}_C \mathbf{C}_Z * \mathbf{V}_C$ in Eq. (6.42) is the dissipative term. This term can also be written in frequency domain as

$$\mathcal{F}_C \mathbf{C}_Z(\omega)\, \mathbf{V}_C = -\mathcal{F}_C \mathbf{C} \mathbf{F}_{ZC}^T \mathbf{Z}(\omega)\, \mathbf{I}_Z \tag{6.50}$$

$\mathbf{I}_Z$ can be written as function of flux degrees of freedom $\mathbf{\Phi}$ and voltage sources $\mathbf{V}_V$ as

$$\begin{aligned} \mathbf{I}_Z &= -(i\omega) \left[\mathbf{I} + (i\omega)\, \mathbf{F}_{ZC} \mathbf{C} \mathbf{F}_{ZC}^T \mathbf{Z}(\omega)\right]^{-1} \mathbf{F}_{ZC} \mathbf{C} \mathcal{F}_C^T \dot{\mathbf{\Phi}} \\ &\quad -(i\omega) \left[\mathbf{I} + (i\omega)\, \mathbf{F}_{ZC} \mathbf{C} \mathbf{F}_{ZC}^T \mathbf{Z}(\omega)\right]^{-1} \mathbf{F}_{ZC} \mathbf{C} \mathbf{F}_{VC}^T \mathbf{V}_V \end{aligned} \tag{6.51}$$

If we define

$$\bar{\mathbf{m}} = \mathcal{F}_C \mathbf{C} \mathbf{F}_{ZC}^T \tag{6.52}$$

$$\bar{\mathbf{m}}_V = \mathbf{F}_{VC} \mathbf{C} \mathbf{F}_{ZC}^T \tag{6.53}$$

and as in Eq. (28) of Burkard

$$\bar{\mathbf{C}}_Z(\omega) = -(i\omega)\,\mathbf{Z}(\omega)\left[\mathbf{I} + (i\omega)\,\mathbf{F}_{ZC}\mathbf{C}\mathbf{F}_{ZC}^T\mathbf{Z}(\omega)\right]^{-1} \tag{6.54}$$

We can rewrite Eq. (6.51) in terms of the newly defined quantities in Eqs. (6.52), (6.53) and (6.54) as

$$\mathbf{I}_Z = \mathbf{Z}^{-1}(\omega)\,\bar{\mathbf{C}}_Z(\omega)\,\bar{\mathbf{m}}^T\dot{\mathbf{\Phi}} + \mathbf{Z}^{-1}(\omega)\,\bar{\mathbf{C}}_Z(\omega)\,\bar{\mathbf{m}}_V^T\mathbf{V}_V \tag{6.55}$$

Replacing the solution for $\mathbf{I}_Z$ in Eq. (6.55) in Eq. (6.50) we get

$$\mathcal{F}_C\mathbf{C}_Z(\omega)\,\mathbf{V}_C = -\bar{\mathbf{m}}\bar{\mathbf{C}}_Z(\omega)\,\bar{\mathbf{m}}^T\dot{\mathbf{\Phi}} - \bar{\mathbf{m}}\bar{\mathbf{C}}_Z(\omega)\,\bar{\mathbf{m}}_V^T\mathbf{V}_V \tag{6.56}$$

Defining also

$$\mathcal{C}_Z(\omega) = \bar{\mathbf{m}}\bar{\mathbf{C}}_Z(\omega)\,\bar{\mathbf{m}}^T \tag{6.57}$$

and

$$\mathcal{C}_V(\omega) = \bar{\mathbf{m}}\bar{\mathbf{C}}_Z(\omega)\,\bar{\mathbf{m}}_V^T \tag{6.58}$$

We can write the dissipative term in Eq. (6.56) in terms of the quantities in Eqs. (6.57) and (6.58) as

$$\mathcal{F}_C\mathbf{C}_Z(\omega)\,\mathbf{V}_C = -\mathcal{C}_Z(\omega)\,\dot{\mathbf{\Phi}} - \mathcal{C}_V(\omega)\,\mathbf{V}_V \tag{6.59}$$

Note that we have extracted an additional non-dissipative term $\mathcal{C}_V(\omega)\,\mathbf{V}_V$ in the equation above.

Plugging the dissipative term in Eq. (6.59) back in the equation of motion in Eq. (6.42) we get in time domain

$$(\mathcal{C} + \mathcal{C}_Z(t)) * \dot{\mathbf{\Phi}} = \mathbf{Q} - (\mathbf{C}_V + \mathcal{C}_V(t)) * \mathbf{V}_V(t) \tag{6.60}$$

Note that the Eq. (6.60) is more general than Burkard's equation of motion in Eq. (25) of [18] since we allow a general voltage source term $\mathbf{V}_V(t)$ with possible frequency components both at DC and AC. The vector $\mathcal{C}_V(t)$ is due to AC components of $\mathbf{V}_V(t)$. In the case of a DC voltage source term $\mathbf{V}_V$, $\mathcal{C}_V(\omega)\,\mathbf{V}_V(\omega) = 0$ for $\omega \neq 0$ and $\mathcal{C}_V(\omega) = 0$ for $\omega = 0$ so we recover Burkard's equation of motion. Eq. (6.60) will lead to the more general Hamiltonian in Eq. (6.83) below.

It is interesting to note here that since the vector $\dot{\mathbf{\Phi}}$ is equal to the vector of voltages across the Josephson junction branches and tree inductors, the factor $(\mathcal{C} + \mathcal{C}_Z(\omega))$ in Eq. (6.42) is an admittance matrix and the Eq. (6.42) is the KCL for the tree branches.

Taking the time derivative of both sides in Eq. (6.60) we obtain

$$(\mathcal{C} + \mathcal{C}_Z) * \ddot{\mathbf{\Phi}} = \dot{\mathbf{Q}} - \dot{\mathcal{C}}_V * \mathbf{V}_V \tag{6.61}$$

Taking the dissipative term $\mathcal{C}_Z * \ddot{\mathbf{\Phi}}$ to the right-hand side by noting the identity

$$\mathcal{C}_Z * \ddot{\mathbf{\Phi}} = \ddot{\mathcal{C}}_Z * \mathbf{\Phi} \tag{6.62}$$

And using the Eq. (29) $\dot{\mathbf{Q}} = -\frac{\partial U}{\partial \mathbf{\Phi}}$ of Burkard with the potential U

$$U(\mathbf{\Phi}) = -\mathbf{L}_J^{-1}\mathbf{cos}\boldsymbol{\varphi} + \frac{1}{2}\mathbf{\Phi}^T\mathbf{M}_0\mathbf{\Phi} + \mathbf{\Phi}^T\mathbf{N}\mathbf{\Phi}_x \tag{6.63}$$

where

$$\mathbf{M}_0 = \mathcal{G}\mathbf{L}_t^{-1}\mathcal{G}^T \tag{6.64}$$

$$\mathbf{N} = \mathcal{G}\mathbf{L}_t^{-1}\begin{pmatrix} 0 & \mathbf{I}_K \end{pmatrix}^T \tag{6.65}$$

with $\mathbf{L}_t^{-1}$ being the inverse inductance matrix such that

$$\begin{pmatrix} \mathbf{I}_L \\ \mathbf{I}_K \end{pmatrix} = \mathbf{L}_t^{-1}\begin{pmatrix} \mathbf{\Phi}_L \\ \mathbf{\Phi}_K \end{pmatrix} \tag{6.66}$$

and

$$\mathcal{G} = \begin{pmatrix} \mathbf{0} & -\mathbf{F}_{JK} \\ \mathbf{I}_L & -\mathbf{F}_{LK} \end{pmatrix} \tag{6.67}$$

we get

$$\mathcal{C} * \ddot{\mathbf{\Phi}} = -\mathbf{I}_c\mathbf{sin}\boldsymbol{\varphi} - \mathbf{M}_0\mathbf{\Phi} - \ddot{\mathcal{C}}_Z * \mathbf{\Phi} - \dot{\mathcal{C}}_V * \mathbf{V}_V - \mathbf{N}\mathbf{\Phi}_x \tag{6.68}$$

where $\mathbf{I}_c = \frac{\Phi_0}{2\pi}\mathbf{L}_J^{-1}$ is the diagonal matrix of critical currents.

6.2.2 Treatment of resistors and relaxation rate calculations using BKD method

Before writing a Hamiltonian for the equation of motion in Eq. (6.68) we have one more step to do. We again need to stretch Burkard theory slightly to include the resistors $\{R_1, \ldots, R_N\}$ shunting the last stage of the multiport Brune circuit in our analysis. The trick we used for that purpose as described in the main text for the one-port Brune circuit was to replace those resistors by capacitors and to make the substitution $C_j \leftarrow \frac{1}{i\omega R_j}$ for $1 \leq j \leq N$ after we obtained the equation of motion. To do a similar analysis for the multiport Brune circuit, here we extend Burkard's method to include chord resistors.

We start by partitioning the matrix $\mathbf{C}$

$$\mathbf{C} = \begin{pmatrix} \mathbf{C}_0 & \mathbf{0} \\ \mathbf{0} & \mathbf{C}_R \end{pmatrix} \tag{6.69}$$

where $\mathbf{C}_0$ and $\mathbf{C}_R$ are diagonal matrices of size $M \times M$ and $N \times N$, respectively. Diagonal entries of $\mathbf{C}_0$ hold the values of ordinary capacitors in the circuit whereas $\mathbf{C}_R$ is an auxiliary matrix which will be substituted later as

$$\mathbf{C}_R \leftarrow (i\omega)^{-1}\,\mathbf{R}^{-1} \tag{6.70}$$

where $\mathbf{R}$ is the $N \times N$ diagonal matrix holding the values of the resistances shunting the last stage

$$\mathbf{R} = \begin{pmatrix} R_1 & & \mathbf{0} \\ & \ddots & \\ \mathbf{0} & & R_N \end{pmatrix} \tag{6.71}$$

We also partition $\mathcal{F}_C$ respecting the partitioning of $\mathbf{C}$ in Eq. (6.69) as follows

$$\mathcal{F}_C = \begin{pmatrix} \mathcal{F}_{C_0} & \mathcal{F}_{C_R} \end{pmatrix} \tag{6.72}$$

where $\mathcal{F}_{C_0}$, $\mathcal{F}_{C_R}$ are submatrices with M and N columns, respectively.

Now we can decompose the capacitance matrix $\mathcal{C}$ in Eq. (6.46) using Eqs. (6.69) and (6.72) as

$$\begin{aligned} \mathcal{C} &= \begin{pmatrix} \mathbf{C}_J & \mathbf{0} \\ \mathbf{0} & \mathbf{0} \end{pmatrix} + \mathcal{F}_C \mathbf{C} \mathcal{F}_C^T && (6.73) \\ &= \begin{pmatrix} \mathbf{C}_J & \mathbf{0} \\ \mathbf{0} & \mathbf{0} \end{pmatrix} + \mathcal{F}_{C_0} \mathbf{C}_0 \mathcal{F}_{C_0}^T + \mathcal{F}_{C_R} \mathbf{C}_R \mathcal{F}_{C_R}^T && (6.74) \\ &= \mathcal{C}_0 + \mathcal{C}_R && (6.75) \end{aligned}$$

where we defined

$$\begin{aligned} \mathcal{C}_0 &= \begin{pmatrix} \mathbf{C}_J & \mathbf{0} \\ \mathbf{0} & \mathbf{0} \end{pmatrix} + \mathcal{F}_{C_0} \mathbf{C}_0 \mathcal{F}_{C_0}^T && (6.76) \\ \mathcal{C}_R &= \mathcal{F}_{C_R} \mathbf{C}_R \mathcal{F}_{C_R}^T && (6.77) \end{aligned}$$

Making the substitution in Eq. (6.70) we get the following dissipative term on left-hand side of the equation of motion in Eq. (6.68)

$$\begin{aligned} \mathcal{C}_R * \ddot{\mathbf{\Phi}} &= \dot{\mathcal{C}}_R * \dot{\mathbf{\Phi}} && (6.78)\\ &= \left(\mathcal{F}_{C_R}\mathbf{R}^{-1}\mathcal{F}_{C_R}^T\right) * \dot{\mathbf{\Phi}} && (6.79)\\ &= \mathcal{R}^{-1}\dot{\mathbf{\Phi}} && (6.80) \end{aligned}$$

where in the first line we used differentiation property of the convolution operator, in the second line we used the Eqs. (6.70) and (6.77) and in the third line we defined

$$\mathcal{R}^{-1} = \mathcal{F}_{C_R}\mathbf{R}^{-1}\mathcal{F}_{C_R}^T \tag{6.81}$$

which is frequency independent, justifying dropping the convolution operator in Eq. (6.80). Now taking the dissipative term in Eq. (6.80) due to the last shunt resistors $\mathbf{R}$ to the right-hand side of the equation of motion in Eq. (6.68) and noting also the decomposition in Eq. (6.75), we re-write the equation of motion (6.68)

$$\mathcal{C}_0 * \ddot{\mathbf{\Phi}} = -\mathbf{I}_c\mathbf{sin}\boldsymbol{\varphi} - \mathcal{R}^{-1}\dot{\mathbf{\Phi}} - \mathbf{M}_0\mathbf{\Phi} - \ddot{\mathcal{C}}_Z * \mathbf{\Phi} - \dot{\mathcal{C}}_V * \mathbf{V}_V - \mathbf{N}\mathbf{\Phi}_x \tag{6.82}$$

Following Burkard we can write the following Hamiltonian for the lossless part of the dynamics described by the Eq. (6.82)

$$\mathcal{H}_S = \frac{1}{2}\left(\mathbf{Q} - \left(\mathbf{C}_V + \mathcal{C}_V\right) * \mathbf{V}_V\left(t\right)\right)^T \mathcal{C}_0^{-1}\left(\mathbf{Q} - \left(\mathbf{C}_V + \mathcal{C}_V\right) * \mathbf{V}_V\left(t\right)\right) + U\left(\mathbf{\Phi}\right) \tag{6.83}$$

A point to note here is that although $\mathbf{C}_V$ defined in Eq. (6.47) is frequency independent, after the substitution in Eq. (6.70) it will acquire frequency dependence which we will analyze further down below in Chapter (6.2.3).

Comparing again the equation motion in Eq. (61) of BKD with the Eq. (6.82) above we identify

$$\mathbf{R}_{BKD}^{-1} \leftrightarrow \mathcal{R}^{-1} \tag{6.84}$$

where $\mathbf{R}_{BKD}$ is now the resistivity matrix defined in Eq. (25) of BKD. We note however that $\mathbf{R}_{BKD}^{-1}$ is diagonal whereas $\mathcal{R}^{-1}$ is in general non-diagonal.

To compute the contribution of the shunt resistor R_j alone to the relaxation rate we set $R_k = \infty$ for $1 \leq k \leq N$ and $k \neq j$ to write the term $\mathcal{R}^{-1}\dot{\mathbf{\Phi}}$ in the equation of motion in Eq. (6.82) in the frequency domain as

$$\left(i\omega\right)\mathcal{R}^{-1}\mathbf{\Phi}\big|_{R_k\to\infty, k\neq j} = \left(i\omega\right)R_j^{-1}\mathcal{F}_{R_j,C_R}\mathcal{F}_{R_j,C_R}^T\mathbf{\Phi} \tag{6.85}$$

where $\mathcal{F}_{R_j,C_R}$ is the j^{th} column of the matrix $\mathcal{F}_{C_R}$ corresponding to the resistor R_j (or the capacitor C_{R_j}). Comparing now

$$\mathbf{M}_d(\omega) \leftrightarrow (i\omega) R_j^{-1} \mathcal{F}_{R_j,C_R} \mathcal{F}_{R_j,C_R}^T \tag{6.86}$$

where $\mathbf{M}_d(\omega)$ is the dissipation matrix defined in Eq. (72)-(75) of BKD we identify the coupling vector

$$\bar{\mathbf{m}}_{R_j} = \mathcal{F}_{R_j,C_R} \tag{6.87}$$

and the dissipation kernel is given by

$$K_{R_j}(\omega) = \frac{i\omega}{R_j} \tag{6.88}$$

Using Eq. (93) of BKD we define the spectral density of the bath corresponding to the resistor R_j as (correcting the sign and dropping the scale factor)

$$\begin{aligned} J_{R_j}(\omega) &= \operatorname{Im}\left[K_{R_j}(\omega)\right] && (6.89)\\ &= \frac{\omega}{R_j} && (6.90) \end{aligned}$$

Hence the contribution of R_j to the relaxation rate is given by the formula in Eq. (124) of BKD as

$$\frac{1}{T_{1,R_j}} = \frac{4}{\hbar} \left|\left\langle 0 \left| \bar{\mathbf{m}}_{R_j} \cdot \mathbf{\Phi} \right| 1 \right\rangle\right|^2 J_{R_j}(\omega_{01}) \coth\left(\frac{\hbar\omega_{01}}{2k_B T}\right) \tag{6.91}$$

where ω_{01} is the qubit frequency. Here we used flux variable $\mathbf{\Phi}$ and $\bar{\mathbf{m}}_{R_j}$ since we dropped the scale factor in Eq. (6.114) (BKD uses phase variable $\boldsymbol{\varphi}$ and the normalized vector $\mathbf{m}$).

We need to also consider the effect of last shunt resistors on the matrices $\ddot{\mathcal{C}}_Z$ and $\dot{\mathcal{C}}_V$ appearing in the equation of motion in Eq. (6.82) above. For this we first make the following partitioning for the matrix $\mathbf{F}_{ZC}$

$$\mathbf{F}_{ZC} = \begin{pmatrix} \mathbf{F}_{ZC_0} & \mathbf{F}_{ZC_R} \end{pmatrix} \tag{6.92}$$

where the submatrices $\mathbf{F}_{ZC_0}$ and $\mathbf{F}_{ZC_R}$ have M and N columns, respectively.

Then using also the partitioning in Eq. (6.69) and the substitution Eq. (6.70) we can re-write the matrix $\bar{\mathbf{C}}_Z(\omega)$ defined in Eq. (6.54) as $\bar{\mathbf{C}}_{Z,R}(\omega)$

$$\begin{aligned} \bar{\mathbf{C}}_{Z,R}(\omega) &= \bar{\mathbf{C}}_Z(\omega)\big|_{\mathbf{C}_R \leftarrow (i\omega)^{-1}\mathbf{R}^{-1}} && (6.93)\\ &= -(i\omega)\mathbf{Z}_R(\omega)\left[\mathbf{I} + (i\omega)\mathbf{F}_{ZC_0}\mathbf{C}_0\mathbf{F}_{ZC_0}^T\mathbf{Z}_R(\omega)\right]^{-1} && (6.94) \end{aligned}$$

where we have defined

$$\mathbf{Z}_R(\omega) = \mathbf{Z}\left[\mathbf{I} + \mathbf{F}_{ZC_R}\mathbf{R}^{-1}\mathbf{F}_{ZC_R}^T\mathbf{Z}\right]^{-1} \tag{6.95}$$

with

$$\mathbf{Z} = \begin{pmatrix} r_1 & & \mathbf{0} \\ & \ddots & \\ \mathbf{0} & & r_M \end{pmatrix} \tag{6.96}$$

being the diagonal matrix of in-series resistances $r_1, \ldots, r_M$ in the circuit.

Since we will consider resistors one at a time we will take the limit $\mathbf{R} \to \infty$ (which corresponds to open circuiting the last stage in the Brune circuit) in Eq. (6.95) above to define

$$\begin{aligned} \bar{\mathbf{C}}_{Z,r}(\omega) &= \bar{\mathbf{C}}_{Z,R}(\omega)\big]_{\mathbf{R}\to\infty} && (6.97) \\ &= -(i\omega)\,\mathbf{Z}\left[\mathbf{I} + (i\omega)\,\mathbf{F}_{ZC_0}\mathbf{C}_0\mathbf{F}_{ZC_0}^T\mathbf{Z}\right]^{-1} && (6.98) \end{aligned}$$

We will see later below that $\bar{\mathbf{C}}_{Z,r}(\omega)$ is proportional to the dissipation kernel due to in-series resistors.

We need to also update the coupling matrix $\bar{\mathbf{m}}$ defined in Eqs. (6.52) above to account for the effect of shunt resistors on the terms due to in-series resistors. First we again make a partitioning

$$\mathcal{F}_C = \begin{pmatrix} \mathcal{F}_{C_0} & \mathcal{F}_{C_R} \end{pmatrix} \tag{6.99}$$

Then using this partitioning and Eqs. (6.52), (6.69), (6.70) and (6.92) we can write the decomposition

$$\bar{\mathbf{m}} = \bar{\mathbf{m}}_0 + \bar{\mathbf{m}}_R(\omega) \tag{6.100}$$

where we defined

$$\bar{\mathbf{m}}_0 = \mathcal{F}_{C_0}\mathbf{C}_0\mathbf{F}_{ZC_0}^T \tag{6.101}$$

$$\bar{\mathbf{m}}_R(\omega) = (i\omega)^{-1}\,\mathcal{F}_{C_R}\mathbf{R}^{-1}\mathbf{F}_{ZC_R}^T \tag{6.102}$$

Here, however, we will only use the zeroth order term in Eq. (6.101) to define

$$\mathcal{C}_{Z,r}(\omega) = \bar{\mathbf{m}}_0\bar{\mathbf{C}}_{Z,r}(\omega)\,\bar{\mathbf{m}}_0^T \tag{6.103}$$

Note that the frequency dependent factors $(i\omega)^{-1}$ appearing in higher orders terms due to the coupling matrix $\bar{\mathbf{m}}_R(\omega)$ in Eq. (6.102) above can be absorbed in the corresponding $\bar{\mathbf{C}}_Z(\omega)$ matrices if one wants to investigate higher order effects.

Comparing Eq. (6.82) with the equation of motion of BKD (Eq. (61) in [17]) we make the following identification

$$\mathbf{M}_d \leftrightarrow \ddot{\mathcal{C}}_{Z,r} \tag{6.104}$$

$$\mathbf{M}_d(\omega) \leftrightarrow -\omega^2 \mathcal{C}_{Z,r}(\omega) \tag{6.105}$$

where on the left we have the dissipation matrix defined in BKD and on the right we have the dissipation matrix appearing in Eq. (6.82). The capacitance matrix $\mathcal{C}_0$ in Eq. (6.82) maps directly to the capacitance matrix $\mathbf{C}$ in BKD and the stiffness matrices $\mathbf{M}_0$ appearing in Eq. (6.82) and BKD map to each other.

To do a dissipation analysis we will treat the Eq. (6.82) as an equation of motion of BKD and we will do a Caldeira-Leggett analysis using the identification in Eq. (6.105). By Eq. (64) in BKD we have

$$\mathbf{M}_d(\omega) = \bar{\mathbf{m}} \bar{\mathbf{L}}_Z^{-1}(\omega) \bar{\mathbf{m}}^T \tag{6.106}$$

And by Eq. (6.103)

$$\mathcal{C}_{Z,r}(\omega) = \bar{\mathbf{m}}_0 \bar{\mathbf{C}}_{Z,r}(\omega) \bar{\mathbf{m}}_0^T \tag{6.107}$$

Hence by using Eq. (6.105) we further identify

$$\bar{\mathbf{L}}_Z^{-1}(\omega) \leftrightarrow -\omega^2 \bar{\mathbf{C}}_{Z,r}(\omega) \tag{6.108}$$

Coupling matrices $\bar{\mathbf{m}}$ and $\bar{\mathbf{m}}_0$ map to each other directly

$$\bar{\mathbf{m}} \leftrightarrow \bar{\mathbf{m}}_0 \tag{6.109}$$

To compute the contribution of each resistor to the relaxation rate $1/T_1$ we will treat each resistor seperately. In that case by Eq. (73) in BKD we have

$$K(\omega) = \bar{\mathbf{L}}_Z^{-1}(\omega) \tag{6.110}$$

where $K(\omega)$ is a scalar. Hence by Eq. (6.108) we get

$$K_j(\omega) = -\omega^2 \bar{\mathbf{C}}_{Z,r_j}(\omega) \tag{6.111}$$

for the equation of motion in Eq. (6.82), where we defined

$$\bar{\mathbf{C}}_{Z,r_j}(\omega) = \bar{\mathbf{C}}_{Z,r}(\omega)\big|_{r_k=0,\, for\, k\neq j} \tag{6.112}$$

$$= -i\omega r_j \left[1 + i\omega r_j \mathbf{F}_{r_j,C_0} \mathbf{C}_0 \mathbf{F}^T_{r_j,C_0}\right]^{-1} \tag{6.113}$$

where $\mathbf{F}_{r_j,C_0}$ is the j^{th} row of the matrix $\mathbf{F}_{ZC_0}$ defined in Eq. (6.92). We note that $\bar{\mathbf{C}}_{Z,r_j}(\omega)$ is a scalar. That is we are treating only the in-series resistor r_j by short circuiting the other in-series resistors setting $r_k = 0$ for $k \neq j$. Note that shunt resistors $\mathbf{R}$ are already open circuited by taking the limit of $\mathbf{R} \to \infty$ in the definition of $\bar{\mathbf{C}}_{Z,r}(\omega)$ in Eq. (6.97). We also define the coupling vector $\bar{\mathbf{m}}_j$ of the bath due to the resistor r_j to the circuit degrees of freedom by taking the j^{th} column of the coupling matrix $\bar{\mathbf{m}}_0$ in Eq. (6.107).

Using Eq. (93) of BKD we define the spectral density of the bath corresponding to the resistor r_j as (again correcting the sign and dropping the scale factor)

$$J_j(\omega) = \mathrm{Im}\left[K_j(\omega)\right] \tag{6.114}$$

We can now write the contribution of the resistor r_j to the relaxation rate using the formula in Eq. (124) of BKD as

$$\frac{1}{T_{1,r_j}} = \frac{4}{\hbar} \left|\langle 0 \left|\bar{\mathbf{m}}_j \cdot \mathbf{\Phi}\right| 1\rangle\right|^2 J_j(\omega_{01}) \coth\left(\frac{\hbar\omega_{01}}{2k_B T}\right) \tag{6.115}$$

where ω_{01} is the qubit frequency. Here we again used flux variable $\mathbf{\Phi}$ and $\bar{\mathbf{m}}_j$ since we dropped the scale factor in Eq. (6.114).

6.2.3 Analysis of voltage source couplings

Now we will update the $\mathbf{C}_V$ and the $\mathcal{C}_V$ matrices to account for the effect of the resistors $\mathbf{R}$ shunting the last Brune stage. Making first the partitioning

$$\mathbf{F}_{VC} = \begin{pmatrix} \mathbf{F}_{VC_0} & \mathbf{F}_{VC_R} \end{pmatrix} \tag{6.116}$$

Then using the definition for $\mathbf{C}_V$ in Eq. (6.47) together with partitionings (6.69), (6.99) and (6.116) we can decompose $\mathbf{C}_V$ as

$$\mathbf{C}_V = \mathbf{C}_{V,0} + \mathbf{C}_{V,R}(\omega) \tag{6.117}$$

where we have defined

$$\mathbf{C}_{V,0} = \mathcal{F}_{C_0} \mathbf{C}_0 \mathbf{F}^T_{VC_0} \tag{6.118}$$

and

$$\mathbf{C}_{V,R}(\omega) = (i\omega)^{-1} \mathcal{F}_{C_R} \mathbf{R}^{-1} \mathbf{F}_{VC_R}^T \tag{6.119}$$

We note the frequency dependence of $\mathbf{C}_{V,R}$.

A similar analysis can be done also for the $\bar{\mathbf{m}}_V$ matrix defined in Eq. (6.53). Then again using the partitioning in Eq. (6.116) and Eqs. (6.53), (6.69), (6.70) and (6.92) we can write the decomposition

$$\bar{\mathbf{m}}_V = \bar{\mathbf{m}}_{V,0} + \bar{\mathbf{m}}_{V,R}(\omega) \tag{6.120}$$

where we defined

$$\bar{\mathbf{m}}_{V,0} = \mathbf{F}_{VC_0} \mathbf{C}_0 \mathbf{F}_{ZC_0}^T \tag{6.121}$$

$$\bar{\mathbf{m}}_{V,R}(\omega) = (i\omega)^{-1} \mathbf{F}_{VC_R} \mathbf{R}^{-1} \mathbf{F}_{ZC_R}^T \tag{6.122}$$

Now using the definition for $\mathcal{C}_V$ in Eq. (6.58) together with the decompositions Eq. (6.100), (6.120) and the updated $\bar{\mathbf{C}}_Z(\omega)$ defined as $\bar{\mathbf{C}}_{Z,R}(\omega)$ in Eq. (6.93) we can re-write $\mathcal{C}_V$ as

$$\begin{aligned} \mathcal{C}_V(\omega) &= \bar{\mathbf{m}}\, \bar{\mathbf{C}}_Z(\omega)\big|_{\mathbf{C}_R \leftarrow (i\omega)^{-1}\mathbf{R}^{-1}} \bar{\mathbf{m}}_V^T & (6.123)\\ &= (\bar{\mathbf{m}}_0 + \bar{\mathbf{m}}_R(\omega))\, \bar{\mathbf{C}}_{Z,R}(\omega) \left(\bar{\mathbf{m}}_{V,0} + \bar{\mathbf{m}}_{V,R}(\omega)\right)^T & (6.124) \end{aligned}$$

Unlike the dissipation matrix $\mathcal{C}_Z$ we will keep the full expression for the term $\mathcal{C}_V(\omega)$ since it is not a dissipative term. However we will combine the frequency dependent term $\mathbf{C}_{V,R}(\omega)$ defined in Eq. (6.119) with $\mathcal{C}_V(\omega)$ in Eq. (6.124) to define

$$\mathcal{C}_{V,R}(\omega) = \mathbf{C}_{V,R}(\omega) + \mathcal{C}_V(\omega) \tag{6.125}$$

Using the matrices defined in Eq. (6.103) and (6.125) above we write again the equation of motion in Eq. (6.82) as

$$\mathcal{C}_0 * \ddot{\mathbf{\Phi}} = -\mathbf{I}_c \mathbf{sin}\boldsymbol{\varphi} - \mathcal{R}^{-1}\dot{\mathbf{\Phi}} - \mathbf{M}_0\mathbf{\Phi} - \ddot{\mathcal{C}}_{Z,r} * \mathbf{\Phi} - \dot{\mathcal{C}}_{V,R} * \mathbf{V}_V - \mathbf{N}\mathbf{\Phi}_x \tag{6.126}$$

The Hamiltonian of the system described by the equation of motion in Eq. (6.126) is given by

$$\mathcal{H}_S = \frac{1}{2}\left[\mathbf{Q} - (\mathbf{C}_{V,0} + \mathcal{C}_{V,R}(t)) * \mathbf{V}_V(t)\right]^T \mathcal{C}_0^{-1} \left[\mathbf{Q} - (\mathbf{C}_{V,0} + \mathcal{C}_{V,R}(t)) * \mathbf{V}_V(t)\right] + U(\mathbf{\Phi}) \tag{6.127}$$

This time-dependent Hamiltonian is the extension of the Hamiltonian given in Eq. (36) of Burkard to a time-dependent voltage source vector $\mathbf{V}_V(t)$.

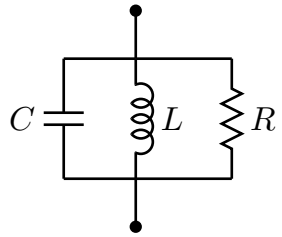

Figure 6.1: Generic shunt resonant stage in lossy Foster circuit

6.3 Lossy Foster Method

Foster's Theorem can be extended to responses with small loss [93]. We start with the partial fraction expansion for $Z(s)$

$$Z(s) = \sum_k \frac{R_k}{s - s_k} \tag{6.128}$$

where R_k's are residues and s_k's are poles. Residues and poles come in complex conjugate pairs. If we define

$$s_k = \xi_k + j\omega_k \tag{6.129}$$
$$R_k = a_k + jb_k \tag{6.130}$$

Collecting terms corresponding to conjugate pairs

$$Z_k(s) = \frac{R_k}{s-s_k} + \frac{R_k^*}{s-s_k^*} \tag{6.131}$$
$$= 2\frac{a_k s - (a_k\xi_k + b_k\omega_k)}{s^2 - 2\xi_k s + \xi_k^2 + \omega_k^2} \tag{6.132}$$

One can show that for physical circuits with small loss ξ_k and b_k are both small quantities [94]. Hence we can approximately write

$$Z_k(s) \cong \frac{2a_k s}{s^2 - 2\xi_k s + \omega_k^2} \tag{6.133}$$

The impedance function of the shunt-resonant circuit as depicted in Fig. (6.1) is

$$Z(s) = \frac{\frac{\omega_0 R}{Q} s}{s^2 + \frac{\omega_0}{Q} s + \omega_0^2} \tag{6.134}$$

with

$$\omega_0^2 = \frac{1}{LC} \tag{6.135}$$

$$Q = \omega_0 RC \tag{6.136}$$

Hence we see that we can realize the function $Z_k(s)$ in Eq. (6.133) by a circuit as in Fig. (6.1) with

$$R = -a_k/\xi_k \tag{6.137}$$

$$\omega_0 = \omega_k \tag{6.138}$$

$$Q = -\omega_k/2\xi_k \tag{6.139}$$

and the impedance in Eq. (6.128) can be realized as in Fig. (6.2) by a series connection of stages in Fig. (6.1).

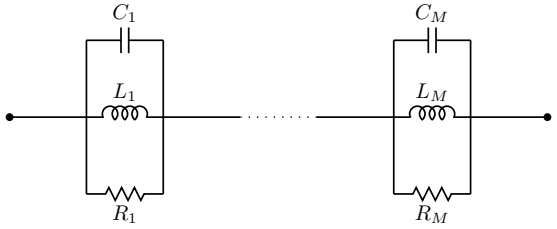

Figure 6.2: Lossy Foster Circuit

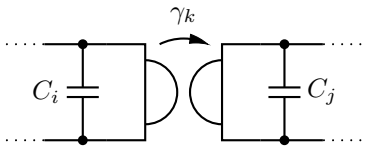

Figure 6.3: A gyrator shunted by tree capacitors C_i and C_j connected to the rest of the circuit. To treat a circuit that contains such an arrangement in the BKD formalism [17] we should assume that there exists a tree which contains the capacitors C_i and C_j and none of the gyrator branches.

6.4 Treatment of capacitor shunted gyrators in BKD formalism

In this section we show how to deal with gyrators in BKD formalism [17]. We assume that every gyrator in the circuit is shunted by two tree capacitors at both of its ports as shown in Fig. (6.3). We also assume that it is possible to choose a tree that contains all the capacitors in the circuit including C_i and C_j and that contains none of the gyrator branches. We will treat gyrator branches as resistive branches. Such a treatment will give us an anti-symmetric resistance matrix $\mathbf{G}$ with $\mathbf{G}_{ij} = \gamma_k$ and $\mathbf{G}_{ji} = -\gamma_k$ to be compared to the resistance matrix $\mathbf{R}$ in the equation of motion Eq. (61) of BKD [17]

$$\mathbf{G} \leftrightarrow \mathbf{R} \tag{6.140}$$

Note that we can assume that the matrix $\mathbf{R}$ corresponds only to gyrator branches such that $\mathbf{R} = \mathbf{G}$ since as noted in BKD [17] one can absorb pure resistances into the dissipation matrix $\mathbf{M}_d$. We will then have the gyration term $-\mathbf{G}^{-1}\dot{\varphi}$ in the equation of motion which will correspond to an additional term $\frac{1}{2}\left(\frac{\Phi_0}{2\pi}\right)^2 \dot{\boldsymbol{\varphi}}^T \mathbf{G}^{-1}\boldsymbol{\varphi}$ in the Lagrangian in Eq. (76) of BKD [17] such that

$$\mathcal{L}_0 = \left(\frac{\Phi_0}{2\pi}\right)^2 \left(\frac{1}{2}\dot{\boldsymbol{\varphi}}^T \mathbf{C}\dot{\boldsymbol{\varphi}} + \frac{1}{2}\dot{\boldsymbol{\varphi}}^T \mathbf{G}^{-1}\boldsymbol{\varphi} - U(\boldsymbol{\varphi})\right) \tag{6.141}$$

and a shift of $-\frac{1}{2}\left(\frac{\Phi_0}{2\pi}\right)\mathbf{G}^{-1}\boldsymbol{\varphi}$ in the momentum in the Hamiltonian in Eq. (78) of BKD [17] such that

$$\mathcal{H}_S = \frac{1}{2}\left(\mathbf{Q}_C - \frac{1}{2}\left(\frac{\Phi_0}{2\pi}\right)\mathbf{G}^{-1}\boldsymbol{\varphi}\right)^T \mathbf{C}^{-1}\left(\mathbf{Q}_C - \frac{1}{2}\left(\frac{\Phi_0}{2\pi}\right)\mathbf{G}^{-1}\boldsymbol{\varphi}\right) + \left(\frac{\Phi_0}{2\pi}\right)^2 U(\boldsymbol{\varphi}) \tag{6.142}$$

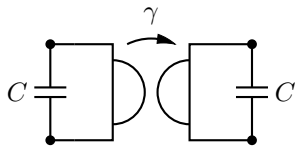

Figure 6.4: A gyrator shunted by two capacitors of the same value C whose Hamiltonian is equivalent to the Hamiltonian of an electron in a uniform magnetic field.

This is to be compared to the Hamiltonian of an electron in a uniform magnetic field; recall

$$\mathcal{H}_e = \frac{1}{2m_e}\left(\mathbf{p} - e\mathbf{A}\left(\mathbf{r}\right)\right)^T\left(\mathbf{p} - e\mathbf{A}\left(\mathbf{r}\right)\right) + \mathbf{V}\left(\mathbf{r}\right) \tag{6.143}$$

where m_e and e are the mass and charge of an electron, respectively and $\mathbf{V}\left(\mathbf{r}\right)$ and $\mathbf{A}\left(\mathbf{r}\right)$ are electric and vector potentials, respectively.

For a magnetic field $\mathbf{B} = B_z\hat{\mathbf{z}}$ in the z-direction we can choose the vector potential $\mathbf{A}\left(\mathbf{r}\right) = -\frac{1}{2}B_z y\hat{\mathbf{x}} + \frac{1}{2}B_z x\hat{\mathbf{y}}$ such that $\mathbf{B} = \nabla \times \mathbf{A}$. Hence $\mathbf{A}\left(\mathbf{r}\right) = -\frac{1}{2}B_z\begin{pmatrix} 0 & 1 \\ -1 & 0 \end{pmatrix}\mathbf{r}$. If we also assume a zero electric potential $\mathbf{V}\left(\mathbf{r}\right) = 0$ then the Hamiltonian in Eq. (6.143) is equivalent to the Hamiltonian of the circuit in Fig. (6.4).

The circuit in Fig. (6.4) has the Hamiltonian

$$\mathcal{H}_s = \frac{1}{2}\left(\mathbf{Q}_C - \frac{1}{2}\left(\frac{\Phi_0}{2\pi}\right)\mathbf{G}^{-1}\boldsymbol{\varphi}\right)^T\mathbf{C}^{-1}\left(\mathbf{Q}_C - \frac{1}{2}\left(\frac{\Phi_0}{2\pi}\right)\mathbf{G}^{-1}\boldsymbol{\varphi}\right) \tag{6.144}$$

with $\mathbf{C} = \begin{pmatrix} C & 0 \\ 0 & C \end{pmatrix}$ and $\mathbf{G} = \begin{pmatrix} 0 & \gamma \\ -\gamma & 0 \end{pmatrix}$. Hence if we make the correspondence for the canonical variables

$$\mathbf{Q}_C \;\leftrightarrow\; \mathbf{p} \tag{6.145}$$

$$\left(\frac{\Phi_0}{2\pi}\right)\boldsymbol{\varphi} \;\leftrightarrow\; \mathbf{r} \tag{6.146}$$

then we can relate

$$C \;\leftrightarrow\; m_e \tag{6.147}$$

$$\gamma^{-1} \;\leftrightarrow\; eB_z \tag{6.148}$$

6.5 Derivation of the effective Kirchhoff's voltage law

6.5.1 Effective Kirchhoff's voltage law for the one-port state-space Brune circuit

Here we present the effective Kirchhoff analysis for the Kirchhoff's voltage law for the one-port state-space Brune circuit in Fig. (4.4). The treatment here will be along similar lines with the analysis we did in Chapter (4.3) to get the effective Kirchhoff's current law.

We start by writing the Kirchhoff's voltage law for the circuit in Fig. (4.4)

$$\mathbf{F}^{\mathrm{T}}\mathbf{V}_{\mathrm{tr}} = \mathbf{V}_{\mathrm{ch}}$$

where the voltages are partitioned as

$$\mathbf{V}_{\mathrm{tr}} = \left(V_J, \mathbf{V}_L, \mathbf{V}_Z, \mathbf{V}_T^{(tr)}\right) \tag{6.149}$$

$$\mathbf{V}_{\mathrm{ch}} = \left(\mathbf{V}_C, \mathbf{V}_T^{(ch)}\right) \tag{6.150}$$

and the loop matrix matrix $\mathbf{F}^{\mathrm{T}}$ is partitioned by Eq. (4.68) as

$$\mathbf{F}^{T} = \begin{pmatrix} \mathbf{F}_{JC}^{T} & \mathbf{F}_{LC}^{T} & \mathbf{F}_{ZC}^{T} & \mathbf{F}_{TC}^{T} \\ \mathbf{F}_{JT}^{T} & \mathbf{F}_{LT}^{T} & \mathbf{F}_{ZT}^{T} & \mathbf{F}_{TT}^{T} \end{pmatrix}$$

We will show that we can get an effective Kirchhoff's voltage law

$$\left(\mathbf{F}^{\mathrm{T}}\right)^{eff}\mathbf{V}_{\mathrm{tr}}^{eff} = \mathbf{V}_{\mathrm{ch}}^{eff}$$

for some effective loop matrix $\left(\mathbf{F}^{\mathrm{T}}\right)^{eff}$ partitioned as

$$\left(\mathbf{F}^{\mathrm{T}}\right)^{eff} = \begin{pmatrix} \left(\mathbf{F}_{JC}^{T}\right)^{eff} & \left(\mathbf{F}_{LC}^{T}\right)^{eff} & \left(\mathbf{F}_{ZC}^{T}\right)^{eff} \end{pmatrix}$$

by eliminating the transformer branches' voltage variables

$$\mathbf{V}_{\mathrm{tr}}^{eff} = (V_J, \mathbf{V}_L, \mathbf{V}_Z) \tag{6.151}$$

$$\mathbf{V}_{\mathrm{ch}}^{eff} = \mathbf{V}_C \tag{6.152}$$

First we note the following in the circuit in Fig. (4.4)

$$\mathbf{V}_T^{(ch)} = -\mathbf{V}_L \tag{6.153}$$

Hence by the transformer voltage relations we have

$$\begin{aligned} \mathbf{V}_T^{(tr)} &= \mathbf{N}\mathbf{V}_T^{(ch)} && (6.154)\\ &= - \mathbf{N}\mathbf{V}_L && (6.155) \end{aligned}$$

where $\mathbf{N}$ is the diagonal turns ratio matrix defined in Eq. (4.79).

Now writing voltages of the chord capacitors as a function of voltages of tree branches in the circuit in Fig. (4.4) we get

$$\mathbf{V}_C = \mathbf{F}_{JC}^T V_J + \mathbf{F}_{LC}^T \mathbf{V}_L + \mathbf{F}_{ZC}^T \mathbf{V}_Z + \mathbf{F}_{TC}^T \mathbf{V}_T^{(tr)} \tag{6.156}$$

with

$$\mathbf{F}_{JC}^T = \begin{pmatrix} 1 \\ \vdots \\ 1 \end{pmatrix} \tag{6.157}$$

$$\mathbf{F}_{LC}^T = \begin{pmatrix} 1 & & & \\ 1 & 1 & \mathbf{0} & \\ \vdots & \vdots & \ddots & \\ 1 & 1 & \cdots & 1 \\ 1 & 1 & \cdots & 1 \end{pmatrix} \tag{6.158}$$

$$\mathbf{F}_{ZC}^T = \begin{pmatrix} 1 & & & \\ 1 & 1 & \mathbf{0} & \\ \vdots & \vdots & \ddots & \\ 1 & 1 & \cdots & 1 \\ 1 & 1 & \cdots & 1 \end{pmatrix} \tag{6.159}$$

$$\mathbf{F}_{TC}^T = \begin{pmatrix} 0 & & \mathbf{0} \\ 1 & \ddots & \\ \vdots & \ddots & 0 \\ 1 & \cdots & 1 \end{pmatrix} \tag{6.160}$$

where $\mathbf{F}_{JC}^T$ is a vector of length $(M+1)$ and $\mathbf{F}_{LC}^T$, $\mathbf{F}_{ZC}^T$, $\mathbf{F}_{TC}^T$ are matrices of size $(M+1) \times M$.

Using Eqs. (6.155) and 6.156 we get

$$\mathbf{V}_C = \mathbf{F}_{JC}^T V_J + (\mathbf{F}_{LC}^T - \mathbf{F}_{TC}^T \mathbf{N})\mathbf{V}_L + \mathbf{F}_{ZC}^T \mathbf{V}_Z \tag{6.161}$$

from which we conclude

$$\left(\mathbf{F}_{JC}^{T}\right)^{eff} = \mathbf{F}_{JC}^{T} \tag{6.162}$$
$$\left(\mathbf{F}_{LC}^{T}\right)^{eff} = \mathbf{F}_{LC}^{T} - \mathbf{F}_{TC}^{T}\mathbf{N} \tag{6.163}$$
$$\left(\mathbf{F}_{ZC}^{T}\right)^{eff} = \mathbf{F}_{ZC}^{T} \tag{6.164}$$

and the effective Kirchhoff's voltage law

$$\left(\mathbf{F}^{T}\right)^{eff}\mathbf{V}_{\mathrm{tr}}^{eff} = \mathbf{V}_{\mathrm{ch}}^{eff} \tag{6.165}$$

Comparing above Eqs. (6.162)-(6.164) with (4.84), (4.86) and (4.89) of Section (4.3) we conclude

$$\left(\mathbf{F}_{JC}^{T}\right)^{eff} = \left(\mathbf{F}_{JC}^{eff}\right)^{T} \tag{6.166}$$
$$\left(\mathbf{F}_{LC}^{T}\right)^{eff} = \left(\mathbf{F}_{LC}^{eff}\right)^{T} \tag{6.167}$$
$$\left(\mathbf{F}_{ZC}^{T}\right)^{eff} = \left(\mathbf{F}_{ZC}^{eff}\right)^{T} \tag{6.168}$$

Hence

$$\left(\mathbf{F}^{T}\right)^{eff} = \left(\mathbf{F}^{eff}\right)^{T} \tag{6.169}$$

6.5.2 Effective Kirchhoff's voltage law for the multiport Brune circuit

In this section we will derive an effective Kirchhoff's voltage law for multiport Brune circuit in Fig. (5.11). We write Kirchhoff's voltage law

$$\mathbf{F}^{\mathrm{T}}\mathbf{V}_{\mathrm{tr}} = \mathbf{V}_{\mathrm{ch}} \tag{6.170}$$

with partioning in Eqs. (5.94) and (5.95) for voltage vectors $\mathbf{V}_{\mathrm{tr}}$ and $\mathbf{V}_{\mathrm{ch}}$ respectively. We note that the relation in Eq. (6.170) derives from a graph theoretical analysis [18] of the multiport Brune network.

We will further partition voltage vectors $\mathbf{V}_{T}^{(tr)}$ and $\mathbf{V}_{T}^{(ch)}$ for the transformer branches as follows

$$\mathbf{V}_{T}^{(tr)} = \left(\mathbf{V}_{n}^{(R)}, \mathbf{V}_{\mathbf{T}}^{(R)}, \mathbf{V}_{\boldsymbol{\nu}}^{(R)}\right) \tag{6.171}$$
$$\mathbf{V}_{T}^{(ch)} = \left(\mathbf{V}_{n}^{(L)}, \mathbf{V}_{\mathbf{T}}^{(L)}, \mathbf{V}_{\boldsymbol{\nu}}^{(L)}\right) \tag{6.172}$$

where

$$\mathbf{V}_{n}^{(R)} = \left(V_{n_1}^{(R)}, \ldots, V_{n_M}^{(R)}\right) \tag{6.173}$$

$$\mathbf{V}_{\mathbf{T}}^{(R)} = \left(\mathbf{V}_{\mathbf{T}_1}^{(R)}, \ldots, \mathbf{V}_{\mathbf{T}_{M+1}}^{(R)}\right) \tag{6.174}$$

$$\mathbf{V}_{\boldsymbol{\nu}}^{(R)} = \left(\mathbf{V}_{\boldsymbol{\nu}_1}^{(R)}, \ldots, \mathbf{V}_{\boldsymbol{\nu}_M}^{(R)}\right) \tag{6.175}$$

and

$$\mathbf{V}_{n}^{(L)} = \left(V_{n_1}^{(L)}, \ldots, V_{n_M}^{(L)}\right) \tag{6.176}$$

$$\mathbf{V}_{\mathbf{T}}^{(L)} = \left(\mathbf{V}_{\mathbf{T}_1}^{(L)}, \ldots, \mathbf{V}_{\mathbf{T}_{M+1}}^{(L)}\right) \tag{6.177}$$

$$\mathbf{V}_{\boldsymbol{\nu}}^{(L)} = \left(V_{\boldsymbol{\nu}_1}^{(L)}, \ldots, V_{\boldsymbol{\nu}_M}^{(L)}\right) \tag{6.178}$$

with

$$\mathbf{V}_{\mathbf{T}_j}^{(L)(R)} = \begin{pmatrix} V_{\mathbf{T}_j,1}^{(L)(R)} \\ \vdots \\ V_{\mathbf{T}_j,N}^{(L)(R)} \end{pmatrix} \tag{6.179}$$

$$\mathbf{V}_{\boldsymbol{\nu}_j}^{(R)} = \begin{pmatrix} V_{\boldsymbol{\nu}_j,2}^{(R)} \\ \vdots \\ V_{\boldsymbol{\nu}_j,N}^{(R)} \end{pmatrix} \tag{6.180}$$

where $\mathbf{V}_{\mathbf{T}_j}^{(L)(R)}$ are vectors of length N for $1 \leq j \leq M+1$ and $\mathbf{V}_{\boldsymbol{\nu}_j}^{(R)}$ are vectors of length $(N-1)$ for $1 \leq j \leq M$.

We will move in the opposite direction to the direction we have chosen in Section (5.5) through the multiport Brune circuit while deriving effective loop matrices. That is we will start at the leftmost part of the multiport Brune circuit in Fig. (5.11) and move to the right. For simplicity we again assume that all of the ports of the multiport Brune circuit are shunted by Josephson junctions as shown in Fig. (5.18); we get the relation

$$\mathbf{V}_{\mathbf{T}_1}^{(L)} = \mathbf{V}_J \tag{6.181}$$

where $\mathbf{V}_J$ is the vector holding the voltages across the Josephson junctions shunting the ports of the multiport Brune circuit.

The voltages of inter-stage transformers are given by Eq. (5.114)

$$\mathbf{V}_{\mathbf{T}_j}^{(R)} = \mathbf{T}_j^T \mathbf{V}_{\mathbf{T}_j}^{(L)} \tag{6.182}$$

for $1 \leq j \leq M+1$, where $\mathbf{T}_j$ is the $(N \times N)$ Belevitch transformer matrix of the j^{th} stage. The voltages of consecutive inter-stage transformers are related by

$$\mathbf{V}_{\mathbf{T}_{j+1}}^{(L)} = \mathbf{A}_j^T \mathbf{e}_1 V_{r_j} + \boldsymbol{\upsilon}_j^T V_{L_j} + \mathbf{A}_j^T \mathbf{V}_{\mathbf{T}_j}^{(R)} \tag{6.183}$$

for $1 \leq j \leq M$, where $\mathbf{e}_1 = \begin{pmatrix} 1 & 0 & \dots & 0 \end{pmatrix}^T$ is the unit vector, $\mathbf{A}_j$ is the $(N \times N)$ matrix defined in Eq. (5.123) and $\boldsymbol{\upsilon}_j$ is the row vector defined in Eq. (5.125).

We can write the voltage V_{C_j} across the capacitor C_j at the j^{th} stage as

$$V_{C_j} = V_{L_j} + V_{r_j} + \mathbf{e}_1^T \mathbf{V}_{\mathbf{T}_j}^{(R)} \tag{6.184}$$

We are now going to iterate over the index j starting at $j = 1$ through the stages in the multiport Brune circuit using the Eqs. (6.181), (6.182), (6.183) and (6.184)

$$
\begin{aligned}
\mathbf{V}_{\mathbf{T}_1}^{(R)} &= \mathbf{T}_1^T \mathbf{V}_{\mathbf{T}_1}^{(L)} = \mathbf{T}_1^T \mathbf{V}_J \\
\mathbf{V}_{\mathbf{T}_2}^{(L)} &= \mathbf{A}_1^T \mathbf{e}_1 V_{r_1} + \boldsymbol{v}_1^T V_{L_1} + \mathbf{A}_1^T \mathbf{V}_{\mathbf{T}_1}^{(R)} = \mathbf{A}_1^T \mathbf{e}_1 V_{r_1} + \boldsymbol{v}_1^T V_{L_1} + \mathbf{A}_1^T \mathbf{T}_1^T \mathbf{V}_J \\
V_{C_1} &= V_{L_1} + V_{r_1} + \mathbf{e}_1^T \mathbf{V}_{\mathbf{T}_1}^{(R)} = V_{L_1} + V_{r_1} + \mathbf{e}_1^T \mathbf{T}_1^T \mathbf{V}_J \\
\mathbf{V}_{\mathbf{T}_2}^{(R)} &= \mathbf{T}_2^T \mathbf{V}_{\mathbf{T}_2}^{(L)} = \mathbf{T}_2^T \mathbf{A}_1^T \mathbf{e}_1 V_{r_1} + \mathbf{T}_2^T \boldsymbol{v}_1^T V_{L_1} + \mathbf{T}_2^T \mathbf{A}_1^T \mathbf{T}_1^T \mathbf{V}_J \\
\mathbf{V}_{\mathbf{T}_3}^{(L)} &= \mathbf{A}_2^T \mathbf{e}_1 V_{r_2} + \boldsymbol{v}_2^T V_{L_2} + \mathbf{A}_2^T \mathbf{V}_{\mathbf{T}_2}^{(R)} \\
&= \mathbf{A}_2^T \mathbf{T}_2^T \mathbf{A}_1^T \mathbf{e}_1 V_{r_1} + \mathbf{A}_2^T \mathbf{e}_1 V_{r_2} + \mathbf{A}_2^T \mathbf{T}_2^T \boldsymbol{v}_1^T V_{L_1} + \boldsymbol{v}_2^T V_{L_2} + \\
&\quad + \mathbf{A}_2^T \mathbf{T}_2^T \mathbf{A}_1^T \mathbf{T}_1^T \mathbf{V}_J \\
V_{C_2} &= V_{L_2} + V_{r_2} + \mathbf{e}_1^T \mathbf{V}_{\mathbf{T}_2}^{(R)} \\
&= \mathbf{e}_1^T \mathbf{T}_2^T \mathbf{A}_1^T \mathbf{e}_1 V_{r_1} + V_{r_2} + \mathbf{e}_1^T \mathbf{T}_2^T \boldsymbol{v}_1^T V_{L_1} + V_{L_2} + \\
&\quad + \mathbf{e}_1^T \mathbf{T}_2^T \mathbf{A}_1^T \mathbf{T}_1^T \mathbf{V}_J \\
\mathbf{V}_{\mathbf{T}_3}^{(R)} &= \mathbf{T}_3^T \mathbf{V}_{\mathbf{T}_3}^{(L)} \\
&= \mathbf{T}_3^T \mathbf{A}_2^T \mathbf{T}_2^T \mathbf{A}_1^T \mathbf{e}_1 V_{r_1} + \mathbf{T}_3^T \mathbf{A}_2^T \mathbf{e}_1 V_{r_2} + \\
&\quad + \mathbf{T}_3^T \mathbf{A}_2^T \mathbf{T}_2^T \boldsymbol{v}_1^T V_{L_1} + \mathbf{T}_3^T \boldsymbol{v}_2^T V_{L_2} + \mathbf{T}_3^T \mathbf{A}_2^T \mathbf{T}_2^T \mathbf{A}_1^T \mathbf{T}_1^T \mathbf{V}_J \\
\mathbf{V}_{\mathbf{T}_4}^{(L)} &= \mathbf{A}_3^T \mathbf{e}_1 V_{r_3} + \boldsymbol{v}_3^T V_{L_3} + \mathbf{A}_3^T \mathbf{V}_{\mathbf{T}_3}^{(R)} \\
&= \mathbf{A}_3^T \mathbf{T}_3^T \mathbf{A}_2^T \mathbf{T}_2^T \mathbf{A}_1^T \mathbf{e}_1 V_{r_1} + \mathbf{A}_3^T \mathbf{T}_3^T \mathbf{A}_2^T \mathbf{e}_1 V_{r_2} + \mathbf{A}_3^T \mathbf{e}_1 V_{r_3} + \\
&\quad + \mathbf{A}_3^T \mathbf{T}_3^T \mathbf{A}_2^T \mathbf{T}_2^T \boldsymbol{v}_1^T V_{L_1} + \mathbf{A}_3^T \mathbf{T}_3^T \boldsymbol{v}_2^T V_{L_2} + \boldsymbol{v}_3^T V_{L_3} + \mathbf{A}_3^T \mathbf{T}_3^T \mathbf{A}_2^T \mathbf{T}_2^T \mathbf{A}_1^T \mathbf{T}_1^T \mathbf{V}_J \\
V_{C_3} &= V_{L_3} + V_{r_3} + \mathbf{e}_1^T \mathbf{V}_{\mathbf{T}_3}^{(R)} \\
&= \mathbf{e}_1^T \mathbf{T}_3^T \mathbf{A}_2^T \mathbf{T}_2^T \mathbf{A}_1^T \mathbf{e}_1 V_{r_1} + \mathbf{e}_1^T \mathbf{T}_3^T \mathbf{A}_2^T \mathbf{e}_1 V_{r_2} + V_{r_3} + \\
&\quad + \mathbf{e}_1^T \mathbf{T}_3^T \mathbf{A}_2^T \mathbf{T}_2^T \boldsymbol{v}_1^T V_{L_1} + \mathbf{e}_1^T \mathbf{T}_3^T \boldsymbol{v}_2^T V_{L_2} + V_{L_3} + \\
&\quad + \mathbf{e}_1^T \mathbf{T}_3^T \mathbf{A}_2^T \mathbf{T}_2^T \mathbf{A}_1^T \mathbf{T}_1^T \mathbf{V}_J \qquad (6.185) \\
\vdots \quad \vdots \quad \vdots
\end{aligned}
$$

Hence from the above relations we define the following for $1 \leq j \leq M$ and $1 \leq k \leq M$

$$
\begin{cases}
\left(\mathbf{F}_{LC}^T\right)^{eff}(j,k) = 0 & for\ j < k \leq M \\
\left(\mathbf{F}_{LC}^T\right)^{eff}(j,k) = 1 & for\ k = j \\
\left(\mathbf{F}_{LC}^T\right)^{eff}(j,k) = \mathbf{e}_1^T \mathbf{T}_{k+1}^T \boldsymbol{v}_k^T & for\ k = j-1 \\
\left(\mathbf{F}_{LC}^T\right)^{eff}(j,k) = \mathbf{e}_1^T \mathbf{T}_j^T \mathbf{A}_{j-1}^T \mathbf{T}_{j-1}^T \ldots \mathbf{A}_{k+1}^T \mathbf{T}_{k+1}^T \boldsymbol{v}_k^T & for\ 1 \leq k \leq j-2
\end{cases}
\qquad (6.186)
$$

$$\begin{cases} \left(\mathbf{F}_{ZC}^{T}\right)^{eff}(j,k) = 0 & for\ j < k \leq M \\ \left(\mathbf{F}_{ZC}^{T}\right)^{eff}(j,k) = 1 & for\ k = j \\ \left(\mathbf{F}_{ZC}^{T}\right)^{eff}(j,k) = \mathbf{e}_1^T\mathbf{T}_j^T\mathbf{A}_{j-1}^T\mathbf{T}_{j-1}^T\ldots\mathbf{A}_{k+1}^T\mathbf{T}_{k+1}^T\mathbf{A}_k^T\mathbf{e}_1 & for\ 1 \leq k \leq j-1 \end{cases} \tag{6.187}$$

and for $1 \leq k \leq N$

$$\begin{cases} \left(\mathbf{F}_{JC}^{T}\right)^{eff}(j,k) = \mathbf{e}_1^T\mathbf{T}_1^T\mathbf{e}_k & for\ j = 1 \\ \left(\mathbf{F}_{JC}^{T}\right)^{eff}(j,k) = \mathbf{e}_1^T\mathbf{T}_j^T\mathbf{A}_{j-1}^T\mathbf{T}_{j-1}^T\ldots\mathbf{A}_1^T\mathbf{T}_1^T\mathbf{e}_k & for\ 1 < j \leq M \end{cases} \tag{6.188}$$

To compute effective loop submatrices for $j > M$ we note from Eq. (6.185) the following

$$\begin{aligned} \mathbf{V}_{\mathbf{T}_{M+1}}^{(L)} &= \mathbf{A}_M^T\mathbf{T}_M^T\ldots\mathbf{A}_2^T\mathbf{T}_2^T\mathbf{A}_1^T\mathbf{e}_1V_{r_1} + \ldots + \mathbf{A}_M^T\mathbf{e}_1V_{r_M} + \\ &\quad + \mathbf{A}_M^T\mathbf{T}_M^T\ldots\mathbf{A}_2^T\mathbf{T}_2^T\boldsymbol{\upsilon}_1^TV_{L_1} + \ldots + \boldsymbol{\upsilon}_M^TV_{L_M} + \\ &\quad + \mathbf{A}_M^T\mathbf{T}_M^T\ldots\mathbf{A}_1^T\mathbf{T}_1^T\mathbf{V}_J \end{aligned} \tag{6.189}$$

Writing also the voltage relations for the last stage transformer using Eq. (6.182)

$$\mathbf{V}_{\mathbf{T}_{M+1}}^{(R)} = \mathbf{T}_{M+1}^T\mathbf{V}_{\mathbf{T}_{M+1}}^{(L)} \tag{6.190}$$

And noting

$$\mathbf{V}_{C_R} = \mathbf{V}_{\mathbf{T}_{M+1}}^{(R)} \tag{6.191}$$

$$= \mathbf{T}_{M+1}^T\mathbf{V}_{\mathbf{T}_{M+1}}^{(L)} \tag{6.192}$$

We conclude using Eq. (6.189)

$$\begin{aligned} \mathbf{V}_{C_R} &= \mathbf{T}_{M+1}^T\mathbf{A}_M^T\mathbf{T}_M^T\ldots\mathbf{A}_2^T\mathbf{T}_2^T\mathbf{A}_1^T\mathbf{e}_1V_{r_1}\ldots + \mathbf{T}_{M+1}^T\mathbf{A}_M^T\mathbf{e}_1V_{r_M} + \\ &\quad + \mathbf{T}_{M+1}^T\mathbf{A}_M^T\mathbf{T}_M^T\ldots\mathbf{A}_2^T\mathbf{T}_2^T\boldsymbol{\upsilon}_1^TV_{L_1}\ldots + \mathbf{T}_{M+1}^T\boldsymbol{\upsilon}_M^TV_{L_M} + \\ &\quad + \mathbf{T}_{M+1}^T\mathbf{A}_M^T\mathbf{T}_M^T\ldots\mathbf{A}_1^T\mathbf{T}_1^T\mathbf{V}_J \end{aligned} \tag{6.193}$$

From Eq. (6.193) above we define for $1 \leq k \leq M$

$$\begin{cases} \left(\mathbf{F}_{LC}^{T}\right)^{eff}(j,k) = \mathbf{e}_{j-M}^T\mathbf{T}_{M+1}^T\mathbf{A}_M^T\mathbf{T}_M^T\ldots\mathbf{A}_{k+1}^T\mathbf{T}_{k+1}^T\boldsymbol{\upsilon}_k^T & for\ k < M\ and\ M+1 \leq j \leq M+N \\ \left(\mathbf{F}_{LC}^{T}\right)^{eff}(j,k) = \mathbf{e}_{j-M}^T\mathbf{T}_{M+1}^T\boldsymbol{\upsilon}_M^T & for\ k = M\ and\ M+1 \leq j \leq M+N \end{cases} \tag{6.194}$$

$$\left\{ \left(\mathbf{F}_{ZC}^{T}\right)^{eff}(j,k) = \mathbf{e}_{j-M}^{T}\mathbf{T}_{M+1}^{T}\mathbf{A}_{M}^{T}\mathbf{T}_{M}^{T}\ldots\mathbf{A}_{k+1}^{T}\mathbf{T}_{k+1}^{T}\mathbf{A}_{k}^{T}\mathbf{e}_{1} \quad for\ M+1 \leq j \leq M+N \right. \tag{6.195}$$

And for $1 \leq k \leq N$

$$\left\{ \left(\mathbf{F}_{JC}^{T}\right)^{eff}(j,k) = \mathbf{e}_{j-M}^{T}\mathbf{T}_{M+1}^{T}\mathbf{A}_{M}^{T}\mathbf{T}_{M}^{T}\ldots\mathbf{A}_{1}^{T}\mathbf{T}_{1}^{T}\mathbf{e}_{k} \quad for\ M+1 \leq j \leq M+N \right. \tag{6.196}$$

Hence from Eqs. (6.186), (6.187), (6.188) and (6.194), (6.195), (6.196) we conclude

$$\left(\mathbf{F}^{T}\right)^{eff}\mathbf{V}_{\mathrm{tr}}^{eff} = \mathbf{V}_{\mathrm{ch}}^{eff} \tag{6.197}$$

with

$$\left(\mathbf{F}^{T}\right)^{eff} = \begin{pmatrix} \left(\mathbf{F}_{JC}^{T}\right)^{eff} & \left(\mathbf{F}_{LC}^{T}\right)^{eff} & \left(\mathbf{F}_{ZC}^{T}\right)^{eff} \end{pmatrix} \tag{6.198}$$

and comparing Eqs. (6.186), (6.187), (6.188) and (6.194), (6.195), (6.196) to Eqs. (5.128), (5.133) and (5.136) of Section (5.5) we conclude

$$\left(\mathbf{F}^{T}\right)^{eff} = \left(\mathbf{F}^{eff}\right)^{T} \tag{6.199}$$

6.6 State-space equations for Burkard type linear circuits with $\mathbf{F}_{ZK} \neq 0$ and $\mathbf{F}_{VK} \neq 0$

Here we show how to derive state-space equations for Burkard [18] type circuits with relaxed conditions $\mathbf{F}_{ZK} \neq 0$ and $\mathbf{F}_{VK} \neq 0$. This allows us to bypass fitting process and directly arrive at the state-space description for this specific class of circuits.

Let the state vector be $\mathbf{x} = \begin{pmatrix} \mathbf{I}_L \\ \mathbf{I}_K \\ \mathbf{V}_C \end{pmatrix}$.

Writing KVL for $\mathbf{V}_C$

$$\begin{aligned} \mathbf{V}_C &= \mathbf{F}_{LC}^T \mathbf{V}_L + \mathbf{F}_{VC}^T \mathbf{V}_V + \mathbf{F}_{ZC}^T \mathbf{V}_Z \\ &= \mathbf{F}_{LC}^T \dot{\mathbf{\Phi}}_L + \mathbf{F}_{VC}^T \mathbf{V}_V + \mathbf{F}_{ZC}^T \mathbf{Z} \mathbf{I}_Z \\ &= \mathbf{F}_{LC}^T \mathbf{L} \dot{\mathbf{I}}_L + \mathbf{F}_{VC}^T \mathbf{V}_V - \mathbf{F}_{ZC}^T \mathbf{Z} \mathbf{F}_{ZC} \mathbf{C} \dot{\mathbf{V}}_C - \mathbf{F}_{ZC}^T \mathbf{Z} \mathbf{F}_{ZK} \mathbf{I}_K \end{aligned}$$

where we have assumed $\mathbf{L}_{LK} = 0$ (which in general non-zero in Burkard). Rearranging

$$\mathbf{F}_{LC}^T \mathbf{L} \dot{\mathbf{I}}_L - \mathbf{Z}_{CC} \mathbf{C} \dot{\mathbf{V}}_C = \mathbf{Z}_{CK} \mathbf{I}_K + \mathbf{V}_C - \mathbf{F}_{VC}^T \mathbf{V}_V \tag{6.200}$$

where we defined

$$\begin{aligned} \mathbf{Z}_{CC} &= \mathbf{F}_{ZC}^T \mathbf{Z} \mathbf{F}_{ZC} \\ \mathbf{Z}_{CK} &= \mathbf{F}_{ZC}^T \mathbf{Z} \mathbf{F}_{ZK} \end{aligned}$$

Writing KCL for $\mathbf{I}_L$

$$\begin{aligned} \mathbf{I}_L &= -\mathbf{F}_{LC} \mathbf{I}_C - \mathbf{F}_{LK} \mathbf{I}_K \\ &= -\mathbf{F}_{LC} \mathbf{C} \dot{\mathbf{V}}_C - \mathbf{F}_{LK} \mathbf{I}_K \end{aligned}$$

Rearranging

$$\mathbf{F}_{LC} \mathbf{C} \dot{\mathbf{V}}_C = -\mathbf{I}_L - \mathbf{F}_{LK} \mathbf{I}_K \tag{6.201}$$

Writing KVL for $\mathbf{V}_K$

$$\begin{aligned} \mathbf{V}_K &= \mathbf{F}_{LK}^T \mathbf{V}_L + \mathbf{F}_{VK}^T \mathbf{V}_V + \mathbf{F}_{ZK}^T \mathbf{V}_Z \\ &= \mathbf{F}_{LK}^T \dot{\mathbf{\Phi}}_L + \mathbf{F}_{VK}^T \mathbf{V}_V + \mathbf{F}_{ZK}^T \mathbf{Z} \mathbf{I}_Z \\ &= \mathbf{F}_{LK}^T \mathbf{L} \dot{\mathbf{I}}_L + \mathbf{F}_{VK}^T \mathbf{V}_V - \mathbf{F}_{ZK}^T \mathbf{Z} \mathbf{F}_{ZC} \mathbf{C} \dot{\mathbf{V}}_C - \mathbf{F}_{ZK}^T \mathbf{Z} \mathbf{F}_{ZK} \mathbf{I}_K \end{aligned}$$

Rearranging

$$-\mathbf{F}_{LK}^T\mathbf{L}\dot{\mathbf{I}}_L + \mathbf{L}_K\dot{\mathbf{I}}_K + \mathbf{Z}_{KC}\mathbf{C}\dot{\mathbf{V}}_C = -\mathbf{Z}_{KK}\mathbf{I}_K + \mathbf{F}_{VK}^T\mathbf{V}_V \tag{6.202}$$

where we defined

$$\begin{aligned}\mathbf{Z}_{KK} &= \mathbf{F}_{ZK}^T\mathbf{Z}\mathbf{F}_{ZK}\\ \mathbf{Z}_{KC} &= \mathbf{F}_{ZK}^T\mathbf{Z}\mathbf{F}_{ZC}\end{aligned}$$

We can now write the time evolution of the state $\mathbf{x}$ using Eqs. (6.200), (6.201) and (6.202)

$$\begin{pmatrix} \mathbf{F}_{LC}^T\mathbf{L} & \mathbf{0} & -\mathbf{Z}_{CC}\mathbf{C} \\ \mathbf{0} & \mathbf{0} & \mathbf{F}_{LC}\mathbf{C} \\ -\mathbf{F}_{LK}^T\mathbf{L} & \mathbf{L}_K & \mathbf{Z}_{KC}\mathbf{C} \end{pmatrix}\dot{\mathbf{x}} = \begin{pmatrix} \mathbf{0} & \mathbf{Z}_{CK} & \mathbf{I} \\ -\mathbf{I} & -\mathbf{F}_{LK} & \mathbf{0} \\ \mathbf{0} & -\mathbf{Z}_{KK} & \mathbf{0} \end{pmatrix}\mathbf{x} + \begin{pmatrix} -\mathbf{F}_{VC}^T \\ \mathbf{0} \\ \mathbf{F}_{VK}^T \end{pmatrix}\mathbf{V_V} \tag{6.203}$$

For the input-output relations we write KCL for $\mathbf{I}_V$

$$\mathbf{I}_V = -\mathbf{F}_{VC}\mathbf{C}\dot{\mathbf{V}}_C - \mathbf{F}_{VK}\mathbf{I}_K \tag{6.204}$$

We can write state-space matrices

$$\mathbf{A} = \begin{pmatrix} \mathbf{F}_{LC}^T\mathbf{L} & \mathbf{0} & -\mathbf{Z}_{CC}\mathbf{C} \\ \mathbf{0} & \mathbf{0} & \mathbf{F}_{LC}\mathbf{C} \\ -\mathbf{F}_{LK}^T\mathbf{L} & \mathbf{L}_K & \mathbf{Z}_{KC}\mathbf{C} \end{pmatrix}^{-1}\begin{pmatrix} \mathbf{0} & \mathbf{Z}_{CK} & \mathbf{I} \\ -\mathbf{I} & -\mathbf{F}_{LK} & \mathbf{0} \\ \mathbf{0} & -\mathbf{Z}_{KK} & \mathbf{0} \end{pmatrix} \tag{6.205}$$

$$\mathbf{B} = \begin{pmatrix} \mathbf{F}_{LC}^T\mathbf{L} & \mathbf{0} & -\mathbf{Z}_{CC}\mathbf{C} \\ \mathbf{0} & \mathbf{0} & \mathbf{F}_{LC}\mathbf{C} \\ -\mathbf{F}_{LK}^T\mathbf{L} & \mathbf{L}_K & \mathbf{Z}_{KC}\mathbf{C} \end{pmatrix}^{-1}\begin{pmatrix} -\mathbf{F}_{VC}^T \\ \mathbf{0} \\ \mathbf{F}_{VK}^T \end{pmatrix} \tag{6.206}$$

Matrices $\mathbf{C}$ and $\mathbf{D}$ are to be determined after solving Eq. (6.203) for $\dot{\mathbf{V}}_C$ and substituting it in Eq. (6.204).

Note that $\left\{\ \mathbf{A},\ \mathbf{B},\ \mathbf{C},\ \mathbf{D}\ \right\}$ gives an admittance description. The impedance description is given by $\left\{\ (\mathbf{A}-\mathbf{B}\mathbf{D}^{-1}\mathbf{C}),\ \mathbf{B}\mathbf{D}^{-1},\ -\mathbf{D}^{-1}\mathbf{C},\ \mathbf{D}^{-1}\ \right\}$.

Bibliography

[1] Peter W. Shor, "Polynomial-Time Algorithms for Prime Factorization and Discrete Logarithms on a Quantum Computer", SIAM J. Comput., 26(5), 1484–1509, (1997).

[2] Seth Lloyd, "Universal Quantum Simulators", Science 273, 1073 (1996).

[3] J. Ignacio Cirac, Peter Zoller, "Goals and opportunities in quantum simulation", Nature Physics 8, 264–266 (2012).

[4] J. R. Johansson, P. D. Nation, and F. Nori, "QuTiP 2: A Python framework for the dynamics of open quantum systems.", Comp. Phys. Comm. 184, 1234 (2013).

[5] Peter W. Shor, "Scheme for reducing decoherence in quantum computer memory", Phys. Rev. A 52, R2493(R), (1995).

[6] Peter W. Shor, "Fault-tolerant quantum computation", in 37th Symposium on Foundations of Computing, IEEE Computer Society Press, 1996, pp. 56-65.

[7] Alexei Y. Kitaev, "Fault-tolerant quantum computation by anyons", Ann. Phys., 303, 2-30, (2003).

[8] Barbara M. Terhal, "Quantum Error Correction for Quantum Memories", Lecture Notes of the 44^{th} IFF Spring School "Quantum Information Processing", (Forschungszentrum Jülich, 2013), arXiv:1302.3428.

[9] Y. Nakamura, Yu. A. Pashkin, J. S. Tsai, "Coherent control of macroscopic quantum states in a single-Cooper-pair box", Nature 398, 786-788, 1999.

[10] Audrey Cottet, "Implementation of a quantum bit in a superconducting circuit", PhD thesis, Université Paris VI, (2002).

[11] Caspar H. van der Wal, A. C. J. ter Haar, F. K. Wilhelm, R. N. Schouten, C. J. P. M. Harmans, T. P. Orlando, Seth Lloyd, and J. E. Mooij, "Quantum Superposition of Macroscopic Persistent-Current States", Science 290, 5492 (2000).

[12] John M. Martinis, S. Nam, J. Aumentado, and C. Urbina, "Rabi Oscillations in a Large Josephson-Junction Qubit", Phys. Rev. Lett. 89, 117901, (2002).

[13] Jens Koch, Terri M. Yu, Jay Gambetta, A. A. Houck, D. I. Schuster, J. Majer, Alexandre Blais, M. H. Devoret, S. M. Girvin, R. J. Schoelkopf, "Charge-insensitive qubit design derived from the Cooper pair box", Phys. Rev. A 76, 042319, (2007).

[14] Jens Koch, V. Manucharyan, M. H. Devoret, and L. I. Glazman, "Charging Effects in the Inductively Shunted Josephson Junction", Phys. Rev. Lett. 103, 217004, (2009).

[15] Michel H. Devoret, Robert J. Schoelkopf, "Superconducting Circuits for Quantum Information: An Outlook", Science 339, 6124, (2013).

[16] Michel H. Devoret, in *Quantum fluctuations,* Les Houches, Elsevier, Amsterdam, (1997).

[17] G. Burkard, R. H. Koch, and D. P. DiVincenzo, "Multi-level quantum description of decoherence in superconducting qubits", Phys. Rev. B 69, 064503 (2004).

[18] G. Burkard, "Circuit theory for decoherence in superconducting charge qubits", Phys. Rev. B 71, 144511 (2005).

[19] D. Vion, A. Aassime, A. Cottet, P. Joyez, H. Pothier, C. Urbina, D. Esteve, M.H. Devoret, "Manipulating the quantum state of an electrical circuit", Science 296, (2002).

[20] Alexandre Blais, Ren-Shou Huang, Andreas Wallraff, S. M. Girvin, and R. J. Schoelkopf, "Cavity quantum electrodynamics for superconducting electrical circuits: an architecture for quantum computation," Phys. Rev. A **69**, 062320 (2004).

[21] Alexandre Blais, Jay Gambetta, A. Wallraff, D. I. Schuster, S. M. Girvin, M. H. Devoret, and R. J. Schoelkopf, "Quantum information processing with circuit quantum electrodynamics," Phys. Rev. A **75**, 032329 (2007).

[22] Hanhee Paik, D. I. Schuster, Lev S. Bishop, G. Kirchmair, G. Catelani, A. P. Sears, B. R. Johnson, M. J. Reagor, L. Frunzio, L. Glazman, S. M. Girvin, M. H. Devoret, and R. J. Schoelkopf, "Observation of high coherence in Josephson junction qubits measured in a three-dimensional circuit QED architecture," Phys. Rev. Lett. **107**, 240501 (2011).

[23] DiVincenzo, D. P. Fault-tolerant architectures for superconducting qubits. Phys. Scr. T137, 014020 (2009).

[24] David P. DiVincenzo, "The Physical Implementation of Quantum Computation", Fortschr. Phys. 48, 771 (2000).

[25] A. A. Houck, J. A. Schreier, B. R. Johnson, J. M. Chow, Jens Koch, J. M. Gambetta, D. I. Schuster, L. Frunzio, M. H. Devoret, S. M. Girvin, R. J. Schoelkopf, "Controlling the spontaneous emission of a superconducting transmon qubit", Phys. Rev. Lett. 101, 080502 (2008).

[26] David C. McKay, Ravi Naik, Philip Reinhold, Lev S. Bishop, David I. Schuster, "High contrast qubit interactions using multimode cavity QED", arXiv:1402.7036.

[27] David P. DiVincenzo, Firat Solgun, "Multi-qubit parity measurement in circuit quantum electrodynamics", New J. Phys., Vol. 15, 075001, (2013).

[28] N. D. Mermin, *Quantum Computer Science: An Introduction* (Cambridge University Press, 2007).

[29] Eric Dennis, Alexei Kitaev, Andrew Landahl, and John Preskill, "Topological quantum memory," J. Math. Phys. **43**, 4452-4505 (2002).

[30] M. O. Scully and K. Druhl, "Quantum eraser: A proposed photon correlation experiment concerning observation and 'delayed choice' in quantum mechanics," Phys. Rev. A **25**, 2208-2213 (1982).

[31] D. Gottesman, "Fault-Tolerant Quantum Computation with Higher-Dimensional Systems," Chaos Solitons Fractals **10**, 1749-1758 (1999), Sec. 5.

[32] C. W. J. Beenakker, D. P. DiVincenzo, C. Emary, and M. Kindermann, "Charge Detection Enables Free-Electron Quantum Computation," Phys. Rev. Lett. **93**, 020501 (2004).

[33] Hans-Andreas Engel and Daniel Loss, "Fermionic Bell-State Analyzer for Spin Qubits," Science **309**, 586-588 (2005).

[34] B. Trauzettel, A. N. Jordan, C. W. J. Beenakker, and M. Buttiker, "Parity meter for charge qubits: An efficient quantum entangler," Phys. Rev. B **73**, 235331 (2006).

[35] Joseph Kerckhoff, Luc Bouten, Andrew Silberfarb and Hideo Mabuchi, "Physical model of continuous two-qubit parity measurement in a cavity-QED network," Phys. Rev. A **79**, 024305 (2009).

[36] Kevin Lalumiere, J. M. Gambetta, and Alexandre Blais, "Tunable joint measurements in the dispersive regime of cavity QED," Phys. Rev. A **81**, 040301(R) (2010).

[37] L. Tornberg and G. Johansson, "High-fidelity feedback-assisted parity measurement in circuit QED," Phys. Rev. A **82**, 012329 (2010).

[38] Wenjin Mao, Dmitri V. Averin, Rusko Ruskov and Alexander N. Korotkov, "Mesoscopic Quadratic Quantum Measurements," Phys. Rev. Lett. **93**, 056803 (2004).

[39] Wei Feng, Peiyue Wang, Xinmei Ding, Luting Xu, and Xin-Qi Li, "Generating and stabilizing the GHZ state in circuit QED: Joint measurement, Zeno effect and feedback," Phys. Rev. A **83**, 042313 (2011).

[40] J. M. Chow, L. DiCarlo, J. M. Gambetta, A. Nunnenkamp, Lev S. Bishop, L. Frunzio, M. H. Devoret, S. M. Girvin, R. J. Schoelkopf, "Entanglement Metrology Using a Joint Readout of Superconducting Qubits," Phys. Rev. A **81**, 062325 (2010).

[41] S. Filipp, P. Maurer, P. J. Leek, M. Baur, R. Bianchetti, J. M. Fink, M. Goeppl, L. Steffen, J. M. Gambetta, A. Blais, A. Wallraff, "Two-Qubit State Tomography using a Joint Dispersive Read-Out," Phys. Rev. Lett. **102**, 200402 (2009).

[42] L. DiCarlo, J. M. Chow, J. M. Gambetta, Lev S. Bishop, B. R. Johnson, D. I. Schuster, J. Majer, A. Blais, L. Frunzio, S. M. Girvin, and R. J. Schoelkopf, "Demonstration of two-qubit algorithms with a superconducting quantum processor," Nature **460**, 240-244 (2009).

[43] D. Riste, J. G. van Leeuwen, H.-S. Ku, K. W. Lehnert, and L. DiCarlo, 'Initialization by measurement of a two-qubit superconducting circuit," Phys. Rev. Lett. 109, 050507 (2012).

[44] Simon J. Devitt, Kae Nemoto, and William J. Munro, "Quantum error correction for beginners," Rep. Prog. Phys. 76, 076001 (2013).

[45] Gabrielle Denhez, Alexandre Blais, and David Poulin, "Quantum error correction benchmarks for continuous weak parity measurements," Phys. Rev. A 86, 032318 (2012).

[46] Martin Suchara, Sergey Bravyi, Barbara M. Terhal, "Constructions and Noise Threshold of Topological Subsystem Codes," J. Phys. A **44**, 155301 (2011).

[47] Robert Raussendorf and Jim Harrington, "Fault-tolerant quantum computation with high threshold in two dimensions," Phys. Rev. Lett. **98**, 190504 (2007).

[48] Dave Bacon, "Operator Quantum Error Correcting Subsystems for Self-Correcting Quantum Memories," Phys. Rev. A **73**, 012340 (2006).

[49] Panos Aliferis and Andrew W. Cross "Subsystem fault tolerance with the Bacon-Shor code," Phys. Rev. Lett. **98**, 220502 (2007).

[50] Andrew W. Cross, David P. DiVincenzo, and Barbara M. Terhal, "A comparative code study for quantum fault-tolerance," Quant. Inf. Comp. **9**, No. 7/8, 0541-0572 (2009).

[51] David P. DiVincenzo, "Fault tolerant architectures for superconducting qubits," Phys. Scr. T **137** 014020 (2009).

[52] Austin G. Fowler, Ashley M. Stephens, and Peter Groszkowski, "High threshold universal quantum computation on the surface code," Phys. Rev. A **80**, 052312 (2009).

[53] Clare Horsman, Austin G. Fowler, Simon Devitt, Rodney Van Meter, "Surface code quantum computing by lattice surgery," New J. Phys. **14**, 123011 (2012) .

[54] S. Bravyi, G. Duclos-Cianci, D. Poulin, and M. Suchara, "Subsystem surface codes with three-qubit check operators," Quant. Inf. Comp. Vol. 13, No. 11&12, pp. 0963-0985 (2013).

[55] Fumiko Yamaguchi, Kae Nemoto, and William J. Munro, "Quantum error correction via robust probe modes," Phys. Rev. A **73**, 060302(R) (2006).

[56] Simon E. Nigg and Steven M. Girvin, "Stabilizer quantum error correction toolbox for superconducting qubits," Phys. Rev. Lett. 110, 243604 (2013).

[57] Matthias Steffen, Shwetank Kumar, David P. DiVincenzo, J. R. Rozen, George A. Keefe, Mary Beth Rothwell, and Mark B. Ketchen, "High-Coherence Hybrid Superconducting Qubit," Phys. Rev. Lett. **105**, 100502 (2010).

[58] B. R. Johnson, M. D. Reed, A. A. Houck, D. I. Schuster, Lev S. Bishop, E. Ginossar, J. M. Gambetta, L. DiCarlo, L. Frunzio, S. M. Girvin, and R. J. Schoelkopf, "Quantum Non-demolition Detection of Single Microwave Photons in a Circuit," Nature Physics **6**, 663 - 667 (2010).

[59] Matteo Mariantoni, H. Wang, T. Yamamoto, M. Neeley, Radoslaw C. Bialczak, Y. Chen, M. Lenander, Erik Lucero, A. D. O'Connell, D. Sank, M. Weides, J. Wenner, Y. Yin, J. Zhao, A. N. Korotkov, A. N. Cleland, and John M. Martinis, "Implementing the Quantum von Neumann Architecture with Superconducting Circuits," Science **334**, 61-65 (2011).

[60] S. Ramo, J. R. Whinnery, and T. van Duzer, *Fields and Waves in Communication Electronics*, Wiley, New York, 1965.

[61] D. Pozar, *Microwave Engineering*, third edition (Wiley VCH, 2005).

[62] Joseph Helszajn, *Microwave Engineering: Passive, Active and Non-Reciprocal Circuits*, McGraw-Hill, 1992.

[63] Joseph Helszajn, *Nonreciprocal microwave junctions and circulators*, Wiley, 1975.

[64] Giovanni Viola and David P. DiVincenzo, "Hall Effect Gyrators and Circulators", Phys. Rev. X 4, 021019, (2014).

[65] M. Goppl, A. Fragner, M. Baur, R. Bianchetti, S. Filipp, J. M. Fink, P. J. Leek, G. Puebla, L. Steffen, and A. Wallraff, "Coplanar Waveguide Resonators for Circuit Quantum Electrodynamics," J. Appl. Phys. **104**, 113904 (2008).

[66] D. F. Walls and G. J. Milburn, *Quantum Optics*, second edition (Springer, 2008).

[67] R. Vijay, D. H. Slichter, and I. Siddiqi, "Observation of Quantum Jumps in a Superconducting Artificial Atom," Phys. Rev. Lett. **106**, 110502 (2011).

[68] L. Tornberg, Sh. Barzanjeh, and David P. DiVincenzo, "Stochastic-master-equation analysis of optimized three-qubit nondemolition parity measurements", Phys. Rev. A 89, 032314, (2014).

[69] V. Belevitch, "Factorization of scattering matrices with applications to passive network synthesis", Philips Res. Rep., Vol. 18, No. 4, pp. 275-317 (1963).

[70] Robert W. Newcomb, *Linear Multiport Synthesis*, McGraw-Hill Book Company, 1966.

[71] N. Bergeal, R. Vijay, V. E. Manucharyan, I. Siddiqi, R. J. Schoelkopf, S. M. Girvin, and M. H. Devoret, "Analog information processing at the quantum limit with a Josephson ring modulator," Nature Physics **6**, 296 - 302 (2010).

[72] Jens Koch, Andrew A. Houck, Karyn Le Hur, and S. M. Girvin, "Time-reversal symmetry breaking in circuit-QED based photon lattices," Phys. Rev. A **82**, 043811 (2010).

[73] Simons, Rainee N., *Coplanar Waveguide Circuits, Components and Systems*, Wiley Series in Microwave and Optical Engineering (Wiley VCH, 2001).

[74] H. S. Ku, F. Mallet, L. R. Vale, K. D. Irwin, S. E. Russek, G. C. Hilton, K. W. Lehnert, "Design and Testing of Superconducting Microwave Passive Components for Quantum Information Processing," IEEE Trans. Appl. Superconductivity **21**, 452-455 (2011).

[75] S. Poletto, Jay M. Gambetta, Seth T. Merkel, John A. Smolin, Jerry M. Chow, A. D. Corcoles, George A. Keefe, Mary B. Rothwell, J. R. Rozen, D. W. Abraham, Chad Rigetti, and M. Steffen, "Entanglement of two superconducting qubits in a waveguide cavity via monochromatic two-photon excitation," Phys. Rev. Lett. **109**, 240505 (2012).

[76] Austin G. Fowler, Matteo Mariantoni, John M. Martinis, and Andrew N. Cleland, "Surface codes: Towards practical large-scale quantum computation," Phys. Rev. A **86**, 032324 (2012).

[77] Chad Rigetti, Stefano Poletto, Jay M. Gambetta, B. L. T. Plourde, Jerry M. Chow, A. D. Corcoles, John A. Smolin, Seth T. Merkel, J. R. Rozen, George A. Keefe, Mary B. Rothwell, Mark B. Ketchen, and M. Steffen, "Superconducting qubit in waveguide cavity with coherence time approaching 0.1ms," Phys. Rev. B **86**, 100506(R) (2012).

[78] Simon E. Nigg, Hanhee Paik, Brian Vlastakis, Gerhard Kirchmair, Shyam Shankar, Luigi Frunzio, Michel Devoret, Robert Schoelkopf, and Steven Girvin, "Black-box superconducting circuit quantization," Phys. Rev. Lett. **108**, 240502 (2012).

[79] Moe S. Khalil, F. C. Wellstood, and Kevin D. Osborn, "Loss Dependence on Geometry and Applied Power in Superconducting Coplanar Resonators," IEEE Trans. Appl. Supercond. **21**, No. 3, 879-882 (2011).

[80] P. M. Watson and K. C. Gupta, "Design and optimization of CPW circuits using EM-ANN models for CPW components," IEEE Trans. Micro. Th. Tech. **45**(12), 2515-2523 (1997).

[81] C. M. Wilson, F. Persson, T. Bauch, G. Johansson, V. Shumeiko, T. Duty, and P. Delsing, "Tuning the field in a microwave resonator faster than the photon lifetime," Appl. Phys. Lett. **92**, 203501 (2008).

[82] F. R. Ong, M. Boissonneault, F. Mallet, A. Palacios-Laloy, A. Dewes, A. C. Doherty, A. Blais, P. Bertet, D. Vion, and D. Esteve, "Circuit QED with a Nonlinear Resonator: ac-Stark Shift and Dephasing," Phys. Rev. Lett. **106**, 167002 (2011).

[83] M. A. Castellanos-Beltran, K. D. Irwin, G. C. Hilton, L. R. Vale, and K. W. Lehnert, "Amplification and squeezing of quantum noise with a tunable Josephson metamaterial," Nature Physics, **4**, 929 (2008).

[84] J. M. Gambetta, A. A. Houck, and Alexandre Blais, "A superconducting qubit with Purcell protection and tunable coupling," Phys. Rev. Lett. **106**, 030502 (2011).

[85] M. Mariantoni, E. P. Menzel, F. Deppe, M. A. Araque Caballero, A. Baust, T. Niemczyk, E. Hoffmann, E. Solano, A. Marx, and R. Gross, "Planck Spectroscopy and the Quantum Noise of Microwave Beam Splitters," Phys. Rev. Lett. **105**, 133601 (2010).

[86] Georg M. Reuther, David Zueco, Frank Deppe, Elisabeth Hoffmann, Edwin P. Menzel, Thomas Weissl, Matteo Mariantoni, Sigmund Kohler, Achim Marx, Enrique Solano, Rudolf Gross, and Peter Haenggi, "Two-resonator circuit QED: Dissipative Theory," Phys. Rev. B **81**, 144510 (2010).

[87] Io-Chun Hoi, C. M. Wilson, Goran Johansson, Tauno Palomaki, Borja Peropadre, and Per Delsing, "Demonstration of a Single-Photon Router in the Microwave Regime," Phys. Rev. Lett. **107**, 073601 (2011).

[88] Luca Chirolli, Guido Burkard, Shwetank Kumar, and David P. DiVincenzo, "Superconducting resonators as beam splitters for linear-optics quantum computation," Phys. Rev. Lett. **104**, 230502 (2010).

[89] J. T. Shen and S. Fan, "Coherent Single Photon Transport in a One-Dimensional Waveguide Coupled with Superconducting Quantum Bits." Phys. Rev. Lett. **95**, 213001 (2005).

[90] U. M. Titulaer and R. J. Glauber, "Density Operators for Coherent Fields," Phys. Rev. **145**, 1041-1050 (1966).

[91] Jerome Bourassa, Jay M. Gambetta, and Alexandre Blais, "Multi-mode circuit quantum electrodynamics,", Abstract Y29.00005, APS March Meeting, Dallas, 2011.

[92] Foster, R. M., "A reactance theorem", Bell Systems Technical Journal, vol.3, no. 2, pp. 259–267, November 1924.

[93] E. R. Beringer, "Resonant Cavities as Microwave Circuit Elements," in *Principles of Microwave Circuits*, edited by C. G. Montgomery, R. H. Dicke, and E. M. Purcell (MIT Radiation Laboratory, vol. 8, 1945), p. 215, Section 7.4.

[94] Ernst A. Guillemin, *Synthesis of Passive Networks*, (Robert E. Krieger Publishing Company, Huntington, New York, 1977).

[95] Louis Weinberg, "New Synthesis Procedures for Realizing Transfer Functions of RLC and RC Networks", MIT, RLE, Report no. 201, 1951.

[96] O. Brune, *Synthesis of a finite two-terminal network whose driving-point impedance is a prescribed function of frequency*, Doctoral thesis, MIT, 1931.

[97] Firat Solgun, David W. Abraham, and David P. DiVincenzo, "Blackbox quantization of superconducting circuits using exact impedance synthesis", Phys. Rev. B 90, 134504, (2014).

[98] J. Bourassa, F. Beaudoin, Jay M. Gambetta, and A. Blais, "Josephson-junction-embedded transmission-line resonators: From Kerr medium to in-line transmon," Phys. Rev. A 86, 013814 (2012).

[99] Ansys HFSS (High Frequency Structural Simulator), http://www.ansys.com.

[100] B. Gustavsen and A. Semlyen, "Rational approximation of frequency domain responses by vector fitting", IEEE Trans. Power Delivery, vol. 14, no. 3, pp. 1052-1061, July 1999; http://www.sintef.no/Projectweb/VECTFIT/.

[101] M. K. Zinn, "Network Representation of Transcendental Impedance Functions", Bell System Technical Journal 31, 378 (1951).

[102] W. Hendrickx, and T. Dhaene, "A discussion of rational approximation of frequency domain responses by vector fitting", IEEE Trans. Power Systems, vol. 21, no. 1, pp. 441-443, Feb. 2006.

[103] B. Gustavsen and A. Semlyen, "Enforcing passivity for admittance matrices approximated by rational functions", IEEE Trans. Power Systems, vol. 16, no. 1, pp. 97-104, Feb. 2001.

[104] D. P. DiVincenzo, Frederico Brito, and Roger H. Koch, "Efficient evaluation of decoherence rates in complex Josephson circuits," Phys. Rev. B 74, 014514 (2006).

[105] Joshua Dempster, Bo Fu, David G. Ferguson, D. I. Schuster, and Jens Koch, "Understanding degenerate ground states of a protected quantum circuit in the presence of disorder," Phys. Rev. B 90, 094518, (2014).

[106] M. Reagor, Hanhee Paik, G. Catelani, L. Sun, C. Axline, E. Holland, I.M. Pop, N.A. Masluk, T. Brecht, L. Frunzio, M.H. Devoret, L.I. Glazman, R.J. Schoelkopf, "Reaching 10 ms single photon lifetimes for superconducting aluminum cavities", Appl. Phys. Lett. 102, 192604 (2013).

[107] B. Yurke and J. Denker, "Quantum network theory," Phys. Rev. A 29, 1419-1437 (1984).

[108] Ioan M. Pop, Kurtis Geerlings, Gianluigi Catelani, Robert J. Schoelkopf, Leonid I. Glazman, and Michel H. Devoret, "Coherent suppression of electromagnetic dissipation due to superconducting quasiparticles," Nature 508, 369–372 (2014).

[109] M. Stern, Y. Kubo, C. Grezes, A. Bienfait, D. Vion, D. Esteve and P. Bertet, "Flux Qubits in Three-Dimensional Circuit-QED Architecture", arXiv:1403.3871.

[110] Wilkinson, James H. (1984). "The perfidious polynomial". In ed. by Gene H. Golub. Studies in Numerical Analysis. Mathematical Association of America.

[111] Brian D. O. Anderson and Sumeth Vongpanitlerd, *Network Analysis and Synthesis, A Modern Systems Theory Approach*, Dover Publications, Inc., Mineola, New York, 2006.

[112] B. D. O. Anderson, "Riccati Equations, Network Theory and Brune Synthesis: Old Solutions for Contemporary Problems", Dynamical Systems, Control, Coding, Computer Vision, Progress in Systems and Control Theory Volume 25, 1999, pp 1-25.

[113] Delson, Jerome King, *Networks involving ideal transformers*, Dissertation (Ph.D.), California Institute of Technology, (1953).

[114] Athanasios C. Antoulas, *Approximation of Large-Scale Dynamical Systems*, SIAM, Jun 25, 2009.

[115] B. Gustavsen and A. Semlyen, "A Robust Approach for System Identification in the Frequency Domain", IEEE Trans. Power Delivery, vol. 19, no. 3, pp. 1167-1173, July 2004.

[116] Mustafa Celik, Lawrence Pileggi, Altan Odabasioglu, *IC Interconnect Analysis*, Kluwer Academic Publishers, 2002.

[117] V. A. Yakubovic, "The Solution of Certain Matrix Inequalities in Automatic Control Theory", Doklady Akademii Nauk, SSSR, Vol. 143, 1962, pp. 1304-1307.

[118] R. E. Kalman, "Lyapunov Functions for the Problem of Lur'e in Automatic Control", Proceedings of the National Academy of Sciences, Vol. 49, No. 2, Feb. 1963, pp. 201-205.

[119] R. E. Kalman, "On a New Characterization of Linear Passive Systems", Proceedings of the First Allerton Conference on Circuit and System Theory, University of Illinois, Nov. 1963, pp. 456-470.

[120] V. M. Popov, "Hyperstability and Optimality of Automatic Systems with Several Control Functions", Rev. Roumaine Sci. Tech. - Elektrotechn. et Energ., Vol. 9, No. 4, 1964, pp. 629-690.

[121] B. D. O. Anderson, "A System Theory Criterion for Positive Real Matrices", SIAM Journal of Control, Vol. 5, No. 2, May 1967, pp. 171-182.

[122] B. D. O. Anderson and P. J. Moylan, "The Brune Synthesis in State-Space Terms", Circuit Theory and Applications, Vol. 3, 193-199 (1975).

[123] Cauer, W., "*Theorie der linearen Wechselstromschaltungen*", 2nd ed., Akademie-Verlag GmbH, Berlin, 1954.

[124] Cauer, W., "Synthesis of Linear Communication Networks", vols. I and II, 2nd ed., McGraw-Hill Book Company, New York, 1958.

[125] Belevitch, V., "Theory of 2n-terminal networks with applications to conference telephony", Electrical Communication, vol. 27, no. 3, p. 233, September, 1950.

[126] B. D. H. Tellegen, "The gyrator, a new electric network element", Philips Res. Rep. 3, pp. 81-101, April, 1948.

[127] B. D. O. Anderson, "Minimal Gyrator Lossless Synthesis", IEEE Transactions on Circuit Theory, vol. CT-20, no. 1, January 1973.

[128] Bayard, M., "Résolution du problème de la synthèse des réseaux de Kirchhoff par la détermination de réseaux purement réactifs", Câbles et Transmission, vol. 4, no. 4, pp. 281-296, October, 1950.

[129] Leroy, R., "Synthèse de réseaux passifs à n-paires de bornes", Câbles et Transmission, vol. 4, pp. 234-247, July, 1950.

[130] Bayard, M., "Synthesis of N-terminal pair networks", Proc. Brooklyn Polytech. Symp. Mod. Network Synth., vol. I, pp. 66-83, 1952.

[131] Bayard, M., *Théorie des réseaux de Kirchhoff*, Éditions de la Revue d'Optique, Paris, 1954.

[132] Newcomb, R. W., "A Nonreciprocal n-Port Brune Synthesis", Stanford Electronics Laboratories Tech. Rept. 2254-5, November, 1962.

[133] Newcomb, R. W., "The n-Port Brune Section Detailed", Stanford Electronics Laboratories Tech. Rept. 6554-7, December, 1963.

[134] Oono, Y., "Synthesis of a finite 2n-terminal network as the extension of Brune's two-terminal network theory", The Journal of the Institute of Electrical Communication Engineers of Japan, vol. 31, no. 9, pp. 163-181, August, 1948 (in Japanese).

[135] McMillan, B., "Introduction to formal realizability theory, II", Bell System Tech. J., vol. 31, no. 3, pp. 541-600, May, 1952.

[136] Tellegen, B. D. H., "Synthesis of 2n-poles by networks containing the minimum number of elements", J. Math. Phys., vol. 32, no. 1, pp. 1-18, April, 1953.

[137] Duffin, R. J., D. Hazony and N. Morrison, "Network Synthesis Through Hybrid Matrices", Case Institute of Technology Tech. Rept. AFCRL 63-568, August 18, 1964.

[138] Youla, D. C. and G. I. Zysman, "Synthesis of Passive Reciprocal n-Ports", Polytechnic Institute of Brooklyn Electrophysics Memo PIBMRI-1297-65, p. 37, November 8, 1965.

[139] Belevitch, V., "On the Brune process for n-ports", Trans. IRE Circuit Theory, vol. CT-7, no. 3, pp. 280-296, September, 1960.

[140] Newcomb, R. W., "On the n-port Brune resistance extraction", Trans. IEEE Circuit Theory, vol. CT-10, no. 1, p. 125, March, 1963.

[141] Newcomb, R. W., "On the simultaneous diagonalization of two semi-definite matrices," Quart. Appl. Math., vol. 19, pp. 144-146; July, 1961.

Acknowledgements

I would like to first thank my advisor David P. DiVincenzo for accepting me as a PhD student and giving me the opportunity to be a member of the IQI at RWTH Aachen. He guided me patiently in the course of the work that resulted in this thesis and he was always there to help whenever I needed it. I always felt lucky for being a member of IQI.

I would like to thank Guido Burkard not only for accepting to write a report for this thesis but also for being one of the developers of the circuit quantization formalisms that this thesis depends so heavily upon. It is interesting to note how natural it turned out to be to apply his methodology in [18] to quantize Brune circuits. I would like to thank Barbara Terhal for her lectures on quantum information where she was great at explaining concepts in a physical and intuitive way. I would like to thank Hélène for her administrative support and for tolerating my weird sense of humor. I thank Hendrik Bluhm and Carsten Honerkamp for accepting to join my defense committee. I thank Sebastian who just finished a great PhD work and explained me patiently all the regulations for the submission of this thesis, and especially for translating the summary to German.

I greatly enjoyed the last three years thanks to Piotr, Sebastian, Christoph, François, Giovanni, Lauri, Shabir, Adrian, Manuel, Nikolas, Jascha, Fabian and Norbert with whom we shared wonderful moments not only in our offices but also at the bars of Aachen and in the streets of Amsterdam, Berlin, Brugges, Palermo, Luxey, Bordeaux and Istanbul. Thanks to my "bon vivant" friend François for showing us the French way of enjoying the life. "Grazie!" Giovanni for making me start to do sports again and teaching me to enjoy the nature and cooking during almost two years we have been flatmates. I thank all the other members of IQI that I didn't mention here for creating the nice atmosphere of IQI. I thank Can, Aytaç, Yusuf and Ufuk for the time we shared during our lunch breaks. I would like to thank my "musahip" Utku for keeping me company in our trips to Italy, Spain and Portugal. I thank my cousins Murat and Cemil, uncle Muzaffer, aunt Bedriye and all the other members of Deniz Kebap Haus for making my life in Aachen more colorful.

Finally I would like to thank my parents for their love and constant support. Mom I am sure that you will stay strong as always and recover quickly from the surgery. Grandpa, I think that my scientific journey is strongly connected to yours which started in a Village Institute in the early forties, thanks to I. H. Tonguç. And Dad, we would have enjoyed discussing about the quantum computer.